Science

26 July 2013 | $10

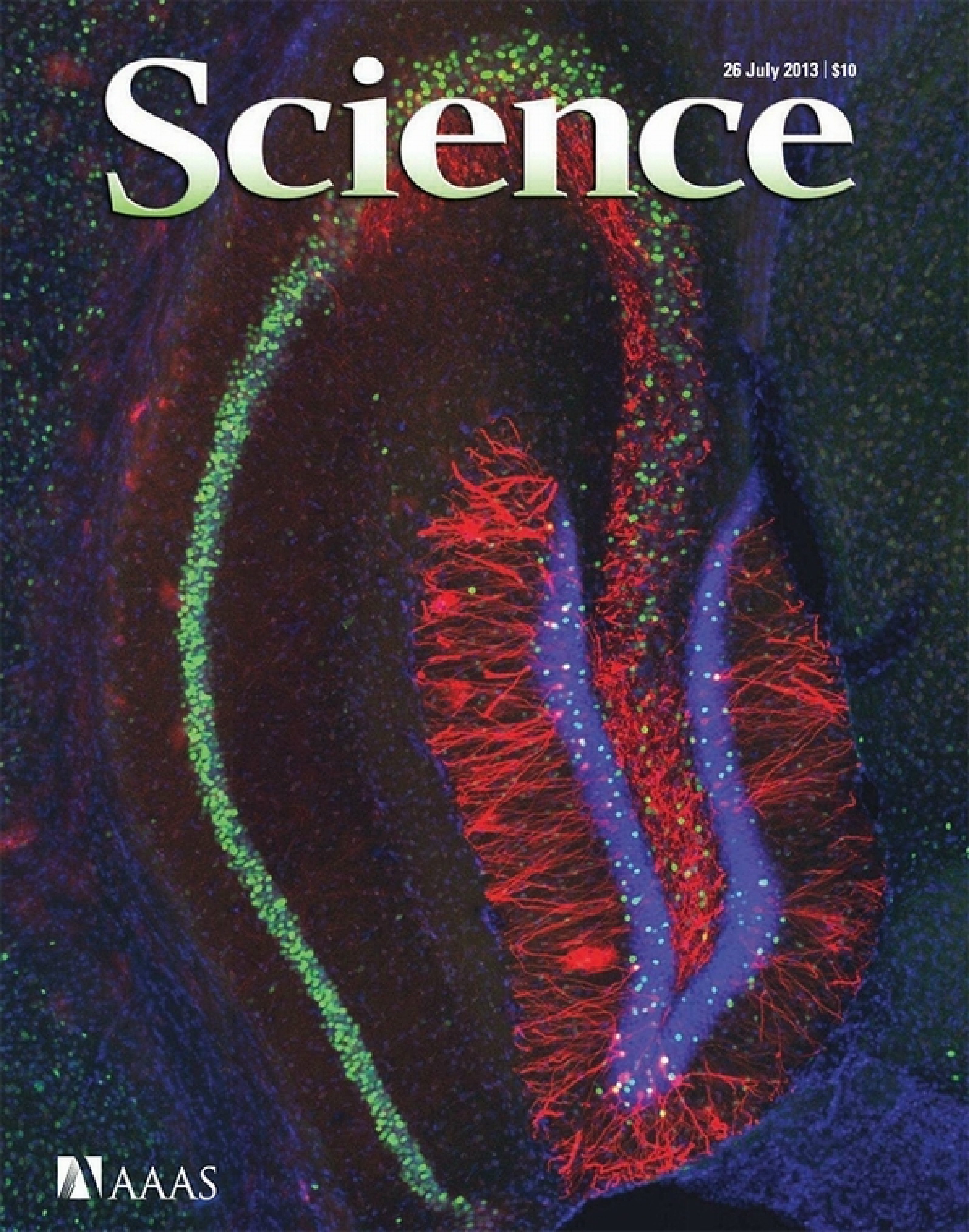

AAAS

CONTENTS continued >>

page 334

page 344

ON THE WEB THIS WEEK

>> *Science* Podcast
Listen to stories on our many genomes, implanting false memories in mice, science in Turkey, and more.

>> Find More Online
Check out *Science* Express, our podcast, videos, daily news, our research journals, and *Science* Careers at **www.sciencemag.org**.

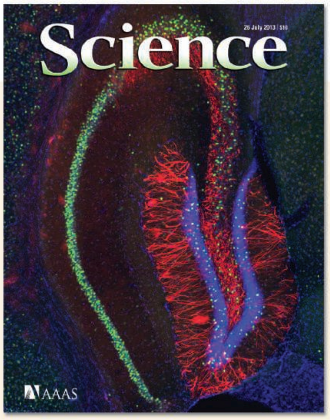

COVER

Immunostained fluorescence microscopy image of memory engram–bearing cells (red) in the dentate gyrus of a mouse hippocampus (image width: 1.5 millimeters). These cells were genetically tricked to express the protein channelrhodopsin-2 during memory formation, thus becoming responsive to light stimulation. When the cells were activated by light, the mice simultaneously associated a genuine memory with an undesirable event (a foot shock) to create a new but false memory. See page 387.

Image: Xu Liu and Steve Ramirez

DEPARTMENTS

REPORTS

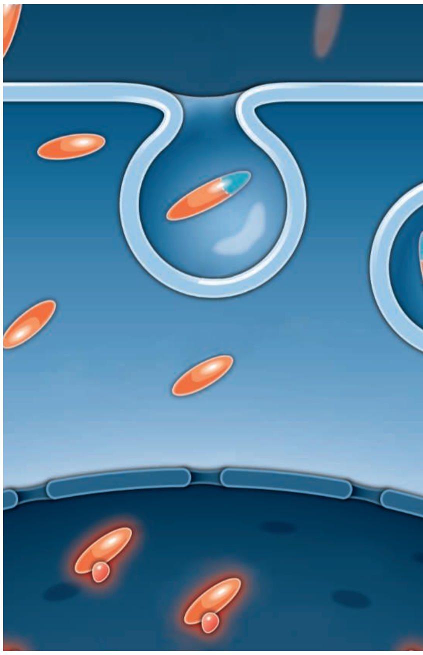

pages 355, 395, & 399

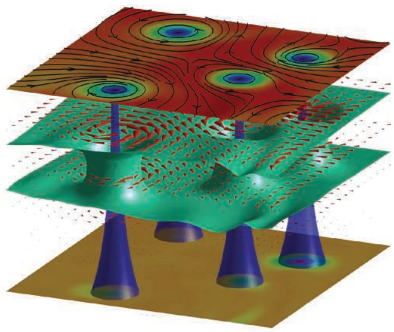

page 368

SCIENCE (ISSN 0036-8075) is published weekly on Friday, except the last week in December, by the American Association for the Advancement of Science, 1200 New York Avenue, NW, Washington, DC 20005. Periodicals Mail postage (publication No. 484460) paid at Washington, DC, and additional mailing offices. Copyright © 2013 by the American Association for the Advancement of Science. The title SCIENCE is a registered trademark of the AAAS. Domestic individual membership and subscription (51 issues): $149 ($74 allocated to subscription). Domestic institutional subscription (51 issues): $990; Foreign postage extra: Mexico, Caribbean (surface mail) $55; other countries (air assist delivery) $85. First class, airmail, student, and emeritus rates on request. Canadian rates with GST available upon request, GST #1254 88122. Publications Mail Agreement Number 1069624. **Printed in the U.S.A.**

Change of address: Allow 4 weeks, giving old and new addresses and 8-digit account number. **Postmaster:** Send change of address to AAAS, P.O. Box 96178, Washington, DC 20090–6178. **Single-copy sales:** $10.00 current issue, $15.00 back issue prepaid includes surface postage; bulk rates on request. **Authorization to photocopy** material for internal or personal use under circumstances not falling within the fair use provisions of the Copyright Act is granted by AAAS to libraries and other users registered with the Copyright Clearance Center (CCC) Transactional Reporting Service, provided that $30.00 per article is paid directly to CCC, 222 Rosewood Drive, Danvers, MA 01923. The identification code for *Science* is 0036-8075. *Science* is indexed in the *Reader's Guide to Periodical Literature* and in several specialized indexes.

THIS WEEK IN Science

EDITED BY STELLA HURTLEY

Neutron Star Measurements

Neutron stars are one of the densest manifestations of matter in the universe. **Yagi and Yunes** (p. 365) examined the moment of inertia of neutron stars, which determines how fast they can spin, and the quadrupole moment and tidal Love number, which determine how much they can be deformed. The findings suggest that these three quantities obey universal relationships that are independent of the internal structure of the stars, implying that measurements of one of the three could accurately predict the other two.

Holographic Turbulence

Turbulence in a superfluid presents an even more challenging theoretical problem than classical turbulence. **Chesler *et al.*** (p. 368) studied simulated superfluid turbulence using holographic duality. The direction of the energy flow in a two-dimensional superfluid was opposite to that in classical fluids—the energy injected at long length scales dissipated at short length scales through the vortices that form in a turbulent superfluid.

Rust Resistance

The rusting of iron and steel can be prevented through the addition of 11% or more chromium. The addition of molybdenum can enhance the corrosion resistance, with a complex interplay between the Cr and Mo atoms. However, if chemical variations exist, corrosion can still occur in localized regions or if the surface layer is mechanically abraded. **Duarte *et al.*** (p. 372) studied the

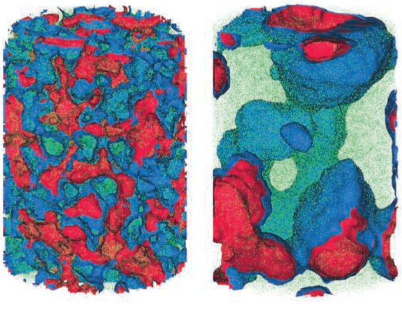

corrosive failure of an iron-based glassy alloy. A combination of atom probe tomography, electron microscopy, and x-ray diffraction was used to build up a near atomistic picture of local variations in the metal as it was heated and allowed to crystallize, and the impact these processes have on the corrosion resistance.

Glucose Control Goes Out on a Limb >>

Roux-en-Y gastric bypass, a surgical procedure used to induce weight loss in morbidly obese patients, often leads to permanent remission of diabetes, even when patients regain weight. Studying a rat model, **Saeidi *et al.*** (p. 406; see Perspective by **Berthoud**) found that the surgically reconfigured intestinal segment (the Roux limb) underwent an adaptive response characterized by increased glucose uptake and utilization, apparently triggered by exposure to undigested nutrients. As a result of this change, the intestine provided a major tissue for whole-body glucose control. Whether the same adaptive response occurs in the human intestine remains to be examined.

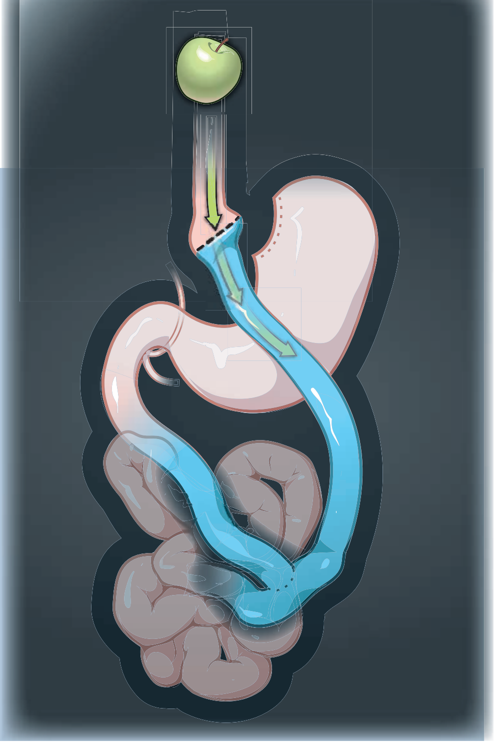

Sweet Variety

Proteins fold into a great variety of shapes—but, topologically, they always start as a more or less straight line of linked amino acids. In contrast, carbohydrates manifest a range of structures in which the sugar building blocks connect through multiple branch points. **Wang *et al.*** (p. 379, published online 26 July; see the Perspective by **Kiessling and Kraft**) designed a versatile precursor that could be transformed into many different branched glycans with distinct building blocks along each branch.

Can You Trust Your Memory?

Being highly imaginative animals, humans constantly recall past experiences. These internally generated stimuli sometimes get associated with concurrent external stimuli, which can lead to the formation of false memories. **Ramirez *et al.*** (p. 387; see the cover) identified a population of cells in the dentate gyrus of the mouse hippocampus that encoded a particular context and were able to generate a false memory and study its neural and behavioral interactions with true memories. Optogenetic reactivation of memory engram–bearing cells was not only sufficient for the behavioral recall of that memory, but could also serve as a conditioned stimulus for the formation of an associative memory.

PTEN Variations

The product of the tumor suppressor gene *phosphate and tensin homolog on chromosome ten* (***PTEN***) is a lipid and protein phosphatase that regulates important cellular processes, including growth, survival, and metabolism (see the Perspective by **Leslie and Brunton**). Though PTEN is best known for effects on the phosphatidylnositol 3-kinase (PI3K) signaling pathway, the PTEN protein is also found in the nucleus. **Bassi *et al.*** (p. 395) found that PTEN's presence in the nucleus was regulated in response to covalent modification of the protein by SUMOylation and phosphorylation. Cells lacking nuclear PTEN showed increased sensitivity to DNA damage and underwent cell death if the PI3K pathway was also inhibited. **Hopkins *et al.*** (p. 399, published online 6 June) discovered an alternative translation start site in human PTEN messenger RNA that allowed expression of a protein, PTEN-Long, with about 170 extra amino acids. The unusual enzyme was released from cells and then taken up into other cells. In a mouse tumor model, uptake of the enzyme inhibited the PI3K pathway and inhibited tumor growth.

A Gene for Early Acceptance

One of the fundamental properties of the immune system is the ability to distinguish self- from nonself–histocompatibility. To gain insight into the evolution and molecular basis of histocompatibility, **Voskoboynik *et al.*** (p. 384) sought to determine the genetic basis for a natural transplantation reaction that occurs in *Botryllus schlosseri*, a colonial urochordate. Compatibility allows vascular fusion among individuals, whereas incompatibility results in an inflammatory rejection response. A single gene determined the outcome of the reaction. Like histocompatibility genes in higher organisms, this gene is polymorphic and is expressed in the tissues that participate in the transplantation reaction.

CREDITS (TOP TO BOTTOM): Y. HAMMOND/SCIENCE; DUARTE ET AL.

Published by AAAS

Additional summaries

Infectious Information?

Much of the recent work on how individuals in social networks behave has relied upon the established Susceptible, Infectious, Recovered model developed in epidemiology. Information, however, differs from disease in one respect, namely that an individual might acquire information and yet not use it (or become "infected" by it). **Banerjee *et al.*** (p. 363) examined the spread of information about microfinance and its adoption in 43 villages in Karnataka, a state in southern India. Adopters of microfinance were more likely to pass information about it on, and a new measure—diffusion centrality—of the first person to learn new information predicted how widely and quickly others would be likely to make use of it.

Not mTORCing

Inhibition of the protein kinase complex mTORC1 has potentially beneficial therapeutic affects that include inhibition of cancer and extension of life span. However, effects of its inhibition in vivo have sometimes been disappointing. One reason may be that the well-studied inhibitor of mTORC1, rapamycin, inhibits some effects of mTORC1 but not others. In line with this idea, **Kang *et al.*** (p. 364) show that the effect of rapamycin depends on the substrate. Characteristics of the phosphorylation sites on various substrates caused them to be phosphorylated with different efficiency by mTORC1. The substrates that were most efficiently phosphorylated were resistant to inhibition of mTORC1. The results explain how various sites, sometimes within the same protein, can differ in their sensitivity to rapamycin.

Order, Order

The structure of glassy materials, which are known to have short-range order but no long-range pattern, continues to be a puzzle. One current theory is that some glassy materials possess icosahedral ordering, a motif that cannot show translational periodicity. **Hirata *et al.*** (p. 376, published online 11 July) obtained diffraction patterns from subnanometer volumes in a metallic glass, which show some, but not all, of the expected features of an icosahedron. Simulations suggest that the patterns arise from icosahedrons distorted to include features of the face-centered cubic structure. This observation is different from the predictions of molecular dynamics simulations and provides pivotal information in understanding the competition between the formation of the globally inexpensive long-range order and the locally inexpensive short-range order.

In a FtsZ

FtsZ is a guanosine triphosphatase that polymerizes into protofilaments at the bacterial division site. FtsZ recruits the accessory division proteins to the septum and also provides mechanical forces needed to constrict the membrane and reduce the cell width. However, how FtsZ generates mechanical force is unclear. While one popular model suggests that mechanical forces are generated by means of a change in FtsZ structure induced by guanosine triphosphate hydrolysis, nucleotide-dependent conformational transitions have yet to be observed in FtsZ monomer structures. Such transitions may be a feature of FtsZ only in its native protofilament-forming state. **Li *et al.*** (p. 392) sought to resolve this question by obtaining high-resolution structures of guanosine diphosphate–bound FtsZ filaments. The results suggest a complex and dynamic FtsZ protofilament network with a high degree of plasticity that is capable of generating forces to drive cytokinesis, during cycles of hydrolysis, while maintaining the structural integrity of individual monomers.

Whence the "Eat Me" Signal?

Cells are surrounded by a lipid bilayer, the composition of which is asymmetrical and serves as a marker of the physiological status of the cell. The phospholipid, phosphatidylserine (PtdSer), is normally found only on the inner leaflet of the membrane, but in dying cells it appears on the cell surface, thus providing the phagocytes tasked with cleaning up such cellular debris with a way to recognize cells undergoing cell death. Such movement of phospholipids within the membrane requires an elusive enzyme known as a scramblase. **Suzuki *et al.*** (p. 403; published online 11 July) identified an enzyme, Xkr8, which appears to act as a scramblase that promotes exposure of PtdSer on the surface of dying mammalian cells. Consistent with such a role, Xkr8 was activated after cleavage by caspase 3, a key protease that promotes apoptotic cell death. Genetic studies with the homolog of Xkr8 expressed in *Caenorhabditis elegans* indicated that the protein played a similar role in tagging dead cells in the nematode worm during development.

H7N9 Adaptation

Puzzling and alarming reports of an outbreak in early 2013 of human infections by a low-pathogenicity avian influenza virus has rocked the poultry industry in central eastern China and brought fears of initiating a human pandemic. Over 130 human cases have been reported with 37 deaths until closure of poultry markets accompanied a near-cessation of human case reports. From surveillance sampling of >10,000 isolates obtained during April 2013, **Zhang *et al.*** (p. 410, published online 18 July) took 37 isolates of avian origin H7N9 and compared them to human H7N9 isolates. The majority of H7N9 isolates came from live poultry markets, although some originated in pigeons. Sequence analysis indicated that the chicken isolates had retained the avian characteristics at sites on the influenza genes for PB2 and the surface hemagglutinin HA, where adaptive mutations have been observed before. Sequence analysis also showed a higher variability in the internal genes than in HA and neuraminidase NA. By using glycan arrays, it was shown that avian and human isolates bound to human, but also to some extent to avian, receptors. As expected, the virus replicated well in chickens without causing disease, whereas in mice only the human isolates were highly pathogenic. The human virus, but not the avian, transmitted between ferrets through the air.

Marcia McNutt is Editor-in-Chief of *Science*.

Leveling the Playing Field

THIS MONTH, THE PRESIDENTS OF THE U.S. NATIONAL ACADEMY OF SCIENCES, THE NATIONAL Academy of Engineering, and the Institute of Medicine—together known as the National Academies—reaffirmed their support for the Committee on Women in Science, Engineering, and Medicine (CWSEM). One of the few standing committees to have the support of all three academies, CWSEM's mandate is to coordinate, monitor, and promote action to increase the participation of women in science, technology, engineering, and mathematics (STEM) disciplines. Given claims that "the leaky pipeline" is a myth, because losses from STEM fields are compensated for by transfers in from other disciplines during the undergraduate years,* is there still a need to advocate for more women in STEM disciplines from a high-level group such as CWSEM?

The answer is a resounding yes. Even if an adequate supply of STEM professionals emerges from undergraduate institutions, data show that women don't advance professionally at the same rate as men. In academia, many women opt for non–tenure-track, part-time, and adjunct faculty positions to accommodate family demands.† Similar trends exist in industry and government sectors, with women holding a higher proportion of part-time, shared, and low-tier positions. As a nation, we are squandering highly trained talent and spending too much time and resources on unnecessary searches and recruitments to replace those who don't advance in their careers or who drop out of the STEM workforce entirely because of work/life issues that affect them disproportionately.

According to a recent study, although women in the United States retire at the same age as men, their retirement income is on average 29% less, because they lose ground in terms of their salary and career advancement with each child they rear. Men, as fathers, experience no such penalty.† Such family issues affect all women in academia but are more pronounced for women in the STEM disciplines, where women remain underrepresented in many fields.

Although work/family issues are cited as a factor challenging the advancement of all professional women, the coincidence of childbearing years with the period of time when a faculty member must build a strong research portfolio for tenure puts academic women at a particular disadvantage. Too many women believe that they must choose between motherhood and reaching their highest career potential. Further, data show that women also carry a large share of community service work, serving on evaluation panels, committees, advancement efforts, etc., as all organizations strive for diverse input. This contribution is conducted on top of research and teaching responsibilities and counts for little or nothing toward tenure and other advancement milestones. Some universities and other employers have instituted policies that attempt to mitigate these additional burdens, but the dilemma is that the policies may go against unwritten cultural expectations about what young professionals need to do to be successful in the eyes of their peers. If no male faculty members take time out to care for a newborn while on the tenure clock, it is hard to convince a woman that she will not be perceived as less committed to or serious about her career. Policies can only be effective if they take into account the culture of the organization.

CWSEM is working to level the playing field for all women in STEM disciplines, whether they are found in academia, in government, or in industry. The committee shares data and expertise, raises awareness about promising programs and proven successes, and builds a community committed to stemming the waste of talent and resources when careers are stunted unnecessarily. When hundreds of thousands of dollars are invested in the training of each STEM graduate student, supporting CWSEM to help find better ways for all women in STEM occupations to ultimately reach their true potential is a wise investment.

— Marcia McNutt

10.1126/science.1242309

*Y. Xie, A. Killewald, *Is American Science in Decline?* (Harvard Univ. Press, Cambridge, MA, 2012). †M. A. Matson, N. H. Wolfinger, M. Goulden, *Do Babies Matter? Gender and Family in the Ivory Tower* (Rutgers Univ. Press, Rutgers, NJ, 2013).

CREDITS: (TOP) STACEY PENTLAND PHOTOGRAPHY; (RIGHT) ZHUDIFENG/ISTOCKPHOTO.COM

Published by AAAS

EDITED BY GILBERT CHIN AND MARIA CRUZ

DEVELOPMENT

A Dish of Pancreas

Many cell lines of induced pluripotent stem cells (iPSCs) have been generated from tissue taken from patients with various medical conditions. The aim has been to use these as model systems ("disease in a dish") to study the biology of pathogenesis; as the iPSCs differentiate, cellular phenotypes characteristic of the early stages of the disease can reappear. At present, the prognosis of individuals with pancreatic ductal adenocarcinoma (PDAC) is poor, with a survival rate of less than 5%, and early diagnosis is rarely achievable. Furthermore, the available mouse and human cell models do not recapitulate the early stages of progression of this cancer. Kim *et al.* have now generated an iPSC line from a late-stage human pancreatic cancer. The cells resemble the human cancer cells in morphology and histology, and when these cells were injected into immunodeficient mice, pancreatic intraepithelial neoplasia lesions progressed to invasive PDAC. An analysis of these cells identified proteins that are secreted or released, as well as networks, such as TGFß1 and integrin signaling. In particular, the HNF4A pathway is specific for early to intermediate stages of progression. — BAP

Cell Reports **3**, 10.1016/j.celrep.2013.05.036 (2013).

BIOMEDICINE

Without Worms Within

Some humans share several characteristics with pigs, including very similar parasitic worms. *Ascaris* spp. roundworms are large, pungent, and can occur in sufficient numbers to block the gut, pierce the peritoneum, and invade the bile duct. In children, the morbidity caused by a heavy worm infection can have lifelong consequences. Surprisingly perhaps, roundworms can be killed by a *Bacillus thuringiensis* (Bt) toxin a bacterium more usually encountered in crop pest control. Urban *et al.* have been exploring the potential of one Bt toxin, Cry5B, as an anthelmintic (a deworming drug), using young pigs as a human substitute. Experiments on the mode of action in the classic worm model *Caenorhabditis elegans* showed that Cry5B binds to galactose-containing glycolipid receptors found only in invertebrates, and this was confirmed to be the case in *Ascaris*, too. Cry5B was given by gavage to groups of five piglets as spore crystal lysate in two doses (20 mg/kg) at 10 and 12 days after infection, when the penultimate larval worm stage emerges into the gut (unfortunately, there are severe practical constraints on testing the limited-availability Bt toxin on the slow-growing adult worms), and 6 days later, 97% of these larvae were dead and the remainder disabled. The natural product Cry5B could thus be a valuable addition to the anthelmintic roster, especially as resistance is emerging to the standard drugs. — CA

PLoS Negl. Trop. Dis. **7**, e2263 (2013).

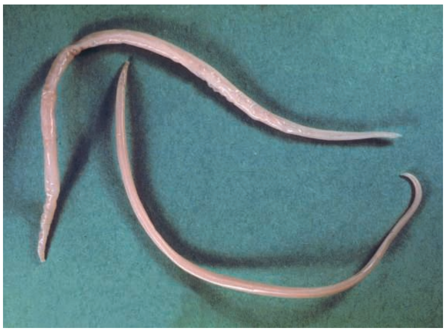

CREDITS (TOP TO BOTTOM): DYCJ/IMAGINECHINA/AP IMAGES; ALAN R. WALKER/WIKIMEDIA COMMONS

ENVIRONMENT

Unintended Consequences

Half a century ago, in what probably seemed like an entirely beneficent central planning program, coal for winter heating was provided free of charge to homes north of the River Huai in China for several decades. Burning this coal released particulate matter that contributed to a decline in air quality. Through a painstaking accumulation of data on suspended particulates in the 1980s and 1990s, coupled to a regression discontinuity design—in essence, assuming that unobservable parameters change smoothly from one side of the river to the other and checking to ascertain whether observable parameters obey this assumption—Chen *et al.* are able to demonstrate that the concentration of particulates shifts abruptly from about 400 mg/m^3 on the south side to 600 mg/m^3 on the north bank. What is rather worrisome is that they also find that life expectancy drops by about 5 years when crossing the river from south to north. The higher mortality rate is due to an increase in cardiorespiratory disease, such as stroke and lung cancer, and not to other cancers. — GJC

Proc. Natl. Acad. Sci. U.S.A. **110**, 10.1073/pnas.1300018110 (2013).

ASTRONOMY

A Captured Black Hole?

NGC 1277, a compact lenticular galaxy located in the Perseus Cluster, hosts a black hole 17 billion times as massive as the Sun. Most galaxies are thought to have a massive black hole at their centers, but it usually represents only 0.1% of the mass of the stellar bulge of the galaxy. The black hole in NGC 1277 accounts for 59% of the stellar bulge mass. Shields and Bonning propose that such an overweight black hole did not form in NGC 1277 but was instead captured from another, much larger galaxy, where ultra-massive black holes are more likely to form. They suggest that the black hole formed through the merger of two giant elliptical galax-

Continued on page 321

Continued from page 319

ies, each containing a massive black hole. The inspiral of the two black holes resulted in the ejection of the larger black hole produced by merger. The ejected black hole then wandered in the core of the cluster until it got captured by NGC 1277 during a chance encounter. — MJC

Astrophys. J. **772**, L5 (2013).

CHEMISTRY

Forcing Patterns onto Graphene

The Diels-Alder reaction is used to create ring compounds between dienes and dienophile, which include a variety of substituted alkenes. A recent study showed that double bonds in the graphene surface can also act as dienophiles at elevated temperatures (50°C). Bian *et al.* harnessed this reactivity for patterning single-layer graphene supported on silica surfaces. They synthesized diene-bearing molecules—cyclopentadiene molecules functionalized either with a Raman-active dye or with electrochemically active ferrocene—and created an ink of these molecules with polyethylene glycol (PEG). They then loaded this ink onto an elastomeric tip array that was mounted on an atomic-force microscope tip and used it to write patterns. The Diels-Alder reaction has a negative activation volume and speeds up at elevated pressure. When sufficient force was applied with the elastomeric tips, the graphene reaction proceeded at room temperature. After washing off the PEG and unreacted molecules,

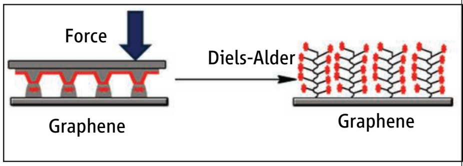

they imaged the patterns with Raman microscopy and observed changes in characteristic graphene bands indicative of covalent bonding at the surface. Cyclic voltammetry studies revealed a much higher coverage than would be expected from the density of reactive double bonds on graphene. The authors suggest that cyclopentadiene is undergoing further oligomerization reactions under these conditions. — PDS

J. Am. Chem. Soc. **135**, 9240 (2013).

SIGNAL TRANSDUCTION

Piping Calcium Around

Understanding the dynamic interactions of the components of signaling networks that control cell function is a central challenge for systems biology. Bandara *et al.* have adapted a strategy from engineers to get a better understanding of the controllers of free calcium concentrations in the cytoplasm and the endoplasmic reticulum; active and passive ion channels, pumps, and other regulatory proteins adjust the calcium levels in these intracellular compartments. Modeling such a system is confounded by incomplete characterization of the various components and variations in the responses of single cells in a population. The authors thus characterized the system with ordinary differential equation models built from detailed time-course measurements from large numbers of individual cells. This allowed them to extract estimates of key parameters and identify those most important to the cellular response. The results revealed the role of presenilin—a protein linked to Alzheimer's disease—in calcium handling and defined a feedback loop that controls the extrusion of calcium. — LBR

Sci. Signal. **6**, ra56 (2013).

EDUCATION

Modeling Conceptual Understanding

Reforms in biology education aim to develop students' understanding of biological processes in the context of systems, both within and across spatial and temporal scales. Concept maps are useful in this regard because they allow students to model their conceptual understanding in a hierarchical manner. Dauer *et al.* describe changes

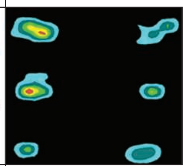

in student-constructed "Gene-to-Evolution" models over a semester of an introductory biology course in order to characterize changes in students' thinking about the genetic basis of evolution. Models were evaluated on the number of structures and relationship branches presented, as well as the quality of language used to describe them. In the first half of the course, models progressed from simple linear structures to complex ones with branches and connections. Over the second half of the course, the architecture of the models declined while the amount of correct information presented in the models continued to increase, suggesting that over time students were able to replace irrelevant information with appropriate language and relationship connections. These results suggest that learning a skill such as concept mapping should not be considered as a remedial activity, but rather as a skill that helps students improve systems thinking through a focus on conceptual relationships and the use of biological language. — MM

J. Res. Sci. Teach. 10.1002/tea.21094 (2013).

AROUND THE WORLD

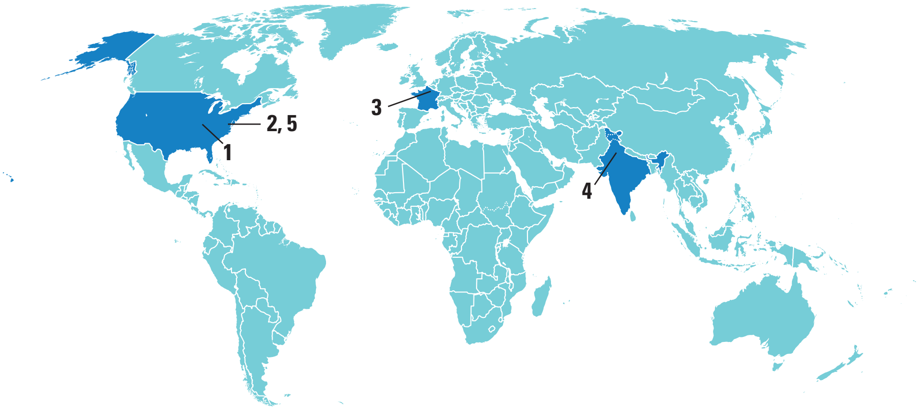

St. Louis, Missouri **1**

Monsanto Withdraws E.U. Patent Applications

In the wake of widespread opposition in Europe to genetically modified (GM) crops—including worldwide protests in May—biotech giant Monsanto announced on 17 July that it would withdraw pending applications for a handful of GM crops in the European Union, including several varieties of corn, a soybean variety, and a sugar beet. The decision, Monsanto president and Managing Director for Europe Jose Manuel Madero told Reuters, would allow the company to focus on its conventional seeds business in Europe. "[W]e are funding the business in a way that we haven't done for more than 15 years," he said. The company will not withdraw its application to renew the approval for insect-resistant MON810 maize, which was originally granted in 1998. MON810 is the only GM crop now grown commercially in Europe, although France, Germany, and Italy have imposed national bans on MON810 maize.

No grow. Protestors in London marched against Monsanto and GM crops in May.

Washington, D.C. **2**

FDA Approves First Medical Device for ADHD Diagnosis

The first medical device for diagnosing attention deficit/hyperactivity disorder (ADHD) in children 6 to 17 years old was approved by the Food and Drug Administration (FDA) last week. Called the Neuropsychiatric EEG-Based Assessment Aid (NEBA), the device measures electrical brain activity through electrodes on the scalp and calculates the ratio of "theta" waves—oscillations in neural firing at frequencies of 4 to 8 hertz—to "beta" waves, which pulse at 13 to 30 hertz. "A couple of decades of research" link a higher proportion of theta activity to beta activity to ADHD in children and adolescents, says Francisco Xavier Castellanos, a child psychiatrist at the New York University Child Study Center in New York City.

Although some researchers are skeptical of the ratio as a diagnostic tool, Castellanos says he's "cautiously optimistic" that the device will help clinicians correctly diagnose the disorder, which affects roughly 3% to 7% of school-aged children in the United States. FDA emphasizes that the device is not intended to be used alone to diagnose ADHD, but as part of a "multistep process based on a complete medical and psychiatric exam."

Paris **3**

Looser Restrictions on Human Embryo Research

The French National Assembly on 16 July approved a new law that aims to ease regulation of research involving human embryos and embryonic stem cells. The new law will permit such research provided it meets four criteria: that it has "scientific relevance"; that it is performed toward "a medical end"; that it "cannot be done without resorting to these embryos or the embryonic stem cells"; and that it respects ethical principles.

The change effectively reverses the French government's stance toward human embryo and stem cell research. Existing

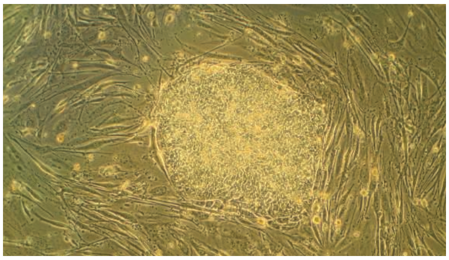

law essentially banned such research unless scientists could show government regulators that there was no other source of cells for their experiments and that the studies could lead to major medical advances.

French researchers say that the shift will bring little immediate change to their day-to-day work, but they hope that the new law will bring more academic freedom and collaboration and that it might make it easier for French researchers to work with industry partners interested in testing therapies derived from human embryo research.

http://scim.ag/Franceembryo

New Delhi **4**

Scientists: Freeze GM Trials

A six-member panel of scientists appointed by India's Supreme Court is seeking a moratorium on open field trials of genetically modified organisms (GMO) pending changes to India's regulatory system. The panel's report, made public on 22 July, states that the system "has major gaps and these will require rethinking,

NOTED

>The National Science Foundation announced 13 winners of its $10,000 BREAD (Basic Research to Enable Agricultural Development) Ideas Challenge on 16 July. Hundreds of agriculture researchers posed ideas for **the most pressing issues facing small farms in developing countries.** Among the winning challenges: proposals to find new ways to use gut biota in livestock to improve animal health and to create "tunable" soil microbe populations.

Worldwide Disease, by the Numbers

The World Health Organization (WHO) has just released its Global Burden of Disease (GBD) report for 2011. After all the debate about differences between WHO estimates and those of the Institute for Health Metrics and Evaluation (IHME) in Seattle, Washington, released last year, their estimates of the top 10 causes of death look very similar (*Science,* 14 December 2012, p. 1414). Both organizations agree on nine of the 10 biggest killers, although they rank them in slightly different orders. The biggest discrepancy is prematurity, which WHO ranks as 10 and IHME as 15. (WHO figures are for 2011; IHME for 2010.)

	WHO GBD 2011	IHME GBD 2010
1	Ischaemic heart disease	Ischaemic heart disease
2	Stroke	Stroke
3	Lower respiratory infections (LRI)	Chronic obstructive pulmonary disease (COPD)
4	Chronic obstructive pulmonary disease (COPD)	Lower respiratory infections (LRI)
5	Diarrhea	Lung cancer
6	HIV/AIDS	HIV/AIDS
7	Trachea, bronchus, and lung cancers	Diarrhea
8	Diabetes	Road injury
9	Road injury	Diabetes
10	Prematurity	Tuberculosis

investment and relearning to fix."

The panel is calling for mandatory "chronic and trans-generational toxicity studies" on rodents and faults the regulatory system for permitting field tests on GM crops like rice and brinjal, or eggplant, because "contamination" of native varieties "can't be ruled out."

If accepted by the court, a moratorium could be the "death knell for all research on genetic modification in India," says Swapan Dutta, chief of crop research at the Indian Council of Agricultural Research in New Delhi. The court will next seek a response from the government.

Washington, D.C. **5**

DOE Science Gets a New Look

U.S. Energy Secretary Ernest Moniz has pulled the trigger on a major shakeup of how the Department of Energy (DOE) manages its research programs. In an 18 July memo, Moniz announced that he will merge management of DOE's science and energy programs under a single undersecretary, who will also oversee the majority of the department's 17 national laboratories. "We must have the ability to closely integrate and move quickly among basic science, applied research, technology demonstration, and deployment," Moniz wrote.

Strengthening those linkages is especially important for deploying the clean energy technologies at the heart of efforts to combat climate change, he added. Moniz didn't say who is in line to get the new undersecretary job, which will oversee some $6 billion in research spending. But the move is getting good reviews from an array of outside groups, who have criticized a 2005 decision to split the energy and science portfolios between two undersecretaries (*Science*, 12 July, p. 119).

FINDINGS

'Female' Chromosome May Leave A Mark on Male Fertility

In humans, it's the Y chromosome that makes men, men—or so researchers have thought. But now scientists suggest that the X chromosome may also play a significant role in maleness. Using a special sequencing technique, the team looked at previously undecipherable portions of the X chromosome and found that it contains scores of genes that are active only in tissue destined to become sperm, researchers reported online this week in *Nature Genetics*. A 50-year-old theory had predicted that X genes would be stable through time and thus be quite similar across most mammals. That proved to be the case in the majority of X chromosome genes in mice and humans—which are also expressed in both sexes. But the new study found that 144 X genes in humans and 197 in mice have evolved since mice and human lineages split 80 million years ago—and many of those genes are expressed only in male germ cells. "The finding suggests that X chromosome gene content is probably changing all the time." says Jianzhi Zhang, an evolutionary geneticist at the University of Michigan, Ann Arbor.

http://scim.ag/Xchrom

New view of X. X chromosomes are not as steady and unchanging as researchers have thought them to be.

Do it. Following a command to imitate her owner, Adila touches the cone.

Copycat Dogs

Our canine pals are capable of copying a human behavior as long as 10 minutes after it's happened, scientists report this month in *Animal Cognition*—something that, until this discovery, only humans and apes were known to do.

Ádám Miklósi, a behavioral ethologist at Eötvös Loránd University in Budapest, worked with Italian dog trainer and Eötvös Loránd graduate student Claudia Fugazza to teach eight female adult pet dogs that ranged in age from 2 to 10 years old and were of various breeds. They wanted to teach the dogs not only to pay attention to a demonstrated behavior ("Do as I do") and imitate it ("Do it"), but also to wait before

>>

CREDITS (TOP TO BOTTOM): (SOURCES) WHO AND IHME; CLAUDIA FUGAZZA/ANIMAL COGNITION; HEMERA/THINKSTOCK

>>FINDINGS

doing so (or "deferred imitation," considered a sophisticated cognitive skill).

Each dog underwent 10 tests—and all the dogs, they found, were capable of deferred imitation. That, Fugazza says, suggests that dogs have declarative memory—long-term memory about facts and events that can be consciously recalled. Fugazza and Miklósi say they hope that trainers take advantage of dogs' willingness to learn by watching our actions. "They do it so naturally, because dogs are predisposed to learn socially from us," Miklósi says. **http://scim.ag/copydogs**

East Antarctic Ice Sheet Not So Stable?

To study future melting of the Greenland and Antarctica ice sheets—and resulting rising sea levels—many scientists look to the past. Current warm temperatures and greenhouse gas levels are reminiscent of the warm Pliocene Epoch that lasted from 5.3 million to 2.6 million years ago. Some data suggest that Pliocene sea levels peaked at perhaps 22 meters higher than today.

While satellite observations suggest that the West Antarctic Ice Sheet (WAIS) is now losing mass, the far larger East Antarctic Ice Sheet (EAIS) seems more stable. But data from the Pliocene suggest that the "stable" ice sheet may be more vulnerable to warming than thought, says Carys Cook, a doctoral student at Imperial College London.

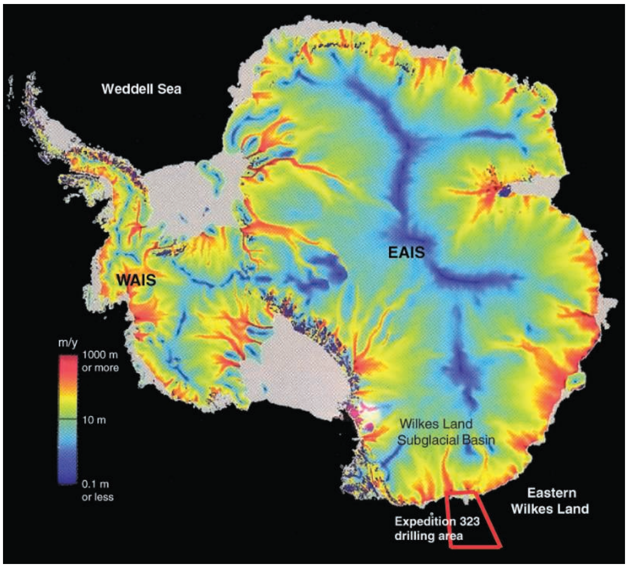

Exposed. Antarctica's Wilkes Land Subglacial Basin was ice-free during parts of the Pliocene.

Cook and her colleagues studied Pliocene sediments in a core off the coast of East Antarctica that reflect continental erosion patterns as the climate warmed and cooled. They found a unique geochemical "fingerprint"—a telltale ratio of neodymium to strontium isotopes—from the now ice-covered Wilkes Subglacial Basin in East Antarctica. For those sediments to have eroded and ended up offshore during the Pliocene, the basin would have had to be exposed by ice retreat, the team reported online on 21 July in *Nature Geoscience*. **http://scim.ag/EAISmelt**

Random Sample

Modern Trackers Decipher Ancient Footsteps

The Namibian San people are renowned trackers, deciphering footprints as a way of life. And these traditional skills can be a boon to archaeologists seeking expert opinions on cave footprints.

Conventional footprint analysis focuses on individual prints but leaves the context to the imagination of archeologists, says Andreas Pastoors, a prehistorian at the Neanderthal Museum in Mettmann, Germany. Pastoors, who has studied cave art in the French Pyrenees since 1988, turned his gaze to the ground this month, hoping to give life to 17,000-year-old footprints left on the floor of the caves.

In a pilot test this month, Pastoors and colleagues brought a trio of footprint-trackers of the Namibian San tribe to four caves nestled in the mountains. After just a few hours in each cave, the team challenged conventional wisdom about some of the footprints.

One print, long regarded as the only ice age shoeprint, was instead the product of a bare foot, the trackers declared. They demystified another track, traditionally interpreted as a ritual dance, as belonging to a child and an adult fetching clay; the footprints in one direction were deeper, hinting that the two were carrying a heavy load in that direction. Pastoors recorded the trackers' conversations to study how they arrive at their conclusions. He plans to take the San back to the caves to do more thorough analyses.

This approach is a "great idea," says Michael Hofreiter, an evolutionary biologist at the University of York in the United Kingdom. The San's interpretations, he adds, are more believable than the "fantasies" of archeologists.

CREDITS (TOP TO BOTTOM): INTEGRATED OCEAN DRILLING PROGRAM; UNIVERSITY OF COLOGNE (2)

PUBLIC HEALTH

Clinical Trials Paused As India Adopts New Rules

The explosive growth of clinical trials in India has slammed into reverse. In the wake of new Indian regulations aimed at protecting trial participants from abuse and unethical practices, a hold has been placed on new trials, including an unknown number funded by the U.S. National Institutes of Health (NIH). "From the beginning of this year, there have been no new clinical trials approved," says Suneela Thatte, a vice president in the Mumbai office of Quintiles, a contract research management firm.

Although human rights activists who pushed for the rules—announced in January—see them as a much-needed corrective to lax oversight of trials in India, others call them an overreaction. Indian officials and NIH top brass are seeking a middle ground that would allow trials to proceed while providing greater safeguards for subjects.

At issue is the liability that companies and institutions face when things go wrong for a trial participant. The new rules change the definition of a trial-related injury or death, essentially expanding the number of scenarios in which participants or their kin would be entitled to compensation. Now included are cases where a participant suffers because he or she received a placebo or did not receive the therapeutic benefit promised by the trial drug. The new rules, imposed by the Indian Ministry of Health and Family Welfare, also require that all ethics committees responsible for approving the protocols for clinical trials be licensed by a national authority.

Indian officials acknowledge that some of the changes are problematic. "There is a concern that the interpretation of adverse effects in these rules is extraordinarily broad, and that effectively means that many kinds of events that are not necessarily due to the trials themselves could be interpreted as being related to them," says K. VijayRaghavan, a biologist who heads India's Department of Biotechnology; he was not involved in framing the rules. VijayRaghavan applauds the government for tightening a weak regulatory framework, but says, "the pendulum went to the other end."

The impact has been felt around the world, including at NIH in Bethesda, Maryland, which according to initial media reports last week suspended about 40 trials that were under way or set to begin this year. "Some [NIH] trials have stopped enrollment and some others have been postponed," NIH said in a statement released last week, adding that "NIH hopes that future changes will enable studies to resume." A researcher who declined to be identified because NIH is restricting comment on the matter said that NIH Director Francis Collins sent a letter to the Indian government seeking relief. NIH has not responded to a query about the letter.

Celebrated case. Protests in India have focused on individuals like singer Sheela Geete (in framed photo), who died in 2010 while in a clinical trial.

CREDIT: *THE WASHINGTON POST*/GETTY IMAGES

Thatte, president of the Indian Society for Clinical Research, says that the new rules could hurt thousands of patients in India if they cause significant delays. "Global clinical trials are competitive," she says. "If one country does not come through with approvals, you make up by going to another country." Indian patients could lose "an opportunity to get access to the latest experimental therapies."

But Thatte does not deny the need for improved regulations to protect the rights of participants and ensure transparency. Some human rights activists go further, accusing multinational pharma companies of using poor Indians as guinea pigs in trials of risky drugs that would cost a lot more to try out on patients in the West.

One leader in this campaign is the Swasthya Adhikar Manch (SAM), or Health Rights Forum, a nonprofit that organized protests and last year filed public interest litigation in the Indian Supreme Court demanding tougher oversight of clinical trials. The petition alleged that drug testing caused hundreds of deaths for which families had received no compensation and that subjects were being recruited without proper informed consent.

In a hearing on the petition on 2 January, India's Supreme Court issued a stern rebuke to the government for its lax oversight. "Uncontrolled clinical trials are causing havoc to human life," the two-judge decision said, adding that the government had "slipped into deep slumber." The court directed the health secretary to take responsibility for oversight; traditionally, that charge has belonged to the Drug Controller General of India. The health department published the new rules weeks after the hearing.

The rules are now being amended to make them more balanced, says Maharaj Kishan Bhan, a former science administrator who serves on a panel that provides scientific advice to the prime minister. Meanwhile, another committee of experts is developing criteria for determining whether an injury or death is related to a trial. Expected in a few months, that report may include guidelines for determining compensation.

"Everybody should know that the Indian system is more stringent now," Bhan says. "The regulatory environment we are in the process of creating should also be predictable, efficient, and balanced."

The turbulence may not end soon, however. On 26 July, the Supreme Court is scheduled to hear arguments from SAM's lawyers about why the government should ban trials of "new chemical entities"—novel compounds that haven't been tested elsewhere.

–YUDHIJIT BHATTACHARJEE

With reporting by Eliot Marshall.

INFECTIOUS DISEASES

Bacterial Meningitis Finds New Niche in Gay Communities

BERLIN—For two young Berliners, what began as a fun night on the town in early May ended in tragedy. The 24-year-olds went home together after an evening out with friends at one of the many gay clubs here. The next day, one of them complained of fever and nausea. He never even made it to the doctor; 2 days later, he was found dead in his flat. The other man had similar symptoms, was hospitalized, and fell into a coma from which he hasn't woken up. Doctors say he has irreversible brain damage.

Both were infected with the bacterium *Neisseria meningitidis*, a notoriously fast killer. After their cases became known, Berlin public health officials found three other meningitis cases among gay men in the preceding months; two of them had died.

At risk. A 21-year-old man gets a meningitis shot at the AIDS Healthcare Foundation in West Hollywood (CA) on 15 April. Scientists have found *N. meningitidis* clusters in gay men in seven cities.

Neisseria meningitidis **clusters in MSM, 2001-2013**

The outbreak, described in a paper in *Eurosurveillance* on 11 July, is part of a series of clusters that has sowed fear in gay communities on both sides of the Atlantic in recent years. Shortly after Germany, France reported three similar cases, and Belgium one. On 3 July, the European Centre for Disease Prevention and Control advised countries to be on the lookout this summer—especially around major gay events—and to identify similar cases in the past. It also suggested vaccination in places where outbreaks occur—advice that Berlin has already followed. In the meantime, scientists are trying to figure out the reasons for the emerging pattern.

N. meningitidis infects people around the globe. Ten percent of us may be walking around with it at any given time; in most cases, the bacterium resides in the mucosa of the nose and throat for a few months without causing any symptoms. In some people, however, it crosses the mucosal barrier and causes meningitis (an infection of the membranes covering the brain), a bloodstream infection called sepsis, or both. The bacteria can cause the blood to clot, cutting off circulation to the extremities, which can make it necessary to amputate fingers, toes, or entire limbs. About 10% of patients die. The recent outbreaks are all *N. meningitidis* serogroup C, a particularly aggressive strain.

Meningococci are transmitted with throat or respiratory secretions, for instance when coughing or kissing, and outbreaks have been described among people living in close quarters, such as cruise ships and military camps. In 2001, Toronto doctors found the first small outbreak—six people, two of whom died—among men who have sex with men (MSM), as epidemiologists call the group. Chicago had a cluster in 2003, Los Angeles in 2012; New York City has seen the biggest outbreak so far, with 22 cases and seven deaths since 2010.

Why this is happening, and why now, is unclear. MSM have higher rates of HIV infection than the general population, which some studies suggest might be a risk factor for getting ill from *N. meningitidis*. But the disease has struck many HIV-negative men as well. The explanation for the clusters may simply be that a gay man carrying the bacterium is most likely to infect another gay man, says Amanda Cohn, an epidemiologist at the U.S. Centers for Disease Control and Prevention in Atlanta. "We have clusters in groups that have strong social networks, and the MSM community is very close," she says.

But Don Weiss, a researcher at the New York City Department of Health and Mental Hygiene, worries that the microbe may have found a new way to transmit. It has occasionally been found in the rectum and the urethra, he notes, suggesting that oral or anal sex could play a role. "If there is some irritation to the mucosa in the rectum, that could be a risk factor." Cigarette smoking, for example, is a known risk factor because it makes the mucosa in the nose and throat easier to invade, he says.

Or the microbe itself might have developed an affinity for rectal or urogenital mucosa. Microbiologist Ulrich Vogel of Germany's National Reference Laboratory for Meningococci in Würzburg, suggests testing whether bacteria isolated from MSM grow better on cells resembling those tissues. Further evidence could come from a case-control study that Weiss is working on, in which New York patients fill out a questionnaire, as do matching MSM, to tease out any behavioral differences.

Scientists are also studying the bacterial genome for answers. Early results show that all European cases belong to one so-called sequence type, known as ST-11, which has caused many recent outbreaks, including the one in New York. "That tells us they are all in the same family, but it is not enough to say that they are directly linked," says Vogel, who plans to fully sequence the German isolates soon. Weiss says that he is sequencing 60 to 80 isolates, most of them ST-11. "We are hoping to see whether there are any particular mutations that go along with being affected if you are MSM."

Over the past decade, many Western countries have added a vaccine that protects against one or more strains of meningitis, including serotype C, to their standard vaccination regimen for children or adolescents. Adults remain unprotected, however, which is why Berlin will start vaccinating its entire MSM population on 27 July. New York City and France also recommend the shots for certain groups of MSM. "The vaccine is cheap and effective," says Wiebke Hellenbrand of the Robert Koch Institute in Berlin. "And thank goodness we have one."

–KAI KUPFERSCHMIDT

CREDIT: DAMIAN DOVARGANES/AP

Published by AAAS

DEVELOPMENT

Biologists Tell Dueling Stories Of How Turtles Get Their Shells

The turtle is an animal wrapped in a mystery. Crocodiles and armadillos armor themselves in an exoskeleton of bony plates, but the turtle goes a step further with a shell that is anchored to its rib cage and spine, making it part of its internal skeleton. Just how the developing turtle embryo builds its fortress—a feat unique among vertebrates—is unclear. But two scenarios are now vying to explain this major evolutionary puzzle.

Until recently, many biologists thought that the turtle shell takes shape from skin cells adjacent to the ribs that are transformed into bone in the course of development. But Japanese developmental biologists have now weighed in with a new scenario, based on comparative studies of chicken, alligator, and soft-shell turtle embryos, in which the shell is a direct outgrowth of bones themselves. At a symposium at a meeting* earlier this month organized to try to reach consensus about turtle evolution, neither view carried the day—and some participants concluded that turtles may have more than one way to build a turtle shell.

"There's no resolution, but there is a step forward," says Jacqueline Moustakas-Verho, an evolutionary developmental biologist at the University of Helsinki who organized the session. A clearer understanding of how turtles build their shells could illuminate another mystery: which group of reptiles turtles evolved from, and their evolutionary path from a shell-less ancestor to the armored beasts of today.

Paleontologists once believed that the shell was akin to the exoskeleton of an armadillo. They thought that its bony substructure emerged from the convergence of bony plates called osteoderms in the embryo. But a decade ago, Scott Gilbert, a developmental biologist at Swarthmore College in Pennsylvania, traced embryonic development in red-eared sliders (*Trachemys scripta*) and snapping turtles (*Chelydra serpentina*) to show that the developing ribs take an unusual turn in turtles, elongating and flattening out, rather than curving around to the ventral wall, as they do in other vertebrates. The broadened bones eventually meet each other to form an underlying bony scaffolding for the shell. The shell itself forms, Gilbert proposed, when the skin cells on the outside receive bone morphogenetic protein (BMP) signals from the ribs. That causes them to harden and encase the scaffolding, forming the carapace. In hard-shell turtles, scutes made of keratin form on the top of this plate.

Some fossil evidence supports the idea that the shell evolved from skin. In thin sections of a proposed 260-million-year-old turtle ancestor called *Eunotosaurus* viewed under a microscope, the bone texture in certain parts of the shell looks like hardened skin cells—perhaps an early stage of shell evolution. And in dermal cells from some modern hard-shell turtles, Gilbert has detected a phosphorylated protein called Smad1, a marker that shows the cells are responding to BMP.

Shell gain. Studies of soft-shell turtles suggest that the shell is an outgrowth of the internal skeleton.

CREDIT: RIKEN

But at the meeting and in the 9 July issue of *Nature Communications*, Shigeru Kuratani and his team from the RIKEN Center for Developmental Biology in Kobe, Japan, proposed a different scenario. They meticulously tracked the emergence of membranes, connective tissues, dermal layers, and bone at each stage of development in soft-shell turtle embryos. Soft-shell turtles have most of the bony substructure of the shell, but it's covered with soft tissue, not scutes.

The researchers reported that the turtle ribs elongate and later broaden at their ends to become spoon-shaped, with a mass of bone at the end that Gilbert and colleagues did not see in their studies. In soft-shell turtles, the rib growth stops short of the dermis. At that point, an outer bone layer called the periosteum sends out bone cells to build up the outer layers of the dorsal shell. The work suggests that the shell comes from the internal skeleton, with no contribution from the skin or exoskeleton, contrary to Gilbert's scenario.

The Kuratani team's work is solid, but whether their picture of shell development holds for all turtles is unclear, Moustakas-Verho says. Paleontologists have long assumed that soft-shell turtles evolved from hard-shell turtles that lost the scutes and some of the bones at the edge of the shell somewhere along the way. Gilbert and others have argued that they might develop differently than other turtles.

Kuratani's RIKEN colleague Tatsuya Hirasawa says that it shouldn't matter if soft-shell turtles preceded or followed hard-shell turtles in evolution. The early developmental stages that he and his colleagues are studying are directed in part by a structure called the carapacial ridge, a lump on the back of the developing embryo that all turtles—and no other vertebrates—have. It controls the growth and distribution of ribs to the sides and ultimately forms the edge of the shell carapace.

Gilbert thinks that both he and Kuratani may be right, with some species depending on dermal cells that engulf the ribs and are triggered by proteins to ossify, while others rely on bone growth only to complete their shells. And at the meeting, several researchers agreed that studies of more species may help clarify how soft-shell turtles are different from hard-shell turtles and what aspects of shell development are common to all turtles, if any. "Just as we say '*Drosophila* development' and not 'insect development' because *Drosophila* development differs from other insects, and just like we say '*Xenopus* development' rather than 'amphibian development' because amphibians differ enormously in their developmental patterns, we might also have to specify our species of turtles," Gilbert says. "Despite the similarity of anatomy, they may use different means to get there."

–NAOMI LUBICK

Naomi Lubick is a freelance writer based in Stockholm.

*10th International Congress of Vertebrate Morphology, 8–12 July, Barcelona, Spain

PARTICLE PHYSICS

At an Impasse, U.S. Particle Physicists Gather by the River to Plan and Dream

In the 1980s and '90s, particle physicists in the United States would gather every few summers at a ritzy Colorado ski resort called Snowmass to take stock of their field and plan their next big projects. Next week, for the first time since 2001, U.S. particle physicists will meet once again for such a retreat. But this time they'll convene in a less lofty spot—the University of Minnesota, Twin Cities—in a meeting billed as "Snowmass on the Mississippi."

The comedown in venue was imposed by recent limits to government spending on conferences, but it seems symbolic of the plight of U.S. particle physics. Adjusted for inflation, the Department of Energy's (DOE's) budget for high-energy physics, now $752 million, has fallen by 15% over the past decade. More U.S. experimenters now work abroad than at the United States' sole particle physics lab, Fermi National Accelerator Laboratory (Fermilab) in Batavia, Illinois, whose flagship accelerator was shut down in 2011. Europe, not the United States, bagged the Higgs boson, the last piece of physicists' standard model of the known particles. And some U.S. physicists are lukewarm about Fermilab's major project for the coming decade: the so-called Long-Baseline Neutrino Experiment (LBNE).

The Snowmass meeting won't settle on a new way forward, says Jonathan Rosner, a theorist at the University of Chicago in Illinois and chair of the American Physical Society's Division of Particles and Fields. Instead, physicists will simply explore all the options for the future, which include schemes as ambitious as a 100-kilometer-long atom smasher or a collider for exotic particles called muons. "What we can provide is a narrative that we can carry forward and explain to nonphysicists why the field deserves continuing support," Rosner says. Physicists will prepare a set of white papers describing the scientific opportunities, he says. A separate Particle Physics Project Prioritization Panel (P5) will set priorities over the next year.

At the time of the last Snowmass meeting, the U.S. particle physics program was the world leader. Fermilab had the world's highest-energy atom smasher, the 7-kilometer-long Tevatron, which blasted protons into antiprotons and had discovered a particle called the top quark. Smaller electron-positron colliders were running at SLAC National Accelerator Laboratory in Menlo Park, California, and at Cornell University.

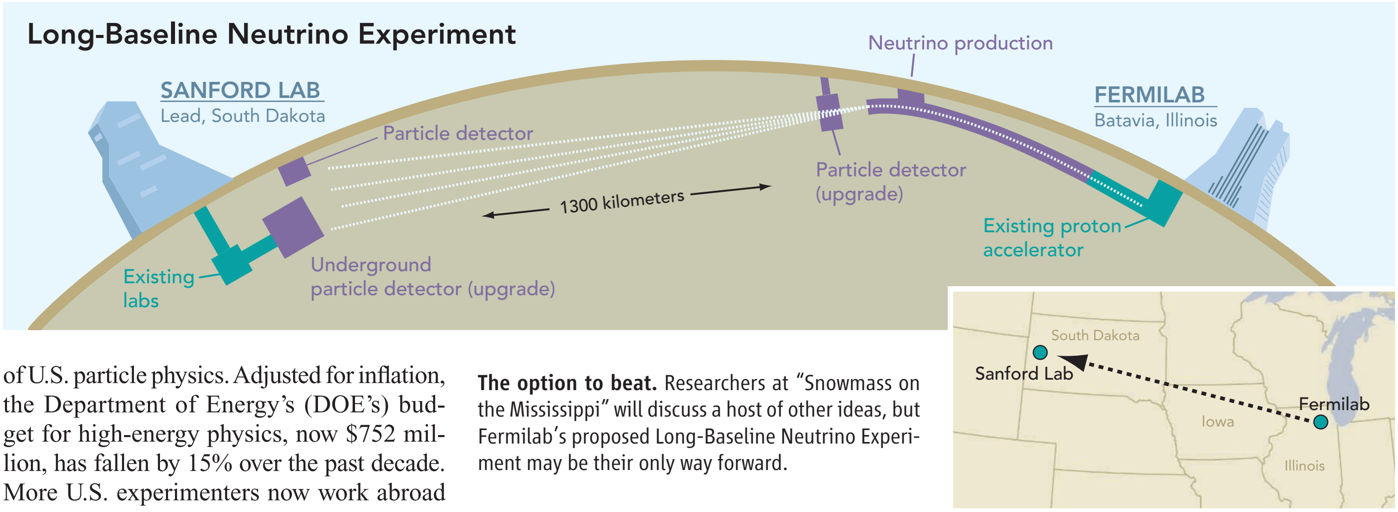

The option to beat. Researchers at "Snowmass on the Mississippi" will discuss a host of other ideas, but Fermilab's proposed Long-Baseline Neutrino Experiment may be their only way forward.

CREDIT: ADAPTED FROM FERMILAB GRAPHIC

But change was on the horizon. The European particle physics laboratory, CERN, near Geneva, Switzerland, was building the 27-kilometer-long Large Hadron Collider (LHC). It would smash protons at an energy much higher than the Tevatron's and hunt such quarry as the Higgs boson, the key to physicists' explanation of how all other fundamental particles get their mass—which it produced last year.

To stay in the game, U.S. physicists proposed building a gigantic straight-shot "linear collider" that would fire electrons into positrons and carry out precision studies of the new particles unearthed in the relatively messy proton collisions at the LHC. At Snowmass, they hammered out a consensus making a linear collider, later dubbed the International Linear Collider (ILC), their priority.

Even some who organized that drive now feel it was a mistake. "A lot of people felt they were forced to agree to the consensus document," says JoAnne Hewett, a theorist at SLAC who helped write it. And in the end, the push for the ILC in the United States came up short. In 2007, DOE balked at the $7 billion price estimate for the United States' half of the project and asked for something more affordable.

That's when the current plan for a neutrino experiment was hatched. In May 2008, P5 released a report that divided particle physics into three "frontiers." On the energy frontier, U.S. physicists would participate on experiments at the LHC. On the cosmic frontier, others would work on underground experiments to detect particles of the dark matter whose gravity binds the galaxies or on astronomical surveys to probe the nature of space-stretching dark energy.

Fermilab would seek its future on the intensity frontier, in experiments that require the highest intensity proton beams. Such beams can be used to generate neutrinos, nearly massless particles that hardly interact with other matter. Neutrinos come in three types that morph into one another as they zip along at near light speed. Fermilab already had an experiment to study those "neutrino oscillations." P5 proposed that the lab pursue a definitive neutrino oscillation experiment, LBNE, which would fire neutrinos 1300 kilometers through Earth to a huge detector in an abandoned gold mine in Lead, South Dakota. Fermilab would then add a new proton source to feed a variety of studies.

LBNE supporters note that neutrino oscillations are promising to study because they are the only solid bit of particle physics that doesn't fit into the standard model. LBNE would probe whether neutrinos and antineutrinos oscillate differently, an asymmetry that could help explain how the universe generated so much more matter than antimatter. Critics counter that neutrino phys-

Published by AAAS

ics is too narrow a field to support the national program. "Even if we measure all the parameters, it really ends there," says David Gross, a theorist at the University of California, Santa Barbara. "The people who do the science work mainly at the universities, and they have voted with their feet: They work at the LHC."

To complicate matters, last year DOE deemed the original $1.9 billion plans for LBNE too expensive and asked for plans to build it in cheaper stages. Some researchers say the chopped-down plans aren't compelling even to neutrino physicists.

But is there really a viable alternative to the current plan? Yes, Gross says. Europe plans a major upgrade of the LHC in 2020, and Japan has hinted that it might want to host the ILC. Fermilab could build parts for overseas efforts, allowing the United States to remain focused on the energy frontier, Gross says. But others say that without a major experiment at Fermilab, the entire U.S. program may become politically unsustainable. They hope that contributions from other countries will restore LBNE to its original scope. Last month, for example, European physicists expressed willingness to work on a neutrino experiment based elsewhere (*Science*, 7 June, p. 1151).

In the end, P5 will likely just tweak the existing plan to include, say, participation in a linear collider in Japan, some physicists say. But others worry that DOE officials may be weighing work on the energy frontier overseas or on the intensity frontier at home as an either-or choice. When Congress last passed a budget in 2012, the House of Representatives advised DOE that it "will be pressed to further prioritize between these two competing directions." Hewett says, "I think the folks who work on the LHC have their heads in the data and don't quite see what could be coming."

Considering the stakes, some physicists say that they'd like to see priorities addressed at Snowmass. "That's our job as scientists because we can't expect a congressman to know if neutrino physics is more important than the Higgs boson," says Harry Weerts, an experimenter at Argonne National Laboratory in Illinois. But given the resentments lingering from the last meeting, organizers are wary of pushing for consensus. That will come later through P5—if it comes at all.

–ADRIAN CHO

SPACE PHYSICS

The Savage Radiation of the Van Allen Belts Is Homegrown

Back in 1958, Explorer 1, the first U.S. satellite, sent back unsettling news: Nearby space was pervaded by radiation intense enough to blind their instruments. The Van Allen radiation belts, extending from about 1000 kilometers to 60,000 kilometers from Earth, have been zapping unlucky satellites—and puzzling space physicists—ever since. Now, at last, researchers have figured out where the electrons that fill the Van Allen belts get their killer energy. A pair of probes launched last year has traced how energy streaming from the sun can boost electrons in the heart of the belts to speeds greater than 99% of the speed of light.

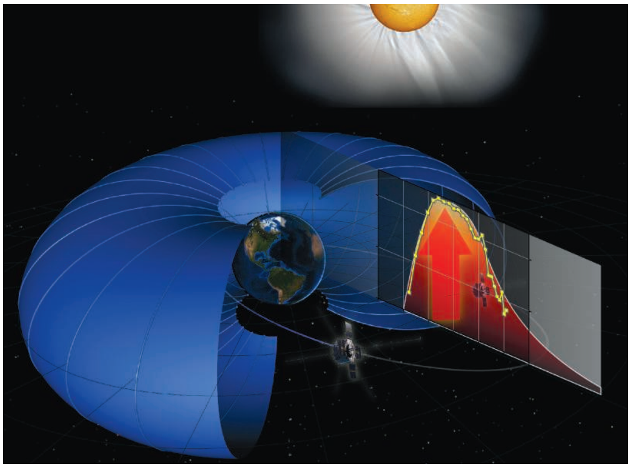

Inner turmoil. Electron energies (yellow curve) detected by two new spacecraft peak inside the radiation belts (including the magnetically defined blue torus) as expected for in situ acceleration (gray curve).

CREDIT: G. REEVES AND M. HENDERSON/LANL

Researchers "have found the key signature" of electrons being accelerated within the Van Allen belts themselves, says space physicist Richard Horne of the British Antarctic Survey in Cambridge, U.K. "It's really exciting, and it looks pretty convincing." Besides solving a mystery as old as the space age, the new explanation should help researchers better forecast onslaughts of Van Allen radiation, allowing satellite operators to minimize disruptions.

Earlier scientific missions could not tell whether the high-energy electrons were pumped in from far outside the belts or accelerated in situ. But NASA's twin Van Allen Probes are "the right satellites in the right orbit with the right instruments," says space physicist Geoffrey Reeves of Los Alamos National Laboratory in New Mexico, deputy principal investigator of a key instrument suite on the mission. One or the other spacecraft cuts through the heart of the belts every couple of hours rather than every 12 hours as previous satellites had. Their instruments cover the full energy range required. And with two coordinated spacecraft, mission team members could precisely calibrate their instruments when they were immersed in the same magnetic fields and charged particles (electrons and protons, mostly).

Little more than a month after launch last August, the two spacecraft thoroughly dissected a half-day–long electron-energizing event 23,000 kilometers up in the outer belt. Rather than finding energy building as electrons from the solar wind diffused inward into the outer belt, as some theories predicted, the data showed that energy surged among low-energy electrons already in the belts, Reeves says. Powerful electromagnetic waves in the solar wind were almost certainly transferring their energy to the resident electrons, boosting them to speeds at which they can fry a satellite's electronics.

It's still unclear which of a half dozen kinds of waves is the primary driver. But the most likely energy source, Reeves says, is so-called chorus waves, so named because, when converted to sound, their natural frequencies resemble a dawn chorus of birds. Chorus waves that are in sync with electrons spiraling about magnetic field lines would regularly boost the energy of an electron the way repeatedly pushing a swing at the same point of its arc drives it higher and higher.

"I'm very excited about this," says space physicist Louis Lanzerotti of the New Jersey Institute of Technology in Newark. Working on the radiation belts "is how I started out in the 1960s," he says. But Lanzerotti agrees with Horne that "we've got a lot to do yet." With a thousand satellites in orbit costing upwards of $250 million each, researchers need to rank the importance of each type of wave in powering up the radiation belts. Then they can work their way back toward the sun along the energy supply chain in order to give better and earlier warnings of radiation crises.

–RICHARD A. KERR

Published by AAAS

Delivering a message. Turkish engineers and architects assemble on 13 July for march on Taksim Square.

TURKEY

For Scientists, Protests Morph Into Fight for Academic Freedom

ISTANBUL, TURKEY—Clearly exhausted, molecular biologist Aslı Tolun smiles wanly as she offers a tangerine from a fruit bowl here in her office at Boğaziçi University in Turkey. Down the hall, her lab is empty. Her graduate students were supposed to administer final exams to undergrads this morning, but they spent all night playing cat and mouse with riot police and are now sleeping. Tolun filled in for them in the exam hall.

The unrest that has gripped the country since May has ebbed a bit. But for Turkish scientists like Tolun, the irony of their situation is starker than ever. On the one hand, tensions between the mostly secular scientific community and the conservative Islamic government are intensifying, encouraging many academics and students to join the still simmering demonstrations. On the other, science is at the heart of the government's ambitions and the focus of its largesse.

"We have ambitious goals," says Cevahir Uzkurt, general director of the Directorate General for Science and Technology of the Ministry of Science, Industry and Technology. By 2023, the 100th anniversary of Turkey's founding, the ruling Justice and Development (AK) Party led by Prime Minister Recep Tayyip Erdoğan aims to triple public research spending to 3% of the gross domestic product, more than quadruple the number of full-time scientists to 300,000, and boost output of peer-reviewed papers to levels comparable with those of countries in Western Europe. Meanwhile, two megaprojects aim to lure back expat talent. Workers have just broken ground on Bio Istanbul, a $1 billion research hospital and real estate development on the city's outskirts. The other is still in planning: a Turkish space agency with its own spaceport.

The government is already backing its words with cash. The annual budget of the Scientific and Technological Research Council of Turkey (TÜBİTAK), the country's monolithic science-funding agency, has shot up 50-fold over the past decade to nearly $500 million in 2012, accounting for the lion's share of central government spending on science; much of that goes to applied research (see graphics on facing page). And across the country, the number of universities has ballooned from 70 a decade ago to 174 today. Many university research labs now measure up to well-funded counterparts in Western Europe and the United States. "State-of-the-art microscopes, brain-scanning equipment: We get whatever we need," says Umran İnan, president of Koç University, perched on a mountain overlooking the Bosphorus strait that divides Istanbul.

But it will take more than lavish spending to buoy Turkey's dispirited academics. "Increasingly, the government tries to control every aspect of life," says a biologist who requested anonymity. Ecologists fear that a draft law will harm biodiversity for the sake of infrastructure (see below). Scientists also complain about dictums to steer clear of sensitive topics like evolution and anything that touches on religion and to shift research priorities to applied topics such as "clean coal" or "biomedical instruments." Such pressure may backfire, warns one dis-

CREDITS (TOP TO BOTTOM): GETTY IMAGES; ÇAĞAN ŞEKERCIOĞLU

Fragile Wetland Will Test Turkey's Resolve In Protecting Biodiversity

Çağan Şekercioğlu is in a race with the bulldozers. The Turkish ornithologist is based at the University of Utah in Salt Lake City, but these days he spends most of his time in a wetland in eastern Turkey. Just 10 square kilometers in area, the Aras River Bird Paradise is home to 36 threatened or endangered species and is one of a handful of long-term ecological research sites in Turkey. Şekercioğlu is trying to document Aras's biodiversity before construction starts on a dam that will flood the wetlands and, he and others say, destroy the fragile habitat.

Vision of the future? Turkey has already dammed the Aras River upstream.

Published by AAAS

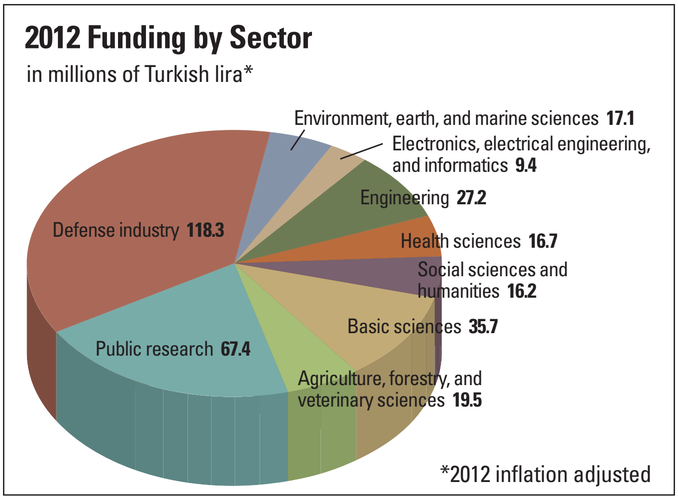

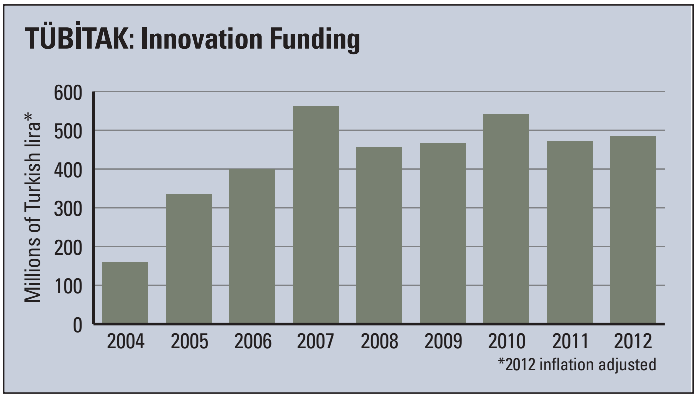

Applying their minds. TÜBİTAK funding for industry, technology, and innovation has risen steadily since 2004 (*top*); a healthy proportion of funding in its main grants program goes to defense research (*left*).

GRAPH SOURCE: TÜBİTAK 2012

gruntled biologist: "We will have to leave if things get worse."

Freedom fighters

Scientists, especially those who trained abroad, have long chafed against the authorities here. "Turkish academia has always been oppressive," says Erol Akçay, an evolutionary biologist now at Princeton University. "It is so very top-down organized," he says. Freedoms that scientists elsewhere take for granted—buying research materials, for example, or attending scientific meetings—require permission slips from bureaucrats. Displease the authorities, Akçay says, and "they can burn your career" by, for example, depriving you of TÜBİTAK funding. "The overall effect is very chilling."

When the AK party was elected to power in 2002, it largely took a hands-off approach to academia. But over the past few years, Akçay says, political meddling with academia "has gotten worse." In 2011, the AK party seized control of the Turkish Academy of Sciences. The reason: The academy "was far from representing the Turkish national scientific community," says its newly appointed president, Ahmet Cevat Acar, a professor in the School of Business Administration at Istanbul University. The root of the academy's ills, he says, is that "nomination for the membership was only by the existing members. … This paved the way for inbreeding."

The takeover did not sit well with most scientists. The academy has become "a body with a majority of members appointed by government and with weak, to say the least, scientific and scholarly records," says Mehmet Ali Alpar, an astrophysicist here at Sabancı University. He joined a mass exodus from the academy—just 30 of the 150 original members remain—and now leads a new opposition academy.

The government has since intervened more boldly in other aspects of scientific discourse. Evolution is a frequent target. For example, a government-run censorship program has blocked websites with educational content related to evolutionary biology. And last month, TÜBİTAK rejected a grant application for a summer school on quantitative evolutionary biology on the grounds that "evolution is a controversial subject."

In the meantime, TÜBİTAK's rising fortunes have come with strings attached. "Most of the money does not flow into basic research," says Akçay, who has tracked the government's annual research spending. Alpar asserts that funding decisions are often made by panels stacked with unqualified reviewers. "Ostensibly the panels are meant to be representative, by which [the government] means all universities from all over the country," he says. "This does not, however, produce scientific quality."

Uzkurt, an engineer by training, brushes off the criticisms. "There might be some reactions to the reform of the higher education system," he says. But ultimately, he contends, the changes that the government is bringing about "will contribute to develop, among other things, academic freedom."

Many scientists-cum-demonstrators see the exact opposite happening. "My graduate students have been out protesting, and I join to protect them from harm," says one Turkish biologist. "By day we work as scientists, and by night we are protestors," another says. "This is a fight for freedom of thought."

–JOHN BOHANNON

Aras is one of dozens of battlegrounds where Turkish scientists and their government are fighting over the environment. The ruling AK party intends to double the number of hydroelectric dams to more than 600 as part of an ambitious 10-year plan to transform the country (see p. 332). Recent dam-building has already destroyed several wetlands.

The Turkish government deserves kudos for improving the nation's air and water quality, says Raşit Bilgin, an evolutionary biologist at Boğaziçi University in Istanbul. But new laws are systematically undermining environmental protection, he and others say. Laws passed in 2010 and 2011 permit mineral exploration in protected areas. In June, the Ministry of Forestry and Water Affairs abolished a requirement for environment impact assessments before infrastructure projects such as bridges and dams are started. A draft law now in parliament would go even further, allowing dams to be built in protected habitats.

Just last month, Şekercioğlu thought he had staved off disaster for Aras. Some 8000 people, including dozens of overseas scientists, signed a petition to the government to cancel the plan to dam the Aras River. Responding to the barrage of concern, the forestry ministry on 18 June recommended that Aras be declared a Nature Conservation Area. Şekercioğlu's elation drained away a day later, when he discovered that the protected status needs the assent of 10 other government agencies—including the Ministry of Development, which awarded the contract to the dam-building company. "Of course they will oppose this and they are very powerful," Şekercioğlu says. He doesn't see favorable odds for the Bird Paradise. "Its chances are less than even," he says. "But I will keep fighting until the end."

–J. B.

Indispensable Outsider

Richard Garwin has helped advise U.S. presidents, IBM, and secret agencies on how to make things work

THE FIRST THING ANYBODY SAYS ABOUT THE physicist/inventor/adviser Richard Garwin is that his graduate school adviser 60 years ago, Enrico Fermi, said that he was the only true genius he'd met. The next thing is that Garwin has advised, sometimes impolitically, every administration since Eisenhower's on every possible technical issue. The third thing is the Garwin joke: It's the French Revolution, an aristocrat is placed in the guillotine, the blade won't drop, "God's will," says the guillotiner, and lets the aristocrat go free; next aristocrat, same thing, blade sticks, "God's will," goes free. The next in line is Garwin, who looks up at the blade and says, "Oh, I see the problem."

Garwin himself agrees that the third, an old joke, could have been written for him. He is a compulsive problem-solver—although his solutions occasionally raise other problems. Prime example: In 1951, Garwin was 23 years old and the hydrogen bomb, which worked only in theory, needed proof. So in a few weeks, Garwin designed an experiment, and a year later Los Alamos National Laboratory in New Mexico had built it and called it Mike, then had taken it to Eniwetok in the South Pacific and set it off. The 11-megaton explosion was 1000 times more powerful than the atomic bomb that flattened two-thirds of Hiroshima. Garwin didn't watch it—he was busy working on more portable H-bombs—and in fact has never seen a nuclear explosion. "I don't need it," he told an interviewer. "I have a good imagination."

Garwin went on to an astonishingly varied career that included fundamental contributions to particle physics, a 41-year career in industry, 47 patented inventions, and 60 years of advising multiple parts of the U.S. government on multiple technical issues. "He's done so damn many things," says Peter Zimmerman, formerly chief scientist at the U.S. Senate Foreign Relations Committee, "that it's hard to single out any one."

Garwin advised then–Energy Secretary Steven Chu on alternatives for dealing with the Fukushima nuclear plant's meltdown in 2011 and on plugging the BP oil well blowout in 2010. In 1981, Garwin pioneered gesture recognition for a touch screen, on the IBM color PC monitor. In 1969, he invented the tensioned cables that would hold a deepwater floating airport steady in large waves; floating airports were never built, but the approach was used for oil-drilling platforms. Since 1968, he's been writing about handling data in health care. The upshot: He is one of 13 people in the world who is a member of all three U.S. National Academies: science, engineering, and medicine.

Nothing ties these fields and functions together, no single intellectual thread. Garwin just likes being useful, he says, and helps solve problems as they arise. And if his

CREDIT: ANAND KAMALAKAR

Published by AAAS

Frequent visitor. Garwin has been a White House adviser off and on since the 1950s.

solution to a problem causes another problem, then he solves that one, too. If a coherent narrative can be imposed on Garwin at all, it is that having solved the hydrogen bomb, he has spent the last 6 decades working to help governments control it.

Precise design

Richard Lawrence Garwin was born in 1928, in Cleveland, Ohio. He graduated from what is now Case Western Reserve University in 3 years, working in his father's sound equipment repair business, and marrying a local girl. In 1947, he moved to the University of Chicago where, in 1949, he received his Ph.D. with Fermi on the radioactive decay of atomic nuclei.

Garwin stayed on at Chicago as an instructor and in 1950 began spending summers consulting at Los Alamos because, as he said, the university paid its faculty members for 9 months but his family ate for 12. In his second summer there, Edward Teller, also at Chicago and consulting at Los Alamos, told him that he and Los Alamos physicist Stanislaw Ulam had a theory that an atomic bomb could be used to trigger a hydrogen bomb, but the theory needed a proof-of-principle. Garwin thought through the options—the configurations, dimensions, and materials that would focus the radiation of an atomic bomb "primary" and trigger thermonuclear fusion in the "secondary"—and decided that designing a real bomb would be just as easy. The Mike test worked, Teller said, "almost precisely" as designed. Later, when Teller got credit for fathering the H-bomb, Garwin didn't argue: By then Garwin had learned, as he said, that when serving the government you could either get something done or get credit for it, but not both.

Meanwhile, particle physics was becoming a science of large teams, large machines, and long waits for experiments, none of which Garwin found agreeable. So in 1952, he took a job at IBM's Watson Scientific Laboratory, then in New York City, where he could, he said, "decide one day what I was going to do the next day." At IBM he worked on everything from the properties of materials under extremely cold conditions, to prototypes of computers controllable by gaze, to the little accelerometer that protects the brains of laptops or other smart devices when they're dropped. In 1957, he took leave from an IBM project to develop a superconducting computer, and with Leon Lederman conceived and conducted, in 4 days, an experiment on the radioactive decay of *mu* mesons that has become part of the modern view of particle physics.

The same year Garwin joined IBM, he was introduced for the first time to the cadre of academics advising the government on science and technology. Centered at Harvard and the Massachusetts Institute of Technology, it included engineer Jerome Wiesner, John F. Kennedy's science adviser, who in 1957 asked Garwin to join the newly forming President's Science Advisory Committee (PSAC). Garwin served an unusual two 4-year terms on PSAC and led several of its panels, in particular, those looking into ballistic missile threats and military aircraft. He helped lay the basis for GPS, drone aircraft, and the electronic battlefield. "I learned a lot," he said.

PSAC also helped Garwin define his ideal job: sitting in a room for 8 hours while generals, admirals, scientists, and corporations explained their problems and he and the rest of the panel proposed answers. He later found the same congenial setting when he joined a secret government advisory group called JASON, also made up of mostly academic scientists. Garwin and IBM had agreed from the start that his job would include spending a third of his time giving advice to the government.

Often that time was devoted to highly classified "black" programs, which bypass open peer review or qualified congressional oversight, making the advice of independent scientists especially valuable. Since the early 1960s, Garwin worked on several types of spy satellites, though he won't say exactly what he did or for whom. Some satellites, whose names haven't been declassified and which Garwin talked National Security Adviser Henry Kissinger into backing, used charge-coupled devices that stored images and sent them back via radio. These satellites' sensitivity to light needed improving. Still others, like the Poppy series, collected not images, but radar signals showing the locations, frequencies, and ranges of Soviet radars. Garwin helped Poppy "a lot," he says, "because I asked, 'Is this how it works?' And they said, 'No, that's not how it works.' And I said, 'Why doesn't it work that way?' And they made it work that way."

Garwin thinks he's been most useful to black programs at the CIA and National Reconnaissance Office (NRO). Apparently they agreed: The CIA awarded him the R.V. Jones award, and NRO declared him one of the 10 Founders of National Reconnaissance. Garwin's special contribution to

A RESTLESS MIND

1951–1952

Designs experiment for "Mike" H-bomb test

1952–on

IBM Watson Scientific Laboratory researcher

1957

With Leon Lederman, *mu* meson experiment

1960s

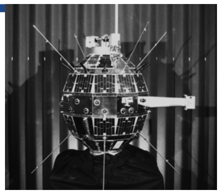

"Poppy" surveillance satellite work

1970

Faults supersonic transport while serving on President's Science Advisory Committee

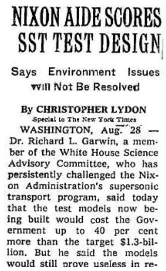

NIXON AIDE SCORES SST TEST DESIGN

Says Environment Issues Will Not Be Resolved

By CHRISTOPHER LYDON
Special to The New York Times

WASHINGTON, Aug. 28 — Dr. Richard L. Garwin, a member of the White House Science Advisory Committee, who has persistently challenged the Nixon Administration's supersonic transport program, said today that the test models now being built would cost the Government up to 40 per cent more than the target $1.3-billion. But he said the models would still prove useless in re-

1973

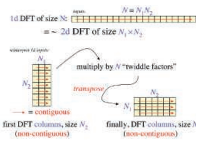

Brokers fast Fourier transform algorithm development

1995

Co-authors JASON review of Comprehensive Nuclear-Test-Ban Treaty

2002

National Medal of Science

2010

Recruited by DOE to help with the *Deepwater Horizon* oil spill

Published by AAAS

the intelligence community, says Robert A. McDonald, director of NRO's Center for the Study of National Reconnaissance in Virginia, is that he pushed them to "stretch their technological limits," and gave them, not the answers they wanted, but "independent, no-holds-barred assessments."

Mass destruction

The issue on which Garwin has worked most intently is arms control—the natural consequence of an involvement with the hydrogen bomb. One way or another, he has helped shape all the treaties to ban nuclear weapons tests since the first treaty talks in 1958. He helped convince President Kennedy to put controls, called Permissive Action Links (PALs), on U.S. nuclear weapons stationed in Europe so that they couldn't be exploded without authority. (Talking later to a Russian scientist at CISAC, the National Academy of Sciences' Committee on International Security and Arms Control, Garwin found out the Russians didn't then have PALs on their bombs in Cuba either.)

Unlike his old friend and colleague Sidney Drell, now retired from the SLAC National Accelerator Laboratory in Menlo Park, California, Garwin isn't trying to take nuclear weapons down to zero: "I don't see the elimination of nuclear weapons," Garwin says, "or even a path in that direction." He's against proliferation of weapons to any countries that don't have them. He's for the immediate reduction in numbers of weapons and further reductions in the future, from the current 5000 in the United States and 17,000 or so worldwide—a point at which, he says, the weapons are more numerous than their targets—down to a few hundred, "enough for any conceivable purpose."

Since 1992, Garwin has worked on nearly every JASON report on the health of nuclear weapons in the U.S. stockpile, most notably the 1995 report certifying that the weapons were a reliable deterrent without having to be tested and that, yes, the country could sign the international Comprehensive Nuclear-Test-Ban Treaty. Noting that he "had a lot to do" with nuclear weapons himself, Garwin said of the JASON report, "I am most pleased to be an author of this document."

Garwin also works on the other half of controlling weapons: missile defense. He's advised, written, and testified on its myriad aspects since 1968, when he and Hans Bethe wrote an article for *Scientific American* outlining the pros and cons that have been debated ever since. He continued arguing through the 1980s debates on Star Wars, the Reagan administration's idea for space-

CREDIT: U.S. PATENT AND TRADEMARK OFFICE

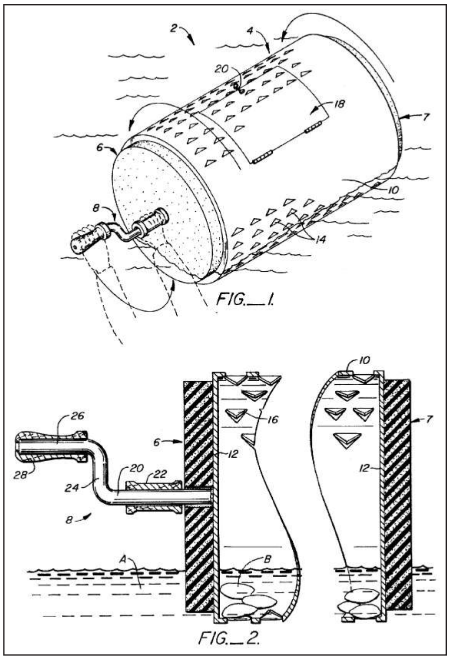

Scrubber. Garwin's mussel washer is one of his 47 inventions covered by U.S. patents.

based defenses. He helped write the so-called Rumsfeld report in 1998 on the missile threat from "rogue states," which missile defense advocates later used to support their views—to Garwin's annoyance but not astonishment. These days, he's arguing with the National Academies' 2012 report on missile defense. The report recommends new radars, which Garwin says would be inadequate to distinguish incoming missiles from decoys. "If you feel compelled to have a missile defense because you've always said missile defense is necessary," he told an interviewer, "go ahead, have a missile defense. But don't spend very much money on it, and don't lie about its performance."

Category of one

If Garwin's advice has a flaw, some of his peers say, it's a sporadic tone-deafness to human or institutional realities. For example, his proposal to intercept enemy missiles during their more targetable boost phase by basing the missile defenses close to potential attackers, such as North Korea, is probably not going to win Chinese or Russian approval. And testifying in Congress against the Nixon administration's plan for a supersonic transport plane, as Garwin did in 1970 while sitting on PSAC, was never in the playbook for presidential advisers. It has been cited as a reason that Richard Nixon disbanded PSAC.

The occasional tone-deafness, says Raymond Jeanloz, a geophysicist and fellow arms-controller at the University of California, Berkeley, doesn't mean that Garwin loses credibility among his advisees. He's showing politicians what, if politics could be sidestepped, might then be possible—"maybe we should be asking whether we could deploy missiles near Vladivostok," Jeanloz says. "He's saying, 'You policymakers have to realize you're excluding a universe of possible solutions.' " The approach is peculiarly Garwinian, Jeanloz says: "He's one of the few people who can get away with it."

Garwin turned 85 this year. Some days he goes to his emeritus office at IBM and dresses in good khakis; when he's working from home, he dresses in older khakis; he wears a tie to go to Washington. He uses public transportation and carries the routes and schedules in his head. He's moved from his home of 55 years because he could no longer climb out to fix the roof and now lives in a modest apartment with the wife he married when they were teens. For lunch when he's at home, his wife often cuts up a fresh pineapple, which they eat for dessert for several days.

"I've never seen him down in the dumps," says Philip Coyle, who was an associate director at Obama's White House Office of Science and Technology Policy (OSTP) where Garwin is a consultant. "Nothing sets him back." In 2002, he won the National Medal of Science. He gets 40 to 60 e-mails per day—on CISAC, JASON, OSTP, and occasionally intelligence business—and only about 10 per Saturday or Sunday. Garwin says that he could stop doing all he does and devote himself to his hobbies, if he had hobbies; or he could go back to science, "but it is unlikely that I would make any significant contributions at this stage," and so, when he sees any probability of a good outcome, he says, "I prefer to do what I have been doing for a long time."

Maybe that's another result of helping the hydrogen bomb into the world: never being able to give up. Drell says that politics will have so large a part in solving the problem of missile defense that he himself has quit arguing about it—but that, he says, is "a cop-out by Sid Drell. Dick Garwin never cops out." William Press, at the University of Texas, Austin, and current member of the President's Council of Advisors on Science and Technology who has worked with Garwin since 1977, says that whenever he tries to duck out of some issue, "I hear Dick's voice—'Bill, those things don't just happen. It's people like me who make them happen.' "

–ANN FINKBEINER

Ann Finkbeiner is a writer in Baltimore, Maryland.

CREDIT: LINCOLN SCHATZ, THE NETWORK (KATHY STACK), GENERATIVE VIDEO STILL, 2012

EDUCATION

An Invisible Hand Behind Plan To Realign U.S. Science Education

Meet the master bureaucrat behind President Obama's controversial proposal to reshuffle the federal government's $3-billion-a-year investment in STEM education

An art exhibit in downtown Washington, D.C. features the pictures and words of 89 Washington movers and shakers. The exhibit at the National Portrait Gallery, entitled The Network, includes high-profile politicians such as Nancy Pelosi, Eric Cantor, and Karl Rove and renowned scientists turned policymakers such as Nobelists Harold Varmus and Steven Chu. A few, like journalist Cokie Roberts, have earned fame for explaining the ways of Washington to the public. And then there's Kathryn Stack.

Stack is deputy associate director for education and human resources at the White House Office of Management and Budget (OMB). The agency exercises vast sway over government spending and regulatory practices yet prefers to operate in the shadows. So Stack's position qualifies her for the Hall of Fame of faceless government bureaucrats. But she's learned a thing or two about wielding power during a 35-year career spanning six administrations.

"Several others [in the exhibit] told me that she knows how to get things done," says Chicago artist Lincoln Schatz, explaining why he chose Stack for the exhibit, which opened in December. "They said few people understand the complexities of large bureaucracies like OMB as well as she does."

Despite her professional mask of anonymity—OMB officials declined to make Stack available for an interview—2013 may be a breakthrough year for Stack. In addition to seeing her picture hang on the walls of the National Portrait Gallery, Stack watched President Barack Obama unveil a budget initiative this spring in which she played an important role: a proposal to radically realign the federal government's $3 billion annual investment in STEM (science, technology, engineering, and mathematics) education.

The 226 programs, which serve students, teachers, and the public, are spread across 13 agencies. The reorganization would cut the number in half (see graphic, next page) and severely curtail STEM activities at the National Institutes of Health (NIH) (see sidebar, p. 340), NASA, and several other so-called mission agencies. At the same time, it would strengthen the efforts of the Department of Education, the National Science Foundation (NSF), and the Smithsonian Institution by designating them as lead agencies.

The proposed reshuffling hit the U.S. scientific community like a bombshell. For starters, they hadn't seen it coming and were miffed that they weren't consulted. "We are disturbed with the nontransparent process by which this proposed consolidation was developed," wrote the Association of American Universities and the Association of Public and Land-grant Universities in a 2 July letter to John Holdren, the president's science adviser.

But being shut out isn't the community's chief complaint. Three months after the plan was sent to Congress as part of the president's 2014 budget request, STEM educators are still waiting for the White House to explain how it drew up the list of programs to be ended, merged, or expanded. They also worry that the reshuffling will damage existing activities by shifting resources away from agencies with unique expertise and tools to do STEM education and asking the lead agencies to take on too much (*Science*, 19 April, p. 258).

Published by AAAS

The big picture. OMB's Kathy Stack is a good example of how a career civil servant can help shape policy at the White House.

At the core of the proposal is an approach to governing, called evidence-based policy, which Stack has long championed at OMB. It calls for killing, reforming, or expanding government programs based on the results of regular, rigorous evaluations of their effectiveness. To officials in both the Bush and Obama administrations, the complex, disparate array of federal STEM education programs seemed ideally suited for the approach.

But critics say that Stack and her OMB colleagues, in their eagerness to consolidate, inverted the strategy, making decisions before the evidence was in. The result is a flawed plan, say the spending committees of both the Senate and House of Representatives. "What is proposed as a consolidation of existing STEM programs … is really the elimination of many proven and successful programs with no evaluation on why they were deemed duplicative or ineffective," the Senate Appropriations Committee wrote last week in a report accompanying its 2014 bill for the Department of Commerce, Department of Justice, NASA, NSF, and several other agencies.

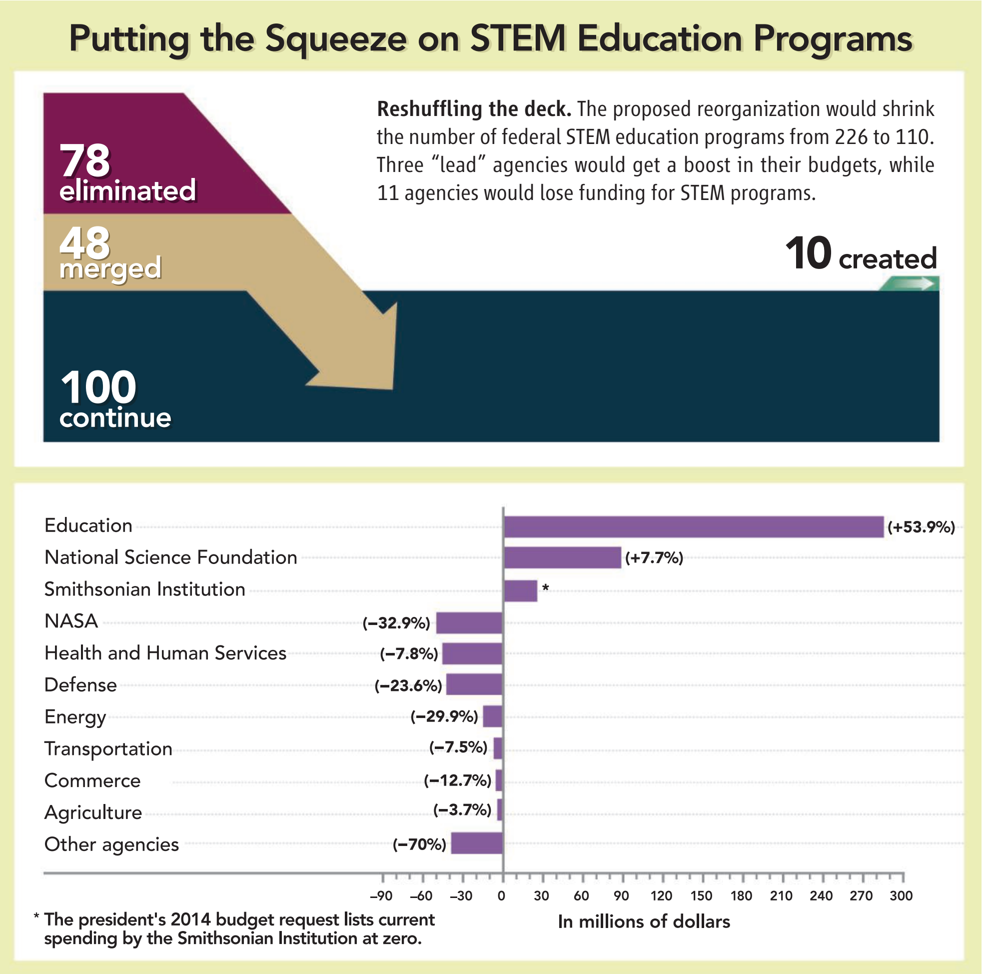

Reshuffling the deck. The proposed reorganization would shrink the number of federal STEM education programs from 226 to 110. Three "lead" agencies would get a boost in their budgets, while 11 agencies would lose funding for STEM programs.

* The president's 2014 budget request lists current spending by the Smithsonian Institution at zero.

CREDIT: ADAPTED FROM OSTP, OR THE WHITE HOUSE OFFICE OF SCIENCE AND TECHNOLOGY POLICY

Looking for evidence

Although evidence-based policy may seem like an obvious way to make the federal government work better, it's not common practice. "Most agencies don't think about outcomes," Stack told the Society for Research on Educational Effectiveness (SREE) in a March 2011 speech. "And most of what they consider to be a rigorous evaluation isn't." At the same time, she noted, "most agencies think that everything they are doing is effective."

In addition to complacency, another major obstacle to implementing evidence-based policy is vested interests, says Robert Gordon, Stack's boss at OMB during the first 4 years of the Obama administration. "People have talked for ages about trying to rationalize and harmonize programs that were overlapping and wasteful," says Gordon, who left OMB in March to become a guest scholar at the Brookings Institution in Washington, D.C. "But it's hard to do because these programs have so many supporters."

Of course, evidence-based policy requires evidence. But the results of previous evaluations of STEM programs were not the driving force in selecting winners and losers, Holdren told the House science committee last month. Instead, he said, the reorganization was intended to "cut back on lower priority or narrow-purpose programs [to] make room for targeted increases in high-priority areas." Better evaluation would be a consequence, not a cause, of the reorganization, he noted. Once the reshuffling was implemented, he told legislators, the administration would be in a better position to carry out "rigorous evaluation and evidence-building strategies."

That's a reasonable approach, says Robert Shea, who was Stack's boss during most of the George W. Bush administration and is now a director in the Washington offices of Grant Thornton, a global professional services firm. "You'll never consolidate all programs with similar objectives," Shea says. "But you want to get a sufficiently small number so that they can be better coordinated."

Such arguments haven't appeased opponents of the proposed reorganization. It has drawn near-unanimous opposition from several of the congressional panels with jurisdiction over one or more of the agencies that would be affected. The House science committee, for example, last week approved a bill to reauthorize NASA programs that would prohibit the administration from implementing "any proposed STEM education and outreach-related changes proposed [for NASA] in the president's 2014 budget request." Senate appropriators were equally dismayed, telling NIH officials on 11 July to put the brakes on their plan to dismantle the NIH's Office of Science Education and related grants program supporting informal health science education.

Likewise, House appropriators last week approved a bill that would restore money in 2014 for STEM education activities at NASA and the National Oceanic and Atmospheric Administration and put the kibosh on a realignment of undergraduate STEM education programs at NSF. The accompanying report also reflected the concerns of many science educators: "The ideas presented in the budget request lack any substantive

implementation plan and have little support within the STEM education community."

On-the-job training

White House officials, including OMB and Stack, aren't publicly saying what they think of such rebukes. Indeed, after spending her entire career inside the federal bureaucracy, Stack knows that civil servants aren't even supposed to make policy. Yet, she has played an outsized role by focusing on how to make the wheels of government turn more smoothly.

"There are policy folks who come in from administration to administration who have great ideas, but they have no idea how government works," she told Schatz, the artist. "I understand the culture and tools, and I know how to translate into action the big visionary ideas that political officials have."

Those who have worked with Stack testify to her extraordinary grasp of the levers of power. "Kathy taught me, rather than the other way around," says Gordon, a political appointee with extensive experience in Democratic policymaking circles. Jon Baron, whose nonprofit Coalition for Evidence-Based Policy conducted an evaluation of STEM education programs during the Bush administration, says that Stack "has been very successful in persuading her political bosses" that rigorous evaluation should be part of policymaking.

Colleagues say it helps that Stack doesn't have her own agenda. "She's tied for the least ideological person in government that I know," says Robert Granger, retiring president of the William T. Grant Foundation. Granger had frequent interactions with Stack when he chaired the National Board for Education Sciences within the Department of Education during the Bush administration. "Instead, she's a terrific public servant who's motivated by what she thinks will help the government spend its money well to help kids." Baron struck a similar chord when he told the SREE audience that "we should be glad that she uses her powers for good, and not evil."

> "I understand the culture and tools, and I know how to translate into action the big visionary ideas that political officials have."
>
> **—Kathryn Stack**

Stack arrived in Washington in 1978 with an undergraduate degree in government from Cornell University to work on education issues within the former Department of Health, Education, and Welfare. In 1982, she moved to OMB and began promoting the idea of using program evaluation to shape policy in education and income assistance programs.

The tide of evidence-based policy was coming in as Stack toiled away at OMB, and she rode the wave. One result: In 1993, Congress passed the Government Performance and Results Act as part of a Clinton-era campaign to "reinvent government." And Stack played a leading role in a similar initiative under George W. Bush known as PART (Program Assessment Rating Tool).

Then, in 2007, Congress passed and President Bush signed the America COMPETES Act, which sought to boost innovation by increasing federal support for research and improving STEM education. One of its provisions called on the government to evaluate existing STEM education programs. Stack asked Baron's center to conduct a review

NIH Teaching Units, Cherished In Schools, May Be Shredded

Two miles north of its Bethesda, Maryland, campus, the National Institutes of Health (NIH) operates a supply warehouse that serves its intramural scientists. The tidy blue and white building stands out along a grimy commercial strip dotted with auto repair shops. And so do its contents: One corner of the warehouse holds what is arguably the finest collection of health science education materials in the world. But the 180 tons of lessons may soon be pulped by a local recycling company rather than used to feed hungry minds.

Since 1994, NIH's Office of Science Education has created lessons covering 19 topics incorporating the latest biomedical discoveries. Designed to appeal to middle and high school students, there's a neurobiology unit that focuses on addiction, for example, and an exploration of biological rhythms that discusses sleep disorders.

Over the years, NIH has distributed more than 450,000 copies of the supplements, free of charge. Although the 2-week units are also available online, the office maintains some 200,000 copies for teachers—probably the vast majority—who might have trouble downloading and copying them at school.

That supply is now in jeopardy, however, as a result of a government-wide restructuring of science education programs (see main story, p. 338). The White House has proposed shutting down NIH's $4-million-a-year education office next year and ending a $15-million-a-year grants program that supports informal science education activities outside the regular classroom. Without a budget, the office won't be able to pay its share of the rent and utilities for the warehouse, and the material could simply be tossed.

The moves could happen as soon as 1 October, the first day of the 2014 fiscal year. NIH officials have refused to allow Bruce Fuchs, an immunologist who has directed the office since 1996, to speak with the media. But outside scientists funded by the grants program and others familiar with the office say that its nine full-time employees have been told they will be reassigned and that contract staff members will be let go.

NIH is keeping its cards close to the vest. "We have not made a final decision about whether the office is closing at the end of fiscal 2013," says Principal Deputy NIH Director Lawrence Tabak. But he acknowledges that NIH is considering all manner of cost-saving options because of the $1.5 billion bite taken out of the agency's overall $30 billion budget by the government-wide cuts known as the sequester. "We have to think about our priorities and see what rises to the top," he says.

Teachers and health science educators around the country say that closing the office would be a tragedy. For the past decade, Jodie Spitze has taught an NIH unit on bioethics to her biology students at Kent-Meridian High School outside Seattle, Washington. She says that the NIH materials fill a big gap. In addition to providing teachers with the latest research results, the units also prepare them to lead classroom discussions of hot-button issues.

"IB [International Baccalaureate] biology has a requirement to teach controversial issues like stem cell research, but there's no strategy to do it," says Spitze, who was featured in a 2008 *Science* article on teaching bioethics in school. Teaching kids how to listen and build a convincing argument based on facts rather than opinions "can be even more important sometimes than the content," she adds. "Otherwise, the kids with the strongest opinions wind up dominating the discussion, which just turns into a debate."

Published by AAAS

that found only 10 of the 115 existing STEM programs had been rigorously evaluated. Of those, only four were found to have achieved their goals, which included raising student achievement in science and math, improving the skills of STEM teachers, attracting more students into STEM careers, and increasing public understanding of science.

Correcting "bad habits"

Stack doesn't claim to be an expert in STEM education. "My education credentials are probably at the bottom," she told her SREE audience. But when the new Obama administration decided to apply evidence-based policy to STEM education, she dove in. "When Obama came in, we moved into overdrive," Stack said. "Within weeks of taking office, they wanted a briefing from OMB on what we could do to improve government. I had learned from my STEM experience that there wasn't a lot of good evaluation out there."

Although neither a scientist nor an educator, Stack was invited to speak to the President's Council of Advisors on Science and Technology (PCAST) in October 2009 as it prepared to launch the first of two studies of ways to improve U.S. science and math education. Stack used the opportunity to explain the rationale behind evidence-based policy.

"We have gotten into some really bad habits," she told PCAST. "We don't challenge our assumptions that existing programs work. We plan evaluations once the programs have been up and running, when it's hard to create an experimental design with a control group. And evaluation officials are rarely part of the discussion when policymakers examine programs." Although Stack said many agencies may not be able to conduct such high-quality evaluations, she told PCAST that "STEM is one area that may be ripest for taking this approach."

Stack and her OMB colleagues decided to offer federal agencies the carrot of additional funding if they teamed up to design STEM education programs that could be evaluated more rigorously. "We said you can have money if you send us proposals to support [certain] research questions and to build capacity" for further evaluation. She said NSF and the Education Department, for example, were "challenged … to come up with a plan to improve teacher professional development."

But money for those and other evaluation experiments dried up after the Republicans took control of the House of Representatives in January 2011 and the president and Congress struck a deal in August to reduce the federal deficit by cutting spending. "As passionate as I am about rigorous evaluation," Stack told SREE, "it will be a hard sell to set aside large pots of money for evaluation." Instead, she suggested agencies look for "natural experiments … that might show where they can cut without hurting student performance."

It is not clear whether the plan crafted by Stack and others at OMB was adjusted before being rolled out by the White House. But its hostile reception suggests that, whatever the plan's technical merits, the Obama administration has done a poor job of selling it politically. The result has been widespread criticism from a research community that has generally applauded this White House's science initiatives.

In a time when every government program is on the chopping block, advocates of STEM education don't expect politicians to exempt their field from scrutiny. But the take-home message from the reorganization controversy, they say, is that politicians should rely on scientists and educators as well as bureaucrats to decide which STEM education programs live and die.

Kathy Stack wouldn't disagree. But her career demonstrates that a faceless bureaucrat can sometimes also be a very powerful voice in setting policy. **–JEFFREY MERVIS**

Jeanne Chowning, who leads a Seattle-based nonprofit organization that uses the NIH materials in teacher training workshops, says: "I don't know anything else out there that is so up-to-date. And you can count on the quality of the resources because they have been developed by top scientists."

In North Carolina, Suzanne Wilkison runs an organization similar to Chowning's. In April, when she learned that NIH was planning to shut down its science education office, she immediately placed an order for 3000 copies of eight NIH units. "I panicked," she admits. "I wanted to make sure we had a 5-year supply."

Principled learning. Teachers Amy Lindahl and Brandon Staton discover how to use NIH's exploring bioethics curriculum at a summer workshop.

CREDIT: JEANNE TING CHOWNING

Joan Thompson, a science consultant for the state's Department of Public Instruction, also placed an order. Next month, North Carolina school officials will pilot an updated course in biomedical technology, now taken by 8000 students each year, which draws upon eight of the NIH modules. Thompson says that the NIH material is a godsend for school administrators, in part because it is aligned with the next wave of education standards that many states are adopting—the Next Generation Science Standards and the Common Core standards for mathematics and reading.

Congress seems to agree that the office is worth preserving. This month, a Senate spending panel told NIH that it should "continue funding these programs in fiscal year 2014," adding that "the Committee is not convinced that the quality of these programs would be maintained if they were moved to other federal agencies."

NIH's Tabak says that "of course we will consider the sentiments of the Senate." But he notes that "we are at a very early stage" of a budget process that could extend well into fall. **–JDM**

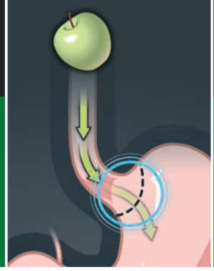

LETTERS

edited by Jennifer Sills

Retraction

THERE ARE SEVERAL PROBLEMS WITH THE REPORT "SPHK1 REGULATES PROINFLAMMATORY responses associated with endotoxin and polymicrobial sepsis" by P. Puneet *et al*. (*1*). Specifically, Figs. 3D and 4B contain images that were generated by author Puneet for the *Science* paper, but had been used in previous publications [see (*2*, *3*)] without her knowledge or consent. Images in Fig. 3D are also found in Fig. 4B. Irregularities in other figures have been suggested, and the validity of the data cannot be confirmed. Finally, sections of the text are similar or identical to sections of (*4*).

For these reasons, the authors below wish to retract the paper. Author Alirio J. Melendez has not been available to sign the Retraction. The National University of Singapore has completed an investigation into the irregularities in this paper and has concluded that sole responsibility for the irregularities rests with author Melendez.

PADMAM PUNEET,[1] CELESTIAL T. YAP,[1] LINGKAI WONG,[2] LAM YULIN,[2] DOW RHOON KOH,[1] SHABBIR MOOCHHALA,[3] JOSEF PFEILSCHIFTER,[4] ANDREA HUWILER[5]

[1]Department of Physiology, National University of Singapore, 117597 Singapore. [2]Department of Chemistry, National University of Singapore, 117543 Singapore. [3]Defence Medical and Environmental Research Institute, DSO National Laboratories, 117510 Singapore. [4]Pharmazentrum Frankfurt, University Hospital, Frankfurt am Main 60590, Germany. [5]Institute of Pharmacology, University of Bern, Bern CH-3010, Switzerland.

References

1. P. Puneet *et al.*, *Science* **328**, 1290 (2010).
2. P. N. Pushparaj *et al.*, *Int. J. Biochem. Cell Biol.* **40**, 1817 (2008).
3. P. N. Pushparaj *et al.*, *Proc. Natl. Acad. Sci. U.S.A.* **106**, 9773 (2009).
4. A. Bouchon *et al.*, *Nature* **410**, 1310 (2001).

Silver Lining of Singapore's Haze

THE POLLUTANT STANDARDS INDEX (PSI), A measure of pollution levels for major air pollutants, reached a historical high of 401 in Singapore on 21 June, as a consequence of forest fires in Sumatra, Indonesia (*1*). A PSI between 101 and 200 is considered unhealthy; between 301 and 400 is hazardous to health; and above 400 is life-threatening to ill and elderly persons.

The ongoing 187 fire hot spots quadruple the number that existed in 1997, when the previous PSI historical maximum was realized (*2*). The majority of these fires are due to land-clearing activities to replace tropical forests by agricultural crops such as oil palm (*3*). Fire land clearing during the intermonsoonal dry season generates smoke ("haze") that can cover neighboring Singapore and Malaysia for days, causing substantial economic losses (*4*). For instance, between 1993 and 1998, the impacts of haze amounted to US$4.5 billion (*5*); the current unhealthy readings could cost the tourism industry of Singapore alone roughly US$1 billion (*6*). Burning has been illegal in Indonesia since 1995 (*7*).

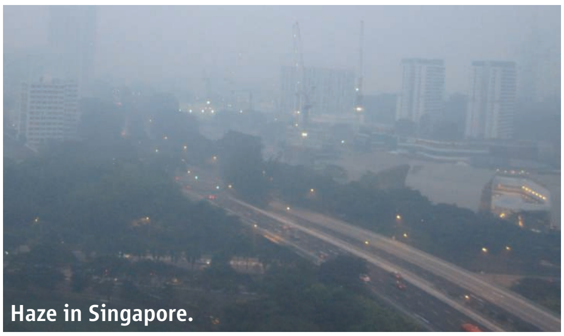

Haze in Singapore.

CREDIT: LUIS ROMAN CARRASCO

The severity of the current situation has led to an escalation of diplomatic tensions between Singapore, Malaysia, and Indonesia. As in previous haze episodes, Singapore officials have demanded actions from the Indonesian central government. Unprecedentedly, Hadi Daryanto, the secretary-general of Indonesia's Forestry Ministry, was recently quoted suggesting that Malaysia- and Singapore-based oil palm companies could be, together with local farmers, responsible for the slash-and-burn practices to clear land (*8*). This sparked reactions from Singapore's Environment and Water Resources Minister, Vivian Balakrishnan, who prompted Indonesian officials to name the companies responsible (*6*). There was also a response from Singapore-based oil palm company Golden Agri-Resources, which assured the public that it does not use slash-and-burn practices, only bulldozers, to clear the land (*9*).

The haze is indicative of much bigger biodiversity and climate change global problems. Tropical deforestation in Southeast Asia will result by 2100 in the loss of 13 to 42% of all regional populations, half of which will represent global species extinctions (*10*). Meanwhile, tropical deforestation will continue to contribute substantially to climate change, causing 15% of global anthropogenic carbon emissions (*11*).

Surprisingly, in contrast with the haze, neither the impending biodiversity disaster nor climate change is able to spark diplomatic actions between regional governments or to irritate the public in the region. Seeking to assign responsibilities for the haze—who benefits and loses from it and who should get compensation—is similar to the necessary process of identifying responsibilities for the biodiversity and climate change crises. In this context, Daryanto's remark is important in that it denotes the need for Indonesian authorities to rethink whether the massive

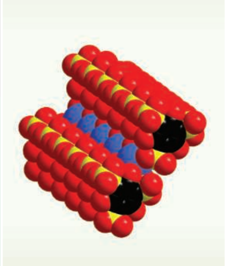

Creating pores for protons

354

IBI Prize Essay

360

exchange between Indonesia and (to a large extent) foreign companies of natural treasures for oil palm is a sustainable strategy.

Paradoxically, given the effectiveness of the haze as a stimulus provoking regional leaders to talk about deforestation, conservationists might even prefer that forests are burned instead of bulldozed. Forests only cleared with bulldozers could mean the end of even the tangential discussions of the deforestation problem, permitting the ongoing silent and nonirritating destruction of Southeast Asian tropical forests.

LUIS ROMAN CARRASCO

Department of Biological Sciences, National University of Singapore, Singapore, 117546, Singapore. E-mail: dbsctlr@nus.edu.sg

References

1. National Environment Agency, PSI Readings; www.nea.gov.sg/psi.
2. AsiaOne News, "Four times as many hotspots in Sumatra now" (19 June 2013); http://news.asiaone.com/News/AsiaOne%2BNews/Malaysia/Story/A1Story20130619-430693.html.
3. J. Miettinen *et al., Glob. Change Biol.* **17**, 2261 (2011).
4. D. J. Lohman, D. Brickford, N. S. Sodhi, *Science* **316**, 376 (2007).
5. T. P. Tomich *et al., Agric. Ecosyst. Env.* **104**, 229 (2004).
6. K. Park, J. Ng, "Singapore smog reaches 'hazardous' all-time high on fires," *Bloomberg Businessweek* (20 June 2013); www.businessweek.com/news/2013-06-19/singapore-urges-indonesia-to-name-firms-in-worst-smog-since-1997.
7. FAO, "Fire Management—Global Assessment 2006" (United Nations Food and Agricultural Organization, Rome, 2007).
8. D. Faridz, Channel NewsAsia, "Singapore, Malaysia share some blame for haze: Indonesian official" (18 June 2013); www.channelnewsasia.com/news/singapore/s-pore-m-sia-share-some/714786.html.
9. Global Post, "Worsening haze from Indonesia angers Singapore, tourists" (19 June 2013); www.globalpost.com/dispatch/news/afp/130619/worsening-haze-indonesia-angers-singapore-tourists-0.
10. B. Brook, N. Sodhi, P. Ng, *Nature* **424**, 420 (2003).
11. G. Van der Werf *et al., Nat. Geosci.* **2**, 737 (2009).

A Statistically Significant Future for Bayes' Rule

B. EFRON'S ENTERTAINING PERSPECTIVE "Bayes' theorem in the 21st century" (7 June, p. 1177) on the past and possible future of the use of Bayes' theorem in statistical inference strategically avoids addressing the use of statistics by nonstatisticians. Unlike most professional statisticians, many empirical scientists are not able to use the method of analysis that best fits their particular problem. In addition, their understanding of the frequentist statistics in which they have been trained has been widely found to be rather abysmal. As John Tukey said in 1964, "Most uses of the classical tools of statistics have been, are, and will be, made by those who know not what they do" (*1*).

This situation has led many to argue for an educational reform in statistical training for empirical scientists, and for increased emphasis on translating between frequentist and Bayesian measures of evidence (*2*). Tentative implementations of both of these projects already exist (*2*), and these attempts merit encouragement and praise, all the more because Bayesian statistics is proving to be particularly useful in many fields.

Reasons for this increased popularity in Bayesian methods are not hard to spot. Much of modern research, particularly in the life sciences, is based on the synthesis of multiple categories of evidence. Data coming from many different studies have to be integrated in order to assess the empirical evidence for a new theory, and Bayesian statistics lends itself very well to this. Working scientists have noticed this, and many are using these tools now. With the increasing statistical literacy of empirical scientists and the growing availability of Bayesian computer software, the future of Bayes' rule, along with that of other approaches to inference, seems well assured.

ROBERT VAN HULST

Department of Biology, Bishop's University, Sherbrooke, QC J1M 1Z7, Canada. E-mail: rvhulst@ubishops.ca

References

1. J. W. Tukey, *Am. Stat.* **19**, 23 (1965).
2. S. Greenland, C. Poole, *Epidemiology* **24**, 62 (2013).

Response

VAN HULST BRINGS UP AN IMPORTANT POINT: Bayesian methods are easier to explain and understand than their frequentist counterparts. An attractive simplicity is exactly what led to Bayesian statistics' overuse, and then disuse, in past epochs. Frequentism is essentially a more cautious and self-critical philosophy, better able to withstand skeptical scrutiny from the scientific world. It will always have a major role to play in real-life scientific inference. There are two potent arrows in the statistician's quiver, and there is no need to go hunting armed with only one.

BRADLEY EFRON

Department of Statistics, Stanford University, Stanford, CA 94305–4065, USA. E-mail: brad@stat.stanford.edu

TECHNICAL COMMENT ABSTRACTS

Comment on "An Update of Wallace's Zoogeographic Regions of the World"

Holger Kreft and Walter Jetz

Holt *et al.* (Report, 4 January 2013, p. 74) propose substantial modifications of Wallace's long-standing zoogeographic regions based on clustering of a pairwise similarity matrix of vertebrate assemblages. We worry about their compromised use of phylogenies and show that a fundamental point of their analysis—i.e., the delineation of new realms—is only weakly supported by their results and conceptually flawed.

Full text at http://dx.doi.org/10.1126/science.1237471

Response to Comment on "An Update of Wallace's Zoogeographic Regions of the World"

Ben G. Holt, Jean-Philippe Lessard, Michael K. Borregaard, Susanne A. Fritz, Miguel B. Araújo, Dimitar Dimitrov, Pierre-Henri Fabre, Catherine H. Graham, Gary R. Graves, Knud A. Jønsson, David Nogués-Bravo, Zhiheng Wang, Robert J. Whittaker, Jon Fjeldså, Carsten Rahbek

Kreft and Jetz's critique of our recent update of Wallace's zoogeographical regions disregards the extensive sensitivity analyses we undertook, which demonstrate the robustness of our results to the choice of phylogenetic data and clustering algorithm. Their suggested distinction between "transition zones" and biogeographic regions is worthy of further investigation but is thus far unsubstantiated.

Full text at http://dx.doi.org/10.1126/science.1237541

Letters to the Editor

Letters (~300 words) discuss material published in *Science* in the past 3 months or matters of general interest. Letters are not acknowledged upon receipt. Whether published in full or in part, Letters are subject to editing for clarity and space. Letters submitted, published, or posted elsewhere, in print or online, will be disqualified. To submit a Letter, go to www.submit2science.org.

Comment on "An Update of Wallace's Zoogeographic Regions of the World"

Holger Kreft[1]* and Walter Jetz[2]

Holt *et al*. (Report, 4 January 2013, p. 74) propose substantial modifications of Wallace's long-standing zoogeographic regions based on clustering of a pairwise similarity matrix of vertebrate assemblages. We worry about their compromised use of phylogenies and show that a fundamental point of their analysis—i.e., the delineation of new realms—is only weakly supported by their results and conceptually flawed.

Dividing the world into regions of similar faunistic or floristic composition and shared evolutionary history is a major aim of biogeography. The most prominent regionalization, Wallace's zoogeographic regions (*1*), has had tremendous influence, but its expert-based nature and lack of quantitative rigor and reproducibility have led to ongoing debates about the number and delineation of regions [reviewed in (*2*, *3*)]. In their Report, Holt *et al*. (*4*) follow recently developed methodology and results for mammals (*3*) and present a quantitative global regionalization that extends to birds and amphibians. Instead of pairwise turnover of species (or genera or families), they used the number of branches in variably resolved phylogenies shared between two assemblages. The integration of global range maps and phylogenetic information to delineate biogeographical regions is promising because it may overcome problems associated with mixed results reported from studies at the species, genus, and family levels (*3*, *5*). However, we believe that the key results of their study—i.e., an integrative delineation of the world's main biogeographical regions and the proposal of five new realms—are largely based on problematic data and methodology, as well as subjective decisions, and thus may have several conceptual flaws.

First, we are concerned about the overall poor and taxonomically and geographically disparate resolution of the tree topologies invoked. These were single trees in which only 40 to 60% of species were resolved, meaning that species' contributions to the regionalization were highly nonuniform and, in some cases, very minor.

Second, only counts of branches, not their actual lengths, were used for quantifying dissimilarity. This will in some cases equate species 20 million years old with those just 20,000 years old and ignores considerable differences in the ages of clades (e.g., amphibians versus birds) and regions. The authors suggest that in mammals, such differences, or even using just species' taxonomic separation instead, would not affect the existence and location of zoogeographic regions. We feel that this casts doubt, in this implementation, on the rigor and relevance of the "phylogenetic" method. New approaches are arising that account for all species in a single quantitative framework and that estimate branch lengths and uncertainty (*6*, *7*). In the midst of such major phylogenetic advances for vertebrates, we support caution over a rush in updating Wallace's regions.

Third, the authors propose the Saharo-Arabian, Sino-Japanese, and Panamanian as new "realms," even though they do not match their criterion of "phylogenetically distinct" regions (containing unique radiations and high degrees of endemism) but instead are well-known biogeographical transition zones where long-separated biota mix (*8*) and thus are of fundamentally different nature. In fact, there are striking similarities between these new realms and a map published 40 years ago that depicts biogeographical core regions as well as broad interjacent transition zones (*9*) (Fig. 1). For instance, it has been shown that the Saharo-Arabian is mainly an impoverished set of Afrotopical lineages, but with strong influences from the neighboring Palearctic and Oriental faunas (*2*, *10*). Similarly, the temperate-tropical transition zone in East Asia and Central America are regions of complex faunistic interchange (*11*). We believe that raising transition zones to the rank of realms is inappropriate and will ultimately hamper biogeographical inference.

Hierarchical clustering identifies transition zones as distinct even if their distinctiveness results from mixing rather than independent evolutionary histories (Fig. 2). Applying clustering algorithms to biogeographical data is particularly challenging because the evolutionary distinctiveness of regions can be diluted by repeated episodes of faunal interchange (*8*). The unweighted pair group method with arithmetic mean (UPGMA) clustering algorithm used by the authors is unable to differentiate between the biogeographical core and transition zones, because transition zones will ultimately be merged with core areas with which they show the greatest affinity (compare Fig. 2D). In our hypothetical example (Fig. 2), the green region identified in the three-cluster solution is clearly qualitatively different from the black and red. Here, ordination plots of all grid cells are more informative in revealing how core regions are connected (Fig. 2C). As shown previously for mammals (*3*), a nonmetric multidimensional scaling (NMDS) ordination including all grid cells would likely have revealed such gradual transitions. The NMDS plots presented by the authors for 11 realms and 20 regions [figures S1 and S2 in (*4*)], however, cannot fully reveal the complexity of biogeographical transitions.

Fourth, there is only limited quantitative support for the status of the new realms. It is a great challenge to determine the number of clusters, and stopping criteria are necessary to identify the most informative parts of a clustering dendrogram (*12*). To this end, the authors inspected how an evaluation metric (percentage between-cluster $p\beta_{sim}$) changed with the number of clusters. Commonly, such plots are used to identify a "knee"—i.e., the point of maximum curvature, as a cutoff point. Holt *et al*.'s cutoff of 95% of global $p\beta_{sim}$ was chosen arbitrarily, and that value is definitely higher than the "knee" in their evaluation curves [figure S8 in (*4*)]. Importantly, an only slightly lower cutoff would alter the results considerably,

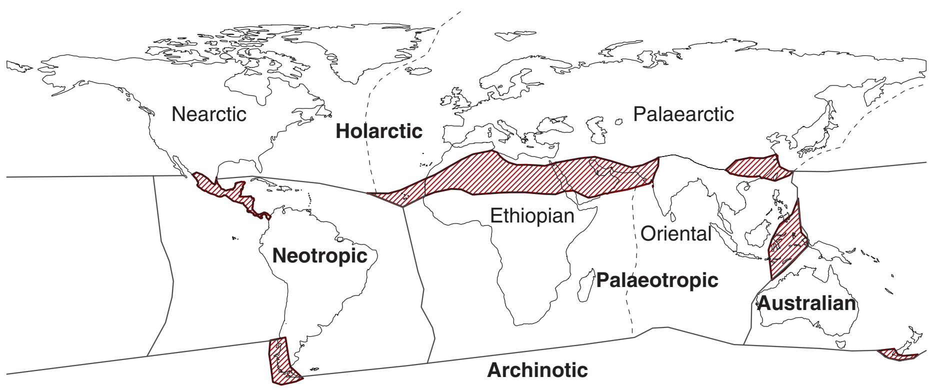

Fig. 1. Map of animal realms with broad biogeographical transition zones highlighted in red [redrawn and modified from (*9*)]. Realm names in bold were taken from the original map; nonbold names have the rank of regions and were taken from an accompanying table.

[1]Biodiversity, Macroecology and Conservation Biogeography Group, Faculty for Forestry and Forest Ecology, Büsgenweg 1, University of Göttingen, 37077 Göttingen, Germany. [2]Department of Ecology and Evolutionary Biology, Yale University, 165 Prospect Street, New Haven, CT 06520–8106, USA.

*Corresponding author. E-mail: hkreft@uni-goettingen.de

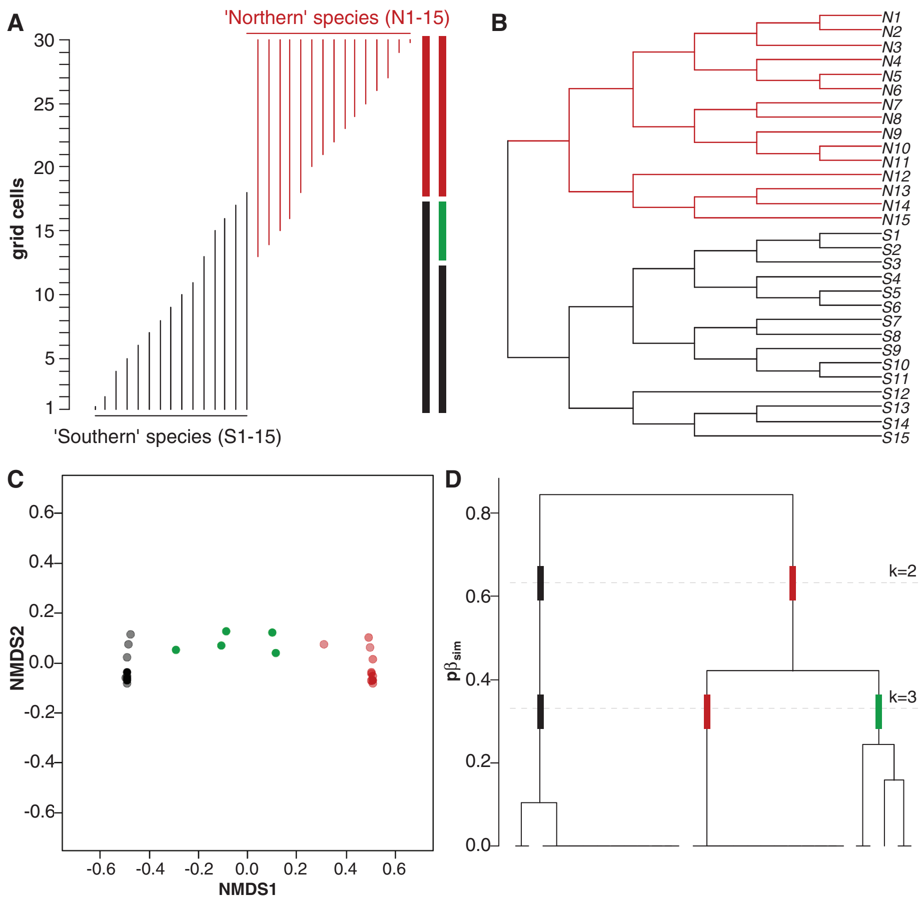

Fig. 2. Hypothetical example illustrating the performance of multivariate methods in a transition zone. (**A**) Two independently evolved species pools (black and red) blend into one another. Each thin line represents the distribution of one species. (**B**) Species' phylogenetic relationships. (**C**) A two-dimensional NMDS ordination solution based on a phylogenetic turnover ($p\beta_{sim}$) matrix based on the species distribution in (A) and the phylogenetic relationships in (B). (**D**) UPGMA dendrogram based on the same matrix. Horizontal dashed lines highlight two alternative cluster solutions, for $k = 2$ and $k = 3$. Red, black, and green color-coding of right-hand vertical bars in (A) and points in (C) signify UPGMA cluster memberships.

as the Saharo-Arabian would collapse into the Afrotropical, the Sino-Japanese into the Palearctic, and the Panamanian into the Neotropical—all resulting in currently recognized realm boundaries (*2*, *3*) that are largely consistent with Wallace (*1*). Alternative stopping rules or procedures to determine the number of clusters (*3*, *12*) would likely have produced different or mixed results.

In conclusion, given the intricate biotic interchange in space and time (*8*, *11*), biogeographers must be aware that expert- and algorithm-drawn boundaries are ultimately only arbitrary, although helpful, constructs that are inherently limited in fully capturing the biogeographical complexity. Regionalizations ideally should account fully for all species and their different evolutionary histories and require very careful interpretation. Promising alternative algorithms (*13*) and fully resolved and dated phylogenies are being developed (*6*), but until such conceptual and methodological issues have been resolved, a separation of new realms may seem premature.

References and Notes

1. A. R. Wallace, *The Geographical Distribution of Animals* (Harper & Brothers, New York, 1876).
2. B. Cox, *J. Biogeogr.* **28**, 511–523 (2001).
3. H. Kreft, W. Jetz, *J. Biogeogr.* **37**, 2029–2053 (2010).
4. B. G. Holt *et al.*, *Science* **339**, 74–78 (2013).
5. Ş. Procheş, S. Ramdhani, *Bioscience* **62**, 260–270 (2012).
6. W. Jetz, G. H. Thomas, J. B. Joy, K. Hartmann, A. O. Mooers, *Nature* **491**, 444–448 (2012).
7. T. S. Kuhn, A. Ø. Mooers, G. H. Thomas, *Methods Ecol. Evol.* **2**, 427–436 (2011).
8. G. J. Vermeij, *Science* **253**, 1099–1104 (1991).
9. P. Müller, Die Verbreitung der Tiere: Grzimeks Tierleben (Kindler, 1973), in *Biogeography*, P. Müller, Ed. (Harper & Row, New York, 1986), vol. 16, pp. 18–20.
10. M. Delany, *Mammal Rev.* **19**, 133–152 (1989).
11. G. G. Simpson, *Am. Sci.* **38**, 361–389 (1950); www.jstor.org/stable/27826322.
12. G. W. Milligan, M. C. Cooper, *Psychometrika* **50**, 159–179 (1985).
13. J. Olivero, R. Real, A. L. Márquez, *Syst. Biol.* **60**, 645–660 (2011).

Acknowledgments: We thank Y. Kisel and P. Weigelt for valuable comments on the manuscript. H.K. acknowledges funding from the German Research Foundation (DFG).

6 March 2013; accepted 14 June 2013
10.1126/science.1237471

Summer Reading

This year we turned to recent AAAS Mass Media Fellows for suggestions and reviews of some thoughtful and enjoyable science titles.

Bellwether Tissue

Breasts: A Natural and Unnatural History. Florence Williams. Norton, New York, 2012. 350 pp. $25.95, C$27,50, £15.99. ISBN 9780393063189. Paper, 2013. $15.95, C$17, £9.99. ISBN 9780393345070.

Lurking in the breast tissue of contemporary women around much of the globe is a complex mixture of industrial, agricultural, and household toxicants. Lactation delivers a portion of these chemicals. What remains a mystery is the long-term health consequence of these chemical exposures to both mother and baby.

In *Breasts: A Natural and Unnatural History*, Florence Williams explores the effects of toxicant exposures on a tissue that establishes itself before birth, flourishes during puberty, and differentiates into functional units at the time of pregnancy. By weaving together clinical cases, cutting-edge research, personal anecdotes, and accounts of individuals affected by exposures, Williams (an editor at *Outside* magazine) unpacks how modern life is changing the landscape of the breast. *Breasts* challenges long-held assumptions about the reason for mammary glands and raises critical questions about life-stage exposures in this dynamic tissue.

DDT and model on Jones Beach, New York, 1948.

How and why breasts evolved are still unclear and surprisingly controversial. Williams argues that this ambiguity undermines our ability to understand the breast as a functional organ capable of responding to an increasingly complex chemical environment. She speculates that the view of breasts as an evolutionary "sexual signal" (rather than a nutrient delivery system) may be behind certain theories in the social sciences that posit breasts evolved as "a courtship device" for females or "a first pass filter" for males wishing to find a fecund female. Williams deconstructs these evolutionary scenarios, citing examples of reproductive success among small-breasted women and the fact that pregnancy typically results in well-endowed breasts. It is likely that breasts evolved to create storage spaces for the fat required to facilitate ovulation and nutrients needed to sustain an offspring.

Framing breasts as an evolutionary sexual embellishment is not without consequences. Williams argues that the view of breasts as objects of desire disconnects them from the larger ecosystem. Understanding the environmental health implications of toxicant-exposed breasts requires teasing apart complex interactions between tissue and environment. As one researcher interviewed by Williams succinctly states, "We've got to be more scientific about it."

To illustrate a less-than-scientific approach to breasts, Williams recounts in jarring detail the first breast enhancement surgery using silicone-filled implants. These implants evaded safety testing, and although the Food and Drug Administration eventually began to regulate medical devices by the mid-1970s, the implants managed to escape the formal approval process. Williams draws a parallel between lax safety standards for these early implants and the establishment of the Toxic Substances Control Act of 1976, which excluded 62,000 chemicals from regulatory oversight.

Some of these substances have subsequently been identified in breast milk (and, in fact, are detected in Williams's own breast milk). The problem with chemicals in breast milk, explains Williams, is that they are biomagnified, sometimes reaching levels that would surpass federal safety standards if these same chemicals were found in food. The presence of toxicants in the breast is only part of the story. The timing of an exposure is often equally critical. Rats, for example, have a "window of susceptibility," corresponding to puberty, during which they are most strongly affected by toxicants—just one of several possible developmental milestones that could become a target of toxicity.

In spite of data from animal studies, how environmental exposures influence breast biology in humans remains a black box. Breast tissue exhibits a certain degree of plasticity, which allows it to respond to both the endogenous hormonal cues of puberty or pregnancy and structurally similar synthetic molecules found in plastics and pesticides. Animal studies demonstrate that toxicants resembling estrogens not only alter the growth of milk ducts, they have transgenerational effects that render an offspring more susceptible to tumor formation in adulthood. Williams is careful to qualify this research, citing the difficulty of translating findings in animals to humans and the even greater challenge of linking exposure to health outcome in humans.

In *Breasts*, Williams urges readers to see breasts through an ecological lens, as a sentinel tissue capable of responding to an environment that has become increasing hostile. Her message is cautionary but not entirely pessimistic. The weight of scientific evidence for the breast as a target of toxicants is mounting. The time for preventing exposures has arrived. Breasts are environmental bellwethers worthy of serious consideration.

– **Kelly A. Hogan**[1]

Extinct, Yet Still Evolving

My Beloved Brontosaurus: On the Road with Old Bones, New Science, and Our Favorite Dinosaurs. Brian Switek. Scientific American/Farrar, Straus, and Giroux, New York, 2013. 266 pp. $26, C$30, £17.99. ISBN 9780374135065.

Dinosaurs tend to evoke childhood nostalgia for elementary school picture books and museum field trips, but some, including science writer Brian Switek, never outgrow their youthful fascination with these enormous lizards. In *My Beloved Brontosaurus: On the Road with Old Bones, New Science, and Our Favorite Dinosaurs*, Switek passionately and playfully explores scientists' evolving perception of the wild, wonderful dinosaur world, emphasizing at every turn the dynamic nature of their field despite its now inanimate subjects.

Although dinosaurs have been dead for millions of years, researchers are constantly uncovering new specimens and developing analytical techniques that allow them to reevaluate what we think we know about their lives and deaths. Switek introduces this theme in the very title of his book, which refers to the *Brontosaurus* identity crisis. Many of us, including Switek, were taught while growing up that *Brontosaurus* was the prototypical long-necked, four-

[1]Department of Environmental Health Sciences, School of Public Health, University of Michigan, 1415 Washington Heights, Ann Arbor, MI 48109, USA. E-mail: kahogan@umich.edu

Charles R. Knight's 1897 reconstruction of *Brontosaurus*.

legged vegetarian. But it turns out that these dinosaurs should more properly be called *Apatosaurus*, as Yale paleontologist O. C. Marsh christened them in 1877 on the basis of partial remains of a juvenile sauropod from Colorado. The name *Brontosaurus* entered the picture in 1879, when Marsh thought more complete remains from Wyoming represented a distinct genus. In 1903, Elmer Riggs showed that decision was erroneous. At that point *Apatosaurus* should have had priority, but for unknown reasons "*Brontosaurus*" stuck around, working its way into museum displays, books, and children's imaginations and creating confusion to this day.

With the *Brontosaurus* episode setting the stage, the remainder of the book explores other aspects of dinosaur anatomy, phylogeny, and behavior that paleontologists have wrestled with over the years. Switek intersperses his rich, well-researched scientific and historical discussions with personal anecdotes and cultural signposts, weaving together a narrative that reveals the current state of the field as well as some of the wrong turns along the way. Topics covered include dinosaur sex (in the chapter "Big Bang Theory"); what dinosaur roars may have actually sounded like; and dinosaur skin, which in at least some cases appears to have been painted in vivid hues and covered with feathers.

Although it can be difficult to adjust to some of these changes, such as *Brontosaurus*'s renaming or technicolored *Tyrannosaurus rex*, Switek assures us that they are all for the best. After discussing how today's vision of agile, intelligent animals actively engaging with their environments and each other has replaced the early imaginings of dull, lumbering behemoths mired in swamps, he concludes that "there is no question that the dinosaurs we're bringing to life today are far more beautiful and complex than their earlier incarnations."

Throughout *My Beloved Brontosaurus*, it's clear that Switek is deeply attached to and moved by his prehistoric subjects. For some readers, though, this conviction may not be enough to explain why we should care about these extinct giant reptiles or how they are relevant to our modern lives. In response to any such doubters, Switek argues that dinosaurs provide a unique and invaluable perspective on life, evolution, and ourselves: "Pick any dinosaur you like, and that ancient creature is undeniable proof that our planet has a history so deep that we can barely comprehend it, that life has changed dramatically over time, and that extinction is the ultimate fate of all species. Nothing so majestically encapsulates these simple, powerful truths of nature quite like a dinosaur."

– Rachel Bernstein[1]

[1]A freelance science writer based in San Francisco. E-mail: rbernstein@gmail.com

CREDITS: (LEFT) CHARLES R. KNIGHT/WIKIMEDIA COMMONS; (RIGHT) RESOURCE ASSESSMENT AND CONSERVATION ENGINEERING/ALASKA FISHERIES SCIENCE CENTER/NOAA

Fish Gold Rush

Billion-Dollar Fish: The Untold Story of Alaska Pollack. Kevin M. Bailey. University of Chicago Press, Chicago, 2013. 302 pp. $25, £17.50. ISBN 9780226022345.

Ubiquitous substrate of frozen fish sticks, fish and chips, and fake crab meat, Alaska pollock (*Theragra chalcogramma*) is invisible to consumers, though it is the largest and most lucrative fishery in the United States. Pollock does not have the depth of cultural history attached to its more charismatic Alaskan neighbors, salmon and king crab. It is prized for all of the attributes that make it mundane and suited to industrial anonymization: its mild white flesh; low fat content; large, dense, nearly pure schools; and huge spawning aggregations above the continental shelf.

An ecologist with a feel for the social dimensions of fishery management, Kevin Bailey has over 30 years of experience, primarily at the Alaska Fisheries Science Center. In *Billion-Dollar Fish*, he considers the question of why the Alaska pollock fishery in the eastern Bering Sea has stabilized into a model of sustainability (by some accounts) while other fisheries have struggled and crashed. Is the current state of the fishery a quirk of pollock biology or human culture? a victory of management and political negotiation? a contingency of history?

Bailey believes the relative success of the Alaskan pollock fishery lies in the influence of science on its management, made possible by the youth of the fishery and the timing of its development. He writes in a workmanlike style but lightens his account with sporadic portraits of colorful and powerful personalities from the commercial fishing business and its environmentalist antagonists. He is, however, relatively stingy with human details from the recent heated negotiations over the development of the catch-share system.

Valuable catch.

Alaska pollock lacks a long fishing tradition; until after World War II, the species was mostly left to the seabirds, sea lions, and fur seals. The U.S. government didn't get involved in the fishery until the late 1970s, when environmentalism was changing the way Americans thought about natural resources.

Nineteenth-century scientists believed the efforts of human fishers to be too humble before the power of natural processes to have any effect on the bounty of the great fish stocks. Some sense of a finite resource began to intrude with the advent of steam-powered trawlers in 1883, but the general mood remained optimistic well into the 20th century. Even environmental champion Rachel Carson viewed unexploited fish stocks as wasted, much as many Americans viewed land untilled and rivers left to run to the sea. Fish were cheap nutrition to feed the world's hungry.

In 1976, the United States extended an exclusive fishing zone 200 miles into the eastern Bering Sea, limiting the access of giant international factory trawlers from Japan, Korea, Poland, Portugal, and the then Soviet Union. The realities of representational democracy made regulation of foreign fishing vessels easier than imposing similar controls on domestic fleets. Because fishermen are, in Bailey's experience, a species of pugnacious, independent risk-takers with an aversion to government interference, establishing an early precedent for quotas and monitoring catches was, he believes, essential to imposing science-based management on the pollock fishery.

When the Alaskan king crab population crashed hard in the early 1980s, many crab fishermen jumped aboard new joint ventures in Alaska pollock. By 1990, the fleet was twice the size needed to catch the quota mandated by government scientists, and operators engaged in a furious race to get the biggest share. A war developed between the big, Seattle-based factory ships and the shore-side processors in Alaska that serviced smaller catcher vessels.

A legislative solution—arrived at through closed-door negotiation and attached by Senator Ted Stevens as a rider to the federal 1998 general appropriations bill—introduced a catch-share system that assigned quotas to fishing sectors and permitted individual operators to lease quota shares attached to their boats. It restricted the number of operators allowed to compete in the market and the size of vessels, which improved efficiency, reduced bycatch, and put an end to the dangerous race. The system has been effective but has locked up a public resource among a fixed set of players.

Bailey remains ever aware of the limits of population modeling for maintaining the fishery and the ecosystem connected to it, as revealed by a decade of decline in Alaska pollock stocks. *Billion-Dollar Fish* conveys the story of pollock with his skeptical, but affectionate, eye for industrial and environmental claims alike.

– Elizabeth Lester[1]

Lucid Experiences of Altered Reality

Hallucinations. Oliver Sacks. Knopf, New York, 2012. 343 pp. $26.95. ISBN 9780307957245. Picador, London. £18.99. ISBN 9781447208259.

In the early 1970s, eight people were admitted to different psychiatric hospitals across the United States for hearing voices. None were insane; researchers had instructed them to complain about hearing voices to hospital staff. Other than fabricating their names and occupations, they were told to tell the truth and behave normally. The purpose of the experiment was twofold: could hospitals distinguish between sane and insane people, and was there a bias toward assuming people with auditory hallucinations were mentally ill? The study revealed not only that the psychiatrists were unable to make the distinction but also that they assumed hallucinations were concrete evidence of a mental illness, such as schizophrenia. This was a troubling conclusion because although people with schizophrenia generally have hallucinations, the reverse is not necessarily true: hallucinations are not indicative of insanity.

In his latest book, *Hallucinations*, neurologist and best-selling author Oliver Sacks details the incredible range of apparitions that completely sane people experience. Each chapter describes a medical condition—such as migraine, epilepsy, or hearing loss—that can cause a mix of visual, auditory, and tactile hallucinations. Sacks uses firsthand accounts to bring these conditions to life and to introduce the scientific research behind them. Many of these first-person accounts came from his readers, who hoped that their stories might help remove the stigma associated with hallucinations. These personal narratives become increasingly compelling as the hallucinations described progress from benign (hearing musical sounds or seeing a gathering of medieval characters) to painful or terrifying (feeling excruciating sensations in phantom limbs or sensing the presence of malevolent beings).

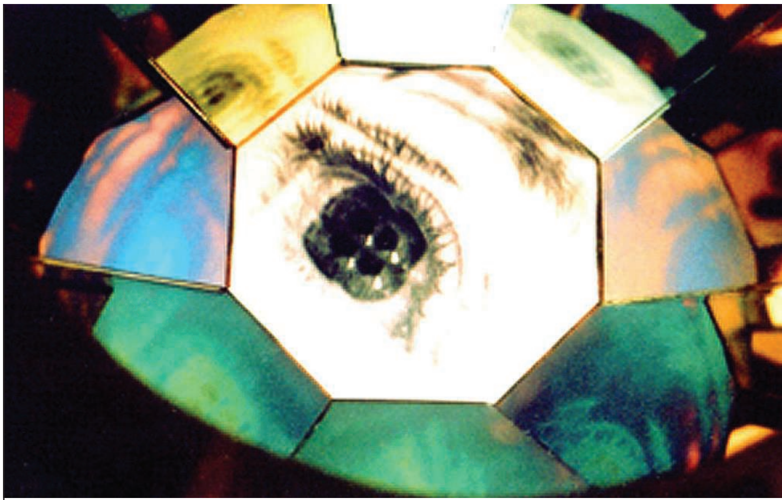

Altered perceptions.

One of the most unsettling accounts came from a woman with narcolepsy. Her condition was not like Hollywood's comical version of the disorder. In addition to falling asleep at random moments, she experienced sleep paralysis and visual and auditory hallucinations. In a letter to Sacks, she described one of her episodes. As she was falling asleep, her body became completely paralyzed. She felt at first as though something were sitting on her back; then it lay down next to her. "I laid eyes on an abnormally tall man in a black suit. He was greenishly pale, sick-looking, with a shock-ridden look in the eyes. I tried to scream, but was unable to move my lips or make any sounds at all." Slowly she came out of her sleep paralysis, and the apparition vanished. Though the experience felt real, the woman understood it was not—a capacity that separates her from the insane.

As the 1970s experiment demonstrated, there is no categorical list of symptoms that can be used to diagnose someone with a mental illness. However, a defining feature of sane people who hallucinate is that they lead ordinary lives—their hallucinations do not affect how they interact with other people. When Sacks establishes that the book will focus on hallucinations that can occur in transient, "'organic' psychoses," he offers this explanation: "The hallucinations often experienced by people with schizophrenia … demand a separate consideration, a book of their own, for they cannot be divorced from the often profoundly altered inner life and life circumstances of those with schizophrenia."

Today, sane people assume their hallucinations are not real because contemporary society has no place for ghosts, witches, or elves. But, as Sacks remarks, because hallucinations seem real, "one must wonder to what extent hallucinatory experiences have given rise to our art, folklore, and even religion." This is just one of the many fascinating questions that Sacks introduces but leaves to the reader for further exploration.

Hallucinations will be accessible to a wide audience. Sacks includes explanations behind each disorder but never becomes overly clinical. He provides a popular survey of an otherwise esoteric topic. The book will appeal to readers who would never think to open a neuroscience or clinical psychology journal but would nevertheless be interested in the research results it reports. Although the book's structure has a textbook feel, the first-person accounts produce an intimate tone that draws in the reader. If you catch yourself talking to friends about each new medical revelation, there is a reason: Sacks's fascination with the brain is contagious.

– Lauren DiPerna[2]

[1]Ecological Society of America, 1900 M Street, NW, Suite 700, Washington, DC 20036, USA. E-mail: llester@esa.org

[2]A freelance writer based in San Francisco. E-mail: freelance.place.work@gmail.com

CREDIT: DIANNE HARRIS/WELLCOME IMAGES

A Measure for Accounting

Why Calories Count: From Science to Politics. Marion Nestle and Malden Nesheim. University of California Press, Berkeley, 2012. 298 pp. $29.95, £20.95. ISBN 9780520262881.

Why Calories Count: From Science to Politics lives up to its subtitle. In it, Marion Nestle and Malden Nesheim cover just about all aspects of the humble calorie. The topic is of interest to most of us. Averaged across the world, we eat about a million calories per year. Those of us who live in the United States have a two in three chance of being overweight or obese, which means at some point we consumed a few too many.

Written by academics (Nestle and Nesheim are nutrition scientists at, respectively, New York University and Cornell University), the text does not shy away from being dry, something that might inhibit its more widespread appeal. But readers comfortable with graphs and references to the literature will find that the book really delivers the facts through clear, short chapters from a host of perspectives.

For starters, the calorie, as Nestle and Nesheim explain, is physics. Energy is neither created nor destroyed. We need energy to function and move. In addition, the calorie is chemistry. Lavoisier proposed oxidation as the main reaction of metabolism, and he was proven correct. Along with such historical tidbits, the authors introduce more obscure chemistry topics such as doubly labeled water and ketones.

Of course the calorie is also biology. Our bodies have encoded feedback loops that help us maintain our weight in times of starvation but leave us weak to the charms of food when it is abundant. Geneticists debate whether there is a "thrifty gene" responsible for these systems or whether they can be explained by a "drifty gene."

Americans in particular face an abundance of food. Nestle and Nesheim cite that on average we have about 3900 calories available per day, almost twice the U.S. Department of Agriculture (USDA) recommended guideline for daily consumption.

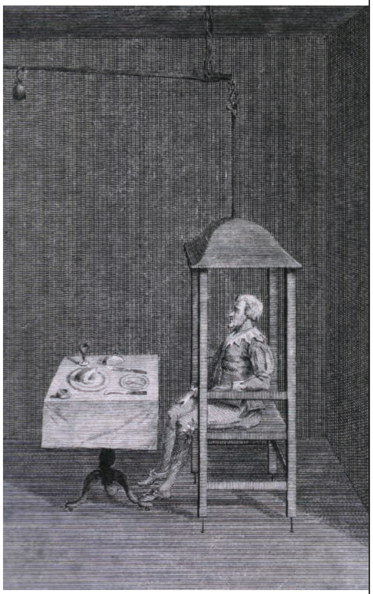

Santorio Sanctorius's balance for tracking the effects of his food intake on his weight.

This abundance not only poses a problem because we can't stop eating, it additionally creates its own economic pressures that keep us spiraling into overconsumption. Beholden to stockholders and competing in a market flooded with supply, food companies fine-tune marketing strategies to get us to eat more and more of their products. The book does a decent job of outlining various political pressures that created and continue to exacerbate this environment, although it doesn't go into much detail.

The authors thoroughly explain the history and logic behind the USDA nutrition labels, which many food companies would rather erase from their packages. That history is dominated by Wilbur O. Atwater (1844–1907), the "father of modern nutrition science," whose determinations of the number of calories in each gram of protein (4), carbohydrate (4), and fat (9) are still used in the United States. The actual values, as we learn, vary from food to food and are slightly different from the "official" estimates.

Which brings us to the largest issue regarding calories. What is known is, embarrassingly, not that much. Our ignorance is not the fault of nutrition scientists but stems from human nature. When surveyed about our calorie intake, we always underestimate. When asked to document our calorie intake, we modify our eating patterns. And not many people want to be lab rats, although Nestle and Nesheim discuss experiments where the "volunteers" (in one case they are prison inmates) were either overfed or underfed. Some of these studies are now recognized as unethical. Thus, when it comes to quantitative nutrition studies, the uncertainties can often overwhelm the signal. But one thing is repeatedly confirmed, despite the noise from diet gurus: as far as body weight, it matters more how much you eat than what you eat.

Whether you're interested in the twin public health crises of obesity and malnutrition, curious about the process of digestion, or just looking for a scientifically supported path to a beach body, you should find *Why Calories Count* an enlightening read.

– Kerstin Nordstrom[1]

Stories for the Bar

The Drunken Botanist: The Plants That Create the World's Great Drinks. Amy Stewart. Algonquin Books, Chapel Hill, NC, 2013. 399 pp. $19.95. ISBN 9781616200466. Timber Press, London. £14.99. ISBN 9781604694765.

Amy Stewart's ode to potable horticulture offers a bacchanal for science-minded alcohol enthusiasts. *The Drunken Botanist* opens in Portland, Oregon, at a convention of garden writers, where Stewart is trying to convince Scott Calhoun, a cactus and agave expert, that gin is a fabulous drink. Calhoun isn't persuaded, so she tempts him by describing a gin, jalapeno, cilantro, and cherry-tomato concoction that sounds tasty and like it belongs at a boutique cocktail bar in San Francisco or New York. (Those who want to experiment can find the recipe in the book.)

Tonic source (*Cinchona* bark).

Calhoun is sold, and the pair embark on a day-long adventure chasing down ingredients for this spicy cocktail. At a local store, they browse bottles of liquor and mixers, whose ingredients Stewart describes with almost drunken pleasure. "This is horticulture! In all of these bottles!" She recounts, "Before we left, we stood in the doorway for a minute and looked around us. There wasn't a bottle in the store that we couldn't assign a genus and species to." Her excitement about the biological heritage of the various spirits is almost intoxicating. Stewart then provides a quick taxonomy of bourbon, absinthe, vodka, and beer. Although it's usually hard to get excited about taxonomy, somehow in the context of potions we drink on a regular basis, Stewart breathes some life into the often arcane subject.

This opening scene with its glimpse into the multifaceted botanical world of alcoholic drinks hints at what follows. Unfortunately, the remainder of the book leaves one thirsty for the kind of adventure story Stewart had in Portland. Instead, it generally reads like a mash-up of botanical-history tome; cocktail-recipe book; do-it-yourself agriculture guide; and an abridged encyclopedia of the trees, roots, leaves, fruits, flowers, and seeds that come in contact with, flavor, or are made into your booze of choice.

However, the book more than makes up for its lack of a cohesive story line with its ample supply of anecdotes. These are perfect for sharing at a cocktail party or summer barbecue with scientists, historians, lawyers, cooks, or mixologists—basically with anyone who enjoys a fine drink. For example, you can impress your chemist friends with your knowledge of why scotch tastes better with a splash of water. It turns out that water causes flavor-

[1]Institute for Research in Electronics and Applied Physics, University of Maryland, College Park, MD 20742, USA. E-mail: knordstr@umd.edu

ful fatty acids to separate from the alcohol, freeing them to hit your taste buds more effectively. Or you can engage a lawyer with how trademark law affected marketing of Coca-Cola or Angostura bitters. In the late 19th century, a U.S. judge ruled that "no one could trademark the name of an ingredient or another term that simply describes what the product is." According to the book, that ruling prevented manufacturers from monopolizing the words "coca" or "angostura" in product names. (That tidbit is an especially relevant throwback today in light of the U.S. Supreme Court's recent decision against the patenting of natural genes.)

With tales like these, Stewart manages to bring to life the main characters in the drinks we sip. For those of us who aren't professional beer tasters or wine connoisseurs, the book lends a new appreciation for what it takes to fill the aisles of the neighborhood liquor store and the glassware in the bars and restaurants we frequent. The people crafting these drinks are, in their own way, scientists who experiment with nature, the same way field biologists do. We just happen to reap the fruits of their efforts in a cup rather than an academic journal.

After all, "around the world, it seems, there is not a tree or shrub or delicate wildflower that has not been harvested, brewed, and bottled. Every advance in botanical exploration or horticultural science brought with it a corresponding uptick in the quality of our spirituous liquors." And after reading *The Drunken Botanist*, you'll probably want to try some of these advances—new liquors, liqueurs, mixers, flowers, and herbs you didn't know about before. Stewart has helpfully provided numerous recipes to get you started. Cheers!

– Daniela Hernandez[1]

What the Woodpecker Saw

Arcadian America: The Death and Life of an Environmental Tradition.
Aaron Sachs. Yale University Press, New Haven, CT, 2013. 496 pp. $35, £25. ISBN 9780300176407.

Just when Aaron Sachs is settling into his career, caught up in his new job and his young family, a pileated woodpecker, with a flash of its distinctive red head among the trees, spurs him onto a journey down memory lane. But before digging into his deeply personal story, Sachs slips back in time to 1831 Boston and drifts from the heart to the head to dwell in the safer realm of ideas. In *Arcadian America: The Death and Life of an Environmental Tradition*, he considers modern-day environmental problems such as climate change by looking to an earlier time of unprecedented environmental change.

To find his subjects, Sachs (a historian at Cornell University) uses the same techniques that could help him spot a woodpecker. He pays attention to his peripheral vision to see beyond the obvious and catch the unexpected. His characters tend toward the wallflowers, his settings toward the liminal spaces just beyond the edge of what we might notice when scanning a landscape. So instead of reporting on the usual environmental issues of 19th century United States, such as deforestation and the urban blights of sewage, industrial waste, and disease, his focus is on garden cemeteries.

In response to the pressures of economic development and the associated environmental degradation, some antebellum Americans embraced rural cemeteries to solve two concerns at once. The wilderness parks in the city served as an escape for the living and a home for the dead. Sachs's Arcadians designed cemeteries around the ideals of conservation, community, and a sense of repose: Not only could visitors enjoy the meandering trails, these parks could offer the added comfort of an eternal resting place for themselves and their loved ones. These urban wilderness preserves still provide habitats for a diverse array of plants and animals, including, of course, the woodpecker.

Thomas Chambers's *Mount Auburn Cemetery* (mid-19th century).

As Sachs traces the movements of his characters forward in time through the Civil War, and from east to west, then back east again, he slowly reveals his personal Arcadian tale. We learn that he also traveled from east to west, retreated to the wilderness, and sought rural cemeteries to find comfort in the face of startling loss. When his painful memories retreat to the back of his mind, the woodpecker peeks in from the periphery to remind him of his open questions and the work yet to be done.

He is concerned with advancement at a personal level; he wants to know the right things to say and do when he and his loved ones are confronted with grief. At the level of community, nation, and globe, he is concerned with resolving the current environmental crisis. Sachs notes that through his journey he has become more resilient and muses that perhaps for the future of ecosystems, resilience is a better goal than restoration.

I agree that ecosystem resilience is worth further consideration, so I flipped to the extensive Notes section (84 pages, more than 830 entries) to find Sachs's reference. Disappointingly, I found psychology research about human resilience by Stuart Hauser (a beloved cousin and mentor to Sachs) and others but no reference for the environmental application mentioned in the text.

The Arcadians built wilderness cemeteries as an expression of their integrated concern for human and environmental well-being, and Sachs stays true to their legacy. He achieves a rich and compelling emotional context by weaving the Arcadians' stories together with his own.

In the past, emotionally charged language had a place in scholarly discourse, and perhaps it is now making a comeback. Sachs's accessible and engaging style in *Arcadian America* retains scholarly credibility while drawing people into the discussion through emotional traction. More scholarly work should be written this way, because readers are inevitably guided by emotion as well as intellect. Like the woodpecker, matters of the heart may be illusive, but they ultimately demand attention, like the tap-tap-tapping of the bird's beak against the tree or the flash of color at the edge of the woods.

– Marissa Weiss[2]

[1]*Wired*, 520 Third Street, 3rd Floor, San Francisco, CA 94107, USA. E-mail: dfhernandez@gmail.com

[2]Department of Horticulture, Cornell University, Ithaca, NY 14853, USA. E-mail: msw27@cornell.edu

ENVIRONMENTAL ECONOMICS

Determining Benefits and Costs for Future Generations

The United States and others should consider adopting a different approach to estimating costs and benefits in light of uncertainty.

K. Arrow,[1] M. Cropper,[2,3*] C. Gollier,[4] B. Groom,[5] G. Heal,[6] R. Newell,[3,7,8] W. Nordhaus,[9] R. Pindyck,[10] W. Pizer,[3,11] P. Portney,[3,12] T. Sterner,[3,13] R. S. J. Tol,[14,15] M. Weitzman[16]

In economic project analysis, the rate at which future benefits and costs are discounted relative to current values often determines whether a project passes the benefit-cost test. This is especially true of projects with long time horizons, such as those to reduce greenhouse gas (GHG) emissions. Whether the benefits of climate policies, which can last for centuries, outweigh the costs, many of which are borne today, is especially sensitive to the rate at which future benefits are discounted. This is also true of other policies, e.g., affecting nuclear waste disposal or the construction of long-lived infrastructure.

A declining discount rate (DDR) schedule, as used by the governments of France and the United Kingdom (*1*, *2*), means that all benefits and costs occurring in a given year are discounted at the same rate, but this rate declines over time. In contrast, the United States and other countries use discount rates that are constant over time; a lower constant discount rate is sometimes used to evaluate projects that affect future generations. We summarize the arguments in favor of using a DDR schedule and discuss the problems in using different constant discount rates to evaluate inter- and intragenerational benefits. The use of a DDR schedule would avoid these problems.

What Does the Discount Rate Represent?

There are two rationales for discounting future benefits, one consumption- and the other investment-based. The consumption rate of discount reflects the rate at which society is willing to trade consumption in the future for consumption today. Basically, we place a lower value on the consumption of future generations, because we assume that future generations will be wealthier than we are and that the utility people receive from an extra dollar of consumption declines as their level of consumption increases. To illustrate, if per capita consumption grows at 1.3% per year, in 200 years it will be more than13 times today's value. So a dollar of consumption received 200 years from now will therefore be "worth" less than it is today (*3*).

The investment approach says that, as long as the rate of return to investment is positive, we need to invest less than a dollar today to obtain a dollar of benefits in the future. Under the investment approach, the discount rate is the rate of return on investment. If there were no distortions (e.g., taxes) or inefficiencies in markets, the consumption rate of discount would equal the rate of return on investment. There are, however, many reasons why the two may differ (*4*), which is why the U.S. Office of Management and Budget (OMB) requires projects involving intragenerational benefits and costs to be evaluated twice, once by using a constant discount rate of 3% to approximate the consumption rate of discount and, separately, by using a discount rate of 7%—the real, pretax average return on private investment. For regulations with important intergenerational benefits or costs, OMB advises analysts to consider an additional lower but positive discount rate (*5*).

Using a constant discount rate for intergenerational benefits and costs that is lower than the rate used to evaluate intragenerational benefits and costs can lead to inconsistencies in decision-making. In a recent regulatory impact analysis of Corporate Average Fuel Economy standards for motor vehicles (*6*), benefits associated with reduced GHG emissions were discounted at a lower rate than fuel savings associated with the proposed standards. This resulted in benefits occurring in the same year being discounted at different rates. This is clearly inappropriate (*7*). Consistency in decision-making requires that the same discount rate must be applied to all certain benefits and costs that occur in the same year, irrespective of whether the project has intra- or intergenerational consequences. With a DDR schedule, benefits and costs in a given year are discounted at the same rate, but the rate declines over time.

PRESENT VALUE OF A CASH FLOW OF $1000 RECEIVED AFTER *T* YEARS

t	Value ($) of $1000 at a discount rate of 1%	4%	7%	Equally likely 1% or 7% expected value	Certainty equivalent (%)
1	990.05	960.79	932.39	961.22	3.94
10	904.84	670.32	496.59	700.71	3.13
50	606.53	135.34	30.20	318.36	1.28
100	367.88	18.32	0.91	184.40	1.02
150	223.13	2.48	0.03	111.58	1.01
200	135.34	0.34	0.00	67.67	1.01
300	49.79	0.01	0.00	24.89	1.01
400	18.32	0.00	0.00	9.16	1.01

Present value of a cash flow of $1000 received after *t* years. Expected value is the average of values from the 1% and 7% columns.

Why Might the Discount Rate Decline?

Uncertainty about future discount rates leads to a DDR schedule (*8*). This can be illustrated by a simple example. Suppose we wish to discount $1000 received *t* years from now to the present. The net present value (NPV) of $1000 = $1000*exp(–*rt*), where *r* is the discount rate. If the discount rate is 4%, the NPV of $1000 received in 100 years is $18.32 (see the table).

But future discount rates are inherently uncertain. Suppose that we think the interest rate is equally likely to be 1% or 7% in 100 years. We evaluate the NPV using its expected value (*9*), averaging the

[1]Stanford University, Stanford, CA 94305, USA. [2]University of Maryland, College Park, MD 20742, USA. [3]Resources for the Future, Washington, DC 20036, USA. [4]Toulouse School of Economics, 31000 Toulouse, France. [5]London School of Economics, London WC2A 2AE, UK. [6]Columbia Business School, New York, NY 10027, USA. [7]Nicholas School of the Environment, Duke University, Durham, NC 27708, USA. [8]National Bureau of Economic Research, Cambridge, MA 02138, USA. [9]Cowles Foundation, Yale University, New Haven, CT 06511, USA. [10]Sloan School of Management, Massachusetts Institute of Technology, Newton, MA 02159, USA. [11]Sanford School of Public Policy, Duke University, Durham, NC 27708, USA. [12]University of Arizona, Tucson, AZ 85721, USA. [13]University of Gothenburg, SE-405 30 Gothenburg, Sweden. [14]Univeristy of Sussex, Sussex BN1 9SL, UK. [15]Institute for Environmental Studies and Department of Economics, Vrije Universiteit, 1081 HV Amsterdam, Netherlands. [16]Harvard University, Cambridge, MA 02138, USA.

*Corresponding author: cropper@rff.org

results obtained using the 1% and 7% rates [$184.40 = (367.88 + 0.91)/2]. The fact that the expected NPV of $1000—$184.40—is much larger than the NPV of $18.32 computed using the mean interest rate (mean of 1% and 7% = 4%), follows from the shape of the discounting function. As the table illustrates, uncertainty about the discount rate, combined with constant exponential discounting, will always yield a higher expected NPV than using the mean discount rate with 100% certainty. This effect is magnified as *t* increases.

Despite the uncertainty in discount rates, the relation between the expected NPV in any two adjacent years can be expressed in terms of a certainty-equivalent discount rate (the single rate, which, when applied with 100% certainty, results in the same NPV as when multiple rates are applied with less than 100% certainty). Using equally likely 1% and 7% discount rates, the expected NPV of $1000 received in year 101 is $182.53, and in year 100 is $184.40, which is $182.53 (1.0102). This 1.02% change is the certainty-equivalent discount rate used to discount benefits from year 101 to 100. As the table illustrates, the certainty-equivalent discount rate is less than the mean discount rate and declines over time, as the present values at 1% dominate the expected NPV (*10*).

The decline in the certainty-equivalent discount rate over time follows from the assumption that the discount rate is uncertain. In the more general case, in which future discount rates are uncertain and may vary from one year to the next, the change in certainty-equivalent discount rates over time depends on the joint probability distribution of the yearly discount rates. If the yearly discount rates are independent and identically distributed, then the certainty-equivalent discount rate is constant; low rates in one year, uncorrelated over time, tend to be offset by high rates in another. If there is correlation among the forecasted discount rates, there is a high chance of long periods of persistently low discount rates and an associated high present value of benefits, thus certainty-equivalent discount rates will decline over time (*11*, *12*).

Estimation and Impacts of a DDR

Future discount rates are inherently uncertain because of uncertainty in the rates of growth in consumption and return to investment. They must be predicted using a combination of empirical models and judgment. Whether future predicted discount rates are correlated is an empirical issue. Various models of per capita consumption growth for the United States (*13*, *14*) suggest that the rate of growth in consumption is stochastic and that deviations from long-term trends are positively correlated.

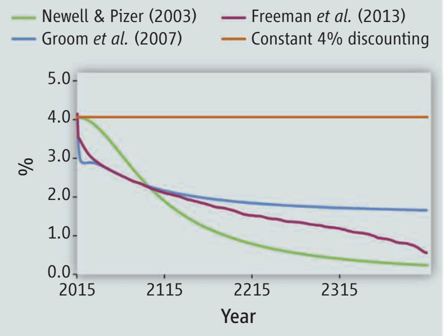

Estimated declining discount rate schedules. From (*11*, *16*, *17*).

Other literature has estimated certainty-equivalent discount rates based on historical time series of interest rates (*15*). Models estimated from two centuries of data on long-term, high-quality government bonds (primarily U.S. Treasury bonds) suggest correlation in uncertainty about bond yields (*11*, *16*, *17*), which implies that the certainty-equivalent discount rate declines over time. DDR schedules estimated by fitting different statistical models to these data are shown in the figure.

Does the use of a DDR make a difference? The DDR schedules shown in the figure make a considerable difference to estimates of the social cost of carbon (SCC) (i.e., the present value of damages from emitting a ton of carbon dioxide), compared with using a constant exponential discount rate. In these studies, estimates of the social cost of carbon are increased by as much as two- to threefold by using a DDR, compared with using a constant discount rate of 4%, the historic mean return on U.S. Treasury bonds. For example, if we hold the path of damages constant, the SCC in 2000 increases from $10.70 per ton of CO_2 (in 2013 U.S. dollars), using a constant discount rate of 4%, to $19.50 using the DDR in (*11*), $26.10 using (*17*), and $27.00 using the DDR in (*16*).

There are compelling arguments for using a DDR schedule. For simplicity, we have focused on uncertainty in the discount rate, but a DDR can also be obtained using an approach that looks at underlying uncertainty in consumption (*12*, *18*, *19*). Implicit in using a model based on future discount rate uncertainty is the need to update the DDR as future information is observed.

An important practical question is how a DDR schedule should be determined if it is to be used for project analysis. As the figure illustrates, estimates of the DDR vary considerably depending on the underlying statistical model. As with choosing a constant exponential discount rate, empirical estimates of a DDR using an investment- or a consumption-based approach will require human judgment about the appropriate models to use to capture uncertainty about future discount rates.

References and Notes

1. D. Lebègue *et al.*, *Le prix du temps et la décision publique* (La documentation Française, Paris, 2005).
2. HM Treasury, *Green Book: Appraisal and Evaluation in Central Government* (Stationery Office, London, 2003); https://www.gov.uk/government/publications/the-green-book-appraisal-and-evaluation-in-central-governent.
3. Formally, the consumption discount rate is given by the Ramsey formula. See (*18*) for details.
4. R. Kocherlakota, *J. Econ. Lit.* **34**, 42 (1996).
5. U. S. Office of Management and Budget, *Circular A-4: Regulatory Analysis* (OMB, Washington, DC, 2003); www.whitehouse.gov/omb/circulars_default/.
6. EPA, Final Rulemaking to Establish Light-Duty Vehicle Greenhouse Gas Emission Standards and Corporate Average Fuel Economy Standards: Regulatory Impact Analysis (EPA420-R-10-009, EPA, Washington, DC, 2010).
7. Benefits and costs were treated as certain in this analysis. Uncertainty in benefits or costs is usually handled via sensitivity analysis and, sometimes, by assuming a probability distribution over benefits or costs.
8. In addition to the effect of uncertainty in the discount rate, there are reasons why the discount rate might decline over time even in the absence of uncertainty. For example, the discount rate may decline because of declining productivity and population growth (*20*).
9. M. L. Weitzman, *Am. Econ. Rev.* **91**, 260 (2001).
10. M. L. Weitzman, *J. Environ. Econ. Manage.* **36**, 201 (1998).
11. R. Newell, W. Pizer, *J. Environ. Econ. Manage.* **46**, 52 (2003).
12. C. Gollier, *Pricing the Planet's Future: The Economics of Discounting in an Uncertain World* (Princeton Univ. Press, Princeton, NJ, 2012).
13. J. H. Cochrane, *J. Polit. Econ.* **96**, 893 (1988).
14. S. G. Cecchetti, P. Lam, N. C. Mark, *Am. Econ. Rev.* **90**, 787 (2000).
15. This literature includes models of interest rate determination for the United States (*11*, *16*, *17*); Australia, Canada, Germany, and the UK (*19*, *21*); and France, India, Japan, and South Africa (*21*).
16. B. Groom *et al.*, *J. Appl. Econ.* **22**, 641 (2007).
17. M. Freeman, B. Groom, K. Panopoulou, T. Pantelidis, "Declining discount rates and the Fisher effect: Inflated past, discounted future" (Centre for Climate Change Economics and Policy Working Paper No. 129, Grantham Research Institute on Climate Change and the Environment, Working paper no. 109, London School of Economics, London, 2013).
18. K. J. Arrow *et al.*, "How should benefits and costs be discounted in an intergenerational context? The views of an expert panel" (Discussion paper 12-53, Resources for the Future, Washington, DC, 2012).
19. C. Gollier *et al.*, *Econ. Policy* **23**, 757 (2008).
20. W. D. Nordhaus, *Proc. Natl. Acad. Sci. U.S.A.* **107**, 11721 (2010).
21. C. Hepburn, P. Koundouri, E. Panopoulou, T. Pantelidis, *J. Environ. Econ. Manage.* **57**, 140 (2009).

Acknowledgments: T.S. is supported by Sweden's FORMAS COMMONS program.

10.1126/science.1235665

MEDICINE

Why Does Gastric Bypass Surgery Work?

Surgical rearrangement of the gut stimulates a growth response that reprograms glucose metabolism and reverses diabetes.

Hans-Rudolf Berthoud

Bariatric surgery to alter the digestive tract is currently the only effective treatment option with sustained beneficial effects on body weight and comorbidities such as type-2 diabetes (*1*, *2*). Identifying the mechanisms that underlie these remarkable outcomes could help guide the development of "knifeless" approaches that may one day replace quite invasive surgeries (which often result in serious complications). Changes in circulating gut hormones induced by bariatric interventions could affect signaling to the brain and other organs, changing energy intake and expenditure, as well as glucose production and disposal (*3*, *4*). On page 406 of this issue, Saeidi *et al*. (*5*) propose another possibility—that the rearranged gut itself improves glucose homeostasis. This may explain why gastric bypass surgery patients can stop taking diabetes medications before substantial weight loss has occurred. This radically new view of bariatric surgery is therefore not based on how the changed gut "talks" to the rest of the body by humoral and neural signaling, but rather on metabolic consequences of the surgery within the gut itself.

Saeidi *et al*. examined a rodent model of a type of gastric bypass surgery called Roux-en-Y (see the figure), in which food passes directly from a small stomach pouch into the jejunum, a distal part of the small intestine. To handle this uncontrolled influx of undigested food, the gut wall adapts by increasing its size and mass (*6*, *7*). Because building new tissue requires energy, the rearranged gut takes up more glucose, as Saeidi *et al*. observed by in vivo imaging. Metabolomic, proteomic, and gene-expression analyses further revealed that glucose preferably enters the pentose phosphate and other glycolytic pathways that provide substrates for nucleotide and protein synthesis, consistent with accelerated tissue growth. Most important, and as an "unintended" by-product of increased glucose uptake by the expanding gut tissue, systemic glucose concentrations are reduced and the diabetic state is reversed.

To determine whether undigested food is the primary trigger for the glucose-gobbling hypertrophic response, Saeidi *et al*.

Neurobiology of Nutrition Laboratory, Pennington Biomedical Research Center, Louisiana State University System, Baton Rouge, LA 70808, USA. E-mail: berthohr@pbrc.edu

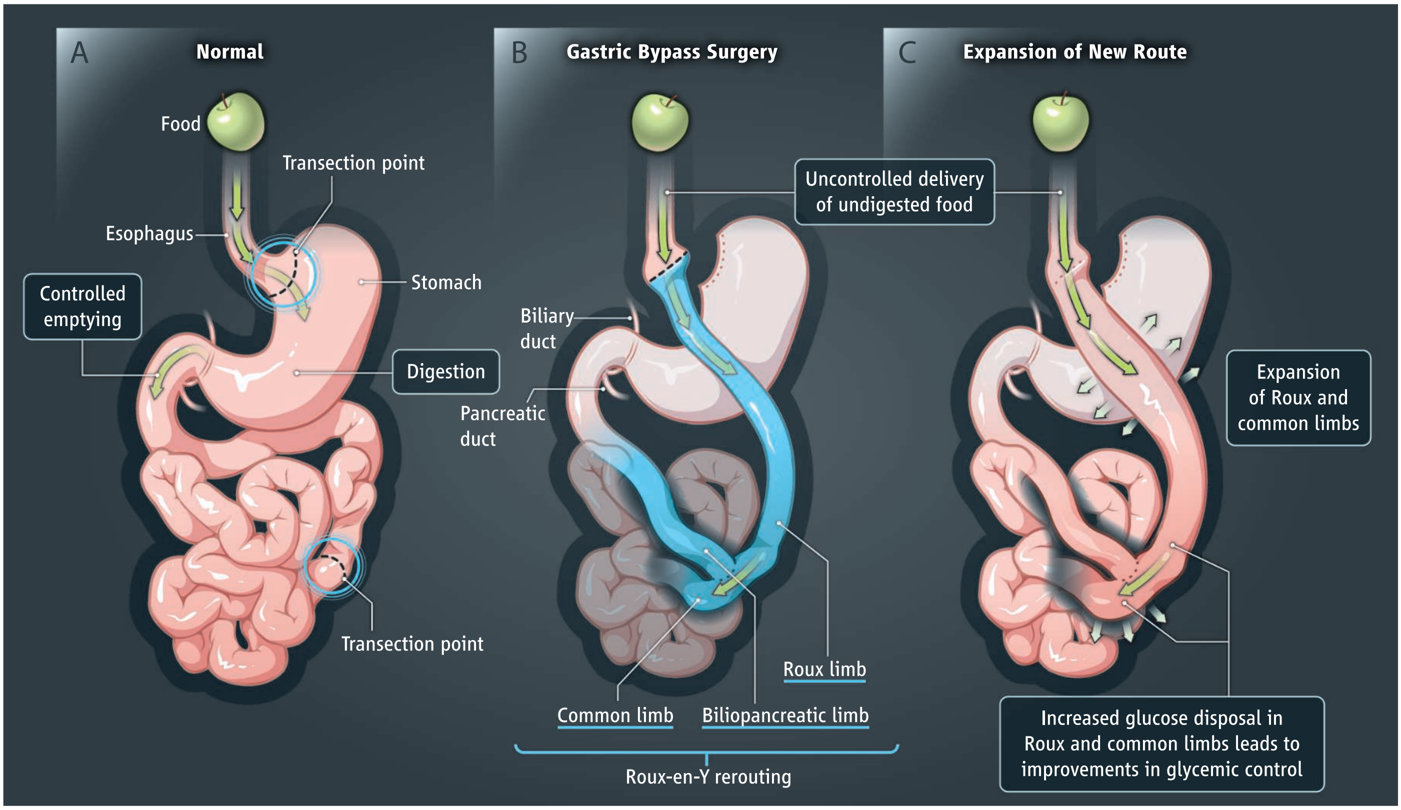

CREDIT: Y. HAMMOND/SCIENCE

Metabolic consequences. (**A**) In the normal human gut, predigested food in the stomach is delivered to the upper small intestine (duodenum) in a controlled manner for digestion and absorption. The normal gut uses up to 15% of total body energy requirements. (**B**) In Roux-en-Y gastric bypass surgery, undigested food has unhindered access to a different part of the small intestine (the newly created Roux limb). Bile acids and pancreatic enzymes reach the undigested food through the biliopancreatic limb to form the common limb of the Y-shaped arrangement (highlighted in blue). (**C**) To adapt to the new digestive route, the Roux and common limbs grow in diameter and absorptive capacity, thereby increasing their energetic needs (glucose). This increase in gut glucose disposal improves whole-body glucose homeostasis and contributes to the antidiabetic effects of gastric bypass surgery.

transposed a piece of jejunum between the esophagus and the stomach in the rat, and found the same hypertrophic response and similar improvements in glycemic control. Altogether, Saeidi *et al*. clearly demonstrate that entry of undigested food into the small intestine triggers reprogramming of glucose metabolism to allow for tissue growth, and that the resulting increase in intestinal glucose disposal improves glycemia. Although a direct causal role was not established for improved glucose homeostasis by either preventing the hypertrophic response or reprogramming glucose metabolism, the combined findings strongly suggest such a role, at least for this rat model.

One factor that has been shown to stimulate gut hypertrophy is glucagon-like peptide 2 (GLP-2) (*8*), but what is it in the undigested food that triggers hypersecretion of GLP-2 and the metabolic reprogramming response? Is it related to the absence of bile acids and pancreatic digestive enzymes in the Roux limb that are particularly important for the absorption of fat? This idea is supported by findings in both rodents and humans that after gastric bypass surgery, there is a decreased preference for fat, likely the result of difficulties with fat absorption (*9*, *10*). Another question concerns the time course of enhanced intestinal glucose use. Doubling or even quadrupling of the intestinal mass does not happen overnight. Saeidi *et al*. report that maximal expansion was reached at 1 month. It will be important to monitor gut tissue growth earlier, as hypersecretion of incretins (hormones that augment insulin secretion) and improvements of glycemic control occur as early as 10 days after surgery in humans (*11*). Assessment of a full time course of the adaptive response and its consequences for glucose use, all while controlling for weight loss, will be revealing.

Are the similar beneficial effects of different types of bariatric surgeries on glycemic control mediated by the same mechanism (*12*)? For much less intrusive surgical interventions, such as sleeve gastrectomy, gastric emptying mechanisms and normal digestion are preserved to some extent, so there might be less of an adaptive hypertrophic response. To date, gut hypertrophy has not been examined after this much simpler surgery. There also is the question of whether the mechanism proposed by Saeidi *et al*. in the rat is applicable to bariatric surgeries in humans. When control subjects were given the same low amounts of food eaten by surgical patients, the same rapid improvements in glycemic control were observed (*13*, *14*), suggesting that acute calorie restriction rather than gut hypertrophy is important for diabetes remission, at least during the early postsurgical period, before substantial weight loss has occurred.

Will the mechanism identified by Saeidi *et al*. eventually lead to "knifeless" metabolic interventions—"bypassing the bypass," as the authors put it? The answer hinges on the possibility to enhance glucose disposal in the gut (or in any other organ) by pharmacological and/or nutritional approaches. In the meantime, there's the old-fashioned approach—exercise.

References

1. H. Ling *et al*., *Pharmacotherapy* 10.1002/phar.1277 (2013).
2. K. A. Holes-Lewis *et al*., *Am. J. Med. Sci.* **345**, 284 (2013).
3. D. E. Cummings, J. Overduin, K. E. Foster-Schubert, *J. Clin. Endocrinol. Metab.* **89**, 2608 (2004).
4. C. W. le Roux *et al*., *Ann. Surg.* **243**, 108 (2006).
5. N. Saeidi *et al*., *Science* **341**, 406 (2013).
6. M. B. Mumphrey, L. M. Patterson, H. Zheng, H. R. Berthoud, *Neurogastroenterol. Motil.* **25**, e70 (2013).
7. C. F. Hansen *et al*., *PLoS ONE* **8**, e65696 (2013).
8. D. L. Sigalet *et al*., *Dig. Dis. Sci.* **51**, 1557 (2006).
9. H. Zheng *et al*., *Am. J. Physiol. Regul. Integr. Comp. Physiol.* **297**, R1273 (2009).
10. C. W. le Roux *et al*., *Am. J. Physiol. Regul. Integr. Comp. Physiol.* **301**, R1057 (2011).
11. R. Peterli *et al*., *Obes. Surg.* **22**, 740 (2012).
12. M. A. Stefater *et al*., *Endocr. Rev.* **33**, 595 (2012).
13. I. Lingvay *et al*., *Diabetes Care* 10.2337/dc12-2316 (2013).
14. M. A. Lips *et al*., *Clin. Endocrinol.* 10.1111/cen.12254 (2013).

10.1126/science.1242673

OCEANS

How Nitrogen Is Lost

The supply and composition of organic matter control the processes by which fixed nitrogen is lost from the ocean.

Bess B. Ward

As in the back garden, productivity in the ocean is often limited by the availability of nutrients, principally nitrogen (N) and phosphorus (P). On a global scale, the rates of nitrogen fixation (input) and nitrogen loss (output) are believed to be roughly equal. Both rates are, however, very uncertain. Nitrogen loss processes occur in subsurface water and sediments and depend on the supply of organic matter, derived from primary production in surface waters. Reports in the last few years have changed our understanding of the controls and pathways responsible for nitrogen loss.

Two main processes are responsible for nitrogen loss: denitrification and anaerobic ammonium oxidation (anammox). These processes rely on fundamentally different organisms and metabolic pathways. Denitrification is the sequential reduction of nitrate (NO_3) to dinitrogen gas (N_2) via oxidized intermediates, whereas anammox combines ammonium (NH_4) and nitrite (NO_2) to yield N_2. Most denitrifying organisms obtain their carbon (C) for growth from organic matter produced by phytoplankton, whereas anammox bacteria fix their own CO_2 into biomass. Most denitrifiers consume and degrade organic matter, releasing dissolved inorganic nitrogen (including NH_4 and NO_2). Anammox bacteria require a source of NH_4 and NO_2, derived from the breakdown of organic matter by other microbes (see the figure).

Anammox is a slow process mediated by bacteria with minimum generation times of nearly 2 weeks. Most marine bacteria and their grazers have generation times of a few hours to a few days at most, and it was therefore surprising when only anammox was reported in marine environments, including open-ocean regions containing very low oxygen concentrations [oxygen minimum zones (OMZs)] (*1*). In these regions, denitrification had been assumed to be the sole process responsible for nitrogen loss.

The source of NH_4 and NO_2 to support anammox in the absence of denitrification was a mystery. Organic matter in the ocean has a well-established average composition based on the primary producers from which it derives. Complete decomposition and mineralization of this material to form CO_2 and N_2 gases can occur by denitrification and anammox in the ratio of 71:29. Any other ratio requires the supply of nitrogen or carbon from an additional source (*2*). Reports of 100% anammox (*3*) suggested major inconsistencies either in the experiments or in our understanding of carbon and nitrogen cycling in the ocean.

Department of Geosciences, Princeton University, Princeton, NJ 08544, USA. E-mail: bbw@princeton.edu

Published by AAAS

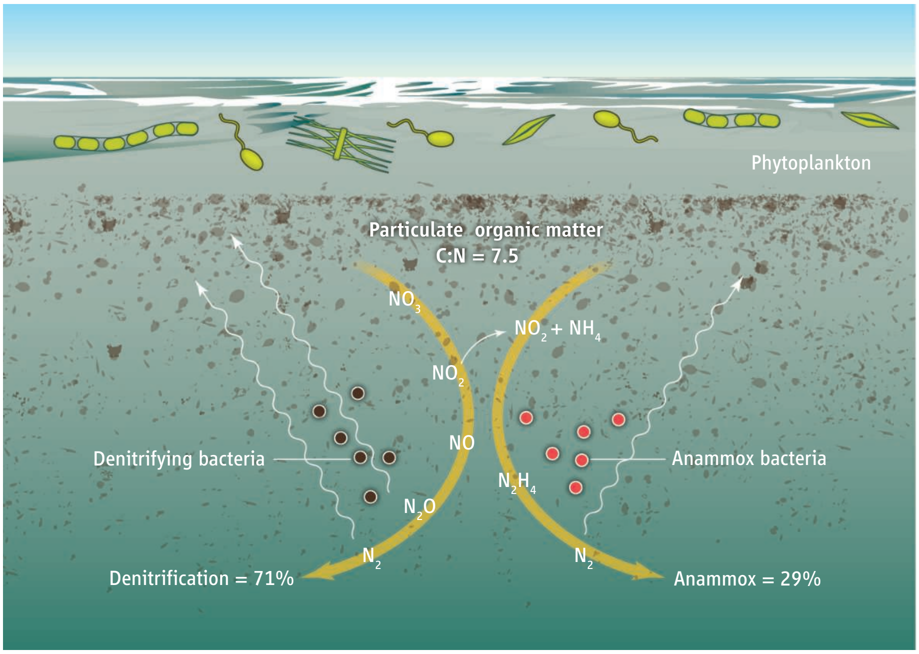

Drivers of nitrogen loss. The two bacterial processes leading to nitrogen loss in oxygen minimum zones of the ocean depend on the supply of organic matter from the surface layer. Recent studies explain how the rates and proportions of denitrification and anammox are controlled in ocean waters and sediments.

Subsequent investigations of denitrification and anammox in the major OMZs of the world ocean reported either anammox (*1*, *4*) or denitrification (*5*, *6*), but rarely both. Two hypotheses were suggested to explain the apparent lack of denitrification in some locations. Lam *et al*. (*7*) suggested three alternative sources for ammonium (nitrite concentrations are normally sufficient in OMZ waters): microaerobic respiration, that is, organic matter degradation at the expense of oxygen; transport of ammonium from sediments or by lateral advection from other water masses; and dissimilatory nitrate reduction to ammonium ($NO_3 \rightarrow NH_4$). However, there is no oxygen in OMZ waters most of the time (*8*), such that even intermittent oxygen supply cannot support the necessary degradation rates for microaerobic respiration. Transport of ammonium from sediments and dissimilatory nitrate reduction may both contribute to the ammonium supply, but not at rates sufficient to support the observed consumption by anammox (*9*).

According to the second hypothesis, denitrification occurs in OMZs, but its distribution is patchy in space and time as a result of an episodic supply of organic matter (*1*, *10*). It was suspected that the limited scope of the small number of expeditions to date provided only tiny snapshots of the OMZs, thus having missed major episodes of denitrification. In this scenario, denitrification is patchy and dynamic in range, whereas anammox is slow, steady, and consistent, but ultimately dependent upon denitrification for the supply of dissolved inorganic nitrogen (DIN).

Recent findings appear to resolve the controversy in favor of the second hypothesis. In a transect along the coast of South America (the eastern tropical South Pacific OMZ), Dalsgaard *et al*. (*11*) detected both anammox and denitrification. Anammox occurred at almost every station at low rates, whereas denitrification was less commonly detected but occurred at very high rates at a few stations. When averaged over their data set, the ratio of nitrogen loss as N_2 from denitrification and anammox was 72:28, close to the expected ratio and far from the dominance by anammox previously reported from the same region on the basis of a few measurements (*1,4*).

Independently, work in my lab found that the overall loss rate depends on the amount of organic matter added and that the ratio of denitrification:anammox depends on the carbon to nitrogen ratio (C:N) of the available substrate. In both sediments (*12*) and OMZ waters (*13*), natural organic material with a C:N ratio very close to the ocean average (~7.5) resulted in a denitrification:anammox ratio of 70:30—almost exactly the predicted ratio. Incubations augmented with amino acids or sucrose plus ammonium had higher and lower anammox proportions, respectively, in line with the C:N ratios of these substrates.

In the OMZ, where DIN can only come from the degradation of organic matter in the water column (see the figure), the total rate of nitrogen loss and the relative contributions of denitrification and anammox must be constrained by the supply of organic matter. The extensive field measurements by Dalsgaard *et al*. (*11*) show that denitrification and anammox are differently distributed in time and space. Our experiments (*12*, *13*) provide an explanation for those differences in terms of the composition of the episodic organic matter supply. Thus, no major revision of the nitrogen cycle, nor transport of DIN independently of organic matter supply, is required to explain nitrogen loss in OMZs.

Although these recent reports appear to resolve a major controversy, further complications may be hidden under the cover of denitrification. Most denitrifiers consume organic matter, but some obtain the energy for CO_2 fixation from the oxidation of reduced sulfur compounds. Usually, these organisms are considered to be important only in sediments, but recent evidence of sulfide oxidation (*14*) and of active expression of autotrophic sulfur oxidation genes (*15*) suggest that a cryptic sulfur cycle is linked to denitrification in the OMZs. Organic matter thus may not be the only control on denitrification rates in these regions.

Denitrification and anammox together, occurring in the OMZs and ocean sediments, effectively consume the organic material sinking out of the surface waters and account for all the oceanic nitrogen loss. The dependence of nitrogen loss rates on organic matter supply implies a tightly coupled oceanic nitrogen cycle, which controls the fertility of surface waters.

References and Notes

1. B. Thamdrup *et al*., *Limnol. Oceanogr.* **51**, 2145 (2006).
2. W. Koeve, P. Kähler, *Biogeosci.* **7**, 2327 (2010).
3. M. M. Kuypers *et al*., *Proc. Natl. Acad. Sci. U.S.A.* **102**, 6478 (2005).
4. M. R. Hamersley *et al*., *Limnol. Oceanogr.* **52**, 923 (2007).
5. J. C. Nicholls *et al*., *Limnol. Oceanogr.* **52**, 156 (2007).
6. B. B. Ward *et al*., *Nature* **461**, 78 (2009).
7. P. Lam *et al*., *Proc. Natl. Acad. Sci. U.S.A.* **106**, 4752 (2009).
8. B. Thamdrup, T. Dalsgaard, N. P. Revsbech, *Deep Sea Res. Part I Oceanogr. Res. Pap.* **65**, 36 (2012).
9. T. Kalvelage *et al*., *Nat. Geosci.* **6**, 228 (2013).
10. B. B. Ward *et al*., *Deep Sea Res. Part I Oceanogr. Res. Pap.* **55**, 1672 (2008).
11. T. Dalsgaard *et al*., *Limnol. Oceanogr.* **57**, 1331 (2012).
12. A. R. Babbin, B. B. Ward, *Environ. Sci. Technol.* **47**, 4189 (2013).
13. A. R. Babbin *et al*., American Society for Limnology and Oceanography Aquatic Sciences Meeting, New Orleans, LA, 17 to 22 February 2013, abstract SS33-26.
14. D. E. Canfield *et al*., *Science* **330**, 1375 (2010).
15. F. J. Stewart *et al*., *Environ. Microbiol.* **14**, 23 (2012).

Acknowledgments: B. Chang, A. Babbin, and A. Jayakumar reviewed an early version of the manuscript.

10.1126/science.1240314

Published by AAAS

CHEMISTRY

Proton Conduction with Metal-Organic Frameworks

Further development of microporous crystalline materials as proton conductors may lead to better electrolyte membranes for fuel cells.

George K. H. Shimizu, Jared M. Taylor, SiRim Kim

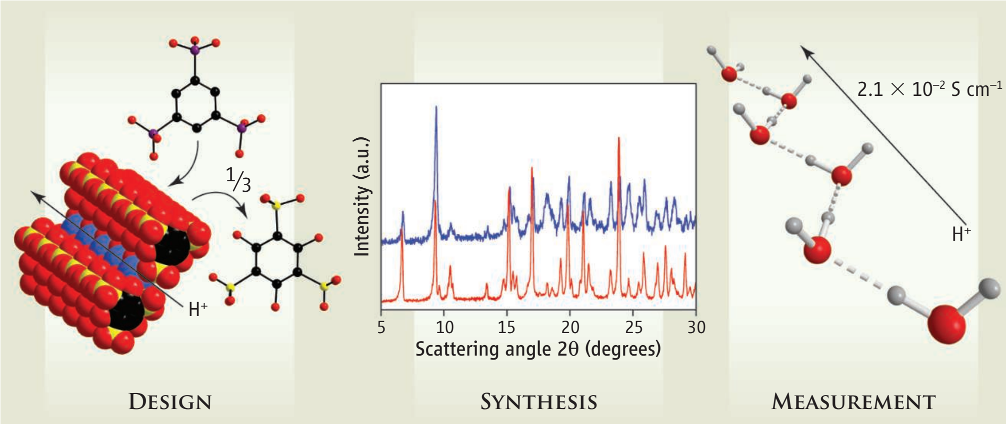

Improving proton conductors. The molecular structure of PCMOF2½, which can conduct protons along a molecular chain. Improvements in measured proton conductivity can be enabled through execution (as depicted by the x-ray diffraction peaks that provide structural information) to design new frameworks for further evaluation.

Proton-exchange membrane fuel cells (PEMFCs) generate electricity because the electrons generated by the reaction of hydrogen and oxygen must travel through an external circuit; the membrane electrolyte only transfers protons. The membrane materials of choice have been ionomeric polymers, such as sulfonated fluoropolymers (Nafion), that achieve proton conductivities of up to 1 S cm^{-1}, but the requirement to keep these materials hydrated limits their operating temperature and efficiency. Metal-organic frameworks (MOFs), in which inorganic assemblies are joined by organic linkers, have inherent porosity that could be exploited for the development of proton-conducting membranes. Among recent studies of experimental proton-conducting MOFs [e.g., (*1*)], two general targets for PEMFC operation have emerged: developing better materials for operations under humid conditions (below 100°C), and developing efficient anhydrous proton conductors that could unlock the cost efficiencies enabled by humidity-independent operation above 100°C.

Efficient ion conduction requires the facile movement of charge through a material. Proton conduction can be envisaged as best occurring through a pathway of sites of equal proton affinity separated by an energy barrier that is as small as possible. Beyond protonation and deprotonation, this arrangement of donor and acceptor sites must open transport pathways, so any design must also encompass supramolecular considerations.

The improvement of materials is facilitated when changes in properties can be directly related to changes in structure. Unlike polymers, MOFs are crystalline, and x-ray techniques provide atomic-level structures. Progress requires an iterative cycle of design, synthesis and characterization, and functional assessment (see the figure). The crystallinity of MOFs, coupled with the many options for structural modification, enables molecular-level design and hence structural optimization. Porosity, which in itself can facilitate unwanted fuel crossover in a PEMFC, can be used to advantage by filling pores with water or a nonvolatile proton carrier.

The field of proton-conducting MOFs has its roots in layered metal phosphonates (*2*). These materials can show exceptional proton conductivities (>10^{-2} S cm^{-1}) but also are prone to swelling in humid atmospheres, which may cause unwanted mechanical stress during PEMFC operation. Kitagawa and co-workers expanded the proton-conducting realm to traditional coordination polymers more broadly [see (*3*) and references therein], especially for the temperature regime from 20° to 75°C. In 2009, Hurd *et al.* (*4*) and Kitagawa and co-workers (*5*) incorporated amphiprotic heterocycles into MOFs as proton carriers to obtain conductivities in the 10^{-4} S cm^{-1} range at temperatures above 100°C.

The ability to "decorate" parent MOF structures allows for incorporation of acidic groups with spatial predictability, such as a sulfonated MIL-53 analog (*6*). Several MOF structures have now been reported that conduct at 10^{-3} S cm^{-1} or higher by incorporating phosphonate groups (*7*), or secondary ions such as polycarboxylates (*8*) or ammonium (*9*), as proton transfer sites. The highest degrees of proton conductivity in MOFs were both reported in the past year and are both greater than 10^{-2} S cm^{-1} for PCMOF2½ (*10*), a mixed sulfonate-phosphonate MOF that exploits isomorphous replacement, and for MIL-101 loaded with a mixture of H_2SO_4 and H_3PO_4 (*11*).

The latter example also shows the potential stability of MOFs, which need to be robust to address challenges of practical proton conductors. Taylor *et al.* reported a MOF that retained proton conductivity greater than 10^{-3} S cm^{-1} after immersion in boiling water for 1 week (*12*). With the ever-increasing number of robust MOF scaffoldings available for derivatization, finding materials that are stable in the presence of water and over the required temperature range for fuel cell operation should not be an insurmountable hurdle.

From a broader perspective, even a MOF that is not highly robust can, because of its crystallinity, help establish structure-activity relations—for example, by direct visualization of a proton transfer pathway because of confinement of carriers in pores (*13*) or as a calibration tool for modeling studies. Horike *et al.* recently reported an anhydrous MOF with a crystallographically located proton transfer pathway of turnstile-like hydrogen phosphate and imidazolium ions (*14*). The authors refer to the solid as a "plastic crystal" because of the ability of components to

Department of Chemistry, University of Calgary, Calgary, Alberta T2N 1N4, Canada. E-mail: gshimizu@ucalgary.ca; jjaredddd@gmail.com; srkim@ucalgary.ca

reorient in the solid state. This study touches on perhaps the most intriguing prospect for MOFs regarding ion conduction: that they can exhibit dynamic behavior in the solid state (*15*) with reversibility and often with retention of crystallinity.

Although advances in absolute conductivity and robustness have been made, there are still substantive challenges for MOF proton conductors. With respect to the MOF itself, even better conductors can be envisaged that balance robustness and dynamics in a framework with three-dimensional proton transfer pathways. For incorporation in an engineered membrane electrode assembly (MEA), the brittleness of MOF materials will need to be addressed. A mixed-matrix polymer would stabilize the MOF mechanically while offering conduction pathways through the polymer, the MOF, and the interfaces, depending on the extent of loading. Wu *et al*. (*16*) and Liang *et al*. (*17*) have recently reported promising results in this direction. Compatibility with the electrode components is an issue for any electrolyte; optimizing the interfaces in MEAs is itself a large domain of research. Given that MOFs are being studied for a broad expanse of electrochemical applications beyond electrolytes (*18*, *19*), if one were to conjure a boldly optimistic scenario, MOFs could be used for all parts of a fuel cell (electrolytes, electrodes and catalyst supports, and gas-diffusion layers) where variations on a framework could yield different components with appropriate choice of metals, linkers, and guest catalyst loadings.

References

1. M. Yoon, K. Suh, S. Natarajan, K. Kim, *Angew. Chem. Int. Ed.* **52**, 2688 (2013).
2. G. Alberti *et al*., *Solid State Ionics.* **58**, 339 (1992).
3. T. Yamada, M. Sadakiyo, H. Kitagawa, *J. Am. Chem. Soc.* **131**, 3144 (2009).
4. J. A. Hurd *et al*., *Nat. Chem.* **1**, 705 (2009).
5. S. Bureekaew *et al*., *Nat. Mater.* **8**, 831 (2009).
6. M. G. Goesten *et al*., *J. Catal.* **281**, 177 (2011).
7. R. M. P. Colodrero *et al*., *Dalton Trans.* **41**, 4045 (2012).
8. M. Sadakiyo *et al*., *J. Am. Chem. Soc.* **131**, 9906 (2009).
9. E. Pardo *et al*., *J. Am. Chem. Soc.* **133**, 15328 (2011).
10. S. Kim, K. W. Dawson, B. S. Gelfand, J. M. Taylor, G. K. H. Shimizu, *J. Am. Chem. Soc.* **135**, 963 (2013).
11. V. G. Ponomareva *et al*., *J. Am. Chem. Soc.* **134**, 15640 (2012).
12. J. M. Taylor, K. W. Dawson, G. K. H. Shimizu, *J. Am. Chem. Soc.* **135**, 1193 (2013).
13. S. C. Sahoo *et al*., *J. Am. Chem. Soc.* **133**, 17950 (2011).
14. S. Horike *et al*., *J. Am. Chem. Soc.* **134**, 7612 (2012).
15. S. Horike, S. Shimomura, S. Kitagawa, *Nat. Chem.* **1**, 695 (2009).
16. B. Wu *et al*., *Chem. Commun.* **49**, 143 (2013).
17. X. Liang *et al*., *Chem. Sci.* **4**, 983 (2013).
18. A. Morozan, F. Jaouen, *Energy Environ. Sci.* **5**, 9269 (2012).
19. S.-I. Li, Q. Xu, *Energy Environ. Sci.* **6**, 1656 (2013).

10.1126/science.1239872

CELL BIOLOGY

Where Is PTEN?

A tumor suppressor protein may function in multiple locations inside and outside the originating cell.

Nicholas R. Leslie[1] and Valerie G. Brunton[2]

There are plenty of examples in biology of finding things in unexpected places, such as bacteria thriving in the stomach or deep in Earth's crust, or proteins that have acquired "moonlighting" functions when in new cellular locations. On pages 399 and 395 of this issue, two reports describe newly identified aspects of the functions of phosphatase and tensin homolog (PTEN), a tumor suppressor protein. Both studies focus on where these functions are fulfilled. Hopkins *et al*. (*1*) describe a secreted form of PTEN that can be transferred between cells, potentially for intercellular tumor suppression. Bassi *et al*. (*2*) present a new mechanism of PTEN regulation in response to DNA damage that controls PTEN localization in the nucleus. Both discoveries have implications for cancer therapy.

PTEN is normally found in the cytosol and sometimes the nucleus. It transiently associates with the inner surface of the plasma membrane where it removes a phosphate group from phosphatidylinositol 3,4,5-trisphosphate (PIP_3) (see the figure) (*3*). Through this lipid phosphatase activity, PTEN suppresses the phosphoinositide 3-kinase (PI3K)–Akt signaling network, which promotes cell growth and proliferation. This has seemed to be the main reason why loss of PTEN function is a common characteristic of human cancers.

The human genome contains only one *PTEN* gene, without related genes sharing its function. Until now, it appeared that *PTEN* encoded only one protein of 403 amino acids. However, Hopkins *et al*. have identified a variant called PTEN-Long that arises from an alternative translational start sequence upstream of the recognized initiation sequence. An antibody that recognizes the protein segment unique to PTEN-Long, combined with mass spectrometry, confirmed its presence in extracts from human breast tissue, mouse embryonic stem cells, and cell lines from multiple lineages. Bioinformatic analyses showed that the amino-terminal extension is well conserved among mammals. Within this extension, a polyalanine sequence resembles a secretion signal, and a string of arginine residues resembles the cell-penetrating domain of the transactivator of transcription (TAT) protein of the human immunodeficiency virus. Release of PTEN-Long from cultured cells depended on the polyalanine sequence and the authors suggested transport through the cell's secretory pathway. A purified fusion protein consisting of red fluorescent protein and PTEN-Long could enter cultured cells when added exogenously; this required the polyarginine stretch. Once inside target cells, PTEN-Long seemed to be functional, as its exogenous application inhibited PI3K-Akt signaling and induced cell death in brain and breast tumor cell lines lacking endogenous PTEN.

Remarkably, secretion of PTEN-Long is not the only mechanism that may allow PTEN to move between cells. Such transfer can also be mediated by membrane vesicles called exosomes (*4*) (each study seemed to distinguish signal peptide–mediated secretion from exosome-mediated release). The potential intercellular transfer of PTEN function is intriguing, particularly with respect to cancer. Could cells with mutated or silenced PTEN, either in a well-developed tumor or normal cells taking their first steps toward cancer, acquire functional PTEN from their neighbors? Indeed, very modest changes in PTEN expression can influence tumor formation (*5*).

Hopkins *et al*. observed less expression of PTEN-Long in each of four breast tumors relative to matched normal breast tissue. However, PTEN-Long was detected in the surrounding stromal tissue of some human breast tumors as well as in a mouse model

[1]Institute of Biological Chemistry, Biophysics and Bioengineering, School of Engineering and Physical Sciences, Heriot Watt University, Edinburgh EH14 4AS, UK. [2]Edinburgh Cancer Research UK Centre, Institute of Genetics and Molecular Medicine, University of Edinburgh, Crewe Road South, Edinburgh EH4 2XR, UK. E-mail: n.r.leslie@hw.ac.uk

Published by AAAS

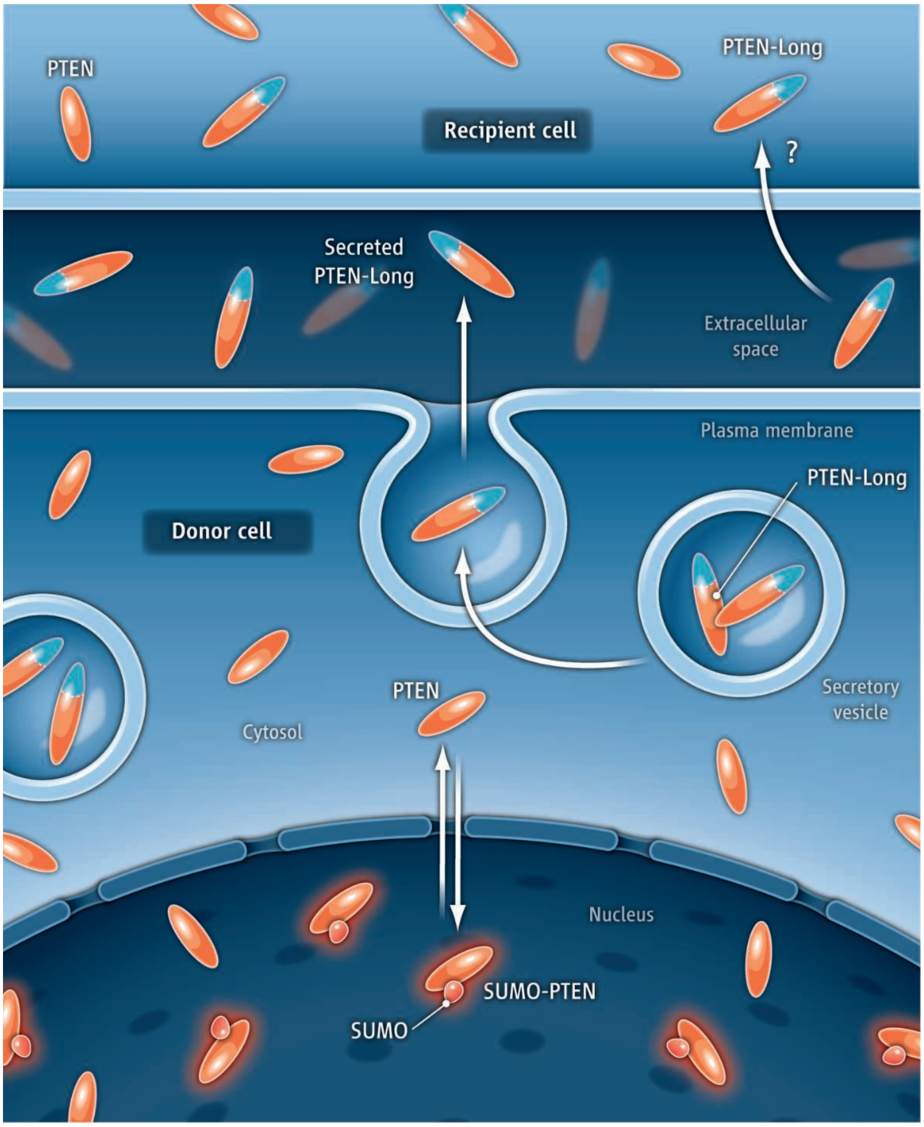

PTEN spreads out. A model shows the secretion of PTEN-Long and the nuclear shuttling of SUMOylated PTEN. It is uncertain how DNA damage influences PTEN SUMOylation and localization or whether endogenous PTEN-Long is found in the cytosol.

of glioma, in which the tumor cells lacked *Pten*. It is well established that intercellular communication between stromal cells in the tumor microenvironment and the tumor cells themselves plays a pivotal role in defining the malignant phenotype (*6*, *7*), including response to therapy (*8*). It will be important to establish whether PTEN-Long expression in stromal cells can influence tumor progression, as it is known that loss of *Pten* in the stroma of mice accelerates tumor initiation and progression (*9*). There are also controversial reports of *PTEN* mutations in mammary tumor stroma (*10*, *11*). Relevant to this, Hopkins *et al*. surveyed the COSMIC tumor sample database and found five somatic missense mutations within the extended region of PTEN-Long that appeared to cause some loss of function.

Intercellular transfer implies that PTEN-Long could be used as a biopharmaceutical to inhibit PI3K signaling, particularly to treat tumors that otherwise lack functional PTEN. Accordingly, Hopkins *et al*. show that intraperitoneal delivery of purified PTEN-Long into mice reduced PI3K-Akt signaling in several tissues, including tumor cell xenografts, and caused tumor regression. These effects were ablated by mutation of either the PTEN-Long active site or the polyarginine sequence that can mediate cell entry. The application of recombinant PTEN-Long to prevent tumor growth in mouse models represents a new therapeutic opportunity. However, there are already many small-molecule inhibitors of the PI3K-Akt signaling pathway, and more than 100 clinical trials are under way to test these compounds (*12*). PTEN-Long has the potential to extend this range of agents, but this success will depend in part on whether PTEN has tumor suppressor functions unrelated to its lipid phosphatase activity and/or function that cannot be phenocopied by pharmacological inhibition of PI3K signaling. Insight into this possibility is provided by Bassi *et al*.

Bassi *et al*. also have identified a longer form of PTEN. In this case, the small protein SUMO (about 100 amino acids) is covalently linked to PTEN, probably at an exposed lysine (Lys^{254}) on one side of the PTEN C2 domain. Cellular fractionation and mutagenesis experiments indicate that SUMOylated PTEN is retained in the nucleus, but that DNA damage reduces its nuclear localization and SUMOylation. How this may relate to data implicating the modification of PTEN with the small protein ubiquitin (76 amino acids) on Lys^{289} in controlling its nuclear import is unclear (*13*). PTEN has been reported to support DNA stability (*14*), and Bassi *et al*. show that it is needed for cells to resolve DNA damage. This effect requires both its catalytic activity and Lys^{254} SUMOylation. Thus, even though loss of PTEN may leave cells sensitive to DNA damage, its loss also provides a PI3K pathway survival signal, the inhibition of which could kill the tumor. Indeed, the authors show that tumor cells lacking PTEN are sensitive to cell death induced by a combination of DNA damage and inhibition of PI3K signaling. This important hypothesis can be tested in clinical trials with inhibitors of the PI3K-Akt pathway.

The new mechanisms by which PTEN may act revealed by Hopkins *et al*. and Bassi *et al*. have the potential to change some established ideas not only about how tissue growth may be regulated, but how cancer develops and how it can be treated. "Where is PTEN?" is becoming an increasingly interesting question.

References

1. B. D. Hopkins *et al*., *Science* **341**, 399 (2013); 10.1126/science.1234907.
2. C. Bassi *et al., Science* **341**, 395 (2013).
3. L. Salmena *et al*., *Cell* **133**, 403 (2008).
4. U. Putz *et al*., *Sci. Signal.* **5**, ra70 (2012).
5. A. Alimonti *et al*., *Nat. Genet.* **42**, 454 (2010).
6. M. J. Bissell, W. C. Hines, *Nat. Med.* **17**, 320 (2011).
7. B. Z. Qian, J. W. Pollard, *Cell* **141**, 39 (2010).
8. M. B. Meads *et al*., *Nat. Rev. Cancer* **9**, 665 (2009).
9. A. J. Trimboli *et al*., *Nature* **461**, 1084 (2009).
10. I. Campbell *et al*., *Cancer Res.* **69**, 6765 (2009).
11. K. Kurose *et al*., *Nat. Genet.* **32**, 355 (2002).
12. B. Vanhaesebroeck, P. K. Vogt, C. Rommel, *Curr. Top. Microbiol. Immunol.* **347**, 1 (2010).
13. L. C. Trotman *et al*., *Cell* **128**, 141 (2007).
14. W. H. Shen *et al*., *Cell* **128**, 157 (2007).

10.1126/science.1242541

CHEMISTRY

A Path to Complex Carbohydrates

A general strategy for synthesizing asymmetrically branched carbohydrates will help to elucidate their biological functions.

Laura L. Kiessling[1,2] and Matthew B. Kraft[1]

Glycans are carbohydrate-containing compounds that include oligosaccharides as well as the carbohydrate parts of glycoproteins or glycolipids. All cells contain glycans, ranging from those that benefit from the development, metabolism, and immune responses of the host to those involved in cancer metastasis or host-pathogen interactions (*1*). The oligosaccharide sequence of a glycan determines which proteins it binds to and can thus profoundly influence its physiological activity. The full complement of glycans has not been determined for any cell type, but recent analyses of known mammalian glycans have revealed that there are underlying sequence patterns (*2*, *3*). It remains difficult to assign functions to specific glycan sequences because the relevant oligosaccharides cannot easily be accessed either by synthesis or by isolation from cells (*4*). On page 379 of this issue, Wang *et al*. report a general and efficient strategy for generating diverse glycans (*5*).

In the past decade, glycan microarrays have emerged as a critical technology for determining the specificity of carbohydrate-binding proteins (*6*). Mammalian glycan microarrays are largely populated with saccharides corresponding to terminal fragments of O- and N-linked glycoproteins and glycolipids. The glycans in these arrays are typically linear or symmetrically branched; therefore, the arrays lack the asymmetrically branched structures present in natural glycans (see the first figure).

Emerging evidence suggests that these asymmetrically branched sequences are important recognition motifs. For example, different array platforms for immobilizing oligosaccharides can lead to differences in protein binding specificity (*6*), suggesting that the density, conformation, or relative orientation of the oligosaccharide units matter. These apparent discrepancies may resolve when oligosaccharides that possess the diversity of substitution patterns found in natural glycans are represented on the glycan arrays. The limitation has been generating this requisite diversity. Glycan sequences are not encoded from a template; consequently, there is no standard means of programming cells to produce specific glycans. It can be difficult to obtain sufficient quantities of pure glycans from biological systems, and synthetic methods have been used to fill this void (*7*).

[1]Department of Chemistry, University of Wisconsin–Madison, Madison, WI 53706, USA. [2]Department of Biochemistry, University of Wisconsin–Madison, Madison, WI 53706, USA. E-mail: kiessling@chem.wisc.edu

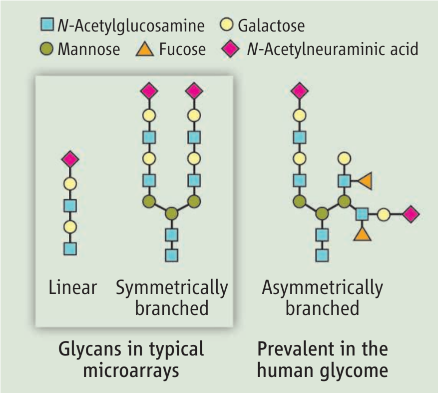

The problems of asymmetry. Current mammalian glycan arrays are populated by linear and symmetrically-branched glycans. Asymmetrically branched *N*-glycans seem to be more prevalent in the human glycome but have been difficult to generate.

Recent progress in the generation of defined oligosaccharides of specific sequences include the development of robust solid-phase methods, an increased understanding of how protecting groups influence the rates and stereoselectivity of glycosylation, and the advent of new protecting groups that enable excellent chemoselectivity (*8*, *9*). These advances in chemical synthesis have been complemented by the identification and engineering of enzymes that can introduce specific monosaccharide units with exquisite site selectivity and stereoselectivity (*10*, *11*).

Wang *et al*. devise a chemoenzymatic synthesis that takes advantage of progress in chemistry and biochemistry. In their strategy, a single key intermediate serves as a platform for enzyme-mediated diversification to afford a wide range of branched *N*-glycans. This key intermediate is a protected version of the pentasaccharide core present in all eukaryotic N-linked glycans. By equipping the sites where branching naturally occurs with orthogonal protecting groups, specific sites within the pentasaccharide can be modified independently. Each protecting group is compatible with the synthetic steps needed to build the pentasaccharide, yet each can be removed without modifying any of the others. In this way, each relevant position can be individually elaborated chemically or enzymatically with additional sugar residues to afford asymmetrically branched *N*-glycans.

Another keystone of their approach is the use of glycosyltransferases. These enzymes have long been used for the practical synthesis of oligosaccharides (*12*). Various naturally occurring and engineered enzymes are now available that mediate selective glycosylation reactions without the need of protecting groups (*13*, *14*). Wang *et al*.'s approach mirrors that of glycan biosynthesis: A core oligosaccharide is first assembled and then customized with a series of enzymatic reactions (see the second figure). For example, the authors first created an asymmetrically branched multiantennary deca-

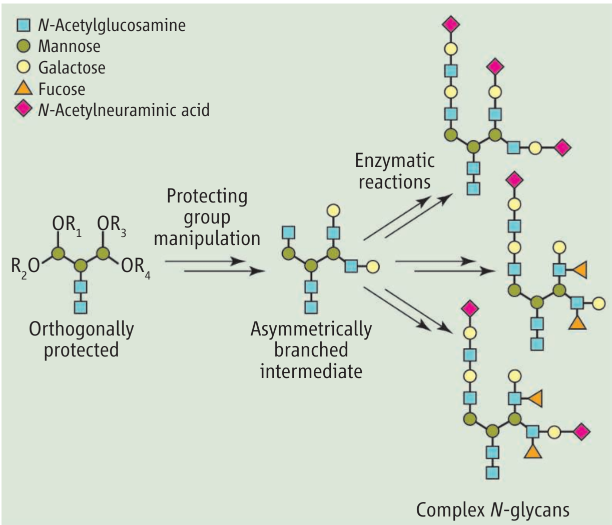

Chemoenzymatic synthesis of branched *N*-glycans. Wang *et al*. start with an orthogonally protected core pentasaccharide common to all N-linked glycans. Selective protecting group manipulation affords an asymmetrically branched intermediate, which can be further elaborated enzymatically to provide a diverse collection of complex *N*-glycans.

Published by AAAS

saccharide with chemical synthesis and then elaborated it with enzymes to provide 13 different complex *N*-glycan structures. They note that 85% of known *N*-glycans are asymmetrically branched and that, in principle, most of these can be accessed by this strategy.

To understand the roles of the core oligosaccharide and the branching structures of *N*-glycans in carbohydrate recognition, Wang *et al*. used a glycan array. They exposed the array to several glycan-binding proteins, including influenza virus hemagglutinins derived from different viral strains. The binding specificities obtained from the arrays containing only linear and symmetrically branched glycans were different than those obtained from arrays with asymmetrically branched glycans. There are mechanisms by which the sequence of each glycan branch can influence protein recognition: Both branches can interact at an extended binding site, one branch could inhibit binding of another, or a symmetric branched glycan could engage in multivalent interactions (*15*).

The results reported by Wang *et al*. take us forward in fulfilling the need for well-defined glycans that match the complexity of those found in nature. Their methods provide the means to evaluate how glycan asymmetry influences the ability of glycan-binding proteins to distinguish between different yet related sequences. The study highlights the advantages of combining insights from chemistry and biology to access compounds that would otherwise be difficult to generate. Powerful tools needed to define the functions of specific glycans within the human glycome are now in our purview.

References

1. A. Varki, *Glycobiology* **3**, 97 (1993).
2. D. B. Werz *et al*., *ACS Chem. Biol.* **2**, 685 (2007).
3. R. D. Cummings, *Mol. Biosyst.* **5**, 1087 (2009).
4. National Academy of Sciences, *Transforming Glycoscience: A Roadmap for the Future* (National Academies Press, Washington, DC, 2012).
5. Z. Wang *et al*., *Science* **341**, 379 (2013).
6. C. D. Rillahan, J. C. Paulson, *Annu. Rev. Biochem.* **80**, 797 (2011).
7. B. Lepenies, J. Yin, P. H. Seeberger, *Curr. Opin. Chem. Biol.* **14**, 404 (2010).
8. C.-H. Hsu *et al*., *Angew. Chem. Int. Ed.* **50**, 11872 (2011).
9. M. A. Walczak, J. Hayashida, S. J. Danishefsky, *J. Am. Chem. Soc.* **135**, 4700 (2013).
10. H. A. Chokhawala *et al*., *ACS Chem. Biol.* **3**, 567 (2008).
11. S. M. Hancock*et al*. *Curr. Opin. Chem. Biol.* **10**, 509 (2006).
12. J. C. Paulson *et al*., *J. Biol. Chem.* **252**, 2363 (1977).
13. L. L. Lairson *et al*., *Annu. Rev. Biochem.* **77**, 521 (2008).
14. University of Georgia Complex Carbohydrates Research Center, Repository of Glyco-Enzyme Expression Constructs; http://glycoenzymes.ccrc.uga.edu/.
15. L. L. Kiessling, R. A. Splain, *Annu. Rev. Biochem.* **79**, 619 (2010).

10.1126/science.1241788

GENETICS

Genome Mosaicism—One Human, Multiple Genomes

The cells in our body do not all contain identical genomes, which has implications for health and disease.

James R. Lupski

With recent advances in genome-wide assays, it is becoming increasingly apparent that a human individual is made up of a population of cells, each with its own "personal" genome. Thus, mosaicism is perhaps much more common within multicellular organisms than our limited genomic assays have detected thus far, and may represent the rule rather than the exception. To what extent does it play a role in normal development and disease?

Chromosomal mosaicism has been recognized clinically for decades, but the application of high-resolution genome-wide analysis tools, such as array comparative genomic hybridization and genomic single-nucleotide polymorphism (SNP) chips has allowed detection of events missed by karyotyping (*1*–*3*). Mosaicism for small intragenic copy number variants (CNVs) was detected in 10% of 30 molecularly diagnosed subjects (*4*), and extensive genomic CNVs have been found in clonal isolates of embryonic stem cells (*5*). In addition, varying levels of mosaicism have been reported in somatic human tissues, including the skin, brain, and blood, and in induced pluripotent stem cells (*6*–*10*). Therefore, our understanding of the frequency and effects of mosaicism is increasing with the development of ever more sensitive methods for detecting genomic variation.

Department of Molecular and Human Genetics, and Department of Pediatrics, Baylor College of Medicine, One Baylor Plaza, Room 604B and Texas Children's Hospital, Houston, TX 77030, USA. E-mail: jlupski@bcm.edu

The Origin of Mosaicism

Mosaicism can arise because of errors that occur during chromosome segregation or DNA replication, leading to chromosome aneuploidy, CNVs, genomic rearrangements, single-nucleotide variation, or repeat expansions and microsatellite instabilities. These mutational processes can occur at any stage of development; in stem cells, differentiating cells, and in terminally differentiated somatic cells.

Both genomic architectural features (e.g., direct and inverted repeats) and DNA sequence characteristics (e.g., CpG dinucleotides) can increase genome instability and susceptibility to mutation. In addition, exogenous sources of DNA damage, such as tobacco smoke and other carcinogens, may lead to somatic mosaicism. Cumulative exposures to exogenous mutagens, as well as ongoing growth of the organism, cell proliferation and renewal, and tissue regeneration, result in accumulation of mutations with age. In addition, early studies suggested that nonallelic homologous recombination–predicted inversions (i.e., structural variations) are mosaic and appear to accumulate as the individual ages (*11*). Somatic mosaicism can also be caused by L1 transposition during embryogenesis (*12*). Some unbalanced translocations appear to originate postzygotically, apparently arising de novo during embryogenesis in a process that is based on homologous interspersed transposable elements as substrates (*13*), and other postzygotic mutational events could potentially arise from recombination-restarted replication forks (*14*).

For both cellular and organismal populations, a balancing act must exist between mutation to generate variation and selection of the variants most fit for that given environment (see the figure). Development itself seems to be a process of strong selective pressure for human genomic integrity. Indeed, single-cell genomic analysis during early development reveals that chromosome instability is common in human cleavage-stage embryos (*15*), and abnormal chromosome complements can be found in about 70% of 14 normally developing human embryos examined (*16*); whereas such extensive genomic abnormalities are rare in live-born individuals. Perhaps mutation is tolerated to a

Published by AAAS

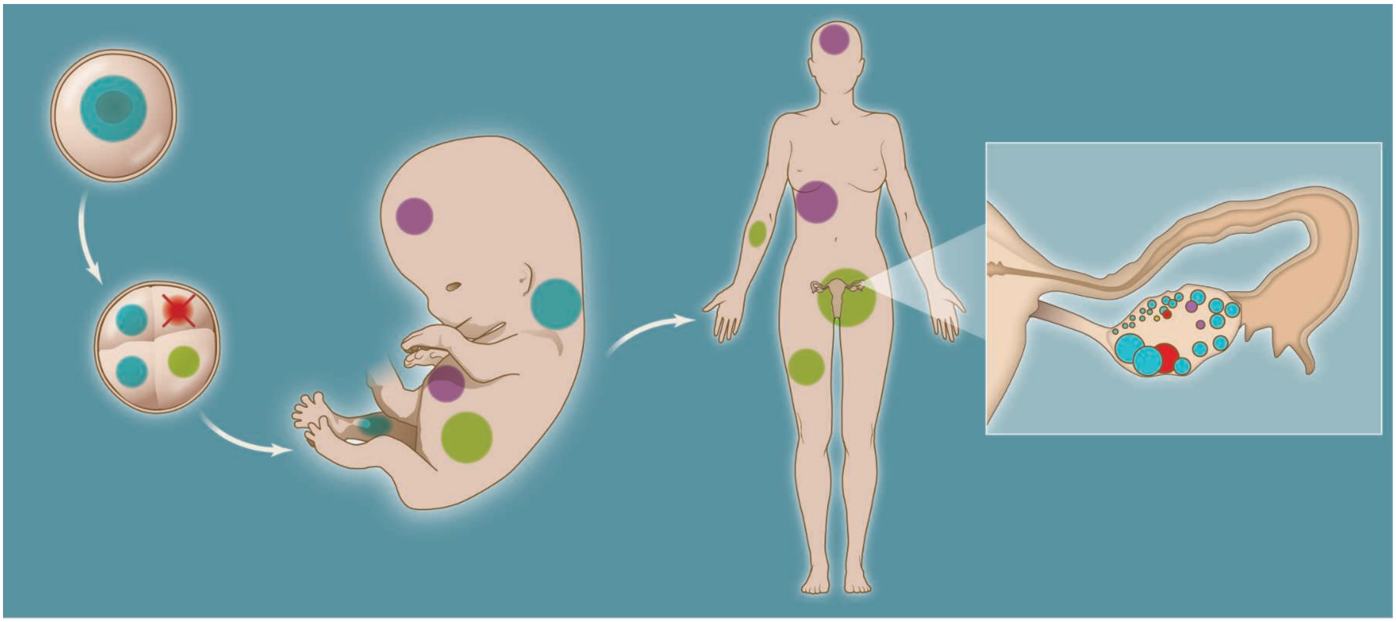

Acquiring mosaicism. Human development from a single fertilized cell to a multicellular organism requires many cell divisions and the genetic material to be replicated many times. Populations of cells (blue) can accumulate mutations at any stage in the life cycle (green, purple, and red). Some impair cellular fitness, and are consequently selected against (red cross); others survive and contribute to tissue mosaicism, which may serve physiological functions.

greater extent, or selection is less restrictive, in a cell-autonomous environment than in the whole organism.

Possible Biological Functions

In terms of pathological functions, somatic mosaicism of terminally differentiated cells has long been known to cause cancer. Recent work shows that somatic mosaicism of nervous system tissues underlies a host of neurodevelopmental and perhaps neuropsychiatric diseases (*17*). However, the extent of somatic mosaicism that is now being reported in a variety of healthy tissues and cell types suggests that it also has physiological functions. The most well-characterized function for genome mosaicism is in the immune system, in which intra-individual lymphocyte genetic diversity is generated by mainly recombination and somatic hypermutation to combat a wide variety of pathogens and antigens. It has also been hypothesized that the complexity and diversity of neuronal cell types in the human brain arose by somatic retrotransposition (*7*, *8*), and that mosaicism might even play a role in normal brain function. However, more work is needed to determine whether somatic mosaicism has direct biological functions in specific tissues.

Clinical Implications

Mosaicism of both somatic tissues and germ cells in humans has several clinical implications. Recurrence risk for unaffected parents who have an affected child and are contemplating a pregnancy may relate to the frequency of new mutations at a given gene or locus, the severity of the phenotype conferred by mosaicism, the type of mutational mechanism, or the sex and age of the mosaic parent. Mosaicism and risk for recurrence in offspring may also relate to the time in embryogenesis at which the de novo mutational event occurred. If the parent is germline mosaic, he or she is at risk for a recurrence of another child with the disease.

Mosaicism is also important for disease mechanism. For example, somatic activating mutations in the protein kinase AKT1 are associated with Proteus syndrome, whereas mosaicism for postzygotic mutations in genes for three core components of the phosphatidylinositol 3-kinase (PI3K)–AKT signaling pathway that enhance signaling can cause a spectrum of related megalencephaly syndromes (*17*).

From a diagnostics standpoint, it is important to realize that genome analyses reflect the average genome of the cells one examines. Thus, for chorionic villus sampling, an abnormality observed may represent confined placental mosaicism. When performing karyotype analysis from a blood sample, only cells stimulated to grow are assayed for chromosomes, whereas total DNA isolated from white blood cells comes from more cell types and thus may detect mosaicism (*1*, *2*). However, none of these approaches informs on the presence of mosaicism in the brain or other tissues and organs. Skin biopsies are more representative of germline genomic constituents than blood cells, particularly with older individuals, likely reflecting the more rapid cell turnover, greater selective evolutionary forces, and multitude of cellular constituents of blood. Eventually, genome analysis of all surgically excised abnormal tissue (tonsils, an appendix, a defective heart valve, or abnormal skeletal muscle), not just cancer, might be considered germane for genome analysis to detect mosaicism—or perhaps even the presence of a foreign viral or microbial genome. Such studies may prove informative in the clinic.

References

1. B. C. Ballif *et al.*, *Am. J. Med. Genet. A.* **140A**, 2757 (2006).
2. S. W. Cheung *et al.*, *Am. J. Med. Genet. A.* **143A**, 1679 (2007).
3. L. K. Conlin *et al.*, *Hum. Mol. Genet.* **19**, 1263 (2010).
4. P. M. Boone *et al.*, *Hum. Mutat.* **31**, 1326 (2010).
5. Q. Liang, N. Conte, W. C. Skarnes, A. Bradley, *Proc. Natl. Acad. Sci. U.S.A.* **105**, 17453 (2008).
6. A. Abyzov *et al.*, *Nature* **492**, 438 (2012).
7. J. K. Baillie *et al.*, *Nature* **479**, 534 (2011).
8. G. D. Evrony *et al.*, *Cell* **151**, 483 (2012).
9. M. O'Huallachain, K. J. Karczewski, S. M. Weissman, A. E. Urban, M. P. Snyder, *Proc. Natl. Acad. Sci. U.S.A.* **109**, 18018 (2012).
10. E. Z. Macosko, S. A. McCarroll, *Nat. Genet.* **44**, 614 (2012).
11. M. Flores *et al.*, *Proc. Natl. Acad. Sci. U.S.A.* **104**, 6099 (2007).
12. H. Kano *et al.*, *Genes Dev.* **23**, 1303 (2009).
13. C. Robberecht, T. Voet, M. Z. Esteki, B. A. Nowakowska, J. R. Vermeesch, *Genome Res.* **23**, 411 (2013).
14. K. Mizuno, I. Miyabe, S. A. Schalbetter, A. M. Carr, J. M. Murray, *Nature* **493**, 246 (2013).
15. E. Vanneste *et al.*, *Nat. Med.* **15**, 577 (2009).
16. A. Mertzanidou *et al.*, *Hum. Reprod.* **28**, 256 (2013).
17. A. Poduri, G. D. Evrony, X. Cai, C. A. Walsh, *Science* **341**, 1237758 (2013).

10.1126/science.1239503

IBI* SERIES WINNER

Engaging High School Students in Research on Smoking Behavior

Exploring Databases, an IBI prize–winning module, enables students to conduct epidemiological research on smoking behavior using a database.

Maureen M. Munn,[1]‡ Hiroki Oura,[2] Mark Gallivan,[3]† Katie Van Horne,[2] Andrew W. Shouse[2]

Increasingly, scientists use information and communications technology to analyze large repositories of existing data. Engaging students in database investigations has great potential for providing authentic research experiences that are low cost and reflect contemporary science practice. Through a collaboration between Genome Sciences and the Institute for Science and Math Education at the University of Washington (UW), we developed Exploring Databases, a high school inquiry-based research project combining neurobiology, epidemiology, statistics, genetics, and database research to answer the question, "Why do some people smoke, and others don't?"

Students and teachers engaged in their research. (Left) Students collaborate as they query the database. **(Right)** During workshops, teachers also work together to test their hypotheses.

PHOTO CREDIT: (LEFT) HIROKI OURA, (RIGHT) RANDY KNUTH

Nicotine addiction remains the most common form of chemical dependence in the United States (*1*). Consequently, despite considerable public health investment, tobacco use is still the leading cause of preventable illness and death in the United States (*2*). Exploring Databases engages students in examining how environmental and genetic factors contribute to smoking addiction by using the Smoking Behavior database.

This database is the result of a previous science education project that involved high school students in planning and conducting a case control study that compared 300 adult smokers and nonsmokers (*3*). Research subjects completed a questionnaire regarding environmental influences on their smoking behavior. They also gave a small blood sample that was used to genotype their DNA at three candidate gene regions shown to be associated with smoking behavior: a deletion in the promoter region of the dopamine receptor gene; a synonymous substitution in the dopamine receptor gene; and a substitution in an intron of the dopa decarboxylase gene (*3*). Questionnaire and genotyping data for each subject were entered into the database.

The Exploring Databases curriculum module consists of seven 1- to 2-hour lessons, including foundational activities and student-led investigations (see supplementary materials). The curriculum is taught by teachers who have attended a professional development workshop. In the first three lessons, students learn different aspects of human subjects research, discuss variation in smoking behavior, and study the biology of nicotine addiction. In lesson 4, students learn the case control study design and epidemiological analysis, including criteria used to distinguish causality from associations (*4*). Lesson 5 focuses on the fundamentals of statistics to estimate the strength and significance of associations. Throughout these lessons, students watch taped interviews of scientists in related fields and explore the role of databases in contemporary research. They develop an overarching hypothesis related to genetic or environmental influences on smoking behavior by reviewing profiles of smokers, examining published research and reflecting on their own experiences.

In lesson 6, student research teams identify questions that address their overarching hypothesis and use the database for hypothesis testing (see the first figure, left). The online database interface provides visual support to guide students as they submit queries, estimate statistics, and interpret their results (see the second figure). Students then apply the criteria for causality to determine whether an association can be considered causal. In lesson 6, students are instructed to conduct, at most, four statistical tests related only to their overarching hypothesis to avoid false-positive results. However, in lesson 7, students "mine" the database by analyzing many questions and exposure combinations to generate a new hypothesis for a future hypothetical research study.

To conclude the module, students create a presentation in PowerPoint or poster format that displays both their results and claims based on the evidence from their analysis and their proposed study. During their research presentations, students participate in scientific argumentation by critiquing the claims of their peers and responding to the questions and comments of others, using a rubric designed by their teacher (*5*).

In developing the module, we adopted the following design principles, which could be applied to other programs:

- Involving teachers, life scientists, and learning scientists as partners in curriculum design (*6*);
- Engaging students in topics that relate to their lives and interests (*7*);
- Developing analytical tasks that focus on the learning goals of the National Research Council science education framework (*8*) and the Next Generation Science Standards (http://nextgenscience.org);
- Providing instructional supports in the curriculum and database to guide student enactment of the research process (*9*);
- Designing the curriculum through an iterative process based on classroom implementation data (field notes, audio and video recordings, interviews, and survey items) and feedback from stakeholders;
- Providing teacher professional development workshops in which teachers

[1]Department of Genome Sciences, University of Washington, Seattle, WA 98195, USA. [2]Learning Sciences and Institute for Science and Math Education, University of Washington, Seattle, WA 98195, USA. [3]Department of Epidemiology, University of Washington, Seattle WA 98195, USA.

*IBI, *Science* Prize for Inquiry-Based Instruction; www.sciencemag.org/site/feature/data/prizes/inquiry/. †Present address: California Department of Public Health, Oakland, CA 94607, USA. ‡Corresponding author: mmunn@uw.edu

Published by AAAS

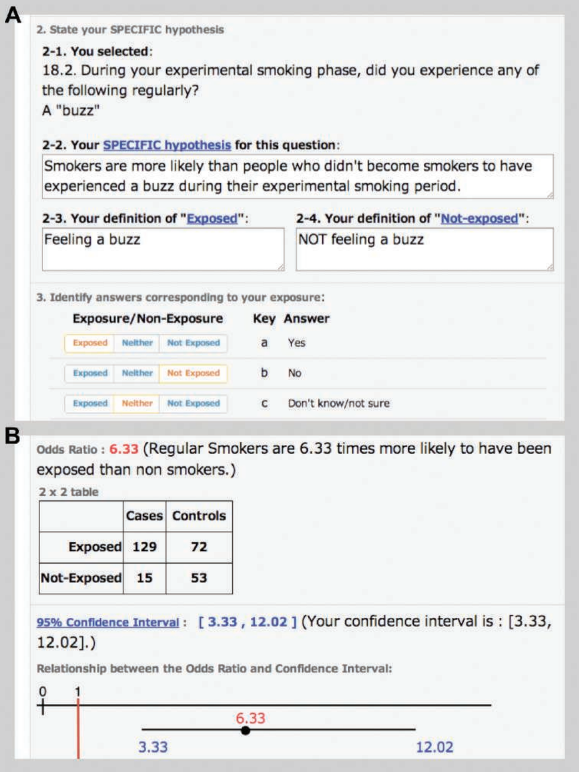

Database input and output pages. (**A**) Users select questions from the database, define specific hypothesis, "Exposed" and "Not-exposed;" select population, submit the query. (**B**) Interprets the result, and determine whether there is a causal relationship.

complete many of the student activities (see the first figure, right) and engage in discussions with lead teachers, scientists, education researchers, and each other; and

• Providing Web-based access to project components, implementation support, and ongoing technical support.

The module has been used in a wide variety of high school science courses, including introductory biology, a biotechnology class for students for whom English is a second language, an Upward Bound seminar, advanced elective courses (e.g., genetics and biotechnology), and Advanced Placement and International Baccalaureate Biology, as well as community college courses. In the 2011–12 academic year, nearly 600 students participated in the project. Through feedback from teachers, classroom observations, and research studies conducted in the classrooms (*10*), we have learned several lessons regarding implementation of the module:

• Students often report that their interest in their investigation topics stems from their observations of smoking practices in their family, friends, and the media.

• Both students and teachers have limited prior experience and images of contemporary scientific practices other than the classical experimental design covered in traditional K–12 science curricula.

• Through their involvement in epidemiological research, students broaden their understanding of contemporary scientific research and methodologies, especially human subjects research.

• A study comparing student learning of scientific research and attitudes toward science after completing a genotyping experiment (*3*) and the database research described here. Students were somewhat more likely to rate genotyping as real science compared to their database research experience, despite associating more scientific tasks with the database experience than genotyping.

• Some students even expressed interest in conducting future case control studies focused on drug addiction in the future.

About the authors

(Left to right) Maureen Munn is the Director of Education Outreach in UW Genome Sciences, where she develops science education projects that integrate authentic genomics research into high school classrooms. **Hiroki Oura** is a Ph.D. candidate in the UW Institute for Science and Math Education focusing on curriculum, instructional, and technology design to develop students' scientific understanding and reasoning skills through authentic inquiry. **Mark Gallivan** is a M.P.H. graduate from the UW Department of Epidemiology and current Applied Epidemiology Fellow at the California Department of Public Health. **Katie Van Horne** is a graduate researcher at the UW Institute for Science and Math Education, focusing on how to engage all youth in contemporary scientific practices while taking into account their personal interests and identities. **Andrew Shouse** is the Associate Director of the UW Institute for Science and Math Education focusing on equitable science education in formal and informal settings and communication of research to policy and practice audiences.

PHOTO CREDITS: HANK CLARK, KATIE VAN HORNE, MIKA OTANI

References and Notes

1. American Society of Addiction Medicine, "Public policy statement on nicotine dependence and tobacco" (ASAM, Chevy Chase, MD, 2010).
2. Centers for Disease Control and Prevention (CDC), *MMWR Morb. Mortal. Wkly. Rep.* **60**, 1207 (2011).
3. M. Munn *et al.*, *Investigating the Effects of Genes and Environment on Smoking Behavior* (Univ. of Washington, Seattle, 2010); https://gsoutreach.gs.washington.edu/files/investigating_smoking_behavior_jan2011.pdf.
4. A. B. Hill, *Proc. R. Soc. Med.* **58**, 295 (1965).
5. P. Bell, in *Internet Environments for Science Education*, M. C. Linn, E. A. Davis, P. Bell, Eds. (Erlbaum, Mahwah, NJ, 2004), pp. 115–143.
6. National Research Council, *Learning Science in Informal Environments: People, Places, and Pursuits* (National Academies Press, Washington, DC, 2009).
7. P. Bell, M. C. Linn, *Int. J. Sci. Educ.* **22**, 797 (2000).
8. National Research Council, *A Framework for K-12 Science Education: Practices, Crosscutting Concepts, and Core Ideas* (National Academies Press, Washington, DC, 2012).
9. M. C. Linn, E. A. Davis, P. Bell, *Internet Environments for Science Education* (Lawrence Erlbaum Associates, Mahwah, NJ, 2004).
10. H. Oura, K. Van Horne, A. W. Shouse, M. Munn, R. Knuth, in *The Future of Learning: Proceedings of the 10th International Conference of the Learning Sciences*, J. van Aalst, K. Thompson, M. J. Jacobson, P. Reimann, Eds., 2 to 6 July 2012, Sydney, Australia (ICLS and Univ. of Sydney, Sydney, 2012), vol. 2, pp. 41–48.

Acknowledgments: This project is funded by an NSF ITEST award, DRL-0929181. The predecessor project was supported through SEDAPA grant R25 DA013180 from National Institute on Drug Abuse (NIDA), NIH. The program content is solely the responsibility of the authors and does not necessarily represent the official views of the NSF, NIDA, or NIH. We wish to acknowledge project co-principal investigators P. Bell and J. Akey at the University of Washington; D. Nickerson and G. Jarvik, principal investigators of the predecessor project, the WISE development team in the Technology Enhanced Learning in Science center at the University of California, Berkeley, especially H. Terashima; many advising scientists, especially N. Weiss, UW Professor of Epidemiology; the many contributors to the curriculum, especially M. Brown; project evaluators R. Knuth and S. Levias; the many teachers who have implemented the curriculum in their classroom; and, of course, their students.

Supplementary Materials

www.sciencemag.org/cgi/content/full/341/6144/360/DC1

10.1126/science.1229999

Lifeline in the desert. The Colorado River supplies virtually all of southern Nevada's water.

ISTOCKPHOTO/AQUALANDPHOTOGRAPHY

AAAS PACIFIC DIVISION

Can the Southwest Manage Its Thirst?

LAS VEGAS – Concerned about ebbing water levels at nearby Lake Mead and the future of the Colorado River that fills it, southern Nevada's water management agency aims to curb water use in greater Las Vegas by 20%. Even if successful, however, this conservation plan alone will fall short of meeting the area's water needs in 2035, according to research presented at the 94th annual meeting of the AAAS Pacific Division.

The population of the Las Vegas Valley has nearly tripled in two decades, although this growth has slowed recently. Of the seven states that draw their water from the Colorado River, five, including Nevada, are among the country's fastest growing states.

Several researchers at the meeting presented computer modeling studies aimed at helping resource managers in the arid West, where population growth and climate change are putting increasing pressure on the region's water supply. "We are taking outputs from global climate models and hydrological models and bridging the gap between science and what the decision-maker community needs," said Sajjad Ahmad of the University of Nevada, Las Vegas.

The conference, held 16 to 19 June, drew hundreds of scientists, students, professionals and the public to the University of Nevada, Las Vegas. Over 75 students, including some from as far away as Nigeria, presented their work in oral and poster sessions. The Pacific Division is the oldest of the four AAAS regional divisions, which bring together scientists and nonscientific communities to discuss issues with immediate local impacts.

Even if the Southern Nevada Water Authority meets its 20% conservation target by 2035, in that time the demand for water will still grow to the point where there will be essentially no surplus available in case of drought or other spikes in water use, Ahmad reported. Combining conservation with a slowdown in population growth could provide a healthier surplus, as long as Las Vegas' population does not exceed 2.6 million. (Currently at 2 million, the city's population is on course to reach 3.2 million by 2035.)

Finding an alternative water source may be equally controversial. State and federal agencies have approved the building of a pipeline that would supply Las Vegas with groundwater pumped from northern Nevada. This plan has been hotly contested by a variety of groups, however, and is currently being challenged in Nevada state court.

Alternatively, Nevada could build a desalination plant near the coast of California or Mexico. Authorities could then arrange a "paper trade" that would exchange desalinated seawater for an additional share of Lake Mead's water. On a unit-cost basis alone, the desalination option is cheaper compared to pipeline plan, Ahmad reported, but it would use twice as much energy and its carbon footprint would be 48% higher.

Another study presented in the symposium offered a new approach to forecasting the Colorado River's spring-summer "streamflow," or the volume of water flowing past a fixed point in the river. This approach should be useful to managers who must decide how much water to release for agricultural use or to conserve behind dams, especially as climate change is expected to bring about more frequent and extreme floods and droughts.

Ajay Kalra of the Desert Research Institute in Las Vegas has identified several regions of the Pacific Ocean where changes in sea surface temperature appear to be statistically linked to the Colorado River's streamflow. The changes in these regions can account for about 90% of the observed variation in the river's streamflow over the last century, with 1 to 4 months lead-time. The method is useful because it provides quantitative estimates instead of probabilities. And, because it eschews complex physical climate models for a statistical, data-driven modeling approach, it is relatively "simple and parsimonious," Kalra said. *–Kathy Wren*

AAAS

New Dues Rates Approved for 2014

The AAAS Board of Directors has approved a dues increase for 2014. The new rates are effective for membership terms beginning after 31 December 2013. As listed below, they do not include postage or taxes for international members, which is additional. For more information, contact the AAAS Membership Office at 202-326-6417, or www.aaas.org/membership.

Regular professional members	$153
Postdocs and K-12 teachers	$99
Emeritus members who receive print *Science*	$115
Students	$75
Patrons	$310
Institutional rate for print for high schools and public libraries	$360
All other institutions receiving print	$1282

Published by AAAS

The Diffusion of Microfinance

Abhijit Banerjee,* Arun G. Chandrasekhar,* Esther Duflo,* Matthew O. Jackson*

READ THE FULL ARTICLE ONLINE
http://dx.doi.org/10.1126/science.1236498

Cite this article as A. Banerjee *et al.*, *Science* **341**, 1236498 (2013). DOI: 10.1126/science.1236498

Introduction: How do the network positions of the first individuals in a society to receive information about a new product affect its eventual diffusion? To answer this question, we develop a model of information diffusion through a social network that discriminates between information passing (individuals must be aware of the product before they can adopt it, and they can learn from their friends) and endorsement (the decisions of informed individuals to adopt the product might be influenced by their friends' decisions). We apply it to the diffusion of microfinance loans, in a setting where the set of potentially first-informed individuals is known. We then propose two new measures of how "central" individuals are in their social network with regard to spreading information; the centrality of the first-informed individuals in a village helps significantly in predicting eventual adoption.

Methods: Six months before a microfinance institution entered 43 villages in India and began offering microfinance loans to villagers, we collected detailed network data by surveying households about a wide range of interactions. The microfinance institution began by inviting "leaders" (e.g., teachers, shopkeepers, savings group leaders) to an informational meeting and then asked them to spread information about the loans. Using the network data, the locations in the network of these first-informed villagers (or injection points), and data regarding the villagers' subsequent participation, we estimate the parameters of our diffusion model using the method of simulated moments. The parameters of the model are validated by showing that the model correctly predicts the evolution of participation in each village over time. The model yields a new measure of the effectiveness of any given node as an injection point, which we call communication centrality. Finally, we develop an easily computed proxy for communication centrality, which we call diffusion centrality.

Results: We find that a microfinance participant is seven times as likely to inform another household as a nonparticipant; nonetheless, information transmitted by nonparticipants is important and accounts for about one-third of the eventual informedness and participation in the village because nonparticipants are much more numerous. Once information passing is accounted for, an informed household's decision to participate is not significantly dependent on how many of its neighbors have participated. Communication centrality, when applied to the set of first-informed individuals in a village, substantially outperforms other standard network measures of centrality in predicting microfinance participation in this context. Finally, the simpler proxy measure—diffusion centrality—is strongly correlated with communication centrality and inherits its predictive properties.

Discussion: Our results suggest that a model of diffusion can distinguish information passing from endorsement effects, and that understanding the nature of transmission may be important in identifying the ideal places to inject information.

FIGURES AND TABLES IN THE FULL ARTICLE

SUPPLEMENTARY MATERIALS

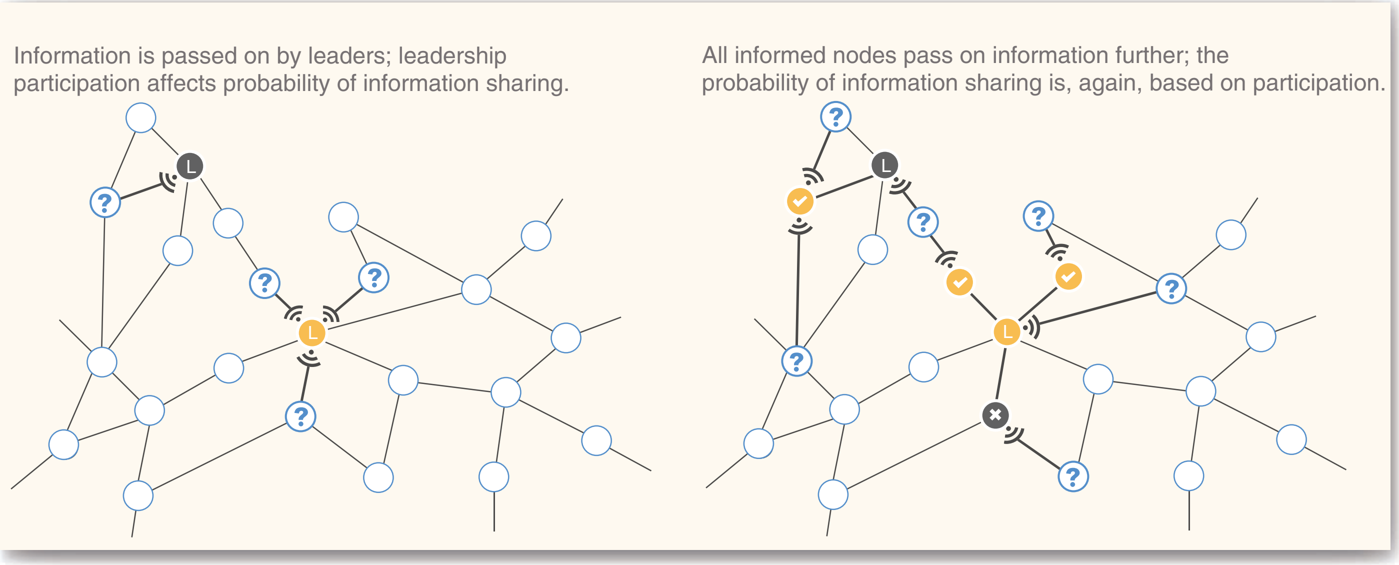

Diffusion of information and participation. (**Left**) First-informed households have decided whether to participate and stochastically pass on information to their neighbors. (**Right**) Participation may affect the probability of passing information. Newly informed nodes make their decisions, possibly being influenced by the decisions of their neighbors. After newly informed nodes make their participation decisions, all informed nodes engage in another round of stochastic communication.

The list of author affiliations is available in the full article online.
*Corresponding author. E-mail: banerjee@mit.edu (A.B.); arungc@stanford.edu (A.G.C.); eduflo@mit.edu (E.D.); jacksonm@stanford.edu (M.O.J.)

The Diffusion of Microfinance

Abhijit Banerjee,[1]* Arun G. Chandrasekhar,[2,3]* Esther Duflo,[1]* Matthew O. Jackson[3,4,5]*

To study the impact of the choice of injection points in the diffusion of a new product in a society, we developed a model of word-of-mouth diffusion and then applied it to data on social networks and participation in a newly available microfinance loan program in 43 Indian villages. Our model allows us to distinguish information passing among neighbors from direct influence of neighbors' participation decisions, as well as information passing by participants versus nonparticipants. The model estimates suggest that participants are seven times as likely to pass information compared to informed nonparticipants, but information passed by nonparticipants still accounts for roughly one-third of eventual participation. An informed household is not more likely to participate if its informed friends participate. We then propose two new measures of how effective a given household would be as an injection point. We show that the centrality of the injection points according to these measures constitutes a strong and significant predictor of eventual village-level participation.

How to implant useful information into social networks so that it benefits the maximum number of people is a question of great importance for policy-makers. Although simulations (*1*) and analytic results (*2*) suggest that the choice of initial injection points in a diffusion process (the first persons to be informed) affects the ultimate reach of the process, there is little empirical evidence concerning whether this is actually the case in real-life examples, and if so, in what ways (*3*). Moreover, the answer to this question crucially depends on the model of information transmission. As information about a new product diffuses through a social network, what are the factors that influence whether an individual chooses to adopt or purchase that product?

We consider two main factors. First, individuals have to be aware of the product before they can adopt, which is more likely when more of their friends can tell them about it. Second, the adoption decisions of informed individuals might be influenced by the decisions of their friends. To account for these factors, we developed a simple model of information diffusion that allows us to (i) distinguish information passing among neighbors from direct influence of neighbors' participation decisions, and (ii) distinguish information passing by participants versus nonparticipants.

We then proceeded in four steps. First, we derived model parameter estimates from a uniquely rich data set on network structure and participation in microfinance in 43 rural villages in Karnataka, a state in southern India. The network data were collected in anticipation of the introduction of services in these villages by a microfinance institution, Bharatha Swamukti Samsthe (BSS), and were drawn from detailed surveys of households covering a wide range of interactions. BSS then entered these villages and provided us with data on participation in microfinance at regular intervals.

An important feature of this context is that the set of potential injection points is known. BSS relies on word-of-mouth communication to reach potential borrowers. When its representatives start working in a village, they begin by inviting a set of "leaders" (e.g., teachers, shopkeepers, savings group leaders) to an information meeting, and then asking those leaders to spread the information. Network distance to these leaders therefore offers a proxy for access to information about microfinance, and our estimation of the structural model is based on the correlation between access to information about microfinance and participation in microfinance.

The results from the structural exercise are of independent interest. We show that to explain the observed patterns, we need to allow for information about microfinance to be transmitted both by those who choose to participate in microfinance and those who do not. On the other hand, once the household is informed that microfinance is available, it does not seem to matter whether the information came from a participant or a nonparticipant (we find no "endorsement" effects).

The second step was to validate these parameter estimates. Validation is important because the variation that identifies these estimates is non-experimental and may be partly driven by homophily (the tendency of individuals to be linked to others with similar characteristics) or correlated unobserved stimuli or shocks (*4*). We show that the spreading pattern generated by simulating the model, given the observed injection points and estimated parameters, is similar to what we observe in the time series data, which were not used in the estimation of the model.

In the third step, we used the model as a basis for a measure of what we call communication centrality, which identifies how effective any given node would be as an injection point according to the parameters of the model. We show that the communication centrality of the set of original injection points in a village is strongly correlated with participation in that village. Communication centrality of the injection points outperforms the other standard measures of centrality (of the same injection points) in terms of predicting microfinance participation in the cross section of villages.

Although these findings show that BSS would benefit from using communication centrality to maximize participation, this measure has the disadvantage of being informationally demanding: To compute it, we need to know not only the network structure, but also the patterns of diffusion in a sample of villages required for model estimation. Thus, the fourth and final step is to develop a measure in the spirit of communication centrality that does not require estimation of the model and yet can still serve as a proxy for communication centrality. We propose a simple measure along these lines that we call diffusion centrality, and we show that it is strongly correlated with communication centrality and inherits much of its predictive properties (at least in our context).

Context and Data

Our initial sample was a list of 75 villages where BSS was planning to start operating within the following year. These villages are spread across five districts in Karnataka, with a median distance of 46 km from other villages in the sample; typically the villages are far enough from each other that we can regard them as independent systems for the questions that we are asking. These villages are, by and large, linguistically homogeneous but heterogeneous in terms of caste. The most common primary occupations are agricultural work, sericulture, and dairy production. Until BSS's entry, these villages had almost no exposure to microfinance institutions and had limited access to any type of formal credit.

In 2006, 6 months before BSS's entry into any village, we conducted a baseline survey in all 75 villages. This survey consisted of a village questionnaire, a full census that collected data on all households in the villages, and a detailed follow-up survey fielded to a subsample of individuals. In the village questionnaire, we collected data on the village leadership, the presence of preexisting nongovernmental organizations (NGOs) and savings self-help groups (SHGs), and various geographical features of the area (such as rivers, mountains, and roads). In the household census, we gathered demographic information, GPS coordinates, and data on a variety of amenities (e.g., roofing material, type of latrine, quality of access to electric power) for every household in each village.

[1]Department of Economics, Massachusetts Institute of Technology, Cambridge, MA 02142, USA. [2]Microsoft Research New England, Cambridge, MA 02142, USA. [3]Department of Economics, Stanford University, Stanford, CA 94305, USA. [4]Santa Fe Institute, Santa Fe, NM 87501, USA. [5]CIFAR, Toronto, Ontario M5G 1Z8, Canada.

*Corresponding author. E-mail: banerjee@mit.edu (A.B.); arungc@stanford.edu (A.G.C.); eduflo@mit.edu (E.D.); jacksonm@stanford.edu (M.O.J.)

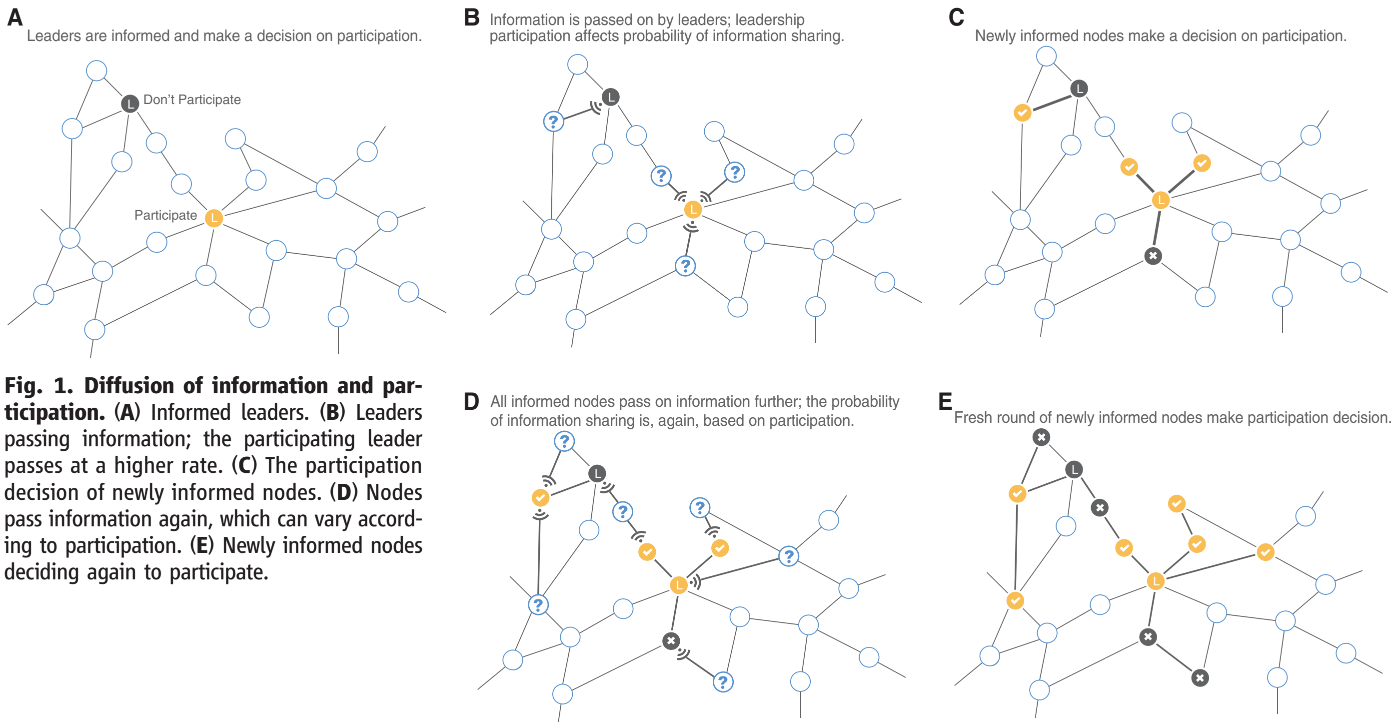

Fig. 1. Diffusion of information and participation. (**A**) Informed leaders. (**B**) Leaders passing information; the participating leader passes at a higher rate. (**C**) The participation decision of newly informed nodes. (**D**) Nodes pass information again, which can vary according to participation. (**E**) Newly informed nodes deciding again to participate.

After the village and household modules were completed, a detailed individual survey was administered to a subsample of villagers. Respondents were randomly selected, and we stratified sampling by religion and geographic sublocation. More than half of the BSS-eligible households (i.e., those with females between the ages of 18 and 57) in each stratification cell were randomly sampled. Individual surveys were administered to eligible members and their spouses, yielding a sample of about 46% of all households per village, and we corrected some of our measures for missing data. The individual questionnaire asked for information including age, caste, education, language, native home, and occupation. So as to not prime the villagers to join BSS or suggest any possible connection with BSS (which would enter the villages later), we did not ask for explicit financial information.

These individual surveys also included a module that collected social network data along 12 dimensions: names of those who visit the respondent's home, those whose homes the respondent visits, kin in the village, nonrelatives with whom the respondent socializes, those from whom the respondent receives medical advice, those from whom the respondent would borrow money, those to whom the respondent would lend money, those from whom the respondent would borrow material goods (kerosene, rice, etc.), those to whom the respondent would lend material goods, those from whom the respondent gets advice, those to whom the respondent gives advice, and those with whom the respondent goes to pray (at a temple, church, or mosque) (*5*).

In 2007, after we finished data collection, BSS began operations in some of these villages. By the time we finished collecting data for this study in early 2011, BSS had entered 43 of the villages. Across a number of demographic and network characteristics, the villages they entered look similar to the ones they did not (*6*). Our analyses focus on the 43 villages in which BSS introduced its program.

In these villages, BSS provided us with regular administrative data on who joined the program, which we matched with our demographic and social network data. When BSS started to work in a village, it sought out a number of predefined leaders whom they expected to be well-connected within the village (e.g., teachers, leaders of self-help groups, and shopkeepers). BSS first held a private meeting with leaders that were amenable to it, and credit officers explained the program and asked the leaders to help organize a meeting to present information about microfinance to the village. These leaders play an important part in our identification strategy, as they function as injection points for microfinance in the village. We used the full set of predesignated leaders, as opposed to the subset of leaders who actually worked with BSS in each village (both because this is endogenous—whether or not a leader worked with BSS could correlate with omitted variables that may bias estimation—and because we did not always have this information).

Model and Structural Estimation

Our simple model of diffusion on a network is depicted in Fig. 1. We model the diffusion of participation as a process on the household-level network, with participation decisions being made at the household level. As such, a node represents a household (which is the appropriate unit for microfinance). The model can be summarized as follows:

1) An initial set of households is informed (injection points).

2) The initial households decide whether to participate.

3) In each subsequent period, households that have been informed in previous periods pass information to each of their neighbors, independently, with probability q^P if they are participants and with probability q^N if they are not.

4) Newly informed households then decide whether to participate. This decision may depend on a newly informed household's characteristics and potentially on the previous participation choices of their neighbors who told that household about microfinance (*7*). Previously informed households do not have a second chance to decide.

5) The process stops after T periods of information passing.

If $q^N = 0$, so that only participating households pass information, and $T = \infty$, then this is a variant of the standard Susceptible, Infectious, Recovered (SIR) model (*8*, *9*). By allowing it to operate only for T periods, we study what happens in finite time (because after enough rounds, everyone would be informed). Both the finite horizon and the fact that nonparticipants can pass information are important realistic features in most applications.

To capture endorsement effects, let p_{it} denote the probability that an individual who was just

Table 1. Parameter estimates of the structural model. q^N represents the probability that a household that is informed about microfinance but has decided not to participate transmits information to a neighbor in a given period, and q^P represents the probability that a household that is informed and has decided to participate transmits information to a neighbor in a given period. λ is the coefficient in Eq. 1 on the fraction of neighbors that informed a household about microfinance who themselves decided to participate. We use village-level Bayesian bootstrap estimates of the model parameters with 1000 draws to compute the standard errors of the parameter estimates (in parentheses).

	q^N	q^P	λ	$q^N - q^P$
Information model	0.050 (0.01)	0.350 (0.124)	—	−0.300 (0.126)
Information model with endorsement	0.050 (0.007)	0.500 (0.234)	−0.200 (0.146)	−0.450 (0.234)

informed about microfinance decides to participate, where p_{it} is a function of the individual's characteristics X_i [which can account for homophily based on observables (10, 11)] and peer decisions. We model it as a logistic function:

$$\log\left(\frac{p_{it}}{1-p_{it}}\right) = X_i'\beta + \lambda F_{it} \qquad (1)$$

where F_{it} is a fraction whose denominator is the number of i's neighbors who informed i about the program and whose numerator is the number of these individuals who participate in microfinance, λ represents the change in the log-odds ratio of household i participating because of a change in the fraction of neighbors who informed i that chose to participate, and β represents a vector of coefficients that describe how the log-odds ratio of participation changes as characteristics X_i change. (In table S4, we also experiment with different weights on different neighbors based on their centrality in the network.)

In what follows, the information model constrains λ to be equal to zero, whereas the information model with endorsement effects estimates λ.

Estimation

The model was estimated using the method of simulated moments (MSM) (12, 13). Specifically, we chose parameters to minimize an objective function that is a quadratic form of the distance between moments observed in the data and the same moments as predicted by the model for a specific combination of parameters. We selected parameters so that the following moments predicted by the model best matched the actual moments in the villages:

1) The share of leaders who participate in microfinance.

2) The share of households with no participating neighbors that participate.

3) The share of households in the neighborhood of a participating leader that participate.

4) The share of households in the neighborhood of a nonparticipating leader that participate.

5) The covariance of household participation with the share of its neighbors that participate.

6) The covariance of household participation with the share of its second-degree neighbors that participate.

Model estimation proceeds in three steps. First, we estimate β via logistic regression using the participation decisions among the set of leaders (who are assumed to be informed of the program). X consists of a rich set of covariates including quality of access to electricity, quality of latrines, number of beds, number of rooms, the number of beds per capita, and the number of rooms per capita. These covariates vary substantially across the nearly 1140 leaders throughout the 43 villages, and so the parameters are tightly estimated.

Second, to estimate q^N, q^P, and λ (or any subset of these in the restricted models), we proceed as follows. The parameter space Θ is discretized (henceforth we use Θ to denote the discretized parameter space) and we search over the entire set of possible parameters. For each possible choice of $\theta \in \Theta$, we simulate the model 75 times, each time allowing as many rounds of communications in the diffusion process as the number of trimesters that a given village was exposed to microfinance (typically 5 to 8). For each simulation, moments 2 to 6 are calculated. Next, we take the average over the 75 runs. This gives us the vector of average simulated moments, which we denote $m_{\text{sim},r}$ for village r. We let $m_{\text{emp},r}$ denote the vector of empirical moments for village r. Finally, we choose the set of parameters that minimizes the criterion function, namely

$$\hat{\theta} = \arg\min_{\theta\in\Theta}\left[\frac{1}{R}\sum_{r=1}^{R} m_{\text{sim},r}(\theta) - m_{\text{emp},r}\right]' \times \hat{W}\left[\frac{1}{R}\sum_{r=1}^{R} m_{\text{sim},r}(\theta) - m_{\text{emp},r}\right] \qquad (2)$$

where $\hat{W}$ is a weighting matrix obtained by first using this estimation with an identity matrix weight, obtaining a first-stage estimate $\tilde{\theta}$, and then estimating the optimal weighting matrix making use of $\tilde{\theta}$.

Third, to estimate the distribution of $\hat{\theta}$, we use a simple Bayesian block-bootstrap algorithm. The bootstrap takes into account the fact that decisions are interrelated across household within villages but assumes independence of networks across villages (because villages are far apart). This method allows us to estimate standard errors in a computationally simple manner for an MSM model that requires numerous runs of a complicated diffusion process (14). The estimation procedure and bootstrap are explained in detail in the supplementary material.

Identification of the Diffusion Model

The first set of moments combined with the injection points allow us to identify the parameters of the model. The intuition behind the identification of endorsement effects and differential information effects in our application can be clarified by a simple two-by-two example. Imagine, for example, that $q^N = 0.05$ and $q^P = 0.35$ (these are the estimated parameters that we report in Table 1). Also assume for sake of discussion that an informed individual with no participating friend joins with probability 0.22, whereas an informed individual with all participating friends joins with probability 0.32 (corresponding to λ = 0.5).

Consider four individuals: One of them has one friend who is a leader, and this leader takes up microfinance; the second one has one friend who is a leader but does not participate in microfinance; the third has four friends who are leaders, and all participate in microfinance; the fourth has four friends who are leaders, and none of them participate in microfinance. On average, if the model runs for seven periods (the average number of periods we observe in a village), the probability that the first person is informed is $0.95 = 1 - (0.65)^7$. Similarly, the probability that the second person is informed is 0.3. The probability that the third person is informed is essentially 1, and the probability that the fourth person is informed is 0.76. Although the difference in the fraction of informing friends who take up microfinance, which is the source of the endorsement effect, is exactly the same for person 1 versus person 2 as it is for person 3 versus person 4 (it is 1 in both cases), the difference in participation between persons 1 and 2 (0.24) is much larger than the difference in participation between persons 3 and 4 (0.15). This difference captures the pure information effect.

To see the pure endorsement effect, let one of the four leaders who are friends with person 4 participate. The probability that person 3 and person 4 are informed is now more or less the same (about 1) and therefore, in a pure–information effect world, they would behave identically. However, if there is an endorsement effect, these two will behave quite differently. Under the parameter assumptions above, person 3, who has a

higher fraction of informing friends who participate, is more likely to participate (0.32 versus 0.24 for person 4).

The fact that these parameters are formally identified in the context of our model does not mean that they could not be spurious. As often in network-based studies, causal interpretation of the correlation between the decisions of connected people as the result of information transmission or endorsement (which is partly what we use to identify the model) is potentially questionable. This is, of course, the standard identification problem with observational data on networks.

First, imagine that the data are generated by a model wherein all households know about microfinance but differ on preferences. The probability of participating is modeled as a logistic probability model,

$$\log\left(\frac{p_i}{1-p_i}\right) = X_i'\beta + \nu_i \qquad (3)$$

where ν_i is a preference shock that can be correlated with ν_j, where, for instance, i and j are neighbors in the graph. In such a model, one may worry that the correlations in preference generate cross-sectional participation patterns that look like diffusion. It is possible that, for example, households with neighbors who participate are themselves more likely to need microfinance (in ways that we cannot pick up with our demographic information) because, for example, neighbors may share a common activity or may have common access to finance. In that case, the interpretation of our parameters as capturing the effect of j's decision on i's choice would be inappropriate.

In this alternative model, however, the diffusion of microfinance would not follow specific time patterns of participation based on network distances from first-informed individuals, whereas our model makes specific predictions about the pattern of diffusion over time. A test of the model is thus whether the empirical time series of adoption matches a corresponding simulation of the model, given the set of parameters we estimate.

Second, even if our model were correct, the presence of unobserved correlated effects influencing participation could bias our estimate of endorsement effects. Consider what would happen if we modify Eq. 1 by including a shock term, ν_i:

$$\log\left(\frac{p_{it}}{1-p_{it}}\right) = X_i'\beta + \lambda F_{it} + \nu_i \qquad (4)$$

Again ν_i is a time-invariant term, unobserved to the econometrician, that may be correlated across network neighbors. In this case, diffusion over time in the data may look similar to what the model would predict, but our cross-sectional identification in the presence of positively correlated shocks could lead us to estimate a spurious positive λ.

Parameter Estimates

Table 1 presents the result of the estimation. The first row presents the parameters of the information model without any endorsement effects: $q^N = 0.050$ and $q^P = 0.350$. Both of these values are significantly different from zero ($P < 0.01$, t test). In addition, we are able to reject equality of the two parameters ($P < 0.01$, t test).

These results highlight the role of nonparticipants in the diffusion process. Even though they pass information at a much lower rate than participants, there are many more nonparticipants in a village than participants, and thus they end up playing an important role. In fact, our estimates indicate that information passing by nonparticipants is responsible for nearly one-third of overall informedness and participation. We calculate this figure by simulating information spread in the model, constraining q^N to be equal to 0 (and setting q^P at what we estimate). The eventual participation would then drop from 20.0% to 13.97%.

The second row of Table 1 presents estimates of the model in which endorsement is included and the villagers potentially pay attention to the participation decisions of their informed neighbors. There is no significant evidence for a positive endorsement effect: Once a household is informed, its decision to participate in microfinance is not significantly affected by whether its neighbors chose to participate themselves. If anything, the point estimate of the endorsement effect is generally negative, and in the supplementary materials we show that depending on the weighting of the friends, it is sometimes (marginally) significantly negative (table S4).

The finding that we cannot reject that $\lambda = 0$ in most specifications, and can reject that it is positive, provides some reassurance that the estimates are not driven by unobserved correlated heterogeneity between neighbors; in that case, we would find a positive λ.

Robustness and Model Validation

There are two main identification concerns: First, we have treated leaders symmetrically with everyone else, but they may be different in ways that are not entirely captured by the impact of observed characteristics on participation. For example, they may be more likely than anyone else to inform their friends about microfinance (e.g., they may have brought some of them with them to the initial meeting) but no more likely to participate themselves. In this case, we would observe a high participation among friends of people who are informed but do not participate themselves, which would drive q^N up, even if no one except the leaders does that.

To address this issue, we estimated three nested variations of the model (table S6). First, we removed moments 3 and 4, which explicitly rely on participation decisions within a leader's neighborhood for identification (table S6, case 1). Second, in addition to removing moments 3 and 4, we excluded observations for which the node in question is a leader when constructing moments 2, 5, and 6 (table S6, case 2). Third, we modified case 2 by also excluding leaders from the neighborhoods of other nodes in the computation of moments 2, 5, and 6 (table S6, case 3). In each case, the parameter estimates were not statistically different from those in our baseline specification and the point estimates were stable.

The second concern is the possibility of correlated shocks we discussed above. As already mentioned, one way to address this issue is to use the estimated parameters to predict the time series of how microfinance participation spreads by village. The time structure of diffusion was not used in the estimation of the parameters; we used correlations between neighbors' ultimate decisions. Thus, checking the time series of participation under the model and seeing whether it matches the data provides a way to validate the model. In particular, if the appearance of diffusion is caused by neighbors having correlated needs but these needs do not exhibit a diffusion pattern over time, then there is no reason why the model would match the data.

In this validation exercise, we focus on what happens after the first trimester has elapsed. This is because in our model a period is simply a round of communication and may not correspond to a fixed period of time. In the villages, more adoption and more rounds of communication occur in the first trimester, when microfinance is new. In other words, there are more "periods" within the first trimester. Moreover, some people may be informed in the first trimester for reasons that have nothing to do with the model—for example, because they happen to have found themselves at the first BSS meeting.

What is the equivalent of the end of the first trimester within our model? We estimate it as the number of model periods required for simulated participation in the model to reach the actual level of participation achieved in that village at the end of the first trimester. For example, in village 1, the actual participation at the end of the first trimester was 13%. In the simulation for that same village, period 1 participation is 9% < 13%, and period 2 participation is 15% > 13%. In this case, we assume that the first trimester is equivalent to two model periods for that village. (In 11 villages, the simulated participation never reached the observed participation at the beginning of period 1, so we could not perform the exercise and thus dropped them from the analysis).

We then ran a regression of the observed microfinance participation rate on the simulated participation rate, using fixed effects for both village and time period (Table 2). Fixed effects for time period are important here to avoid a spurious correlation generated by regressing two monotonically increasing processes (and ones

Table 2. Time series validation. Values shown are coefficients from ordinary least-squares regressions. Each column represents a different regression. The dependent variable is the empirical participation rate in a village in a given period, from trimester 1 to the final trimester corresponding to December 2010. The main independent variable, simulated participation rate, is the mean participation rate in a village in a period (where period 1 corresponds to the empirical period 1 participation rate) across 1000 simulations of the diffusion model. All regressions include fixed effects for village and time period. The demographic controls include number of households, savings, self-help group participation, caste composition, and fraction of households that are leaders, each interacted with time. Standard errors (in parentheses) are clustered at the village level.

	Without demographic controls	With demographic controls
Simulated participation rate	0.921 (0.612)	0.652 (0.261)
Observations	125	125

Table 3. Microfinance participation versus centralities of leaders. Values shown are coefficients from ordinary least-squares regressions. Each column represents a different regression. The dependent variable is the microfinance participation rate of nonleader households in a village. The covariates are various measures of centrality—averaged over the set of leaders—as well as control variables. The controls include number of households, savings, self-help group participation, caste composition, and fraction of households that are leaders. Standard errors (in parentheses) are robust to heteroskedasticity.

Centrality measure	Regression			
	1	2	3	4
Communication	0.766 (0.335)		0.713 (0.428)	
Diffusion		0.022 (0.007)		0.018 (0.009)
Degree			–0.005 (0.006)	–0.003 (0.006)
Eigenvector			3.572 (2.330)	3.692 (2.265)
Betweenness			1.709 (1.776)	1.710 (1.687)
Katz-Bonacich			–0.072 (0.070)	–0.106 (0.063)
Decay			0.032 (0.047)	0.034 (0.045)
Closeness			–1.077 (1.551)	–0.891 (1.496)
R^2	0.406	0.442	0.530	0.515

that both taper off after a few periods) on each other. Similarly, unobserved village-level heterogeneity may generate spurious correlations, which we want to eliminate as well.

Table 2 presents this regression without and with demographic controls. The point estimates suggest strong correlation between incremental changes in the simulated microfinance participation rate and empirical participation rate, even when accounting for the time effects and village fixed effects. Without demographic controls, the coefficient does not have statistical significance at conventional levels under a two-sided test ($P = 0.142$, t test), whereas with demographic controls the estimate is statistically significant ($P = 0.018$, t test). To ensure conservative inference given the likelihood of temporally correlated errors in the regression model, we cluster our standard errors at the village level. This close correspondence between the time series as predicted by the model (after period 1) and the time series we observe in the data suggests that time-invariant omitted variables and homophily are not driving the results.

Application: The Impact of Injection Points

Suppose a microfinance organization like BSS relies on word-of-mouth diffusion to spread information about the availability of microfinance. How will the eventual participation in microfinance depend on whom they approach first?

To analyze this question, we compute for each leader (our injection points) a score. This score is the fraction of households who would eventually participate if this household were the only one initially informed. To compute this fraction, we simulate the model with information passing and participation decisions being governed by the estimated values of q^N, q^P, and β. We call this score the communication centrality of a node.

In our data, because BSS relies on a fixed rule for choosing leaders, there is considerable variation across villages in the average communication centrality of the set of leaders in a village (which is 0.001 at the 10th percentile and 0.13 at the 90th percentile). This is true for other measures of centrality as well. Moreover, this variation does not come from any information BSS has about the village, and hence is likely to be independent of village characteristics. The identification assumption is that the centrality of the leaders is not correlated with the demand for microcredit, including control variables, and it does not seem to be problematic. In table S2, we regress the various measures of leader centralities on the village characteristics used in Table 3, and we find little relationship between the network positions of the leaders and the characteristics of the villages.

Figure 2 exhibits plots of village-level participation in microfinance as a function of communication centrality and degree centrality (for comparison). The communication centrality of the leaders is strongly and significantly correlated with eventual village-level participation, and the correlation is stronger than for degree.

Table 3 shows the results of a series of four regressions of village-level adoption on various measures of average centrality of leaders, after including village-level controls for savings behavior, self-help group participation, caste composition, and fraction of households with BSS-designated leaders (*15*). The first regression shows that communication centrality is strongly correlated with eventual take-up. The third regression shows that this remains true after controlling for a hosts of other measures of centrality, none of which are significant in this specification.

An Approximation of Communication Centrality: Diffusion Centrality

Communication centrality of the injection points is strong predictor of eventual participation in microfinance and should therefore provide guidance to anyone trying to spread the news about microfinance in similar villages. However, it cannot be computed without those estimates, which could be very different if we were interested in the diffusion of other products or even microfinance in a very different context (say, a city). Thus, we propose an approximation of communication centrality—diffusion centrality—that is highly correlated with communication centrality, at least in this setting, but requires considerably less data. In particular, it does not rely on estimating the diffusion model.

We start from our model with $q^N = q^P = q$. Although we have shown that q^N and q^P differ in the data, this can be useful as an approximation in settings where the full model may be difficult to

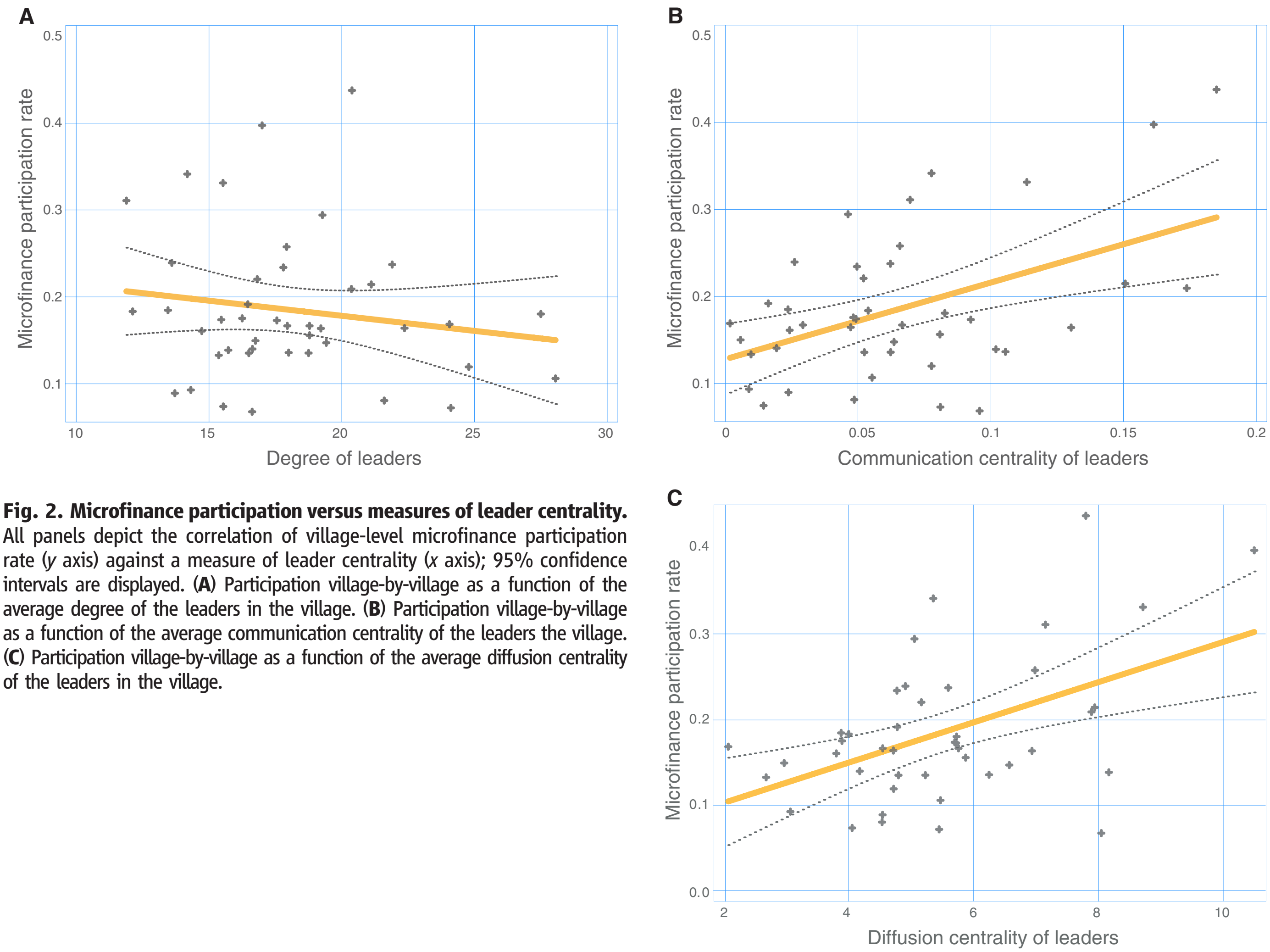

Fig. 2. Microfinance participation versus measures of leader centrality. All panels depict the correlation of village-level microfinance participation rate (*y* axis) against a measure of leader centrality (*x* axis); 95% confidence intervals are displayed. **(A)** Participation village-by-village as a function of the average degree of the leaders in the village. **(B)** Participation village-by-village as a function of the average communication centrality of the leaders the village. **(C)** Participation village-by-village as a function of the average diffusion centrality of the leaders in the village.

estimate. This suggests a simple measure of the centrality or potential influence of each node. We define the diffusion centrality of a node i in a network with an adjacency matrix $\mathbf{g}$, passing probability q, and iterations T, as the ith entry of the vector

$$DC(\mathbf{g}; q, T) := \left[\sum_{t=1}^{T} (q\mathbf{g})^t\right] \cdot 1 \qquad (5)$$

Consider T iterations of information passing from a single initially informed node i where at each iteration every informed node tells each neighbor with probability q. The diffusion centrality of node i then corresponds to the expected total number of times that all nodes taken together hear about the opportunity. If $T = 1$, diffusion centrality is proportional to degree centrality. As $T \to \infty$ it becomes proportional to either Katz-Bonacich centrality or eigenvector centrality, depending on whether q is smaller than the inverse of the first eigenvalue of the adjacency matrix or exceeds it, respectively (*16*). In the intermediate region of T, the measure differs from existing measures.

Any method of computing a measure of diffusion centrality that does not rely on the estimation of the model requires the choice of an appropriate value for q. Extreme values of q lead either to no diffusion or to complete diffusion, and so do not distinguish nodes. We choose a prominent intermediate value of q: the inverse of the first eigenvalue of the adjacency matrix, $\lambda_1(\mathbf{g})$. This is the critical value of q for which the entries of $(q\mathbf{g})^T$ tend to 0 as T grows if $q < 1/\lambda_1$ and some entries diverge if $q > 1/\lambda_1$.

In essence, diffusion centrality uses our model as a starting point but assumes that everyone spreads information with the same probability q, which is selected such that information spreads at a rate that neither saturates too quickly nor dies out. For each village, we set T to the number of trimesters during which the village was exposed to BSS (6.6 on average). The choice of q and T can be important. However, in our data, diffusion centrality is not very sensitive to the choice of q and T within a reasonable range. In table S7 we compute it for other values of q in the neighborhood of $1/\lambda_1$ and a range of values of T. The identity of the most diffusive leader is robust to these changes. Diffusion centrality is strongly correlated with communication centrality; the correlation is 0.86. Consequently, the average diffusion centrality of the leaders performs equally well in predicting eventual participation (Fig. 2C). This is true even when accounting for demographic control variables (Table 3, column 2) and other standard centrality measures (degree centrality, eigenvector centrality, Katz-Bonacich centrality, betweenness centrality, decay centrality, or closeness centrality). This is robust to choosing values of q and T within a range of 25% around their assumed value here.

These findings highlight the importance of injection points: The correlation with eventual village-level participation (Fig. 2C) implies that an increase in the diffusion centrality of leaders from the 10th percentile to the 90th percentile would lead to an increase in eventual participation in microfinance by 10.7 percentage points.

Conclusion

We estimate a model of diffusion that allows both for information and endorsement effects. In this context, we find no evidence of strong endorsement effects: The role of neighbors in the diffusion

process is to pass information, and even those who are not taking up the program themselves play a role in this process, although their probability to pass information is lower than that of those who adopt the product. This model of pure information diffusion motivates a new centrality measure for measuring the effectiveness of alternative injection points that differs from standard centrality measures and, in our sample, performs better than them. This has important implications for policy makers and firms that are trying to pick the right people to inform in order to ensure that a new idea or product or piece of information reaches the maximum number of people in the network.

The results suggest a number of directions for future work: first, to test how well this new centrality measure does in predicting diffusion patterns when we purposefully vary the centrality of the injection point; second, to understand to what extent it is possible to improve on the theory of information passing and learning used here by introducing more sophisticated approaches to learning and strategic motives for information sharing, and what that implies for choosing the right centrality measures; and third, to use the theoretical insights that come out of that work to understand where, and in what ways, endorsement effects may be important and how best to model them.

References and Notes

1. M. Kitsak *et al.*, Identification of influential spreaders in complex networks. *Nat. Phys.* **6**, 888–893 (2010). doi: 10.1038/nphys1746
2. C. Ballester, A. Calv'o-Armengol, Y. Zenou, Who's who in networks. Wanted: The key player. *Econometrica* **74**, 1403–1417 (2006). doi: 10.1111/j.1468-0262.2006.00709.x
3. There is an old and large literature that studies information diffusion (*17*–*25*). However, empirical evidence on the role of injection points is still sparse.
4. For experimental approaches to controlling for and analyzing the role of homophily in diffusion, see (*26*, *27*).
5. Individuals were allowed to name as many as five to eight network neighbors, depending on the category. The data exhibit almost no top-coding; fewer than 10% of the respondents named the maximum number of individuals in any single category.
6. The main difference is the number of households: Villages that BSS entered had 223.2 households on average (SD = 56.17); those it did not enter had 165.8 households on average (SD = 48.95).
7. One could imagine that households need some time to think, or to process information from their neighbors, before adoption (*21*, *28*). However, in our setting, one period (4 months) encompasses much of this decision time. It may be that in the long run (over a period of years) they would reconsider their decisions, which our model does not address, and so we do not capture long-run reactions to neighbors' experiences. For instance, it could be that there are coordination problems as people wait for others to participate before participating themselves. This seems unrealistic in our context: It takes about 1 to 2 years to learn how neighbors did with microfinance (whether they managed to repay, whether they benefited, etc.). Our data show that most of the adoption of microfinance takes place within the first year in a village (before the first cycle of loans is complete).
8. W. Kermack, A. McKendrick, A contribution to the mathematical theory of epidemics. *Proc. R. Soc. London Ser. A* **115**, 700–721 (1927). doi: 10.1098/rspa.1927.0118
9. N. Bailey, *The Mathematical Theory of Infectious Diseases and Its Applications* (Griffin, London, 1975).
10. S. Aral, Social science: Poked to vote. *Nature* **489**, 212–214 (2012). doi: 10.1038/489212a; pmid: 22972291
11. S. Aral, L. Muchnik, A. Sundararajan, Distinguishing influence-based contagion from homophily-driven diffusion in dynamic networks. *Proc. Natl. Acad. Sci. U.S.A.* **106**, 21544–21549 (2009). doi: 10.1073/pnas.0908800106; pmid: 20007780
12. D. McFadden, A method of simulated moments for estimation of discrete response models without numerical integration. *Econometrica* **57**, 995–1026 (1989). doi: 10.2307/1913621
13. For an example of a method of simulated moments approach used in a spatial setting, see (*29*).
14. For example, 1000 runs of a simulated annealing search would be prohibitively slow.
15. The results are essentially identical without controls.
16. For background on centrality definitions, see (*30*).
17. B. Ryan, N. C. Gross, The diffusion of hybrid seed corn in two Iowa communities. *Rural Sociol.* **8**, 15 (1943).
18. P. Lazarsfeld, B. Berelson, G. Gaudet, *The People's Choice: How the Voter Makes Up His Mind in a Presidential Campaign* (Duell, Sloan and Pearce, New York, 1944).
19. E. Katz, P. Lazarsfeld, *Personal Influence: The Part Played by People in the Flow of Mass Communication* (Free Press, New York, 1955).
20. J. Coleman, E. Katz, H. Menzel, *Medical Innovation: A Diffusion Study* (Bobbs-Merrill, Indianapolis, IN, 1966).
21. A. Foster, M. Rosenzweig, Learning by doing and learning from others: Human capital and technical change in agriculture. *J. Polit. Econ.* **103**, 1176–1209 (1995). doi: 10.1086/601447
22. T. Conley, C. Udry, Learning about a new technology: Pineapple in Ghana. *Am. Econ. Rev.* **100**, 35–69 (2010). doi: 10.1257/aer.100.1.35
23. M. Kremer, E. Miguel, The illusion of sustainability. *Q. J. Econ.* **122**, 1007–1065 (2007). doi: 10.1162/qjec.122.3.1007
24. M. O. Jackson, L. Yariv, in *Handbook of Social Economics*, J. Benhabib, A. Bisin, M. Jackson, Eds. (North Holland, Amsterdam, 2010).
25. R. M. Bond *et al.*, A 61-million-person experiment in social influence and political mobilization. *Nature* **489**, 295–298 (2012). doi: 10.1038/nature11421; pmid: 22972300
26. D. Centola, The spread of behavior in an online social network experiment. *Science* **329**, 1194–1197 (2010). doi: 10.1126/science.1185231; pmid: 20813952
27. S. Aral, D. Walker, Identifying influential and susceptible members of social networks. *Science* **337**, 337–341 (2012). doi: 10.1126/science.1215842; pmid: 22722253
28. B. Jovanovic, Y. Nyarko, Learning by doing and the choice of technology. *Econometrica* **64**, 1299 (1996). doi: 10.2307/2171832
29. G. Topa, Social interactions, local spillovers and unemployment. *Rev. Econ. Stud.* **68**, 261–295 (2001). doi: 10.1111/1467-937X.00169
30. M. O. Jackson, *Social and Economic Networks* (Princeton Univ. Press, Princeton, NJ, 2008).

Acknowledgments: Supported by the NSF Graduate Research Fellowship Program (A.G.C.), NSF grants SES-0647867, SES-0752735, SES-0961481, and SES-1156182, AFOSR and DARPA grant FA9550-12-1-0411, and ARO MURI award W911NF-12-1-0509. D. Acemoglu and various seminar participants provided helpful comments and suggestions. We also thank B. Feigenberg, R. Lewis, B. Plummer, G. Nagaraj, M. Shaukat, J. Guo, T. Rodriguez-Barraquer, A. Sacarny, and X. Tan. The Centre for Microfinance at the Institute for Financial Management and Research and BSS provided valuable assistance. The data and code used in this paper are archived at the Abdul Latif Jameel Poverty Action Lab Dataverse at the Harvard Institute for Quantitative Social Science, http://hdl.handle.net/1902.1/21538.

Supplementary Materials

www.sciencemag.org/content/341/6144/1236498/suppl/DC1
Materials and Methods
Supplementary Text
Tables S1 to S7
Reference (*31*)

13 February 2013; accepted 27 June 2013
10.1126/science.1236498

mTORC1 Phosphorylation Sites Encode Their Sensitivity to Starvation and Rapamycin

Seong A. Kang, Michael E. Pacold, Christopher L. Cervantes, Daniel Lim, Hua Jane Lou, Kathleen Ottina, Nathanael S. Gray, Benjamin E. Turk, Michael B. Yaffe, David M. Sabatini*

READ THE FULL ARTICLE ONLINE
http://dx.doi.org/10.1126/science.1236566

Cite this article as S. A. Kang *et al.*, *Science* **341**, 1236566 (2013).
DOI: 10.1126/science.1236566

Introduction: The mechanistic target of rapamycin (mTOR) complex 1 (mTORC1) protein kinase promotes cell growth by controlling major anabolic and catabolic processes in response to a variety of environmental and intracellular stimuli and is deregulated in aging and human diseases such as cancer and diabetes. Rapamycin, an allosteric inhibitor of mTORC1, is used clinically in organ transplantation and the treatment of certain cancers. Exactly how rapamycin perturbs mTORC1 signaling is poorly understood, and it remains unknown why certain mTORC1 phosphorylation sites are sensitive to the drug, whereas others are not. Here, we test the hypothesis that the inherent capacity of a phosphorylation site to serve as an mTORC1 substrate (a property we call substrate quality) is a key determinant of its sensitivity to rapamycin as well as nutrient and growth factor starvation.

Methods: We measured the in vitro kinase activity of mTORC1 towards short synthetic peptides encompassing single mTORC1 phosphorylation sites and refined the established mTORC1 phosphorylation motif. We introduced subtle mutations into bona fide mTORC1 phosphorylation sites that we found to enhance or reduce their phosphorylation by mTORC1 in vitro and monitored the corresponding changes in the sensitivity of these sites to rapamycin treatment within cells. Finally, we assessed whether the modifications of the mTORC1 phosphorylation sites also altered their sensitivities to nutrient and growth factor starvation.

Results: The response of an mTORC1 phosphorylation site to rapamycin treatment should depend on the balance between the activity of mTORC1 and of the protein phosphatase(s) that dephosphorylates it. We found that the in vitro kinase activity of mTORC1 toward peptides containing established phosphorylation sites strongly correlates with the resistance of the sites to rapamycin within cells. Moreover, the relative affinities of the mTOR kinase domain for the peptides also correlated with its capacity to phosphorylate them. In addition to a preference for either proline or a nonproline hydrophobic residue in the +1 position, our refinement of the mTORC1 phosphorylation motif revealed preferences for noncharged residues surrounding the phosphoacceptor site and for serine over threonine as the phosphoacceptor. Utilizing this improved understanding of the sequence motif specificity of mTORC1, we were able to manipulate mTORC1 activity toward its phosphorylation sites in vitro and alter their sensitivities to rapamycin treatment within cells. mTORC1 phosphorylation sites also varied in their sensitivities to nutrient and growth factor levels and manipulations in substrate quality were sufficient to alter their responses to nutrient and growth factor starvation.

Discussion: Our findings suggest that the sequence composition of an mTORC1 phosphorylation site, including the presence of serine or threonine as the phosphoacceptor, is one of the key determinants of whether the site is a good or poor mTORC1 substrate within cells. Even though the phosphorylation of mTORC1 sites is subject to varied regulatory mechanisms, differences in substrate quality are one mechanism for allowing downstream effectors of mTORC1 to respond differentially to temporal and intensity changes in the levels of nutrients and growth factors or pharmacological inhibitors such as rapamycin. Such differential responses are likely important for mTORC1 to coordinate and appropriately time the myriad processes that make up the vast starvation program it controls. It is likely that the form of hierarchical regulation we describe for mTORC1 substrates also exists in other kinase-driven signaling pathways.

FIGURES IN THE FULL ARTICLE

SUPPLEMENTARY MATERIALS

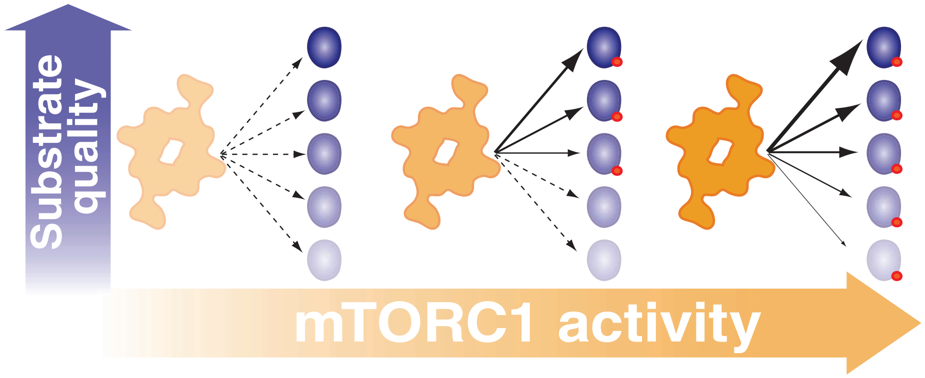

mTORC1 Phosphorylation sites encode their sensitivity to physiological and pharmacological modulators of mTORC1. Substrate quality is an important determinant of how effectively mTORC1 phosphorylates its substrates in the response to both pharmacological and natural regulators of the kinase.

The list of author affiliations is available in the full article online.
*Corresponding author. E-mail: sabatini@wi.mit.edu

mTORC1 Phosphorylation Sites Encode Their Sensitivity to Starvation and Rapamycin

Seong A. Kang,[1,2] Michael E. Pacold,[1,2,3,4] Christopher L. Cervantes,[1,2] Daniel Lim,[5] Hua Jane Lou,[6] Kathleen Ottina,[1,2] Nathanael S. Gray,[3,7] Benjamin E. Turk,[6] Michael B. Yaffe,[2,5,8] David M. Sabatini[1,2,5]*

The mechanistic target of rapamycin (mTOR) complex 1 (mTORC1) protein kinase promotes growth and is the target of rapamycin, a clinically useful drug that also prolongs life span in model organisms. A persistent mystery is why the phosphorylation of many bona fide mTORC1 substrates is resistant to rapamycin. We find that the in vitro kinase activity of mTORC1 toward peptides encompassing established phosphorylation sites varies widely and correlates strongly with the resistance of the sites to rapamycin, as well as to nutrient and growth factor starvation within cells. Slight modifications of the sites were sufficient to alter mTORC1 activity toward them in vitro and to cause concomitant changes within cells in their sensitivity to rapamycin and starvation. Thus, the intrinsic capacity of a phosphorylation site to serve as an mTORC1 substrate, a property we call substrate quality, is a major determinant of its sensitivity to modulators of the pathway. Our results reveal a mechanism through which mTORC1 effectors can respond differentially to the same signals.

The mechanistic target of rapamycin (mTOR) is a serine-threonine kinase that serves as the catalytic subunit of two distinct signaling complexes, mTORC1 and mTORC2 [reviewed in (*1*)]. Both are central regulators of cell growth, and mTORC1 controls key anabolic and catabolic processes in response to diverse cues, including nutrients, energy, and growth factors. mTORC1 is commonly deregulated in human diseases, including cancer, and therefore, there are many efforts to develop drugs that inhibit its kinase activity [reviewed in (*2*, *3*)]. The best known such drug is rapamycin, which in a complex with the 12-kD FK506-binding protein (FKBP12), binds near the mTOR kinase domain (*4*–*7*) and partially inhibits its activity (*8*–*11*). Rapamycin has drawn considerable attention in the last few years not only because of its accepted clinical uses in cancer treatment and organ transplantation (*1*), but also for its capacity to prolong life span in multiple model organisms (*12*–*17*). This has led to great interest in fully understanding the mTORC1 pathway and exactly how rapamycin affects it.

[1]Whitehead Institute for Biomedical Research, Nine Cambridge Center, Cambridge, MA 02142, USA. [2]Department of Biology, Massachusetts Institute of Technology (MIT), 77 Massachusetts Avenue, Cambridge, MA 02139, USA. [3]Department of Cancer Biology, Dana-Farber Cancer Institute, 450 Brookline Avenue, Boston, MA 02115, USA. [4]Department of Radiation Oncology, Dana-Farber Cancer Institute, 450 Brookline Avenue, Boston, MA 02215, USA. [5]David H. Koch Center for Integrative Cancer Research at MIT, 77 Massachusetts Avenue, Cambridge, MA 02139, USA. [6]Department of Pharmacology, Yale University School of Medicine, 333 Cedar Street, New Haven, CT 06520, USA. [7]Department of Biological Chemistry and Molecular Pharmacology, Harvard Medical School, 240 Longwood Avenue, Boston, MA 02115, USA. [8]Department of Surgery, Beth Israel Deaconess Hospital, Harvard Medical School, 330 Brookline Avenue, Boston, MA 02215, USA.

*Corresponding author. E-mail: sabatini@wi.mit.edu

Results and Discussion

Differential Sensitivity of mTORC1 Phosphorylation Sites to Rapamycin

The effects of rapamycin on mTORC1 are less straightforward than initially realized (*18*–*20*). The phosphorylation of several sites that are bona fide mTORC1 substrates—including on the key translational regulator, eukaryotic translation initiation factor 4E binding protein 1 (4E-BP1)—is largely resistant to rapamycin treatment, which may explain the unexpectedly weak efficacy of the drug in several early cancer clinical trials [reviewed in (*21*)]. The differential effects of rapamycin contrast with those of adenosine triphosphate (ATP)–competitive mTORC1 inhibitors, which block the phosphorylation of all mTORC1 phosphorylation sites regardless of their rapamycin sensitivity (*18*, *19*, *22*–*24*). To investigate why rapamycin differentially inhibits mTORC1 sites, we initially confirmed that this is the case under our experimental conditions in human embryonic kidney 293E (HEK-293E) and murine embryonic fibroblast (MEF) cells. Indeed, although Torin1, a specific ATP-competitive inhibitor of mTOR (*18*, *25*), eliminated the phosphorylation of several well-established mTORC1 sites, rapamycin affected that of only a subset of sites (Fig. 1, A and B, and fig. S1).

In Vitro Activity of mTORC1 Toward Substrate Phosphorylation Sites Predicts Their Rapamycin Sensitivity

The extent of phosphorylation of an mTORC1 site within cells should reflect a balance between the activity of mTORC1 and of the phosphatases that dephosphorylate the site. Therefore, it is theoretically possible that certain rapamycin-resistant mTORC1 phosphorylation sites are poorly dephosphorylated so that even the reduced activity of rapamycin-bound mTORC1 is sufficient to keep them phosphorylated. Such a model predicts that rapamycin-sensitive and -resistant sites would have very different rates of dephosphorylation. To test this hypothesis, we treated cells with a dose of Torin1 that completely inhibits mTORC1 (*18*) and monitored the phosphorylation state of several sites over time. The results were remarkably clear: With almost identical kinetics, Torin1 caused the rapid dephosphorylation of all the sites, irrespective of their rapamycin sensitivity (Fig. 1, C and D). Thus, distinct rates of dephosphorylation cannot explain the differential sensitivity of mTORC1 sites to rapamycin.

We considered the alternative possibility that it is the level of mTORC1 activity toward a particular site that determines whether it is sensitive or resistant to rapamycin within cells. Certain mTORC1 phosphorylation sites might be rapamycin-resistant because they are very good substrates for mTORC1, so that even the reduced activity of rapamycin-bound mTORC1 would be sufficient to keep them phosphorylated. Relevant to this model, several mTORC1 substrates (e.g., 4E-BP1 and Grb10) have both rapamycin-sensitive and -resistant sites (Fig. 1B and fig. S2), which indicates that rapamycin sensitivity could be encoded at the level of an individual phosphorylation site rather than a full-length protein. Thus, we measured the in vitro kinase activity of mTORC1 toward short synthetic peptides encompassing single mTORC1 phosphorylation sites rather than toward intact proteins.

The capacity of mTORC1 to phosphorylate the peptides varied greatly and correlated strongly with the resistance of the sites to rapamycin within cells (Fig. 2, A and B, and fig. S2). For example, mTORC1 weakly phosphorylated the peptide containing the rapamycin-sensitive threonine 389 (T389) site of S6K1 but strongly phosphorylated the peptides containing the T37 or T46 sites of 4E-BP1 or S150 of Grb10, which are rapamycin-resistant. The rapamycin-sensitive sites of 4E-BP1 S65 or Grb10 S476 were, like S6K1 T389, weakly phosphorylated. We also measured mTORC1 activity toward peptides containing sites from LARP1 and PATL1, which were identified in phosphoproteomic studies as having a high likelihood of being phosphorylated by mTORC1 but are of unknown rapamycin sensitivity (*26*, *27*). The S766 site of LARP1 turned out to be a good in vitro substrate, comparable to S150 of Grb10, whereas S774 was a poor one (Fig. 2C). It was gratifying to us that, in human cells, Torin1 inhibited the phosphorylation of both sites, whereas rapamycin only inhibited that of S774 (Fig. 2D). Thus, the in vitro activity of mTORC1 toward peptides encompassing mTORC1 phosphorylation sites can

predict the rapamycin sensitivity of the sites within cells.

The rapamycin-FKBP12 complex is reported to be a partial inhibitor of mTORC1 (8–11), and indeed, it attenuated the activity of mTORC1, to some extent, toward every peptide examined (Fig. 2E, bottom). However, it had proportionally much greater effects on sites that are poor substrates, such as T389 of S6K1 and S65 of 4E-BP1 (Fig. 2E, top), to the point that these sites were barely phosphorylated in the presence of the drug. Given the small size of the peptides, the differential activity of mTORC1 toward them likely reflects differences in how the peptides interact with the mTOR kinase domain rather than with other regions of mTORC1. Consistent with this notion, a truncation mutant of mTOR that retains its kinase domain but does not interact with raptor (11, 28, 29), a substrate-binding subunit of mTORC1 (30, 31), had similar peptide preferences and selectivity to those of intact mTORC1 (compare Fig. 2A with Fig. 2F; and see fig. S3). In general, its in vitro activity was more inhibited by rapamycin than that of intact mTORC1 (compare Fig. 2E with Fig. 2G), which may indicate a role for raptor in stabilizing the mTOR domain kinase so that in its absence mTOR is more sensitive to allosteric inhibition by rapamycin. The binding of truncated mTOR to the peptides strongly correlated with its capacity to phosphorylate them (Fig. 2H), which suggested that mTORC1 activity toward peptide substrates is, at least in part, a consequence of their relative affinities for the mTOR kinase domain. Consistent with this possibility, rapamycin-sensitive peptides had higher affinities for substrate (K_m) than resistant peptides in steady-state kinetic analyses of mTORC1 activity (Fig. 2I). Moreover, rapamycin increased K_m values for both types of peptide substrates but had minor effects on the catalytic rate (k_{cat}) values (Fig. 2I). We speculate that when FKBP12-rapamycin binds to a region adjacent to the mTOR kinase domain, it may induce a conformational change in the catalytic pocket of mTOR that reduces the accessibility of substrates. Alternatively, FKBP12-rapamycin may physically obstruct the substrate binding site, which would cause an increase in substrate K_m.

Refinement of the mTORC1 Phosphorylation Motif

To test if a causal relationship exists between the capacity of mTORC1 to phosphorylate a site in vitro and its rapamycin sensitivity within cells, it was first necessary to understand how to modify a site—defined as the phosphoacceptor serine-threonine and four residues on either side—to alter mTORC1 activity toward it. In a positional scanning peptide library screen, mTORC1 showed

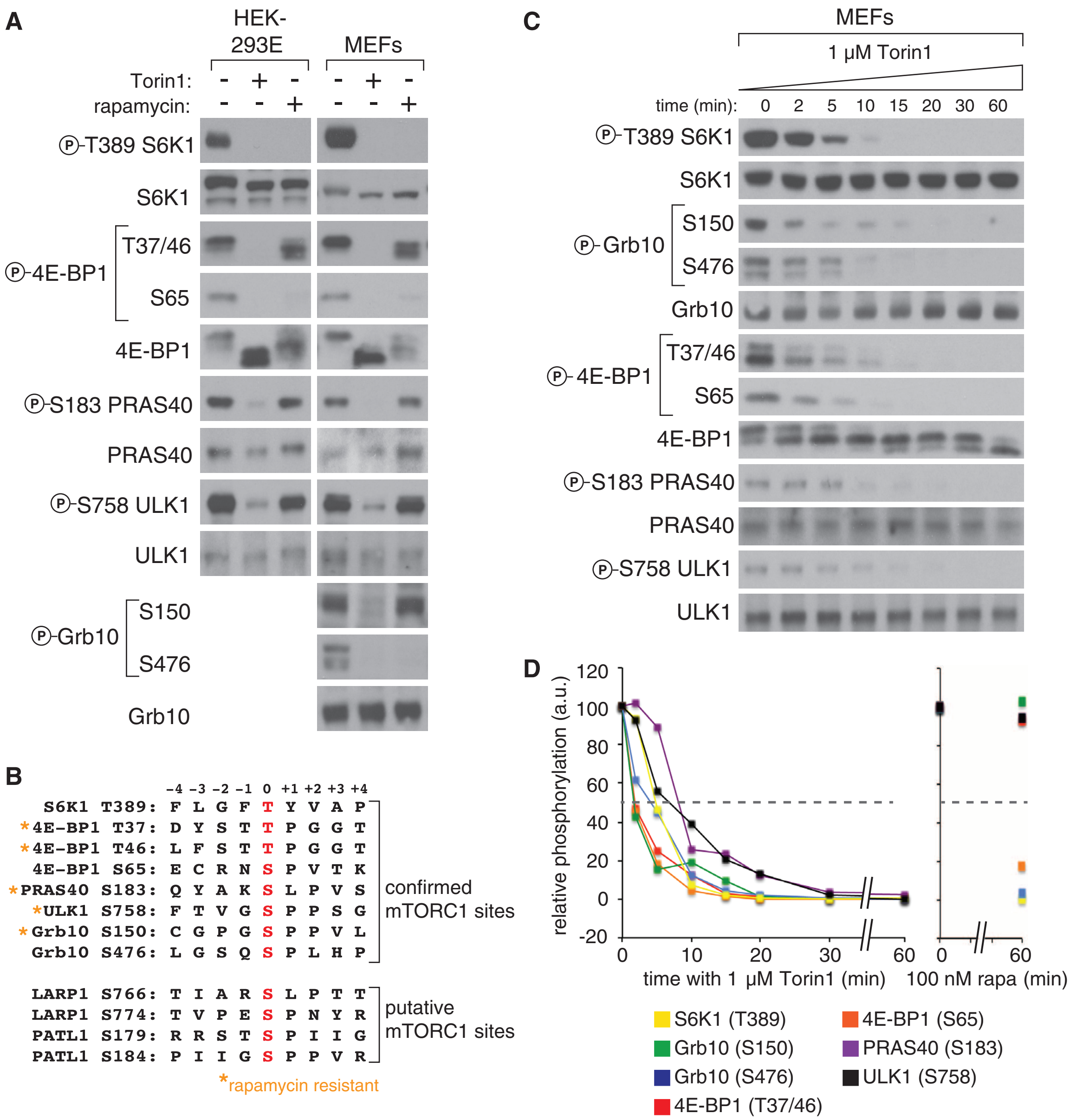

Fig. 1. Rapamycin differentially inhibits mTORC1 phosphorylation sites. (**A**) Responses of known mTORC1 phosphorylation sites in HEK-293E cells and mouse embryonic fibroblasts (p53$^{-/-}$ MEFs) to 1-hour treatments with 100 nM rapamycin, 250 nM Torin1, or vehicle control. Cells were grown in DMEM with 10% FBS and antibiotics. Subsequently, cell lysates were analyzed by immunoblotting for the levels and phosphorylation states of the specified proteins. (**B**) Sequence alignment of known and putative mTORC1 phosphorylation sites. Positions are numbered relative to the central phosphoacceptor serine or threonine, and known rapamycin-resistant sites are indicated. (**C**) Dephosphorylation of mTORC1 phosphorylation sites in response to Torin1. p53$^{-/-}$ MEFs were treated with 1 µM Torin1 and lysed at the indicated time points, and lysates were analyzed as in (A). (**D**) Quantification by densitometry of immunoblots shown in (A) and (C).

a strong preference at the +1 position for proline, hydrophobic (L, V), or aromatic residues (F, W, Y) (Fig. 1B), as well as lesser selectivity at other positions, including glycine at –1 (fig. S3) (*26*). The preference for both proline and nonproline hydrophobic residues in the +1 position is unusual and distinguishes mTORC1 from other proline-directed kinases, such as cyclin-dependent kinases (Cdks) and mitogen-activated protein kinases (MAPKs). Using the Grb10 S150 peptide as a model substrate, we confirmed these preferences and also found that the addition of

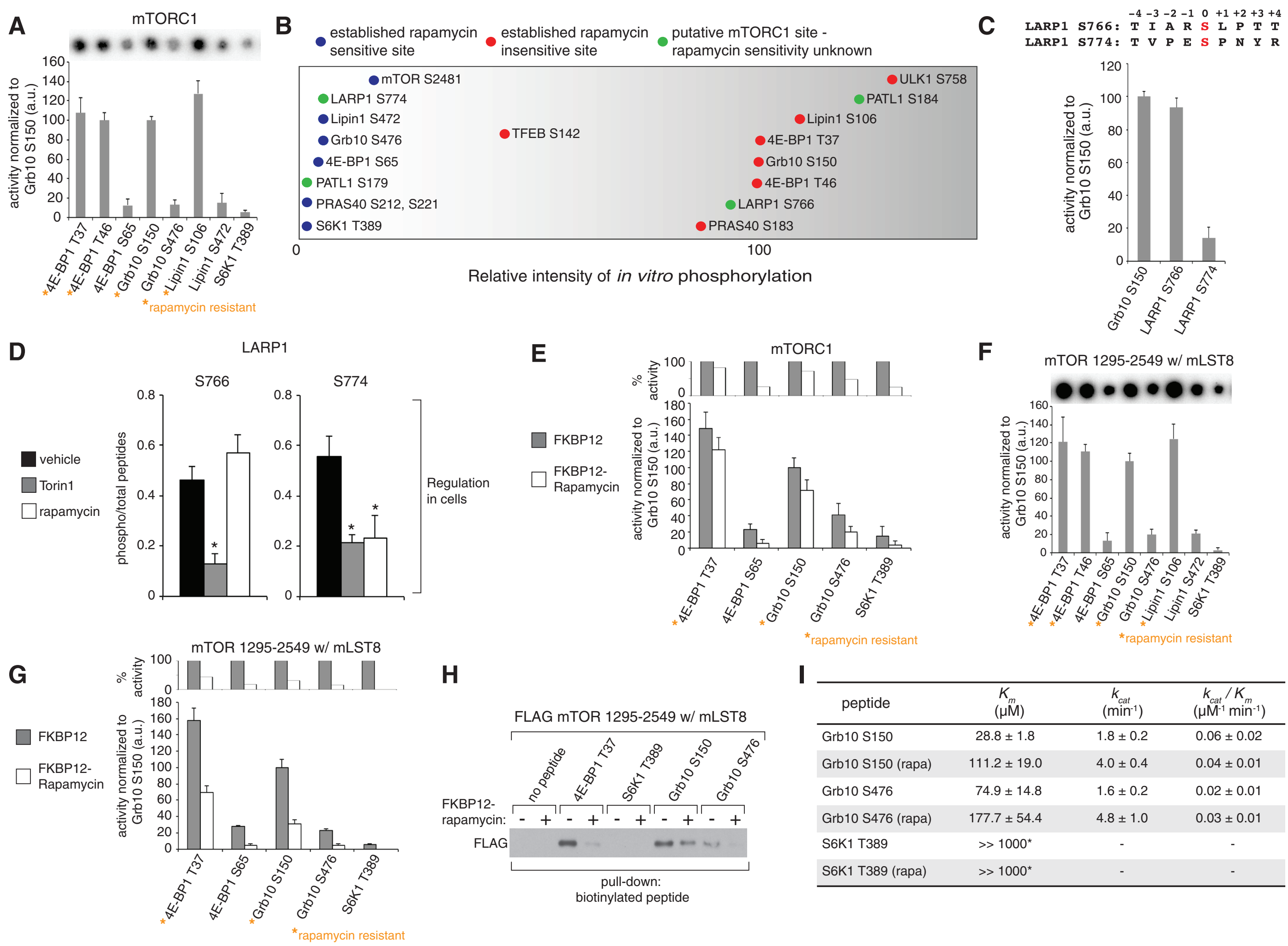

peptide	K_m (μM)	k_{cat} (min^{-1})	k_{cat}/K_m (μM^{-1} min^{-1})
Grb10 S150	28.8 ± 1.8	1.8 ± 0.2	0.06 ± 0.02
Grb10 S150 (rapa)	111.2 ± 19.0	4.0 ± 0.4	0.04 ± 0.01
Grb10 S476	74.9 ± 14.8	1.6 ± 0.2	0.02 ± 0.01
Grb10 S476 (rapa)	177.7 ± 54.4	4.8 ± 1.0	0.03 ± 0.01
S6K1 T389	>> 1000*	-	-
S6K1 T389 (rapa)	>> 1000*	-	-

Fig. 2. The kinase activity of mTORC1 toward peptides encompassing its phosphorylation sites correlates with their resistance to rapamycin. (**A**) In vitro kinase activity of mTORC1 toward a set of short synthetic peptides, each containing an established mTORC1 phosphorylation site, was analyzed by autoradiography (representative example shown). Phosphorylation levels of the specified peptides were quantified by densitometry. Data are means ± SD (n = 3 to 5). (**B**) In vitro kinase activity of mTORC1 toward indicated peptide substrates. Results are displayed as the relative kinase activity of mTORC1 for each peptide, and the rapamycin sensitivity of each site is indicated. The sequences of all indicated phosphorylation sites are available in fig. S2. (**C**) In vitro kinase activity of mTORC1 toward peptides containing indicated LARP1 sites was analyzed as in (A). (**D**) Rapamycin sensitivity of LARP1 phosphorylation sites in cells. FLAG immunoprecipitates from HEK-293E cells stably expressing FLAG-LARP1 and treated with 100 nM rapamycin, 250 nM Torin1, or vehicle control for 1 hour were analyzed by mass spectrometry and phosphorylation ratios determined from chromatographic peak intensities. Data are means ± SD (n = 3). *P < 0.05 for differences between treated and nontreated conditions (Mann-Whitney U test). (**E**) Effects of rapamycin-FKBP12 on mTORC1 activity toward peptide substrates. Experiment was performed and analyzed as in (A), in the presence of recombinant FKBP12 or the complex of FKBP12 and 100 nM rapamycin, by using purified mTORC1 (bottom). Activity normalized to mTORC1 treated with FKBP12 alone for individual peptide substrates (top). (**F**) In vitro kinase activity of the truncation mutant of mTOR toward peptide substrates. Experiment was performed and analyzed as in (A) using the mTOR truncation mutant (amino acid positions 1295 to 2549) in a complex with mLST8. (**G**) Effects of rapamycin-FKBP12 on the activity of truncated mTOR toward peptide substrates. Experiment was performed and analyzed as in (E) by using the mTOR truncation mutant. (**H**) Binding of the peptide substrates to the mTOR kinase domain in the absence and presence of FKBP12-rapamcyin. A pull-down assay with streptavidin-agarose was performed from the mixture of biotinylated peptides encompassing established mTORC1 phosphorylation sites and the FLAG-tagged mTOR truncation mutant in the presence of AMP-PNP and analyzed by immunoblotting for the FLAG tag. For pull-down assays with FKBP12-rapamycin, 100 nM rapamycin was preincubated with 50 ng FKBP12 for 30 min and added to the assay mixtures. (**I**) Steady-state kinetic measurements of mTORC1 kinase activity toward individual peptides encompassing mTORC1 phosphorylation sites. K_m and k_{cat} values of mTORC1 activity toward indicated peptide substrates were determined by measuring the rate of mTORC1 phosphorylation over a range of peptide substrate concentrations (0, 10, 100, 250, 500, and 1000 μM) at a nonlimiting ATP concentration, 500 μM. For kinetic measurements in the presence of FKBP12-rapamycin, 100 nM rapamycin was preincubated with 50 ng FKBP12 for 30 min and added to reaction mixtures. The steady-state kinetic parameters were obtained by fitting the reaction rates to the Michaelis-Menten equation. *Note: K_m exceeds the highest concentration tested for the S6K1 T389 peptide.

hydrophobic or charged residues promoted or decreased, respectively, mTORC1 activity toward them (Fig. 3A). In addition, substitution of the phosphoacceptor serine with threonine (Grb10 S150T) strongly reduced mTORC1 activity toward this peptide (Fig. 3A and fig. S3). The preferences gleaned from modifying the Grb10 S150 peptide were applicable to other mTORC1 substrates. For example, elimination of glutamate and lysine from the 4E-BP1 S65 peptide boosted its phosphorylation by mTORC1 (fig. S4), which led us to notice that poor mTORC1 phosphorylation

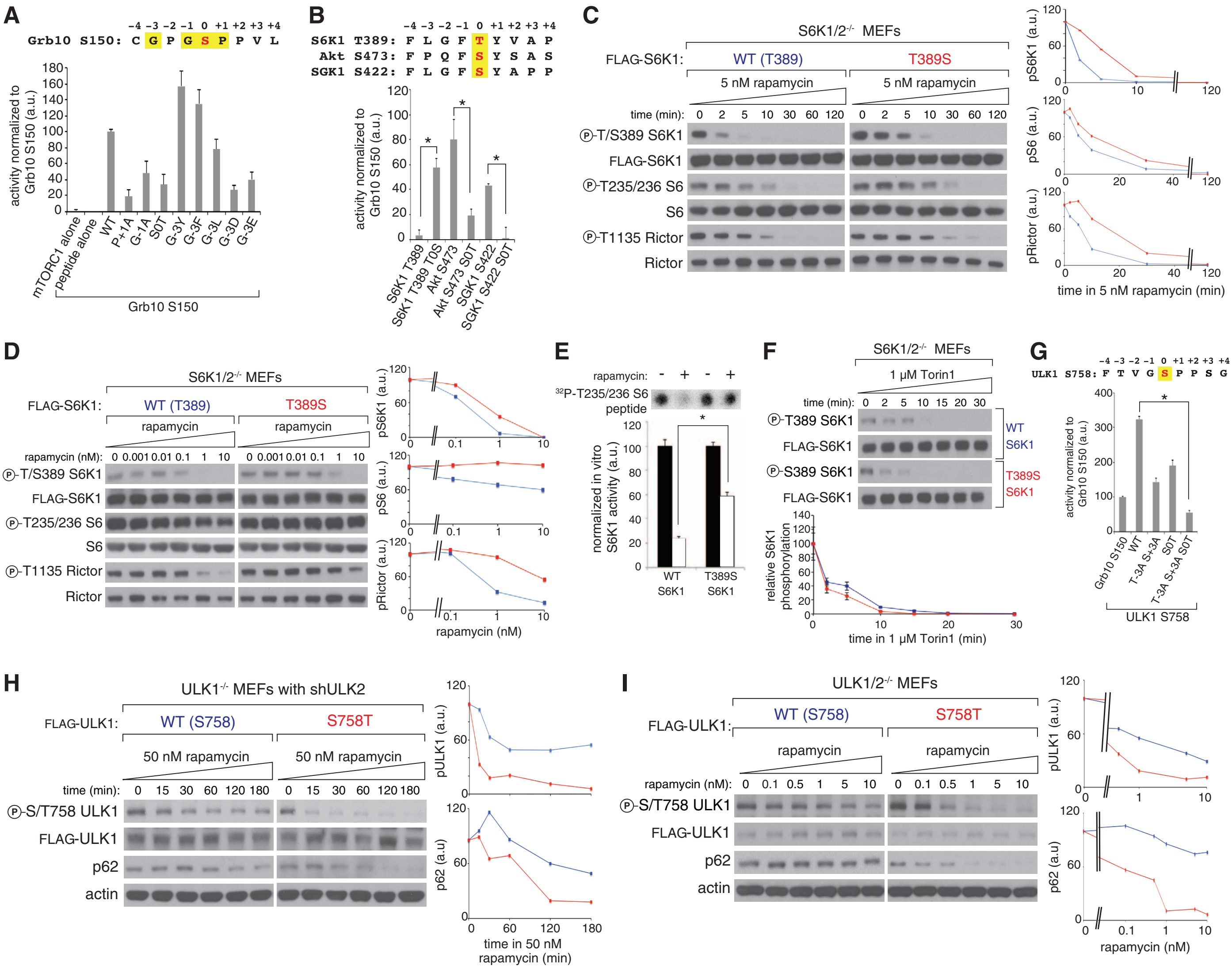

Fig. 3. Conservative modifications to mTORC1 phosphorylation sites are sufficient to alter their sensitivity to rapamycin within cells. (**A**) In vitro kinase activity of mTORC1 toward peptides containing indicated modifications to the Grb10 S150 site were analyzed by autoradiography (representative example shown). Phosphorylation levels of the specified peptides were quantified by densitometry. Data are means ± SD (n = 3 to 5) (*P < 0.05). (**B**) In vitro kinase activity of mTORC1 toward peptides encompassing the hydrophobic motif phosphorylation sites of indicated kinases was analyzed by autoradiography as in (A). Data are means ± SD (*P < 0.05). (**C**) Time-dependent responses of wild-type and mutant T389S S6K1 to rapamycin. S6K1$^{-/-}$S6K2$^{-/-}$ MEFs stably expressing wild-type or T389S S6K1 were treated with 5 nM rapamycin for up to 2 hours. Cell lysates were analyzed by immunoblotting for the levels and phosphorylation states of the specified proteins. Phosphorylation levels of the specified proteins were quantified by densitometry (graphs). Experiments were performed at least three times, and a representative example is shown. (**D**) Concentration-dependent responses of wild-type and mutant S6K1 to rapamycin. S6K1$^{-/-}$S6K2$^{-/-}$ MEFs stably expressing FLAG-tagged wild-type or T389S S6K1 were treated with increasing concentrations of rapamycin for 20 min and analyzed as in (C). (**E**) Effects of rapamycin on in vitro kinase activities of wild-type and mutant T389S S6K1. HEK-293T cells expressing FLAG-tagged wild-type or T389S S6K1 were treated with 50 nM rapamycin or vehicle for 15 min, and the recombinant protein was purified from lysates using FLAG M2 agarose. Subsequently, in vitro kinase activity of wild-type or T389S S6K1 toward a S6 peptide containing the T235 and T236 phosphorylation sites was analyzed by autoradiography and quantified by densitometry. Data are means ± SD (n = 3) (*P < 0.05). (**F**) S6K1$^{-/-}$S6K2$^{-/-}$ MEFs stably expressing wild-type or T389S S6K1 were treated with 1 μM Torin1 for indicated time points. Cell lysates were analyzed as in (C) (representative example shown). Data are means ± SD (n = 3). (**G**) In vitro kinase activity of mTOR toward peptides containing indicated modifications to the ULK1 S758 site were analyzed as in (A). The high level of activity of mTORC1 toward the wild-type ULK1 peptide reflects the fact that it contains more than one site phosphorylated by mTORC1. Data are means ± SD (n = 3) (*P < 0.05). (**H**) Time-dependent responses of wild-type and mutant S758T ULK1 to rapamycin. Experiment was performed and analyzed as in (C) with ULK1$^{-/-}$ MEFs stably expressing a short hairpin RNA against endogenous ULK2, as well as FLAG-tagged wild-type or S758T ULK1. (**I**) Concentration-dependent responses of wild-type and mutant S758T ULK1 to rapamycin. Experiment was performed and analyzed as in (D) for 2 hours with ULK1$^{-/-}$ULK2$^{-/-}$ MEFs stably FLAG-tagged wild-type or S758T ULK1. Note: For all peptide sequences, phosphoacceptor sites are in red text and modified residues in yellow highlight.

sites tend to have several charged residues (Fig. 1C and fig. S2). Most interestingly, however, the preference for serine over threonine as the phosphoacceptor was even stronger within the context of the S6K1 T389 peptide, such that the T389S mutant was a much better mTORC1 substrate than the wild-type peptide (Fig. 3B and fig. S5). Consistent results were obtained for serine-to-threonine changes in the peptides for Akt1 S473 or SGK1 S422, which are mTORC2 substrates within cells but, in peptide form, are phosphorylated by mTORC1 (Fig. 3B). Thus, analysis of the sequence motif specificity of mTORC1 revealed a simple way to test the hypothesis that we can increase the rapamycin resistance of a site by making it a better substrate for mTORC1.

Manipulation Within Cells of the Rapamycin Sensitivity of mTORC1 Substrate Phosphorylation Sites

To do so we stably expressed wild-type or T389S S6K1 in MEFs lacking S6K1 and S6K2 [S6K1$^{-/-}$S6K2$^{-/-}$ MEFs (*32*)] and monitored the effects of various treatment durations or concentrations of rapamycin on the phosphorylation of T/S389 with a phosphospecific antibody that recognizes either site equally well (fig. S6). Upon rapamycin treatment, S389 S6K1 was dephosphorylated with slower kinetics and at higher doses than wild-type S6K1 (Fig. 3, C and D). Moreover, in mutant-expressing cells, the phosphorylation of S6 and rictor, established S6K1 substrates (*33*–*38*), was also more resistant to rapamycin (Fig. 3, C and D), which is consistent with the mutant S6K1 retaining more kinase activity than its wild-type counterpart in rapamycin-treated cells (Fig. 3E). In response to Torin1, wild-type and T389S S6K1 were dephosphorylated with very similar kinetics, which indicated that the phosphatases that act on this site were unaffected by the T389S mutation (Fig. 3F). The serine mutation did not confer complete resistance to rapamycin, perhaps because it does not sufficiently increase the activity of mTORC1 toward S6K1. In addition, it is likely that the intrinsic activity of mTORC1 toward a phosphorylation site is only one of several determinants of its rapamycin sensitivity. Other properties that may have a role include the exact position of the site on the intact protein substrate, the secondary interactions the protein substrate makes with the kinase, and even perhaps its subcellular localization. Nevertheless, a single conservative change to an mTORC1 phosphorylation site is sufficient to alter its response to rapamycin and that of the downstream events the site controls.

We also tested whether making a site a poorer mTORC1 substrate increases its sensitivity to rapamycin within cells. We used ULK1, an inducer of autophagy that mTORC1 negatively regulates, in part by directly phosphorylating it on S758 (*39*–*41*). The ULK1 S758 peptide is an exceptionally good substrate in vitro for mTORC1, likely because it contains more than one phosphorylation site (Fig. 3G). Still, a S758T mutation was sufficient to strongly reduce the activity of mTORC1 toward the peptide (Fig. 3G and fig. S5). Thus, we reconstituted MEFs lacking ULK1 and ULK2 (*42*, *43*) with wild-type or the S758T ULK1 mutant and examined the extent of S/T758 phosphorylation in response to rapamycin, varying either the treatment time or dose of the drug. The phosphospecific S758 antibody recognizes phosphorylation at position 758 when either serine or threonine is the phosphoacceptor (fig. S6). Although the phosphorylation of wild-type ULK1 was, as expected, largely resistant to rapamycin (Fig. 1A), that of the mutant was much more sensitive to rapamycin (Fig. 3H and I). Moreover, in the mutant-expressing cells, rapamycin caused a stronger activation of autophagy, as detected by a greater decrease in p62 and a greater accumulation of LC3-II, than in cells with wild-type ULK1 (Fig. 3, H and I, and figs. S7 and S8) (*44*). Hence, as with S6K1, a conservative change to the ULK1 phosphorylation site is sufficient to alter its sensitivity to rapamycin, as well as that of downstream signaling events, in this case, autophagy induction. These results indicate that the inherent capacity of a phosphorylation site to serve as an mTORC1 substrate (its "substrate quality") affects how it responds to the partial inhibition of mTORC1 caused by rapamycin. The same may be true for mTORC2 because phosphorylation of position 473 of Akt1 was more sensitive to low doses of Torin1 when the normal serine was changed to threonine (fig. S9).

Substrate Quality Is a Determinant of the mTORC1-Regulated Starvation Program

As rapamycin is a pharmacological regulator of mTORC1, we wondered whether mTORC1 phosphorylation sites respond differentially to the physiological inputs that control mTORC1, such as nutrients and growth factors. Note that we found that the same mTORC1 phosphorylation sites that were rapamycin-sensitive were also more sensitive to a partial decrease in the concentration of amino acids in the cell media. For example, the phosphorylation of T389 S6K1, which is extremely rapamycin-sensitive, was strongly reduced when cells were placed in medium with 20% of the normal levels of amino acids (Fig. 4A and fig. S10). In contrast, the same medium did not affect the phosphorylation of S150 Grb10, which is also resistant to rapamycin, and phosphorylation of this site became partially inhibited only when cells were fully deprived of amino acids (Fig. 4A and fig. S10). We obtained analogous results when we varied the amount of serum to which the cells were exposed or when we varied the duration of complete amino acid starvation (Fig. 4, A and B, and fig. S10). Thus, bona fide mTORC1 substrates vary greatly in their responses to the same mTORC1-regulating signals.

To test whether differences in substrate quality might underlie these differences in sensitivity to upstream signals, we used MEF lines expressing the wild-type or the mutant versions of S6K1 or ULK1. Phosphorylation of the T389S S6K1 mutant, which was partially resistant to rapamycin, was also strongly resistant to a reduction in amino acid concentrations, and this resistance was reflected, as before, in the phosphorylation states of the S6K1 substrates S6 and rictor (Fig. 4C). Similarly, the phosphorylation of the S758T ULK1 mutant, which was sensitive to rapamycin, was also sensitive to a reduction in amino acid concentrations and to complete amino acid starvation, as were amounts of p62 and LC3-II (Fig. 4D and figs. S11 and S12). For both kinases, we obtained analogous results when we manipulated serum concentrations (fig. S13). Thus, the substrate property that we call substrate quality affects how mTORC1 substrates respond to both pharmacological and natural regulators of the kinase. Moreover, in a competitive proliferation assay in media containing low concentrations of amino acids, the MEFs expressing T389S S6K1 outcompeted those expressing wild-type S6K1 (Fig. 4E), which indicated that a change in substrate quality can also affect cell behavior.

We conclude that the sequence composition of an mTORC1 phosphorylation site, including the presence of serine or threonine as the phosphoacceptor, is one of the key determinants of whether the site is a good or poor mTORC1 substrate within cells. Even though the phosphorylation of mTORC1 sites is undoubtedly subject to varied regulatory mechanisms, we propose that differences in substrate quality are one mechanism for allowing downstream effectors of mTORC1 to respond differentially to temporal and intensity changes in the levels of nutrients and growth factors, as well as pharmacological inhibitors such as rapamycin (Fig. 4F). Such differential responses are likely important for mTORC1 to coordinate and appropriately time the myriad processes that make up the vast starvation program it controls. Last, it is likely that the form of hierarchical regulation we describe for mTORC1 substrates also exists in other kinase-driven signaling pathways.

Materials and Methods

Materials

Reagents were obtained from the following sources: antibodies to phospho-T389 S6K1, phospho-S235/S236 S6, phospho-T37/T46 4E-BP1, phospho-S65 4E-BP1, phospho-S70 4E-BP1, phospho-T183 PRAS40, phospho-S758 ULK1, phospho-S150 Grb10, phospho-S476 Grb10, phospho-S106 Lipin1, phosphor-S472 Lipin1, phosphor-S1135 rictor, S6K1, 4E-BP1, PRAS40, FLAG, S6, and Rictor from Cell Signaling Technology; an antibody to Grb10 and horseradish peroxidase–labeled antibody against mouse and secondary antibody against rabbit antibody from Santa Cruz Biotechnology; an antibody to p62 from Progen; antibodies to ULK1, FLAG, and β-actin (clone

AC-15), FLAG M2 affinity gel, ATP, FKBP12, amino acids, and insulin from Sigma-Aldrich; [γ-^{32}P]ATP from Perkin-Elmer; FuGENE 6, PhosSTOP, and Complete Protease Cocktail from Roche; rapamycin from LC Laboratories; Dulbecco's modified Eagle's medium (DMEM) from SAFC Biosciences; inactivated fetal calf serum (IFS), fetal bovine serum (FBS), and SimplyBlue Coomassie G from Invitrogen; amino acid–free Roswell Park Memorial Institute (RPMI) medium from U.S. Biological; Superose 6 10/300 GL from GE Healthcare; bicinchoninic acid assay (BCA assay) reagent, protein G–Sepharose, streptavidin agarose, and immobilized glutathione beads from Thermo Scientific; Whatman grade P81 ion-exchange chromatography paper from Fisher Scientific; QIAamp DNA Mini Kit, QuikChange XLII mutagenesis kit, and XL10-Gold Competent

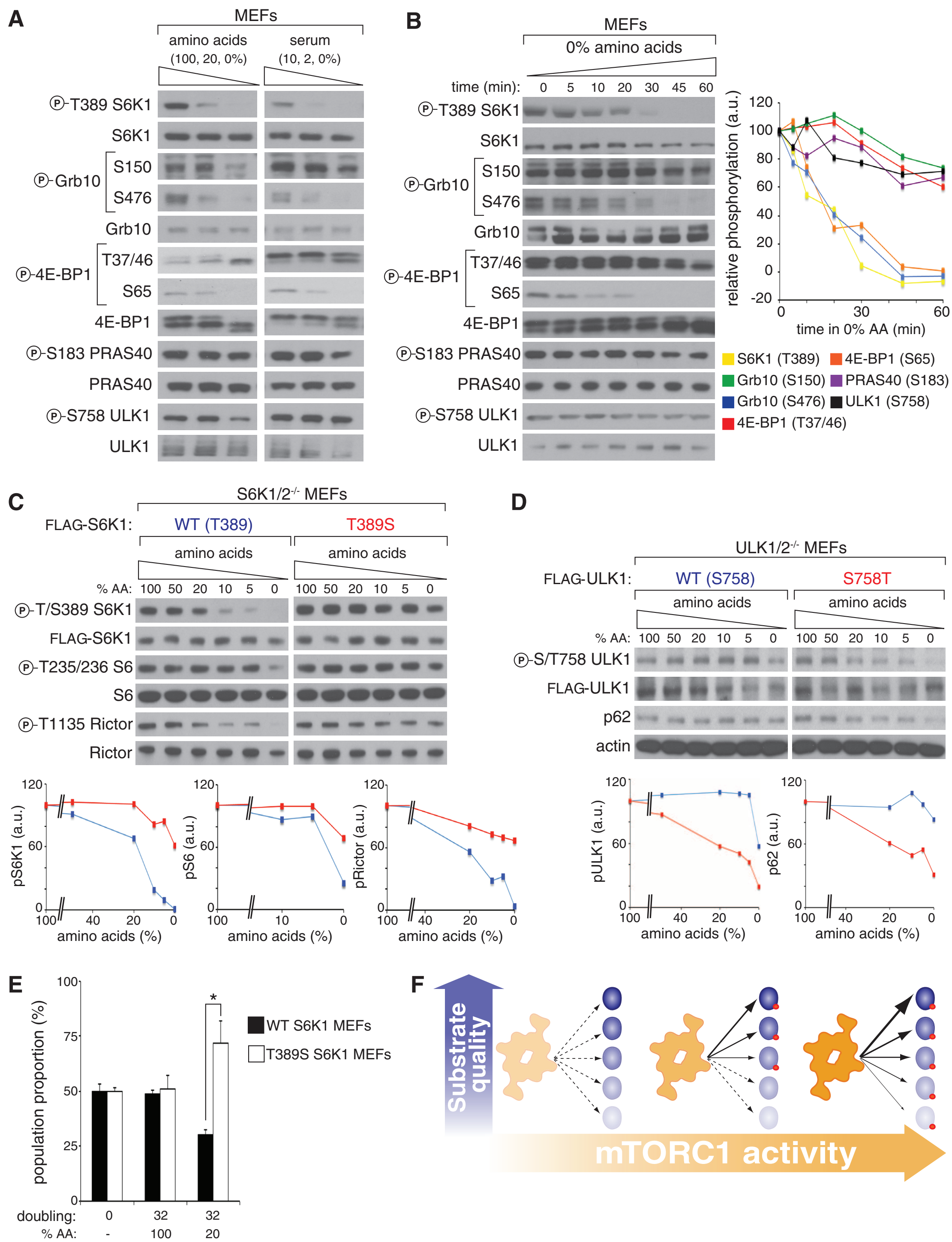

Fig. 4. The sequence composition of mTORC1 phosphorylation sites encodes their sensitivity to physiological signals that regulate mTORC1. (**A**) Differential responses of established mTORC1 phosphorylation sites to partial amino acid or serum starvation. p53$^{-/-}$ MEFs were placed in media with 100, 20, or 0% of the normal levels of amino acids or 10, 2, or 0% FBS for 30 min. Cell lysates were analyzed by immunoblotting for the levels and phosphorylation states of the specified proteins. (**B**) Differential responses of established mTORC1 phosphorylation sites to complete amino acid starvation. p53$^{-/-}$ MEFs were placed in 0% amino acid media for the indicated time points. Cell lysates were analyzed as in (A). Phosphorylation levels of the specified proteins were quantified by densitometry (graph). (**C**) Differential concentration-dependent responses of wild-type and mutant T389S S6K1 to partial amino acid starvation. S6K1$^{-/-}$S6K2$^{-/-}$ MEFs stably expressing FLAG-tagged wild-type or T389S S6K1 were placed in media with 100, 50, 20, 10, 5, or 0% of the normal levels of amino acids for 20 min. Cell lysates were analyzed as in (A). Phosphorylation levels of the specified proteins were quantified by densitometry (graph). (**D**) Differential concentration-dependent responses of wild-type and mutant S758T ULK1 to partial amino acid starvation. Experiment was performed and analyzed as in (C) for 2 hours under partial amino acid starvation with ULK1$^{-/-}$ULK2$^{-/-}$ MEFs stably expressing FLAG-tagged wild-type or S758T ULK1. (**E**) A conservative change to the mTORC1 phosphorylation site S6K1 T389 is sufficient to alter the proliferation rate of cells cultured under partial amino acid starvation. S6K1$^{-/-}$ S6K2$^{-/-}$ MEFs stably expressing barcoded wild-type and T389S S6K1 were mixed in equal number and cultured in either 100% amino acid RPMI with 10% FBS and antibiotics or 20% amino acid RPMI with 10% dialyzed FBS and antibiotics. After 32 population doublings, cells were harvested, and genomic DNA was isolated and analyzed by quantitative real-time PCR. (**F**) Model for the role of substrate quality in the regulation of mTORC1 phosphorylation sites. Substrate quality is an important determinant of how mTORC1 substrates respond to pharmacological and natural regulators of the kinase.

cells from Stratagene; SYBR Green polymerase chain reaction (PCR) Master Mix from AB Applied Biosystems; and SAM2 biotin capture membrane from Promega. Torin1 was provided by Nathanael Gray (Harvard Medical School) (*18*).

Cell Lines and Tissue Culture

HEK-293E and MEFs were cultured in DMEM with 10% FBS and antibiotics. HEK-293T was cultured in DMEM with 10% IFS and antibiotics. HEK-293Es were generously provided by John Blenis (Harvard Medical School), $p53^{-/-}$ MEFs by David Kwiatkowski (Harvard Medical School), $S6K1^{+/+}S6K2^{+/+}$ and $S6K1^{-/-}S6K2^{-/-}$ MEFs by Mario Pende (INSERM U845, Medical School, Paris Descartes University), $ULK1^{+/+}$ and $ULK1^{-/-}$ shULK2 MEFs by Reuben Shaw (Salk Institute), and $ULK1^{+/+}ULK2^{+/+}$ and $ULK1^{-/-}ULK2^{-/-}$ MEFs by Craig Thompson (Memorial Sloan-Kettering Cancer Center).

To generate stable cell lines, mRNA-encoding plasmids were cotransfected with Delta VPR (pLJM60/61 lentivirus) or Gag-pol envelope (pQCXIP/N retrovirus) and cytomegalovirus–vesicular stomatitis virus glycoprotein CMV VSVG) packaging plasmids into actively growing HEK-293T using FuGENE 6 transfection reagent as previously described (*45*). Virus particles containing supernatants were collected at 48 hours posttransfection and spun in a centrifuge to eliminate floating cells, and target cells (100,000 to 1,000,000) were infected in the presence of 8 mg/ml polybrene. The cells were given or split 24 hours postinfection into fresh medium containing, per milliliter, 2 µg puromycin or 1 mg neomycin. mRNA-expressing cells were analyzed 2 to 7 days postinfection.

cDNA Manipulations and Mutagenesis

The mTOR truncation mutant (1295–2549) and LARP1 cDNAs were amplified by PCR, and the products were subcloned into the Sal I and Xho I sites of the FLAG-tagged pQCXIP (puromycin-resistant) retroviral vector for stable expression. The mLST8 cDNA was amplified by PCR, and the product was subcloned into the Not I and Eco RI sites of the pQCXIN (neomycin-resistant) vector for stable expression. The S6K1 and ULK1 cDNAs were amplified by PCR, and the products were subcloned into the Sal I and Not I sites of the pLJM60 (puromycin-resistant) or pLJM61 (neomycin-resistant) lentiviral vector for stable expression. The pLJM60 S6K1, pLJM60/61 ULK1, and pRK5 glutathione *S*-transferase (GST)–tagged mouse Akt1 plasmids were mutagenized with the QuikChange XLII mutagenesis kit with oligonucleotides obtained from Integrated DNA Technologies. The S6K1, ULK1, and Akt1 mutants used in our experiments were T389S, S758T, and S473T, respectively. For barcoding pLJM60 S6K1 constructs, GGATCC (BamH I) and GGTACC (Kpn I) sequences were inserted in front of the start codons of wild-type and T389S S6K1, respectively, by using the QuikChange XLII mutagenesis kit with oligonucleotides obtained from Integrated DNA Technologies.

Cell Treatments and Lysis and Immunoprecipitations

For rapamycin and Torin1 treatments, 70 to 80% confluent cells were treated with dimethyl sulfoxide (DMSO) or inhibitors as indicated in figure legends. Amino acids and serum were titrated as indicated in figure legends. Cells rinsed once with ice-cold phosphate-buffered saline (PBS) and lysed in ice-cold lysis buffer [50 mM HEPES pH 7.4, 40 mM NaCl, 2 mM EDTA, 1 mM orthovanadate, 50 mM NaF, 10 mM pyrophosphate, 10 mM glycerophosphate, and 1% Triton X-100 or 0.3% CHAPS (for immunoprecipitations)] with one PhosSTOP tablet and one tablet of EDTA-free protease inhibitors per 25 ml. The soluble fractions of cell lysates were isolated by centrifugation at 13,000*g* for 10 min. For FLAG immunoprecipitations, 50% slurry of FLAG M2 affinity agarose was added to the lysates, and the mixtures were incubated with rotation for 2 to 6 hours at 4°C. Immunoprecipitates were washed three times with lysis buffer containing 150 mM NaCl. Immunoprecipitated proteins were denatured by the addition of sample buffer, boiled for 5 min, resolved by SDS–polyacrylamide gel electrophoresis (SDS-PAGE), and analyzed by immunoblotting as previously described (*28*).

Purifications of mTORC1 and Truncated mTOR

mTORC1 purification from HEK-293T cells stably expressing FLAG-raptor was performed as described previously (*29*). Purification of the truncated mTOR mutant from HEK-293T cells stably expressing FLAG-mTOR (1295–2549) and mLST8 was also performed as described previously without a gel filtration step (*29*). Purified recombinant proteins were aliquoted and stored at –80°C.

In Vitro Kinase Assays

Individual peptide substrates [GYXXXX(S/T) XXXXGRRRRR] were synthesized by the MIT Koch Institute Biopolymers and Proteomics Core Facility and purified by reversed-phase high-performance liquid chromatography (HPLC). In vitro kinase activity of mTORC1 or truncated mTOR toward peptides was determined by incubating 0.1 to 0.2 mM peptide with ~100 ng mTORC1 or ~20 ng truncated mTOR in reaction buffer (25 mM HEPES pH 7.4, 50 mM KCl, 5 mM $MgCl_2$, and 5 mM $MnCl_2$) containing 50 µM cold ATP and 2 to 5 µCi [γ-^{32}P]ATP for 20 to 30 min at room temperature. Aliquots (3.3 µl) of each reaction were spotted onto P81 ion-exchange chromatography paper in triplicates and quenched in 0.42% H_3PO_4. Paper was washed 8 to 10 times in same solution and dried. Resulting radioactivity was determined by a phosphoimaging device. For kinase assays with rapamycin, 100 nM rapamycin was preincubated with 50 ng FKBP12 for 30 min and added to reaction mixtures. FKBP12 was added in excess to ensure that most of rapamycin would be in an FKBP12-rapamcyin complex.

For S6K1 kinase assays, recombinant S6K1 proteins were purified from HEK-293T stably expressing WT or T389S S6K1 using the same method as for truncated mTOR. S6 peptide substrate (AKRRRLSSLRA) was incubated in 20 µl of reaction mixture consisting of kinase assay buffer (25 mM HEPES, pH 7.4, 50 mM KCl, 5 mM $MgCl_2$, and 5 mM $MnCl_2$), recombinant S6K1, 50 µM ATP, and 2 to 5 µCi [γ-^{32}P]ATP for 30 min at room temperature. Aliquots (3.3 µl) of each reaction were spotted onto P81 ion-exchange chromatography paper in triplicates and quenched in 0.42% H_3PO_4. Paper was washed 8 to 10 times in same solution and dried. Resulting radioactivity was determined by Phosphoimager.

Pull-Down Assay with Biotinylated Peptides

Biotinylated peptides were dissolved in kinase assay buffer, and soluble fractions of cell lysates were collected by centrifugation at 17,000*g* for 10 min. Preincubated mixtures of peptides and 50% slurry of streptavidin-agarose were added to FLAG-tagged mTOR (1295–2549) and incubated in the presence of 500 nM adenylyl-imidodiphosphate (AMP-PNP) for 4 to 12 hours at 4°C. Pull-down mixtures were washed three times with lysis buffer containing 150 mM NaCl. Recombinant mTOR protein was denatured by addition of sample buffer, boiled for 5 min, resolved by SDS-PAGE, and analyzed by immunoblotting as previously described (*28*). For pull-down assays with rapamycin, 100 nM rapamycin was preincubated with 50 ng FKBP12 for 30 min and added to pull-down mixtures.

Steady-State Kinetic Measurements

To determine the kinetic parameters for peptide phosphorylation, assays were conducted in the presence of 40 nM mTORC1, various concentrations of peptide substrates (0, 10, 100, 250, 500, and 1000 µM) and an ATP mixture containing 500 µM cold ATP (at least 10-fold above K_m), and 2 to 5 µCi [γ-^{32}P]ATP in a 30-µl reaction mixture. The reaction was initiated by the addition of the ATP mixture. After incubation at room temperature, aliquots (3 µl) of each reaction were spotted onto P81 ion-exchange chromatography paper and quenched in 0.42% H_3PO_4. The paper was washed 8 to 10 times in same solution and dried. Resulting radioactivity was determined by phosphoimager. For kinetic measurements with rapamycin, 100 nM rapamycin was preincubated with 50 ng FKBP12 for 30 min and added to reaction mixtures. The steady-state kinetic parameters were obtained by fitting the reaction rates to the Michaelis-Menten equation using GraphPad Prism version 5.0 (GraphPad Inc.)

Mass Spectrometric Analyses

LARP1 phosphorylation sites were identified by mass spectrometric analysis of trypsin-digested FLAG-LARP1 purified from HEK293T cells stably overexpressing FLAG-LARP1. The amino acid

positions of all LARP1 phosphorylation sites were numbered according to National Center for Biotechnology Information. Label-free quantification of LARP1 phosphorylation sites was performed with BioWorks Rev3.3 software according to the methodology previously described (*31*, *46*).

Positional Scanning Peptide Library Screening and PWM Generation

Positional scanning peptide library (PSPL) screening was performed. The resulting peptides were analyzed with the truncated mTOR mutant as previously described (*47–49*).

Phosphopeptide Recognition by Phosphospecific Antibodies

Biotinylated phosphopeptides (1 μl) at the indicated concentrations were spotted on a SAM2 Biotin Capture Membrane (Promega) and washed three times in PBST (PBS with Tween-20). Subsequently, the washed membrane was analyzed by immunoblotting as previously described (*28*). Phosphopeptide sequences used are as follows:

T389 S6K1: GGYFLGF[pT]YVAPGRRRRR
T389S S6K1: GGYFLGF[pS]YVAPGRRRRR
S758 ULK1: GGYFTVG[pS]PPSGGRRRRR
S758T ULK1: GGYFTVG[pT]PPSGGRRRRR

Competitive Proliferation Assay

S6K1$^{-/-}$S6K2$^{-/-}$ MEFs stably expressing bar-coded wild-type and T389S S6K1 were mixed in equal numbers (100,000) and placed in 10-cm culture dishes. The mixture of cells was cultured in either 100% amino acid RPMI with 10% FBS and antibiotics or 20% amino acid RPMI with 10% dialyzed FBS and antibiotics. After 32 population doublings, cells were harvested and genomic DNA was isolated using QIAamp DNA Mini Kit. The concentration and purity of DNA were determined by absorbance at 260 to 280 nm. Primers for real-time PCR were obtained from Integrated DNA Technologies. Reactions were run on an Applied Biosystems Prism machine using SYBR Green Master Mix (Applied Biosystems), and the relative abundance of wild-type and T389S S6K1 was calculated. Primer sequences used to produce bar code–specific amplicons are as follows:

WT S6K1 forward:
GTGGTGGTGCGTCGACGGGAT
WT S6K1 reverse:
CACAATGTTCCATGCCAAGT
T389S S6K1 forward:
GTGGTGGTGCGTCGACGGGTA
T389S S6K1 reverse:
CACAATGTTCCATGCCAAGT

References and Notes

1. M. Laplante, D. M. Sabatini, mTOR signaling in growth control and disease. *Cell* **149**, 274 (2012). doi: 10.1016/j.cell.2012.03.017; pmid: 22500797
2. D. A. Guertin, D. M. Sabatini, The pharmacology of mTOR inhibition. *Sci. Signal.* **2**, pe24 (2009). doi: 10.1126/scisignal.267pe24; pmid: 19383975
3. D. Benjamin, M. Colombi, C. Moroni, M. N. Hall, Rapamycin passes the torch: A new generation of mTOR inhibitors. *Nat. Rev. Drug Discov.* **10**, 868 (2011). doi: 10.1038/nrd3531; pmid: 22037041
4. E. J. Brown *et al.*, A mammalian protein targeted by G1-arresting rapamycin-receptor complex. *Nature* **369**, 756 (1994). doi: 10.1038/369756a0; pmid: 8008069
5. D. M. Sabatini, H. Erdjument-Bromage, M. Lui, P. Tempst, S. H. Snyder, RAFT1: A mammalian protein that binds to FKBP12 in a rapamycin-dependent fashion and is homologous to yeast TORs. *Cell* **78**, 35 (1994). doi: 10.1016/0092-8674(94)90570-3; pmid: 7518356
6. C. J. Sabers *et al.*, Isolation of a protein target of the FKBP12-rapamycin complex in mammalian cells. *J. Biol. Chem.* **270**, 815 (1995). doi: 10.1074/jbc.270.2.815; pmid: 7822316
7. J. W. Choi, J. Chen, S. L. Schreiber, J. Clardy, Structure of the FKBP12-rapamycin complex interacting with the binding domain of human FRAP. *Science* **273**, 239 (1996). doi: 10.1126/science.273.5272.239; pmid: 8662507
8. E. J. Brown *et al.*, Control of p70 S6 kinase by kinase activity of FRAP in vivo. *Nature* **378**, 644 (1995). doi: 10.1038/378644c0
9. G. J. Brunn *et al.*, Phosphorylation of the translational repressor PHAS-I by the mammalian target of rapamycin. *Science* **277**, 99 (1997).
10. P. E. Burnett, R. K. Barrow, N. A. Cohen, S. H. Snyder, D. M. Sabatini, RAFT1 phosphorylation of the translational regulators p70 S6 kinase and 4E-BP1. *Proc. Natl. Acad. Sci. U.S.A.* **95**, 1432 (1998). doi: 10.1073/pnas.95.4.1432; pmid: 9465032
11. Z. H. Tao, J. Barker, S. D. H. Shi, M. Gehring, S. X. Sun, Steady-state kinetic and inhibition studies of the mammalian target of rapamycin (mTOR) kinase domain and mTOR complexes. *Biochemistry* **49**, 8488 (2010). doi: 10.1021/bi100673c; pmid: 20804212
12. D. E. Harrison *et al.*, Rapamycin fed late in life extends lifespan in genetically heterogeneous mice. *Nature* **460**, 392 (2009). pmid: 19587680
13. R. A. Miller *et al.*, Rapamycin, but not resveratrol or simvastatin, extends life span of genetically heterogeneous mice. *J. Gerontol. A Biol. Sci. Med. Sci.* **66A**, 191 (2011). doi: 10.1093/gerona/glq178; pmid: 20974732
14. I. Bjedov *et al.*, Mechanisms of life span extension by rapamycin in the fruit fly Drosophila melanogaster. *Cell Metab.* **11**, 35 (2010). doi: 10.1016/j.cmet.2009.11.010; pmid: 20074526
15. S. Robida-Stubbs *et al.*, TOR signaling and rapamycin influence longevity by regulating SKN-1/Nrf and DAF-16/FoxO. *Cell Metab.* **15**, 713 (2012). doi: 10.1016/j.cmet.2012.04.007; pmid: 22560223
16. M. Kaeberlein *et al.*, Regulation of yeast replicative life span by TOR and Sch9 in response to nutrients. *Science* **310**, 1193 (2005). doi: 10.1126/science.1115535; pmid: 16293764
17. O. Medvedik, D. W. Lamming, K. D. Kim, D. A. Sinclair, MSN2 and MSN4 Link Calorie Restriction and TOR to Sirtuin-Mediated Lifespan Extension in Saccharomyces cerevisiae. *PLoS Biol.* **5**, e261 (2007). doi: 10.1371/journal.pbio.0050261
18. C. C. Thoreen *et al.*, An ATP-competitive mammalian target of rapamycin inhibitor reveals rapamycin-resistant functions of mTORC1. *J. Biol. Chem.* **284**, 8023 (2009). doi: 10.1074/jbc.M900301200; pmid: 19150980
19. M. E. Feldman *et al.*, Active-site inhibitors of mTOR target rapamycin-resistant outputs of mTORC1 and mTORC2. *PLoS Biol.* **7**, e38 (2009). doi: 10.1371/journal.pbio.1000038; pmid: 19209957
20. A. Y. Choo, S. O. Yoon, S. G. Kim, P. P. Roux, J. Blenis, Rapamycin differentially inhibits S6Ks and 4E-BP1 to mediate cell-type-specific repression of mRNA translation. *Proc. Natl. Acad. Sci. U.S.A.* **105**, 17414 (2008). doi: 10.1073/pnas.0809136105; pmid: 18955708
21. S. A. Wander, B. T. Hennessy, J. M. Slingerland, Next-generation mTOR inhibitors in clinical oncology: How pathway complexity informs therapeutic strategy. *J. Clin. Invest.* **121**, 1231 (2011). doi: 10.1172/JCI44145; pmid: 21490404
22. C. M. Chresta *et al.*, AZD8055 is a potent, selective, and orally bioavailable ATP-competitive mammalian target of rapamycin kinase inhibitor with in vitro and in vivo antitumor activity. *Cancer Res.* **70**, 288 (2010). doi: 10.1158/0008-5472.CAN-09-1751; pmid: 20028854
23. J. M. García-Martínez *et al.*, Ku-0063794 is a specific inhibitor of the mammalian target of rapamycin (mTOR). *Biochem. J.* **421**, 29 (2009). doi: 10.1042/BJ20090489; pmid: 19402821
24. K. Yu *et al.*, Biochemical, cellular, and in vivo activity of novel ATP-competitive and selective inhibitors of the mammalian target of rapamycin. *Cancer Res.* **69**, 6232 (2009). doi: 10.1158/0008-5472.CAN-09-0299; pmid: 19584280
25. Q. S. Liu *et al.*, Discovery of 1-(4-(4-propionylpiperazin-1-yl)-3-(trifluoromethyl)phenyl)-9-(quinolin-3-yl)benzo[h][1,6]naphthyridin-2(1H)-one as a highly potent, selective mammalian target of rapamycin (mTOR) inhibitor for the treatment of cancer. *J. Med. Chem.* **53**, 7146 (2010). doi: 10.1021/jm101144f; pmid: 20860370
26. P. P. Hsu *et al.*, The mTOR-regulated phosphoproteome reveals a mechanism of mTORC1-mediated inhibition of growth factor signaling. *Science* **332**, 1317 (2011).
27. Y. H. Yu *et al.*, Phosphoproteomic analysis identifies Grb10 as an mTORC1 substrate that negatively regulates insulin signaling. *Science* **332**, 1322 (2011). doi: 10.1126/science.1199484; pmid: 21659605
28. D. H. Kim *et al.*, mTOR interacts with raptor to form a nutrient-sensitive complex that signals to the cell growth machinery. *Cell* **110**, 163 (2002). doi: 10.1016/S0092-8674(02)00808-5; pmid: 12150925
29. C. K. Yip, K. Murata, T. Walz, D. M. Sabatini, S. A. Kang, Structure of the human mTOR complex I and its implications for rapamycin inhibition. *Mol. Cell* **38**, 768 (2010). doi: 10.1016/j.molcel.2010.05.017; pmid: 20542007
30. K. Hara *et al.*, Raptor, a binding partner of target of rapamycin (TOR), mediates TOR action. *Cell* **110**, 177 (2002). doi: 10.1016/S0092-8674(02)00833-4; pmid: 12150926
31. T. R. Peterson *et al.*, mTOR complex 1 regulates lipin 1 localization to control the SREBP pathway. *Cell* **146**, 408 (2011). doi: 10.1016/j.cell.2011.06.034; pmid: 21816276
32. M. Pende *et al.*, S6K1(-/-)/S6K2(-/-) mice exhibit perinatal lethality and rapamycin-sensitive 5′-terminal oligopyrimidine mRNA translation and reveal a mitogen-activated protein kinase-dependent S6 kinase pathway. *Mol. Cell. Biol.* **24**, 3112 (2004). doi: 10.1128/MCB.24.8.3112-3124.2004; pmid: 15060135
33. P. Jenő, L. M. Ballou, I. Novak-Hofer, G. Thomas, Identification and characterization of a mitogen-activated S6 kinase. *Proc. Natl. Acad. Sci. U.S.A.* **85**, 406 (1988). doi: 10.1073/pnas.85.2.406; pmid: 3257566
34. D. J. Price, R. A. Nemenoff, J. Avruch, Purification of a hepatic S6 kinase from cycloheximide-treated Rats. *J. Biol. Chem.* **264**, 13825 (1989).pmid: 2760046
35. J. Chung, C. J. Kuo, G. R. Crabtree, J. Blenis, Rapamycin-FKBP specifically blocks growth-dependent activation of and signaling by the 70 kd S6 protein kinases. *Cell* **69**, 1227 (1992). doi: 10.1016/0092-8674(92)90643-Q; pmid: 1377606
36. D. J. Price, J. R. Grove, V. Calvo, J. Avruch, B. E. Bierer, Rapamycin-induced inhibition of the 70-kilodalton S6 protein kinase. *Science* **257**, 973 (1992). doi: 10.1126/science.1380182; pmid: 1380182
37. C. C. Dibble, J. M. Asara, B. D. Manning, Characterization of Rictor phosphorylation sites reveals direct regulation of mTOR complex 2 by S6K1. *Mol. Cell. Biol.* **29**, 5657 (2009). doi: 10.1128/MCB.00735-09; pmid: 19720745
38. D. Boulbes *et al.*, Rictor phosphorylation on the Thr-1135 site does not require mammalian target of rapamycin complex 2. *Mol. Cancer Res.* **8**, 896 (2010). doi: 10.1158/1541-7786.MCR-09-0409; pmid: 20501647
39. J. Kim, M. Kundu, B. Viollet, K. L. Guan, AMPK and mTOR regulate autophagy through direct phosphorylation of Ulk1. *Nat. Cell Biol.* **13**, 132 (2011). doi: 10.1038/ncb2152; pmid: 21258367
40. C. H. Jung *et al.*, ULK-Atg13-FIP200 complexes mediate mTOR signaling to the autophagy machinery. *Mol. Biol. Cell* **20**, 1992 (2009). doi: 10.1091/mbc.E08-12-1249; pmid: 19225151
41. N. Hosokawa *et al.*, Nutrient-dependent mTORC1 association with the ULK1-Atg13-FIP200 complex required for autophagy. *Mol. Biol. Cell* **20**, 1981 (2009). doi: 10.1091/mbc.E08-12-1248; pmid: 19211835
42. D. F. Egan *et al.*, Phosphorylation of ULK1 (hATG1) by AMP-activated protein kinase connects energy sensing to mitophagy. *Science* **331**, 456 (2011). doi: 10.1126/science.1196371; pmid: 21205641

43. H. Cheong, T. Lindsten, J. M. Wu, C. Lu, C. B. Thompson, Ammonia-induced autophagy is independent of ULK1/ULK2 kinases. *Proc. Natl. Acad. Sci. U.S.A.* **108**, 11121 (2011). doi: 10.1073/pnas.1107969108; pmid: 21690395
44. N. Mizushima, B. Levine, A. M. Cuervo, D. J. Klionsky, Autophagy fights disease through cellular self-digestion. *Nature* **451**, 1069 (2008). doi: 10.1038/nature06639; pmid: 18305538
45. S. M. Ali, D. M. Sabatini, Structure of S6 kinase 1 determines whether raptor-mTOR or rictor-mTOR phosphorylates its hydrophobic motif site. *J. Biol. Chem.* **280**, 19445 (2005). doi: 10.1074/jbc.C500125200; pmid: 15809305
46. M. P. Stokes *et al*., Profiling of UV-induced ATM/ATR signaling pathways. *Proc. Natl. Acad. Sci. U.S.A.* **104**, 19855 (2007). doi: 10.1073/pnas.0707579104; pmid: 18077418
47. J. Mok *et al*., Deciphering protein kinase specificity through large-scale analysis of yeast phosphorylation site motifs. *Sci. Signal.* **3**, ra12 (2010).
48. J. E. Hutti *et al*., A rapid method for determining protein kinase phosphorylation specificity. *Nat. Methods* **1**, 27 (2004). doi: 10.1038/nmeth708; pmid: 15782149
49. J. C. Obenauer, L. C. Cantley, M. B. Yaffe, Scansite 2.0: Proteome-wide prediction of cell signaling interactions using short sequence motifs. *Nucleic Acids Res.* **31**, 3635 (2003). doi: 10.1093/nar/gkg584; pmid: 12824383

Acknowledgments: We thank members of the Sabatini laboratory for helpful discussions, especially S. Wang, D. Kim, C. Thoreen, T. Wang, and J. Cantor and E. Spooner for the mass spectrometric analysis of samples. We also thank M. Pende for the S6K1/2 null cells and R. Shaw and C. Thompson for the ULK1/2 null cells. This work was supported by grants from the NIH (CA103866 and AI047389 to D.M.S.; ES015339, GM59281, and CA112967 to M.B.Y.) and Department of Defense (W81XWH-07-0448 to D.M.S.); awards from the W.M. Keck Foundation and the LAM (lymphangioleiomyomatosis) Foundation to D.M.S.; fellowships from the American Cancer Society and the LAM Foundation to S.A.K. and the Damon Runyon Cancer Research Foundation and the Department of Defense Breast Cancer Research Program to M.E.P. D.M.S. is an investigator of the Howard Hughes Medical Institute. Torin1, the inhibitor used here, is part of a Whitehead–Dana-Farber Cancer Institute patent application on which S.A.K., N.S.G., and D.M.S. are inventors. Shared reagents are subject to a materials transfer agreement.

Supplementary Materials

www.sciencemag.org/content/341/6144/1236566/suppl/DC1
Figs. S1 to S13
References

14 February 2013; accepted 5 June 2013
10.1126/science.1236566

I-Love-Q: Unexpected Universal Relations for Neutron Stars and Quark Stars

Kent Yagi* and Nicolás Yunes

Neutron stars and quark stars are not only characterized by their mass and radius but also by how fast they spin, through their moment of inertia, and how much they can be deformed, through their Love number and quadrupole moment. These depend sensitively on the star's internal structure and thus on unknown nuclear physics. We find universal relations between the moment of inertia, the Love number, and the quadrupole moment that are independent of the neutron and quark star's internal structure. These can be used to learn about neutron star deformability through observations of the moment of inertia, break degeneracies in gravitational wave detection to measure spin in binary inspirals, distinguish neutron stars from quark stars, and test general relativity in a nuclear structure–independent fashion.

One of the largest uncertainties in nuclear physics is the relation between energy density (ρ) and pressure (p) at very high densities, the so-called equation of state (EoS). The interior structure of very compact stars, like neutron stars (NSs) and quark stars (QSs), depends sensitively on their EoS. This, in turn, determines their exterior properties, such as their mass and radius; their rotation rate, characterized by their moment of inertia; and their deformability, characterized by their quadrupole moment and tidal Love number (*1*, *2*).

Department of Physics, Montana State University, Bozeman, MT 59717, USA.

*Corresponding author. E-mail: kyagi@physics.montana.edu

Some astrophysical observations allow us to infer properties of the EoS of compact stars (*3*–*5*). None of these observations, however, is currently accurate enough to select between the many different EoSs that have been proposed or to distinguish between NSs and QSs, which then leads to degeneracies in the extraction of information from observations. For example, gravitational wave (GW) observations of NS binary inspirals may have difficulty in extracting the individual spins, because these are degenerate with the quadrupole moment for nonprecessing binaries (*6*). Similarly, GWs from NS binary inspirals cannot be easily used to test general relativity (GR) because of EoS degeneracies (*7*, *8*). We here find a way to uniquely break these degeneracies through universal I-Love-Q relations between the reduced moment of inertia, $\bar{I}$; tidal Love number, $\bar{\lambda}^{(\mathrm{tid})}$; and quadrupole moment, $\bar{Q}$, that are essentially insensitive to the star's EoS (*9*).

Consider an isolated, slowly rotating NS or QS described by its mass, M_*; the magnitude of its spin angular momentum, J, and angular velocity, Ω; its (spin-induced) quadrupole moment, Q, and its moment of inertia, $I \equiv J/\Omega$. Let us introduce dimensionless quantities $\bar{I} \equiv I/M_*^3$ and $\bar{Q} \equiv -Q/(M_*^3\chi^2)$, where $\chi \equiv J/M_*^2$ is the dimensionless spin parameter (*10*). I determines how fast a body can spin given a fixed J, whereas Q encodes the amount of stellar quadrupolar deformation. They are determined by numerically solving the perturbed Einstein equations for realistic EoSs in a slow-rotation expansion ($\chi \ll 1$) to first and second order in spin, respectively (*9*, *11*).

The slow-rotation approximation requires that χ be small enough such that all equations can be expanded in $\chi \ll 1$. In this approximation, the neglected corrections to I and Q are of $\mathcal{O}(\chi^2)$ smaller than the leading-order contributions. Thus, demanding that any subleading terms be less than 10% of the leading-order ones means that $\chi \ll 0.3$ or equivalently spin frequencies $\ll$ 600 Hz or spin periods $\gg$ 1.7 ms. "True" millisecond pulsars (with periods of ~1 ms) cannot be modeled in a slow-rotation expansion. However, double NS binary pulsars are expected to be spinning much more slowly, and the slow-rotation approximation should be allowed.

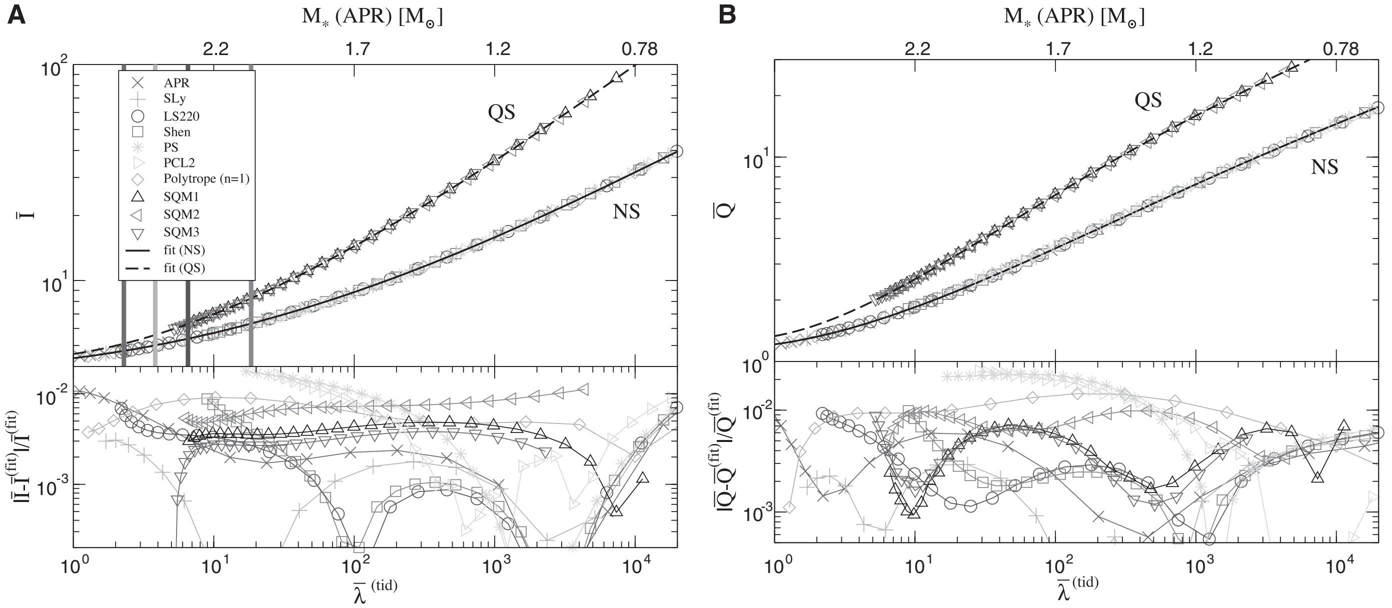

Fig. 1. I-Love and Q-Love relations. (**A** and **B**) (Top) The neutron star (NS) and quark star (QS) universal I-Love and Love-Q relations for various EoSs, together with fitting curves (solid and dashed curves). On the top axis, we show the corresponding NS mass with an APR EoS. The thick vertical lines show the stability boundary for the APS, SLy, LS220, and Shen EoSs from left to right. The parameter varied along each curve is the NS central density, or equivalently the NS compactness, with the latter increasing to the left of the plots. (Bottom) Fractional errors between the fitting curves and numerical results. $M_\odot$ indicates the mass of the Sun.

In the presence of a companion, a NS or a QS will also be quadrupolarly deformed. The quadrupole moment tensor determines the magnitude of this deformation: $Q_{ij} = -\lambda^{(\mathrm{tid})}\varepsilon_{ij}$, where $\lambda^{(\mathrm{tid})}$ is the tidal Love number and ε_{ij} is the quadrupole (gravitoelectric) tidal tensor that characterizes the source of the perturbation (*12*, *13*). The dimensionless tidal Love number, $\bar{\lambda}^{(\mathrm{tid})} = \lambda^{(\mathrm{tid})}/M_*^5$, characterizes the tidal deformability of a star in the presence of a companion, and it can be calculated by treating the tidal effects as a perturbation to an isolated (nonrotating) NS or QS solution (*9*, *13*).

One might have expected universal relations between $\bar{I}$, $\bar{Q}$, and $\bar{\lambda}^{(\mathrm{tid})}$ because $\bar{I} \propto C^{-2}$, $\bar{Q} \propto C^{-1}$, and $\bar{\lambda}^{(\mathrm{tid})} \propto C^{-5}$ for polytropic EoSs in the Newtonian limit (*9*), where $C = M_*/R_*$ is the compactness parameter with R_* the stellar radius. In the slow-rotation and small-deformation approximations, these barred quantities depend on spin only quadratically, and thus the relations are essentially spin-independent.

To find these relations, consider the following realistic EoSs for NSs: APR (*14*), SLy (*15*), Lattimer-Swesty with nuclear incompressibility of 220 MeV (LS220) (*16*), Shen (*17*), PS (*18*), PCL2 (*19*), and a simple $n = 1$ polytropic EoS with $p = K\rho^{1+1/n}$. For the LS220 and Shen EoSs, we adopt a temperature of 0.1 MeV and assume they are neutrino-less and in β-equilibrium. For QSs, we consider the EoSs: SQM1, SQM2, and SQM3 (*19*). We assume the stars are uniformly rotating, with isotropic pressure.

As shown in Fig. 1, the I-Love-Q relations hold universally for each NS and QS sequence, essentially independently of their EoSs for each class. Such relations can be numerically fitted with a polynomial on a log-log scale (*9*), shown in Fig. 1 with solid and dashed black curves:

$$\ln y_i = a_i + b_i \ln x_i + c_i (\ln x_i)^2 + d_i (\ln x_i)^3 + e_i (\ln x_i)^4 \quad (1)$$

where the coefficients are summarized in Table 1. The data in Fig. 1 were obtained by numerically solving the perturbed Einstein equations, which is unavoidable for realistic EoSs. For very simple polytropic EoSs, the equations can be solved analytically in the Newtonian limit, and we obtain similar universal and analytic relations (*9*).

Two possible reasons may explain the I-Love-Q relations. First, the mathematical relations that define I, $\lambda^{(\mathrm{tid})}$, and Q seem to depend mostly on the star's internal structure near its outer layer, where nuclear physics constrains realistic EoSs. The integral that defines I and Q in the Newtonian limit accumulates the most near the NS surface (*9*). This suggests that the relations should lose their universality for unrealistic EoSs that modify the star's internal structure near its surface. We have verified this explicitly by computing these relations for NSs with $n = 2$, 2.5, and 3 polytropic EoSs: the I-Love-Q curves deviate away from those in Fig. 1 as n increases. The NS and QS I-Love-Q relations present different universal behavior because their EoSs are drastically different in the low-density stellar region (*20*).

Table 1. Fit parameters. Estimated numerical coefficients for the fitting formulas of the NS and QS I-Love, I-Q, and Love-Q relations.

y_i	x_i	a_i	b_i	c_i	d_i	e_i
				NS		
$\bar{I}$	$\bar{\lambda}^{(\mathrm{tid})}$	1.47	0.0817	0.0149	2.87×10^{-4}	-3.64×10^{-5}
$\bar{I}$	$\bar{Q}$	1.35	0.697	−0.143	9.94×10^{-2}	-1.24×10^{-2}
$\bar{Q}$	$\bar{\lambda}^{(\mathrm{tid})}$	0.194	0.0936	0.0474	-4.21×10^{-3}	1.23×10^{-4}
				QS		
$\bar{I}$	$\bar{\lambda}^{(\mathrm{tid})}$	1.52	0.0100	0.0418	-2.26×10^{-3}	5.35×10^{-5}
$\bar{I}$	$\bar{Q}$	1.30	0.757	−0.139	7.87×10^{-2}	-7.29×10^{-3}
$\bar{Q}$	$\bar{\lambda}^{(\mathrm{tid})}$	0.286	0.126	0.0900	-1.13×10^{-2}	4.57×10^{-4}

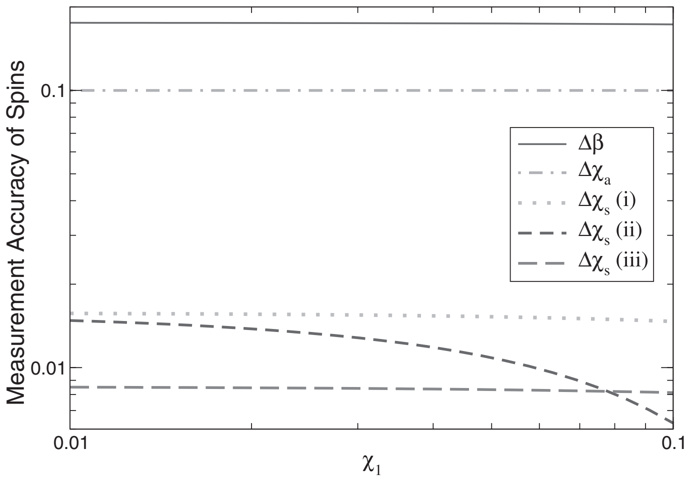

Fig. 2. Breaking spin degeneracies. Measurement accuracy of spin parameters β, χ_s, and χ_a using a Fisher analysis with Advanced LIGO, given a detection at a distance of D_L = 100 Mpc with signal-to-noise ratio ≈ 30. The spin-dependent part of the waveform phase is parameterized with the dimensionless averaged spin, χ_s, and spin difference, χ_a, when using the Love-Q relation and with the effective spin parameter β, constructed from a certain combination of the individual spins, when not using the relation. We consider three different NS binaries [(i), (ii), and (iii)], with parameters $(m_1,m_2) = (1.45,1.35)M_\odot$ and $\chi_1 = \chi_2$, $(m_1,m_2) = (1.45,1.35)M_\odot$ and $\chi_1 = 2\,\chi_2$, and $(m_1,m_2) = (1.4,1.35)M_\odot$ and $\chi_1 = \chi_2$, respectively. Δβ is computed without use of the NS Love-Q relation, whereas $\Delta\chi_{s,a}$ are computed by using this relation. Δβ and $\Delta\chi_a$ are almost identical for all systems, because they are dominated by their priors ($|\beta| < 0.2$ and $|\chi_a| < 0.1$). Thanks to the Love-Q relation, χ_s can be measured to ~0.01.

The second reason is related to the no-hair theorems of GR. Figure 1 shows that the NS and the QS I-Love-Q relations approach each other as compactness is increased and approach the expected I-Love-Q relations for black holes (BHs), that is, $\bar{I} \to 4$, $\bar{\lambda}^{(\mathrm{tid})} \to 0$, and $\bar{Q} \to 1$ (*9*). For BHs, all multipole moments of the exterior spacetime are related to the BH mass and spin (*21*, *22*) because of the no-hair theorems (*23*, *24*). But for NSs and QSs, such relations do not hold because of the lack of no-hair theorems for nonvacuum spacetimes. Our results suggest the existence of NS universal relations that are similar to the BH ones and perhaps hint at the existence of no-hair–like relations for nonvacuum spacetimes.

The I-Love-Q relations suggest an effacing of internal structure. This is not a consequence of the effacement principle (*25*) in GR, because the latter applies only to the motion of BHs. The I-Love-Q relations relate different multipole components of the exterior gravitational field of isolated, nonvacuum compact objects and say nothing about their relative motion.

Double NS binary pulsars may allow measuring I to 10% accuracy in the near future (*26*, *27*). This is because I induces additional periastron precession, as well as precession of the angular momentum vector and the NS spin vectors. The former translates into a time-dependent inclination angle, whereas the latter may force the pulsar beams to sweep in and out of Earth's line of sight. Alternatively, this precession may only cause a change in the observed average pulse shape, as in the Hulse-Taylor binary pulsar, in which case direct measurement may be more difficult.

Given a measurement of I, M, and Ω, the I-Love-Q relations automatically provide the value of $\lambda^{(\mathrm{tid})}$ and Q, assuming the star is either a NS or a QS. The latter would not be easily observable with binary pulsars directly; although Q and $\lambda^{(\mathrm{tid})}$ do induce additional precession, their effect is greatly suppressed relative to that of I. The I-Love-Q relations refer to reduced (barred) quantities, which must be appropriately normalized by the mass and the spin period. A small error in the latter could induce a large error in derived quantities. Such an error is smaller than the nonuniversality of the I-Love-Q relations if the NS spin period is much greater than 8.5 ms, which is the case for the double pulsar binary and a NS binary in the Laser Interferometer Gravitational Wave Observatory (LIGO) band.

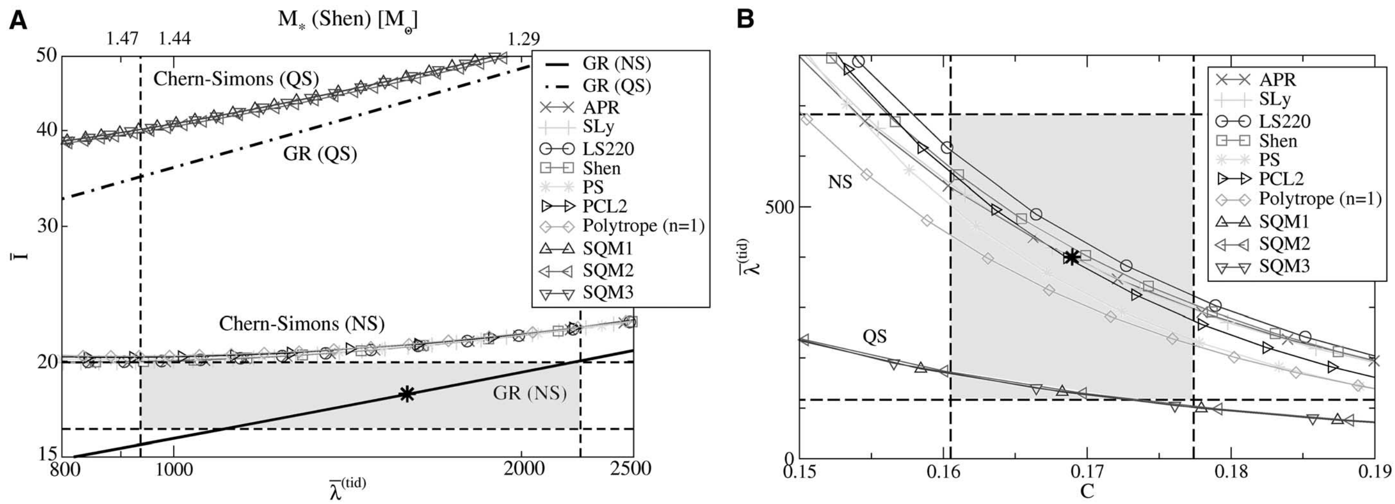

Fig. 3. Testing GR. (**A**) Error box (shaded region) in the I-Love plane, given two independent observations of I and $\lambda^{(\text{tid})}$ consistent with GR (black star) to 10% accuracy with a binary pulsar observation (*26*, *27*) and to 60% with a GW observation (*9*, *12*, *30*, *31*), respectively. The black solid and dotted-dashed lines show the GR NS and QS I-Love relations, respectively, whereas other lines show the relations in dynamical Chern-Simons (CS) gravity, which are still EoS-insensitive. This theory modifies Einstein's by introducing a gravitational parity-violating interaction through a dynamical scalar field, and it is currently constrained only very weakly by known tests and experiments (*32*). Given this observation, any modified theory would be constrained to predict an I-Love relation that runs through this shaded region. The CS I-Love relation lies above the GR one irrespective of the CS coupling constant; thus, this is an example of case a that would place a constraint on the theory that is 6 orders of magnitude stronger than current solar system ones (*33*). (**B**) Error box (shaded region) in the Love-C plane, given two independent observations of $\lambda^{(\text{tid})}$ and C consistent with GR (black star) to 60% accuracy with a GW observation (*9*, *12*, *30*, *31*) and to 5% with a future low-mass x-ray binary observation (*4*), respectively. The Love-C relation is dependent on the EoS, as shown by the spread in the curves. However, the difference between these curves is smaller than the error box, making the Love-C relation effectively EoS-independent and allowing for a generic test of GR.

Given independent measurements of any two members of the I-Love-Q trio, one could also distinguish NSs from QSs, assuming GR is correct. These relations are different for NSs and QSs, even though they are universal within their class of EoSs, as shown in Fig. 1. Given two such measurements with sufficiently small uncertainties, one could determine whether the observed compact object is a NS or a QS.

Interferometric GW detectors are most sensitive to the GW phase. For waves emitted during NS binary inspirals, the phase contains a term proportional to the NSs' spin-induced quadrupole moments, Q_1 and Q_2, and another term proportional to their tidally induced quadrupolar deformations, $\lambda_1^{(\text{tid})}$ and $\lambda_2^{(\text{tid})}$. The former enters with a factor proportional to v^4/c^4, where v is the orbital velocity of binary constituents (*28*), whereas the latter is proportional to v^{10}/c^{10} (*12*), relative to the leading-order term. Because by Kepler's third law $v \propto f^{1/3}$ (where f is the GW frequency), each term has a distinct GW frequency dependence that makes them nondegenerate.

The NS quadrupole moment is degenerate with the NSs' individual spins, because there is a spin-spin interaction term in the GW phase that enters at the same order in v/c as the quadrupole term (*28*). Such a degeneracy may prevent us from simultaneously extracting the quadrupole moment and the individual spins from a GW detection. However, the Love-Q relation can be used to break this degeneracy by rewriting Q as a function of $\lambda^{(\text{tid})}$. If the Love number can be measured with a GW detection, then one can also separately measure the spins, as shown in Fig. 2.

Pulsar observations allow GR tests (*8*) when the gravitational field is much stronger than that in the Solar System (*7*). Unfortunately, these tests are not effective most of the time because of degeneracies between modified gravity effects and the EoS. The I-Love-Q relations can be used to break this degeneracy.

A robust GR test would require at least two independent measurements of any two quantities in the I-Love-Q trio. Given a single measurement, the I-Love-Q relations give us the other two for a NS or a QS in GR. A second independent measurement can then be used as a redundancy test.

Depending on where the two observed values lie in the I-Love-Q plane, different tests are possible. If the two observables lie on the GR NS (QS) I-Love-Q line, then

1) Case a. The object is a NS (QS), and any modified gravity effect must be small enough to fit this observation.

2) Case b. The object is a QS (NS) in a modified gravity theory with the right coupling parameters to still fit this observation.

If the two observables lie on neither GR I-Love-Q line, then the observations would indicate a GR deviation, provided the assumptions made here are correct. An example of such a GR test is given in Fig. 3. One can carry out a similar test by using the Love-C relation (shown in Fig. 3), which is effectively universal.

References and Notes

1. A. E. H. Love, *Proc. R. Soc. London Ser. A* **82**, 73–88 (1909).
2. S. Postnikov, M. Prakash, J. M. Lattimer, *Phys. Rev. D* **82**, 024016 (2010).
3. J. M. Lattimer, M. Prakash, *Phys. Rep.* **442**, 109–165 (2007).
4. F. Ozel, *Rep. Prog. Phys.* **76**, 016901 (2013).
5. For example, the observation of x-ray bursters and low-mass x-ray binaries has allowed for the simultaneous determination of the star's mass and radius to $\mathcal{O}(10)$% accuracy (*4*). Observations of double NS pulsars, such as J0737-3039 (*29*), may allow for the measurement of the moment of inertia to the same accuracy (*26*, *27*). Gravitational wave (GW) observations from binary NS inspirals with second-generation ground-based detectors, such as Advanced LIGO, Advanced Virgo, and KAGRA, may allow for the measurement of the tidal Love number (*12*, *30*, *31*).
6. If the NS binary has misaligned spins, precession may break these degeneracies.
7. C. M. Will, *Living Rev. Relativ.* **9**, 3 (2006).
8. I. H. Stairs, *Living Rev. Relativ.* **6**, 5 (2003).
9. K. Yagi, N. Yunes (2013), http://arxiv.org/abs/1303.1528.
10. Throughout the paper, we use geometric units with G (Newton's gravitational constant) and c (the speed of light) set to unity.
11. J. B. Hartle, *Astrophys. J.* **150**, 1005 (1967).
12. E. E. Flanagan, T. Hinderer, *Phys. Rev. D* **77**, 021502 (2008).
13. T. Hinderer, *Astrophys. J.* **677**, 1216–1220 (2008).
14. A. Akmal, V. Pandharipande, D. Ravenhall, *Phys. Rev. C* **58**, 1804–1828 (1998).
15. F. Douchin, P. Haensel, *Astron. Astrophys.* **380**, 151–167 (2001).
16. J. M. Lattimer, F. Douglas Swesty, *Nucl. Phys. A* **535**, 331–376 (1991).
17. H. Shen, H. Toki, K. Oyamatsu, K. Sumiyoshi, *Nucl. Phys. A* **637**, 435–450 (1998).
18. V. R. Pandharipande, R. A. Smith, *Nucl. Phys. A* **237**, 507–532 (1975).
19. M. Prakash, J. R. Cooke, J. M. Lattimer, *Phys. Rev. D* **52**, 661–665 (1995).
20. J. Lattimer, M. Prakash, *Astrophys. J.* **550**, 426–442 (2001).
21. R. P. Geroch, *J. Math. Phys.* **11**, 2580 (1970).

22. R. O. Hansen, *J. Math. Phys.* **15**, 46 (1974).
23. S. W. Hawking, *Commun. Math. Phys.* **25**, 152–166 (1972).
24. B. Carter, *Phys. Rev. Lett.* **26**, 331–333 (1971).
25. T. Damour, *Gravitational Radiation*, N. Deruelle, T. Piran, Eds. (North-Holland, Amsterdam, 1983).
26. J. M. Lattimer, B. F. Schutz, *Astrophys. J.* **629**, 979–984 (2005).
27. M. Kramer, N. Wex, *Class. Quantum Gravity* **26**, 073001 (2009).
28. E. Poisson, *Phys. Rev. D* **57**, 5287–5290 (1998).
29. M. Burgay *et al.*, *Nature* **426**, 531–533 (2003).
30. T. Hinderer, B. D. Lackey, R. N. Lang, J. S. Read, *Phys. Rev. D* **81**, 123016 (2010).
31. T. Damour, A. Nagar, L. Villain, *Phys. Rev. D* **85**, 123007 (2012).
32. S. Alexander, N. Yunes, *Phys. Rep.* **480**, 1–55 (2009).
33. Y. Ali-Haimoud, Y. Chen, *Phys. Rev. D* **84**, 124033 (2011).

Acknowledgments: We thank E. O'Connor and B. Lackey for providing tabulated EoSs, as well as E. Berti, L. Blanchet, V. Cardoso, T. Hinderer, K. Hotokezaka, M. Kramer, L. Lindblom, F. Nakano, F. Özel, P. Pani, E. Poisson, S. Ransom, L. Rezzolla, M. Shibata, T. Tanaka, and four anonymous reviewers for their comments. We also thank the Yukawa Institute for Theoretical Physics at Kyoto University, where this work was initiated during the Long-Term Workshop YITP-T-12-03 on "Gravity and Cosmology 2012." N.Y. acknowledges support from NSF grant PHY-1114374, as well as support provided by NASA grant NNX11AI49G.

12 February 2013; accepted 20 June 2013
10.1126/science.1236462

Holographic Vortex Liquids and Superfluid Turbulence

Paul M. Chesler,* Hong Liu,* Allan Adams*

Superfluid turbulence is a fascinating phenomenon for which a satisfactory theoretical framework is lacking. Holographic duality provides a systematic approach to studying such quantum turbulence by mapping the dynamics of a strongly interacting quantum liquid into the dynamics of classical gravity. We use this gravitational description to numerically construct turbulent flows in a holographic superfluid in two spatial dimensions. We find that the superfluid kinetic energy spectrum obeys the Kolmogorov $-5/3$ scaling law, with energy injected at long wavelengths undergoing a direct cascade to short wavelengths where dissipation by vortex annihilation and vortex drag becomes efficient. This dissipation has a simple gravitational interpretation as energy flux across a black hole event horizon.

Superfluid turbulence is a non-equilibrium phenomenon dominated by the dynamics of quantized vortices (*1–7*), which drive the system outside the hydrodynamic regime of normal turbulent fluids. Powerful numerical simulations of phenomenological models of vortex dynamics have produced considerable insight. However, a complete theoretical framework remains lacking, and an ab initio study is desirable.

Here, we use holographic duality to study superfluid turbulence in two spatial dimensions. Holographic duality is a precise equivalence between certain systems of quantum matter without gravity and classical gravitational systems in a curved spacetime with one additional spatial dimension (*8–16*). This allows a first-principles study in these systems of superfluid dynamics, including turbulent flows, by using the corresponding gravity description of the superfluid phase. In this framework, dissipation in the gravitational description can be understood in terms of excitations falling through a black hole event horizon. This provides a direct measure of the rate of energy dissipation and its spectrum.

We focus on "non-counterflow" superfluid turbulence (*17–25*). Experimentally, these systems appear to obey Kolmogorov's $-5/3$ scaling law in the kinetic energy spectrum, which suggests a remnant similarity between quantum and classical turbulence. In classical turbulence, this scaling behavior can be understood as a consequence of an energy cascade in which the injected energy is passed from one scale to another without substantial loss. Whether quantum turbulence admits a similar cascade picture—and, if so, whether or when the cascade drives energy to long or to short wavelengths—remain important open questions. Several recent numerical studies of the phenomenological Gross-Pitaevskii equation in a two-dimensional (2D) superfluid (with dissipation put in by hand) observed Kolmogorov scaling but came to conflicting conclusions regarding the direction of the cascade (*26–29*).

To set up our superfluid, consider a quantum field theory in two spatial dimensions with a complex scalar operator, $\psi(x)$, carrying charge q under a global $U(1)$ symmetry. Let $j^\mu(x)$ denote the conserved current operator of this global $U(1)$ symmetry. To induce a superfluid condensate for ψ, we will turn on a chemical potential μ for the $U(1)$ charge. For sufficiently large μ, ψ can develop a nonzero expectation value $\langle\psi\rangle \neq 0$ when the temperature falls below a critical temperature T_c, spontaneously breaking the global $U(1)$ symmetry and driving the system into a superfluid phase.

We now construct a simple holographic model of our 2D superfluid. We begin with a classical field theory in an asymptotically anti–de Sitter spacetime with three spatial dimensions (AdS_4). Under the standard holographic dictionary, the conserved current $j^\mu(x)$ is mapped to a dynamical $U(1)$ gauge field $A_M(x, z)$ in the gravitational bulk, and the scalar operator $\psi(x)$ is mapped to a bulk scalar field $\Phi(x, z)$ carrying charge q under the gauge field A_M (where z is the radial coordinate of AdS_4) (*30*). A nonzero temperature corresponds to adding to the bulk spacetime a black hole whose horizon is a 2D plane extended in boundary spatial directions. Adding a chemical potential corresponds to imposing a boundary condition on the bulk gauge field $A_t = \mu$ at the boundary of AdS_4 (*31*). If the charge q and scaling dimension Δ of ψ lie in certain range (*32*, *33*), a sufficiently large μ drives the bulk scalar field Φ to condense through the Higgs mechanism. Different values of the charge q and potential for Φ define different holographic quantum theories, each with a low-temperature superfluid phase (*34*, *35*). We choose a quadratic potential with a mass for Φ corresponding to ψ having scaling dimension $\Delta = 2$, and we work in the limit of large q [the probe limit of (*33*); see supplementary text].

A superfluid state generically has gapped vortex excitations, which play an important role in our discussion below. Around a vortex, the fluid circulation is quantized. Introducing the (unnormalized) superfluid velocity

$$\mathbf{u} \equiv \frac{\mathcal{J}}{|\langle\psi\rangle|^2}, \quad \mathcal{J} \equiv \frac{i}{2}[\langle\psi^*\rangle\nabla\langle\psi\rangle - \langle\psi\rangle\nabla\langle\psi\rangle^*] \tag{1}$$

the winding number W of a vortex is determined by

$$W = \frac{1}{2\pi}\oint_\Gamma d\mathbf{x}\cdot\mathbf{u} \tag{2}$$

where the path Γ encloses a single vortex and is oriented counterclockwise. Boldface symbols denote vectors along boundary spatial directions; $\mathbf{x} \equiv \{x_1, x_2\}$, where x_i denotes the two spatial directions and $\nabla = \{\partial/\partial x_1, \partial/\partial x_2\}$. Vortices map into the gravitational bulk as flux tubes extending along the AdS radial direction from the boundary, where they have a characteristic size $1/\mu$, to the horizon. Inside the flux tube, the condensate goes to zero, effectively punching a hole through the bulk scalar condensate. Explicit gravity solutions corresponding to a static vortex of arbitrary winding number were previously constructed numerically (*36–38*).

The gravity dual thus provides a first-principles description of superfluid flows involving vortices, as well as tools to describe dissipation in the system. Consider turning on a perturbation of j^μ in the boundary theory, which on the gravity side cor-

Department of Physics, Massachusetts Institute of Technology, Cambridge, MA 02139, USA.

*Corresponding author. E-mail: awa@mit.edu (A.A.); pchesler@mit.edu (P.M.C.); hong_liu@mit.edu (H.L.)

responds to turning on a perturbation of A^M near the boundary. Above T_c, the disturbance quickly falls into the black hole, corresponding to the perturbation in the current j^μ quickly dissipating into heat. Below T_c, however, the scalar condensate essentially "screens" the black hole from boundary. As a result, a $U(1)$ disturbance cannot reach the horizon to dissipate, and the perturbation in the current j^μ persists. This is the bulk realization of the nondissipative nature of a superfluid. In the presence of vortices, the flux tube corresponding to a vortex punches a hole through the bulk scalar condensate. Perturbations may then dissipate by flowing along these flux tubes into the horizon [in a manner somewhat reminiscent of Kelvin waves flowing along vortex strings in 3D quantum turbulence (*7*, *39*)]. This implies that vortices can only dissipate modes with wavelengths smaller than the typical vortex size (Fig. 1). The holographic picture thus strongly suggests a direct cascade on very general grounds.

To quantify the energy flux through the black hole horizon in the probe limit, consider $\mathcal{T}^M_N$, the probe stress tensor of A_M and Φ in the bulk. Covariant conservation of $\mathcal{T}^M_N$ implies that the bulk tensor

$$\tau^M_\mu \equiv \sqrt{-g}\,\mathcal{T}^M_\mu \qquad (3)$$

is conserved

$$\partial_\mu \tau^\mu_\nu = -\partial_z \tau^z_\nu \qquad (4)$$

where g is the determinant of the bulk metric. Equation 4 means that the nonconservation of τ^μ_ν along the boundary directions is equal to the flux τ^z_ν along the radial direction (see supplementary text). The (positive) flux of energy through the horizon

$$Q_{\text{horizon}}(t) \equiv -\int d^2x\ \tau^z_t(t,\mathbf{x},z)|_{\text{horizon}} \qquad (5)$$

is irreversibly lost and should be thought of as energy lost to heat.

We now numerically solve the bulk equations of motion for a variety of initial conditions and describe the resulting turbulent flows (*40*). Working in units in which the temperature is $T = 3/(4\pi)$, we set the chemical potential to be $\mu = 6$ and work within a 100×100 periodic box. A typical initial condition involves a square periodic lattice of winding number $W = \pm 6$ vortices, with winding number alternating at each lattice site and with lattice spacing $b = 100/8$ (*41*) (Fig. 2, left). We evolve the system for a total period of time $\Delta t = 600$. The evolution of the system can be roughly divided into three stages: (i) a homogenization regime ($t < 160$), (ii) a scaling regime ($160 < t < 500$), and (iii) a relaxation regime ($t > 500$). Turbulent behavior, including the Kolmogorov scaling in the kinetic energy, is observed in the scaling regime.

In the homogenization regime, the system evolves from an ordered, inhomogeneous initial state (Fig. 2, left) to a chaotic, quasi-homogeneous state (Fig. 2, right). In this regime, the initial $W = \pm 6$ vortices each decay abruptly into six smaller $W = \pm 1$ vortices. As time passes, vortices of opposite winding number $W = \pm 1$ collide and annihilate. Because vortices in the superfluid are gapped excitations, with the gap scaling as W^2, the merging of vortices is heavily suppressed energetically and is not observed in our simulations.

By time $t \approx 160$, the $W = \pm 1$ vortex annihilation rate begins to decrease, and the system enters the scaling regime. The system is now turbulent,

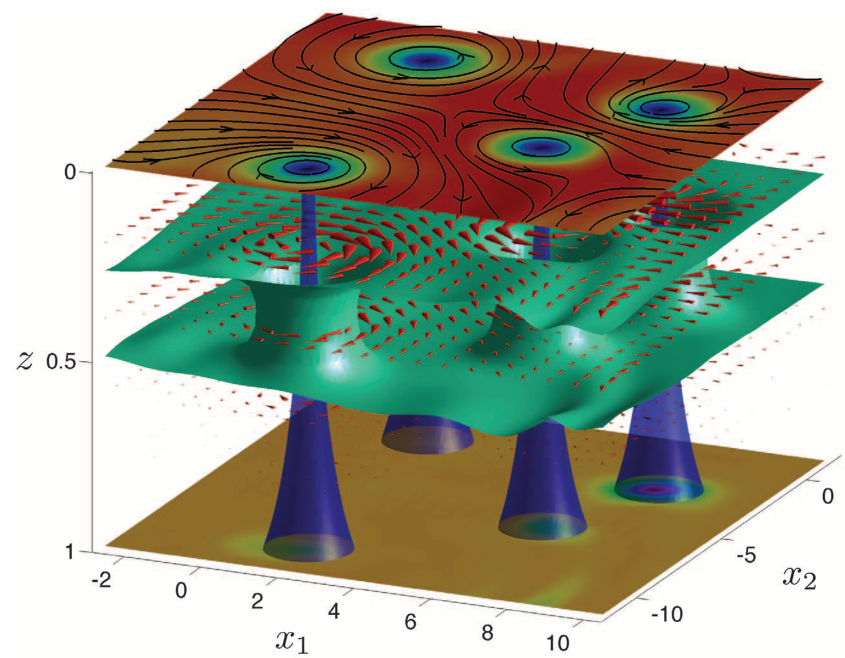

Fig. 1. Holographic description of a superfluid with vortices. The vertical axis is the radial direction z of AdS_4. The planes $z = 0$ and $z = 1$ are the boundary of AdS_4 and the black hole horizon, respectively. The green surface is a surface of constant bulk charge density, with the region between the two slices defining a "slab" of condensate where most bulk charges reside. The slab screens excitations from falling into the horizon. This can be seen from the vector field (red arrows) indicating the energy flux $(-\tau^x_0, -\tau^y_0, -\tau^z_0$ of Eq. 3, which vanishes rapidly below the slab. The vortices (blue tubes) punch holes through this screening slab, providing avenues for excitations to fall into the black hole. The surface $z = 0$ shows the condensate on the boundary (with blue representing zero condensate), superposed with flow lines of the superfluid velocity (Eq. 1). The $z = 1$ surface shows the flux of energy through the horizon. This energy flux is significant (red and green) only near the wake of the moving vortices, as is most easily seen in movies of the simulation available at http://turbulent.lns.mit.edu/Superfluid.

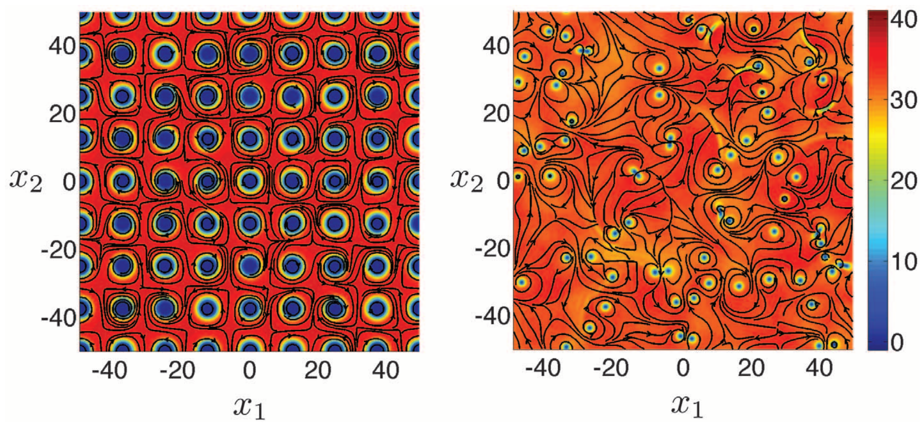

Fig. 2. The superfluid condensate $|\langle\psi\ (t, x)\rangle|^2$ at time $t = 0$ (left) and $t = 300$ (right). Flow lines of the superfluid current $\mathcal{J}\ (t, x)$ (defined in Eq. 1) are superimposed. The superfluid current circulates around the core of each vortex, where the condensate vanishes. The $W = \pm 6$ vortices (left) are much larger than the $W = \pm 1$ vortices (right). The yellow arcs seen in the right panel are waves produced by the annihilation of vortex pairs.

characterized by a random, yet homogeneous (at large scales), distribution of a large number of vortices and antivortices of unit winding (Fig. 2, right). The motion of the vortices is highly irregular, and the location and velocity of the vortex cores at any given time are extremely sensitive to initial conditions.

The defining feature of the scaling regime is that the system exhibits the Kolmogorov $-\frac{5}{3}$ scaling law, which can be seen in the behavior of the "kinetic energy" density

$$\varepsilon_{\text{kin}}(t,\mathbf{x}) \equiv \frac{1}{2}\mathcal{V}^*(t,\mathbf{x})\cdot\mathcal{V}(t,\mathbf{x}) \qquad (6)$$

where $\mathcal{V} = \langle\psi\rangle\mathbf{u}$. If we introduce a spatial Fourier transform, the total "kinetic energy" can be written as an integral over momentum

$$E_{\text{kin}}(t) = \int d^2x\ \mathcal{E}_{\text{kin}}(t,\mathbf{x}) = \int_0^\infty dk\ \varepsilon_{\text{kin}}(t,k) \qquad (7)$$

where

$$\varepsilon_{\text{kin}}(t,k) = \frac{1}{2}\int_0^{2\pi} d\theta\ k\ \mathcal{V}^*(t,\mathbf{k})\cdot\mathcal{V}(t,\mathbf{k}) \qquad (8)$$

with the θ integral summing over directions of **k**. In the original derivation of the $\varepsilon_{\text{kin}} \sim k^{-5/3}$ scaling, Kolmogorov assumed the existence of an inertial range $k \in (\Lambda_-, \Lambda_+)$ where the energy spectrum (per unit mass) depends only on the scale k and the mean rate of energy dissipation per unit mass $\mathcal{E}$. With these assumptions, nonrelativistic dimensional analysis then yields $\varepsilon_{\text{kin}} \sim \mathcal{E}^{2/3}k^{-5/3}$. Although our system is microscopically relativistic, our flows empirically become nonrelativistic well before the onset of the turbulent regime (see supplementary text), so a $k^{-5/3}$ spectrum should be expected when the flow is turbulent and an inertial range appears.

In our simulations, we find that $\varepsilon_{\text{kin}}(t, k)$ does indeed obey a $k^{-5/3}$ scaling (Fig. 3A, red dashed line) during the scaling regime ($160 < t < 500$) over the inertial range $k \in (0.4, 3)$. This translates into length scales (2, 16) (recall that our box size is 100 × 100). The average vortex spacing at this time is about 10, falling in the middle of the scaling region. For $k > 3$, ε_{kin} scales as k^{-3} (Fig. 3A, green dashed line). This behavior appears as soon as the initial $W = 6$ vortices decay and persists until the end of our simulation. This scaling arises from the short-distance behavior of $\mathcal{V}(\mathbf{x})$ near vortex cores, and thus reflects single-vortex physics rather than collective physics or turbulence (see supplementary text).

The $k^{-5/3}$ scaling persists until the end of our simulation at $t = 600$, but for $t > 500$, the scaling behavior becomes less and less sharp (fig. S2, left). By $t = 500$, vortex annihilation has reduced the number of $W = \pm1$ vortices by roughly an order of magnitude. For initial data whose evolution does not generate any vortices, we do not find any universal scaling behavior of ε_{kin}; the scaling behavior $\varepsilon_{\text{kin}} \sim k^{-5/3}$ appears to depend on having a homogeneous vortex liquid (fig. S2, right).

With Kolmogorov scaling established, we now demonstrate that the system exhibits a direct energy cascade. As discussed above, a precise measure of dissipation in our system comes from the dual gravitational physics. In that description, any energy that flows into the horizon is irreversibly lost and therefore should be thought of as energy lost to heat. As Fig. 1 suggests, one can analyze how the flux of energy, $-\tau_t^z$, through the horizon correlates with the location of vortices in the superfluid and with vortex annihilation events, and thereby assess the dissipation mechanisms.

At time $t = 300$, the flux through the horizon (Fig. 3B) is zero nearly everywhere, except in the neighborhood of a few isolated points. Comparison with the right panel of Fig. 2 reveals that the flux is nonzero at points corresponding to the location of vortices. This contribution to the flux persists at all times and is always localized at the position of the vortices; we therefore identify it as vortex drag. Also present (Fig. 3B) are large but sparse contributions to the flux from vortex annihilation events (as can be seen from comparison with Fig. 2); the arcs seen in the upper right corner are remnants of previous vortex annihilation events.

That the energy flux through the horizon is nonzero only in the neighborhood of vortices or vortex annihilation events adds considerable support to the physical picture described in Fig. 1, and suggests that energy is dissipated in the ultraviolet (UV). To quantify this statement, we plot the flux correlation function

$$F(t,r) \equiv \int d^2x \int d\theta\ \tau_t^z(t,\mathbf{x}+\mathbf{r},z)\tau_t^z(t,\mathbf{x},z)\big|_{\text{horizon}} \qquad (9)$$

and the dissipative correlation length $\xi(t)$, defined by the full width at half maximum of $F(t, r)$ at time $t = 300$ (fig. S3); here, θ is the polar angle for **r**, and $r = |\mathbf{r}|$ is its norm. The correlation function is localized about $r = 0$ and rapidly vanishes for large r; after time $t = 100$, $\xi(t) \approx 1$. That $\xi(t)$ is roughly constant reflects the fact that vortex drag and annihilation do not dissipate energy at wildly different scales and that annihilation events, which dissipate at slightly larger length scales than drag, are rare. One can therefore define a dissipative momentum scale $k_{\text{diss}} = 2\pi/\xi \approx 2\pi$. Thus, k_{diss} lies outside of the inertial range, $k_{\text{diss}} > \Lambda_+$. Note that the length scale ξ is measured in units in which $T = 3/(4\pi)$.

The dissipation scales ξ and k_{diss} are controlled by the chemical potential. For example, repeating the same analysis for turbulent flows with $\mu = 7$ modifies the above results in two correlated ways (fig. S4). First, the mean dissipation correlation length ξ decreases by a factor of roughly 1.3. Second, the UV knee in the energy spectrum, Λ_+, which defines the UV end of the scaling regime, increases by a factor of roughly

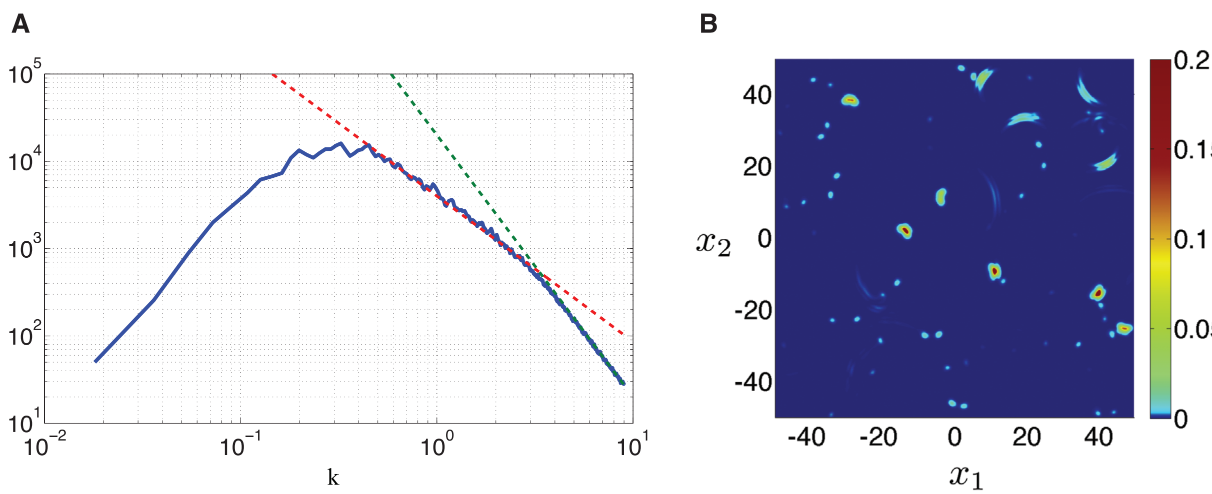

Fig. 3. Energy spectrum and energy flux. (**A**) The energy spectrum $\varepsilon_{\text{kin}}(t,k)$ at time $t = 300$. The red dashed line is the Kolmogorov scaling $k^{-5/3}$, and the green dashed line is k^{-3}. (**B**) The flux of energy, $-\tau_t^z$, through the horizon at time $t = 300$. The flux is zero nearly everywhere except at the location of vortices (shown in Fig. 2) and is largest during vortex annihilation events.

1.3. This correlation reinforces the idea that the knee is set by dissipation at the vortex scale and the vortex core size. By contrast, the infrared (IR) knee at Λ_- is controlled by the injection scale, which is limited in our simulations by the size of our numerical box and the precise mechanism of energy injection via the unstable vortex lattice.

The preference for energy to dissipate in the UV suggests that the system is undergoing a direct cascade: Energy is being transported from the IR through the inertial range $k \in (\Lambda_-, \Lambda_+)$ and dissipated at $k_{\text{diss}} > \Lambda_+$. To test whether this picture is correct, we gently drive the system during the scaling regime by turning on a weak source for the conserved current j^μ, injecting energy into the system. We do this at specific scales k_{inject} and examine whether the injected energy gets transferred to other scales, both in the dual gravitational description and in the superfluid description. The crucial tools are again the energy flux through the horizon (Eq. 5) and the superfluid kinetic energy spectrum (Eq. 8).

In the presence of an external source a_μ for j^μ, Eq. 4 can be integrated to give the rate of change of the bulk energy

$$\partial_t \int d^2\mathbf{x}\, dz[-\tau_t^t(t,\mathbf{x},z)] = Q_{\text{boundary}}(t) - Q_{\text{horizon}}(t) \tag{10}$$

where Q_{horizon} was introduced in Eq. 5 and Q_{boundary} is the power injected from the boundary

$$\begin{aligned} Q_{\text{boundary}} &= -\int d^2x\, \tau_t^z(t,\mathbf{x},z)|_{\text{boundary}} \\ &= \frac{1}{2}\int d^2x\, E_i(t,\mathbf{x})\langle j^i(t,\mathbf{x})\rangle \end{aligned} \tag{11}$$

and E_i is the boundary "electric field" defined by $E_i = -\partial_t a_i + \partial_i a_t$. Up to the prefactor, the last equality is, of course, what one would expect from electromagnetism (see supplementary text). By comparing the controllable injection scale k_{inject} of Q_{boundary} and measuring the dissipative scale k_{diss} at the horizon, we can then extract the direction of energy transfer in the dual gravitational description.

We first consider driving the system at long wavelengths, $k_{\text{inject}} = 0$. During the scaling regime of the turbulent flow, we turn on the following homogeneous "electric" field for a brief period of time

$$\begin{aligned} E_x(t) &= \eta(t - t_o)g(t - t_o), \\ E_y(t) &= -E_x(t) \end{aligned} \tag{12}$$

where η is a small constant, $t_o = 230$, and $g(t)$ is a Gaussian of width 8. The electric field first pushes and then pulls, so the net momentum transferred to the system is approximately zero and is sufficiently weak that no new vortices are formed.

In the dual gravitational description, energy is injected by the electric field in a $k_{\text{inject}} = 0$ mode from the boundary ($z = 0$ in Fig. 1). The injected energy is then transferred via the nonlinear bulk dynamics to ever shorter wavelengths and eventually, via vortices, to the horizon ($z = 1$ in Fig. 1) where it can dissipate. In our simulations, the resulting dissipative correlation length is essentially identical to that of the undriven system (fig. S5). Therefore, the injected energy is dissipated through the vortex cores at the scale $k_{\text{diss}} = 2\pi/\xi \sim 2\pi$. This transfer of energy from the IR injection scale to a UV scale set by the vortex core is a telltale signature of a direct cascade.

The direction of the cascade can also be deduced from the evolution of the kinetic energy spectrum (Eq. 8). Figure 4 shows a comparison of the evolution of the energy spectrum between the driven and undriven systems with the same initial conditions. When the electric field begins to turn on around time $t = 210$, it adds energy to the system at low k. When the electric field turns off around time $t = 260$, the spectra of the driven and undriven systems agree deep in the UV. However, there is a considerable surplus of kinetic energy around $k = 0.4$ for the driven system. As time progresses, this surplus of energy propagates deeper into the UV; there is a flow of energy from the IR to the UV. At time $t = 315$, this results in an upward shift of the entire spectrum for $k > 0.4$ relative to the undriven system. Again, this behavior is a signature of a direct cascade. By contrast, when we inject energy in the UV, $k_{\text{inject}} > \Lambda_+$, the injected energy dissipates away without modifying the kinetic energy spectrum in the IR (fig. S6).

Our results were obtained at finite temperature T; however, from the perspective of the dual gravitational physics, it is expected that the qualitative physics presented above—and in particular, the direction of the cascade—remains the same in the limit of low temperature. In the gravitational description, the finite temperature is encoded by the presence of a black hole whose horizon recedes from the AdS boundary as the temperature is lowered. The low-T limit thus corresponds to the horizon receding deep into the interior. However, as illustrated in Fig. 1, the horizon is screened from $U(1)$ excitations by the presence of a slab of charged condensate, with the position of the slab set by the chemical potential. The slab effectively decouples dynamics near the boundary from dynamics below the slab. Consequently, we do not expect a qualitative change in the near-boundary physics (and hence superfluid physics) in the $T \to 0$ limit. A rigorous check of this intuition will require going beyond the probe limit.

A question much discussed in the literature (*4*–*6*) is whether the Kolmogorov scaling observed in non-counterflow quantum turbulence (*17*–*25*) has a classical origin. For example, experiments in (*17*–*19*) studied turbulence on scales much larger than the typical vortex spacing; at these scales, superfluid flows would be expected to resemble those of classical fluids. Our results

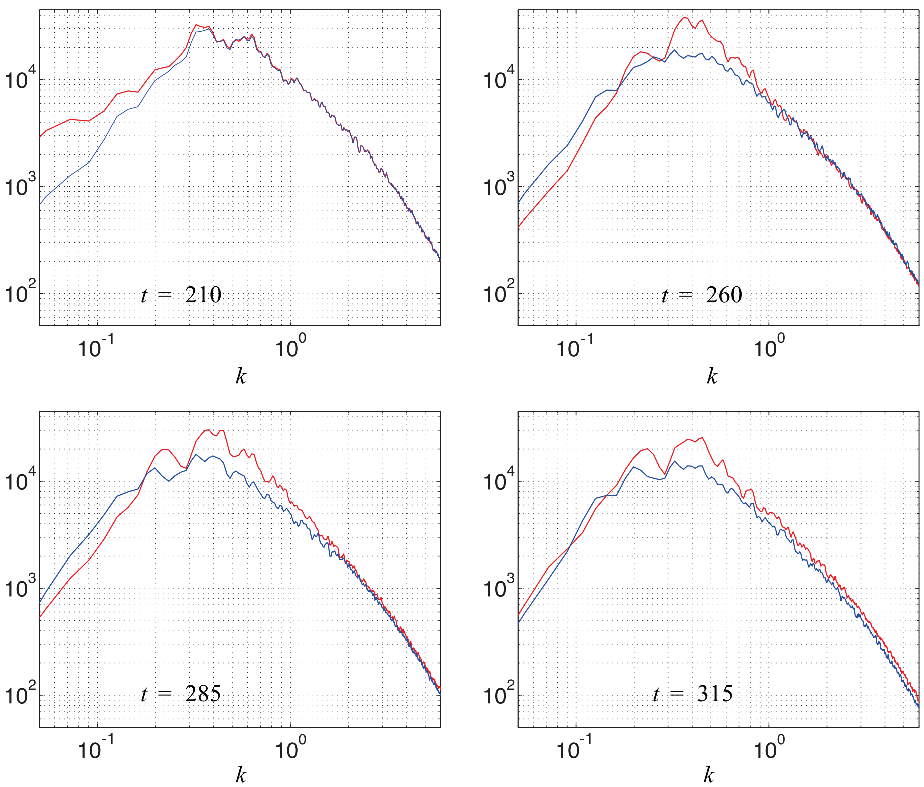

Fig. 4. The time evolution of the energy spectra for driven (red) and undriven (blue) systems. Driving adds energy in the IR in the time range $210 < t < 260$. As time progresses, the added energy propagates from the IR to the UV, where it is dissipated.

suggest that quantum effects are crucial (*42*), because classical turbulence has an inverse cascade in (2+1) dimensions, whereas quantum turbulence—at least in the systems and regimes we have studied—gives a direct cascade. Furthermore, as discussed earlier, the average vortex spacing in our system (~10) falls inside the inertial range (2, 16). Because vortex spacing provides the characteristic length scale at which quantum effects are important, the Kolmogorov scaling observed here would appear to be tightly intertwined with the quantum nature of the fluid. We note that the argument for Kolmogorov scaling only assumes the existence of an inertial range of k values in which the only scale in the system is the overall rate of dissipation, $\mathcal{E}$. This assumption by itself does not require the fluid to be classical or quantum, so the Kolmogorov scaling could well arise from the quantum phenomena seen in our simulations.

Many aspects of superfluid turbulent flow await further investigation, including a better understanding of the physics of vortex drag and annihilation, the dependence of the turbulent phase on parameters such as the mean vortex density, and the physics governing the IR end of the inertial range. Studies of other observables of the superfluid flow, such as velocity statistics, have yielded tantalizing differences between classical and quantum turbulence (*43*, *44*). Attempts to derive the Kolmogorov scaling directly from the holographic dual may also be worthwhile.

Because normal fluids in two spatial dimensions typically experience an inverse cascade, it will be of interest to see how the system behaves depending on the relative weights of the normal and superfluid components. For this purpose, one must go beyond the probe limit we have used here, so as to allow the superfluid flow to interact with the normal fluid component. In the dual gravitational description, this would require inclusion of the back-reaction of the gauge field A_M and scalar field Φ on the bulk geometry, and hence would require the use of numerical relativity to determine the evolution of the system.

References and Notes

1. R. Feynman, *Prog. Low Temp. Phys.* **1**, 17–53 (1955).
2. W. F. Vinen, *Proc. R. Soc. A* **240**, 114–127 (1957).
3. W. F. Vinen, *Proc. R. Soc. A* **240**, 128–143 (1957).
4. W. F. Vinen, *Proc. R. Soc. A* **242**, 489–515 (1957).
5. W. F. Vinen, J. J. Niemela, *J. Low Temp. Phys.* **128**, 167–231 (2002).
6. M. S. Paoletti, D. P. Lathrop, *Annu. Rev. Condens. Matter Phys.* **2**, 213–234 (2011).
7. M. Tsubota, M. Kobayashi, H. Takeuchi, *Phys. Rep.* **522**, 191–238 (2013).
8. J. M. Maldacena, *Adv. Theor. Math. Phys.* **2**, 231 (1998).
9. S. Gubser, I. R. Klebanov, A. M. Polyakov, *Phys. Lett. B* **428**, 105–114 (1998).
10. E. Witten, *Adv. Theor. Math. Phys.* **2**, 253 (1998).
11. S. A. Hartnoll, *Class. Quantum Gravity* **26**, 224002 (2009).
12. C. P. Herzog, *J. Phys. A* **42**, 343001 (2009).
13. J. McGreevy, *Adv. High Energy Phys.* **2010**, 723105 (2010).
14. J. Casalderrey-Solana, H. Liu, D. Mateos, K. Rajagopal, U. A. Wiedemann, http://arxiv.org/abs/1101.0618 (2011).
15. A. Adams, L. D. Carr, T. Schäfer, P. Steinberg, J. E. Thomas, *N. J. Phys.* **14**, 115009 (2012).
16. Holography, for our present purposes, provides a set of tractable toy models of strongly interacting quantum many-body systems with which we can explore the space of what is possible, and possibly generic, in such strongly interacting systems. In the longer term, we aim to build realistic models using these holographic tools. Precisely how robust or transferable the present results are to real-world systems remains an open question.
17. J. Maurer, P. Tabeling, *Europhys. Lett.* **43**, 29–34 (1998).
18. M. R. Smith, R. J. Donnelly, N. Goldenfeld, W. F. Vinen, *Phys. Rev. Lett.* **71**, 2583–2586 (1993).
19. S. R. Stalp, L. Skrbek, R. J. Donnelly, *Phys. Rev. Lett.* **82**, 4831–4834 (1999).
20. E. A. L. Henn, J. A. Seman, G. Roati, K. M. F. Magalhães, V. S. Bagnato, *Phys. Rev. Lett.* **103**, 045301 (2009).
21. J. A. Seman *et al.*, *J. Phys. Conf. Ser.* **264**, 012004 (2011).
22. C. Nore, M. Abid, M. E. Brachet, *Phys. Rev. Lett.* **78**, 3896–3899 (1997).
23. T. Araki, M. Tsubota, S. K. Nemirovskii, *Phys. Rev. Lett.* **89**, 145301 (2002).
24. M. Kobayashi, M. Tsubota, *Phys. Rev. Lett.* **94**, 065302 (2005).
25. N. G. Parker, C. S. Adams, *Phys. Rev. Lett.* **95**, 145301 (2005).
26. T.-L. Horng, C.-H. Hsueh, S.-W. Su, Y.-M. Kao, S.-C. Gou, *Phys. Rev. A* **80**, 023618 (2009).
27. R. Numasato, M. Tsubota, *J. Low Temp. Phys.* **158**, 415–421 (2010).
28. R. Numasato, M. Tsubota, V. S. L'Vov, *Phys. Rev. A* **81**, 063630 (2010).
29. M. T. Reeves, T. P. Billam, B. P. Anderson, A. S. Bradley, *Phys. Rev. Lett.* **110**, 104501 (2013).
30. We label boundary indices by μ, ν, … and bulk indices by M, N, …, with $A_M = (A_\mu, A_z)$.
31. This gravitational system is dual to a conformal field theory; however, conformal symmetry is broken by both the chemical potential and the temperature, so the conformal symmetry plays no role in what follows.
32. S. S. Gubser, *Phys. Rev. D* **78**, 065034 (2008).
33. S. A. Hartnoll, C. P. Herzog, G. T. Horowitz, *Phys. Rev. Lett.* **101**, 031601 (2008).
34. F. Denef, S. A. Hartnoll, *Phys. Rev. D* **79**, 126008 (2009).
35. S. S. Gubser, C. P. Herzog, S. S. Pufu, T. Tesileanu, *Phys. Rev. Lett.* **103**, 141601 (2009).
36. T. Albash, C. V. Johnson, *Phys. Rev. D* **80**, 126009 (2009).
37. M. Montull, A. Pomarol, P. J. Silva, *Phys. Rev. Lett.* **103**, 091601 (2009).
38. V. Keränen, E. Keski-Vakkuri, S. Nowling, K. Yogendran, *Phys. Rev. D* **81**, 126012 (2010).
39. B. V. Svistunov, *Phys. Rev. B* **52**, 3647–3653 (1995).
40. Because different initial conditions lead to qualitatively similar late-time behaviors, we focus for definiteness on a typical example. Images and videos from these simulations are available at http://turbulent.lns.mit.edu/Superfluid.
41. As we discuss below, the winding number $W = \pm 6$ vortices rapidly decay into six $W = \pm 1$ vortices. Therefore, by adjusting the lattice constant and initial winding number, these initial conditions allow us to control the initial density of $W = \pm 1$ vortices.
42. Although our 3D gravitational calculations have been purely classical, the 2D liquid captured by these calculations is a strongly interacting quantum superfluid; the fact that the dynamics of this quantum liquid are captured by classical geometric quantities is an example of the power of the holographic description.
43. M. S. Paoletti, M. E. Fisher, K. R. Sreenivasan, D. P. Lathrop, *Phys. Rev. Lett.* **101**, 154501 (2008).
44. A. C. White, C. F. Barenghi, N. P. Proukakis, A. J. Youd, D. H. Wacks, *Phys. Rev.* **104**, 075301 (2010).

Acknowledgments: We thank L. Lehner, J. McGreevy, D. Pesin, and L. Yaffe for helpful conversations, and S. Hartnoll for pointing out an error in a previous version of this paper. A.A. thanks the Stanford Institute for Theoretical Physics for hospitality during early stages of this work and the Aspen Center for Physics during its completion. Supported by a Pappalardo Fellowship in Physics at MIT (P.M.C.), a Simons Fellowship (H.L.), and U.S. Department of Energy Office of Nuclear Physics grant DE-FG02-94ER40818.

Supplementary Materials
www.sciencemag.org/cgi/content/full/341/6144/368/DC1
Supplementary Text
Figs. S1 to S6
References (*45*, *46*)

3 December 2012; accepted 19 June 2013
10.1126/science.1233529

Element-Resolved Corrosion Analysis of Stainless-Type Glass-Forming Steels

M. J. Duarte,[1,2,3,4]*† J. Klemm,[1]† S. O. Klemm,[1] K. J. J. Mayrhofer,[1] M. Stratmann,[1] S. Borodin,[1] A. H. Romero,[2,5]‡ M. Madinehei,[3] D. Crespo,[3] J. Serrano,[6] S. S. A. Gerstl,[4]§ P. P. Choi,[4] D. Raabe,[4] F. U. Renner[1]*||

Ultrathin passive films effectively prevent the chemical attack of stainless steel grades in corrosive environments; their stability depends on the interplay between structure and chemistry of the constituents iron, chromium, and molybdenum (Fe-Cr-Mo). Carbon (C), and eventually boron (B), are also important constituents of steels, although in small quantities. In particular, nanoscale inhomogeneities along the surface can have an impact on material failure but are still poorly understood. Addressing a stainless-type glass-forming $Fe_{50}Cr_{15}Mo_{14}C_{15}B_6$ alloy and using a combination of complementary high-resolution analytical techniques, we relate near-atomistic insights into increasingly inhomogeneous nanostructures with time- and element-resolved dissolution behavior. The progressive elemental partitioning on the nanoscale determines the degree of passivation. A detrimental transition from Cr-controlled passivity to Mo-controlled breakdown is dissected atom by atom, demonstrating the importance of nanoscale knowledge for understanding corrosion.

The environmental degradation of metals by chemical reactions in humid atmospheres or electrolytes results in substantial worldwide annual losses. In applications where corrosion is a critical factor, typically corrosion-resistant polycrystalline Ni-based materials or relatively inexpensive Fe-based steels are employed. In these stainless materials, Cr plays a vital role

in establishing protective passive oxide films of a few atomic layers (*1*–*3*), which show improved stability by combination with Mo (*4*, *5*). Glassy alloys, including amorphous steels, have gained attention, in part due to their extraordinary corrosion and pitting resistance at comparatively low Cr contents (*6*–*9*). Additionally, an improved mastering of production (*10*) opens promising applications ranging from structural gadgets to biocompatible implant materials (*11*–*13*). Moreover, the chemical and structural homogeneity of amorphous steel alloys have been recognized as an important asset for addressing fundamentally the influence of alloying elements on their macroscopic behavior such as corrosion (*7*, *14*, *15*). The metastable glassy structure can be devitrified by gentle annealing (*16*), which enables well-defined intermediate states of nanoscale elemental inhomogeneity. Although inhomogeneities exist on the nanoscale, the annealed structures are homogeneous on the macro scale. Microscopic insights of bulk material can thus be related to macroscopic performance.

Addressing the nanoscale characteristics of passive films of complex stainless steels remains a challenge. Considerable progress in understanding the laterally averaged structure and chemistry of the ultrathin passive films has been achieved by surface analysis techniques (*6*, *17*, *18*). Despite their importance, however, the influence of nanoscale inhomogeneities on the film reactions such as crystallographic defects, small-scale inclusions, precipitates, grain boundaries, or simple chemical variations along surfaces remains largely unresolved and is still key for advancing modern materials development and corrosion research (*19*–*21*). The passive films effectively change or block the dissolution of metallic materials in their specific environment. A sensitive multi-elemental online detection of dissolved species during their build-up or steady-state regime, together with a finely resolved knowledge of the underlying substrate, makes this effect discernible and permits insight into the fundamental mechanisms of passivation.

We provide a high-resolution near-atomistic view on the relation between bulk and surface microstructure and time-resolved corrosion performance of the stainless-type amorphous and nanocrystalline alloy $Fe_{50}Cr_{15}Mo_{14}C_{15}B_6$ (*22*). Amorphous ribbons were prepared by melt spinning and crystallized by thermal annealing at the selected temperatures for 20 min. The glass transition (T_g = 550°C), the onset of the first and second crystallization (T_{x1} = 602°C, T_{x2} = 641°C), and the melting temperatures (T_m = 1112°C) of the amorphous alloy were obtained by differential scanning calorimetry and serve as an indicator of the structural transformations within the alloy.

Atom probe tomography (APT) (*23*) reconstructions are presented in Fig. 1A (and figs. S1 and S2). Fe, Cr, and Mo are presented in green, blue, and red colors, respectively. Boron and carbon were omitted here for clarity. The lower images correspond to 2- to 5-nm slices from the reconstructions, elucidating the nanoscale partitioning. Isoconcentration surfaces of Cr and Mo are plotted to highlight regions of highest chemical gradients. The average compositions of the different regions are listed in Table 1. The as-quenched ribbons show the broad diffuse x-ray peaks (Fig. 1B) characteristic of an amorphous structure, whereas a uniform elemental distribution by APT confirms their chemical homogeneity. At 620°C, Cr-rich regions of 12-nm average size are formed by elemental redistribution (Fig. 1A). Correlated analyses between x-ray diffraction (XRD) and transmission electron microscopy (TEM) indicate the presence of the carbide phase

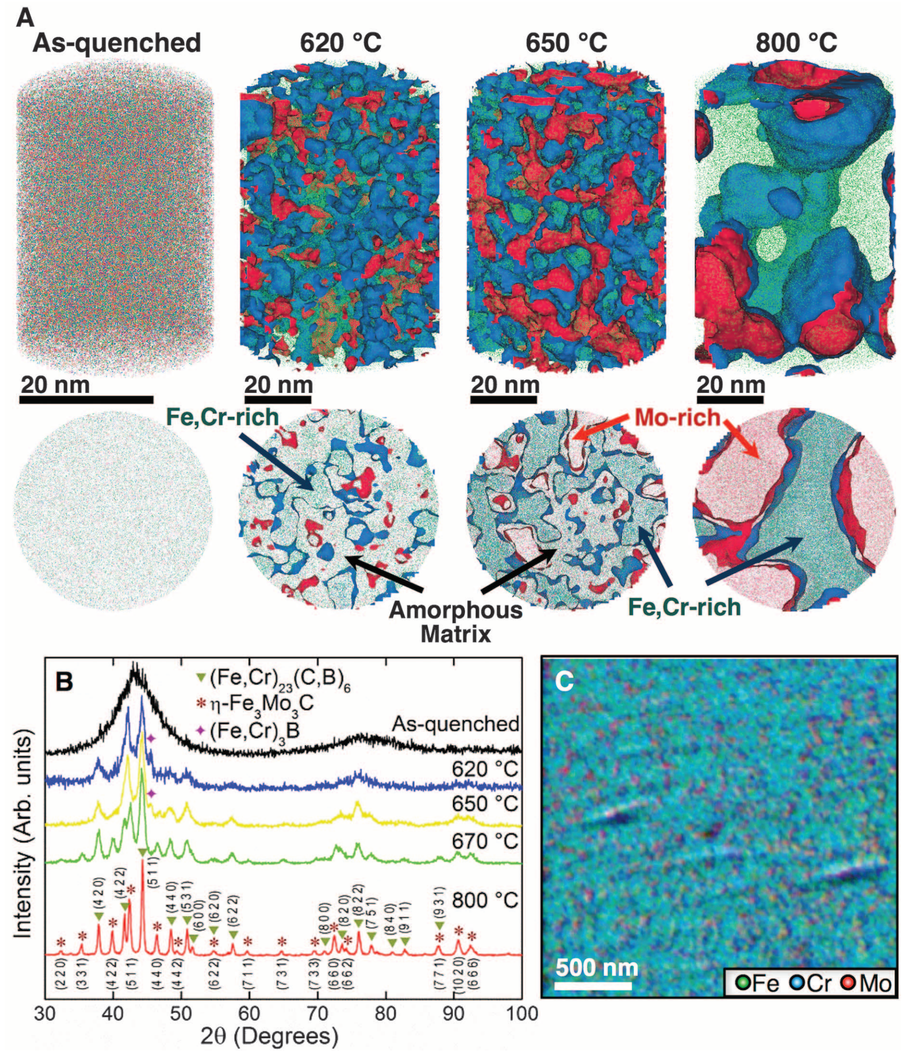

Fig. 1. Microstructure and surface analysis. (**A**) APT reconstructions showing the distribution of the metallic elements (Fe, green; Cr, blue; Mo, red) in the as-quenched, partially and fully crystallized alloys. Isoconcentration surfaces of 22 atomic % Mo in red and 16 atomic % Cr in blue highlight three different regions in the samples annealed for 20 min at 620° and 650°C. Thirty-two atomic % Mo and 15 atomic % Cr isoconcentration surfaces are plotted for the crystallized alloy (60 min at 800°C). Lower images are 2- to 5-nm thick virtual slices of the respective reconstructions revealing the nanoscale partitioning characteristics. (**B**) XRD plots indicating the formation of the different phases. (**C**) Overlap of the individual Fe, Cr, and Mo SAEM maps after crystallization at 800°C.

[1]Department of Interface Chemistry and Surface Engineering, Max-Planck Institut für Eisenforschung GmbH, 40237 Düsseldorf, Germany. [2]Departamento de Materiales, Centro de Investigación y de Estudios Avanzados, Instituto Politécnico Nacional (CINVESTAV-IPN), 76230 Queretaro, Mexico. [3]Departament de Fisica Aplicada, Universitat Politècnica de Catalunya, 08860 Castelldefels, Spain. [4]Department of Microstructure Physics and Alloy Design, Max-Planck Institut für Eisenforschung GmbH, 40237 Düsseldorf, Germany. [5]Max-Planck Institut für Mikrostrukturphysik, 06120 Halle, Germany. [6]Institució Catalana de Recerca i Estudis Avançats (ICREA), Universitat Politècnica de Catalunya, 08860 Castelldefels, Spain.

*Corresponding author. E-mail: j.duarte@mpie.de (M.J.D.); frank.renner@uhasselt.be (F.U.R.)

†These authors contributed equally to this work.

‡Present address: Physics Department, West Virginia University, Morgantown, WV 26506–6315, USA.

§Present address: Electron Microscopy of Eidgenössische Technische Hochschule Zurich (EMEZ), 8093 Zurich, Switzerland.

||Present address: Instituut Voor Materiaalonderzoek, Universiteit Hasselt, 3590 Diepenbeek, Belgium.

$M_{23}(C,B)_6$ (with M=Fe,Cr,Mo). Molybdenum atoms segregate from these carbides to the amorphous matrix, forming additional regions enriched in Mo (red areas at 620°C) until a crystalline η-Fe_3Mo_3C phase is observed at 650°C. M_3B and a solid solution τFe-Cr-Mo are present as intermediate phases only in the 620° to 650°C temperature range. The fully crystallized sample (at 800°C) shows Mo-rich and Cr-rich phases of up to 50 nm in size (see also fig. S3). The chemical composition in the respective regions becomes thermodynamically stable with increasingly sharp boundaries. Most important, for our passivation studies, a percolation of both crystalline phases throughout the fully crystallized sample is observed.

Freshly sputtered starting surfaces were used to ensure reproducibility of the electrochemical measurements and surface analysis. Bombardment with Ar ions essentially cleaned the surfaces from contaminations or any reaction layers formed during annealing (fig. S4). The elemental distribution of the fresh surface of the fully nanocrystalline sample in the scanning Auger EM (SAEM) map (overlaid map in Fig. 1C) closely corresponds to the distribution displayed in the APT slice in Fig. 1A. Although some sputter ripples emerge in the surface morphology, sputtering is thus able to produce an almost ideal cut of the bulk material, and the detailed bulk microstructure information is maintained at the surface.

Micro-electrochemical corrosion tests enabled a large number of tests on one sample and showed an excellent reproducibility (*24*). Depending on the thermal history, the electrochemical corrosion behavior reveals a transition from an extended passive state limited by transpassive Cr dissolution to an early breakdown governed by transpassive Mo dissolution (Fig. 2A in 0.1 M H_2SO_4 and fig. S5 in 0.1 M HCl). The curves obtained are located between the reference behavior of pure Mo and pure Cr. In region (a) of Fig. 2A, oxidizing positive currents indicate the release of metal ions. For the alloys crystallized above 670°C, the steep increase in current is linked to strong metal dissolution. Below 650°C, the annealed and the pristine amorphous alloys show a transition into a further low-current passive region (b). The initial peak indicates the transition of a native oxide film, which is unstable in the electrolyte, toward this passive state. In region (c), the passive film breaks down about 100 mV earlier than the transpassive Cr dissolution of the pure Cr foil. Interestingly, the partially nanocrystalline samples below 620°C show only a moderately larger passive current density. The transition peak (a) is more pronounced, and the final breakdown occurs at the same potential compared with the amorphous alloy. The transition in breakdown behavior appears between 620° and 670°C. The fully nanocrystalline sample (800°C) closely resembles the behavior of pure Mo but is about 100 mV more stable. APT analyses indicate 6 to 7 atomic percent (atomic %) of Cr in the respective Mo-rich phase. In particular, for complex multi-element materials the total current does not reveal sufficient information on the involved elements.

Of particular interest for corrosion performance are the individual elemental contribution and the effectiveness of the passivating elements Cr and Mo (*7*, *25*, *26*). Element-resolved dissolution data were measured online using a scanning flow cell (SFC) with an inductively coupled plasma mass spectrometer (ICP-MS) (*27*) and are illustrated for three selected states in Fig. 2, B to G. The measured concentrations were converted into current densities by application of Faraday's law (*27*–*29*). The sum of all three elemental dissolution current densities, $i_{Diss,Me}$ with Me = Fe, Cr, Mo (gray dashed lines in Fig. 2, B to D), shows good agreement with the measured current density i_m for all three samples. Visible deviations reflect the growth of the 1- to 2-nm passive film and dissolution of carbon and boron. Compared with the bulk composition, the element-specific dissolution stoichiometry (molar fractions)

Table 1. Representative concentration of the metallic components (in atomic %) in the different regions determined by APT and SFC-ICP-MS.

	APT										
Alloy	**Am**	**550°C**	**620°C**		**650°C**			**670°C**		**800°C**	
Zone (Fig.1A)			Cr-rich	Matrix	Cr-rich	Mo-rich	Matrix	Cr-rich	Mo-rich	Cr-rich	Mo-rich
% Fe	59	59	61	58	65	44	59	65	44	65	42
% Cr	19	18	26	19	23	9	19	23	8	22	7
% Mo	22	23	13	23	12	47	22	12	48	13	51
	ICP – MS										
Alloy	**Amorphous (Am)**			**550°C**			**620°C**			**670°C**	**800°C**
Region (Fig. 2)	a	b	c	a	b	c	a	b	c	a	a
% Fe	65	68	63	68	72	63	71	70	64	56	53
% Cr	13	16	20	11	14	19	7	10	17	7	4
% Mo	22	16	17	21	14	18	22	20	19	37	43

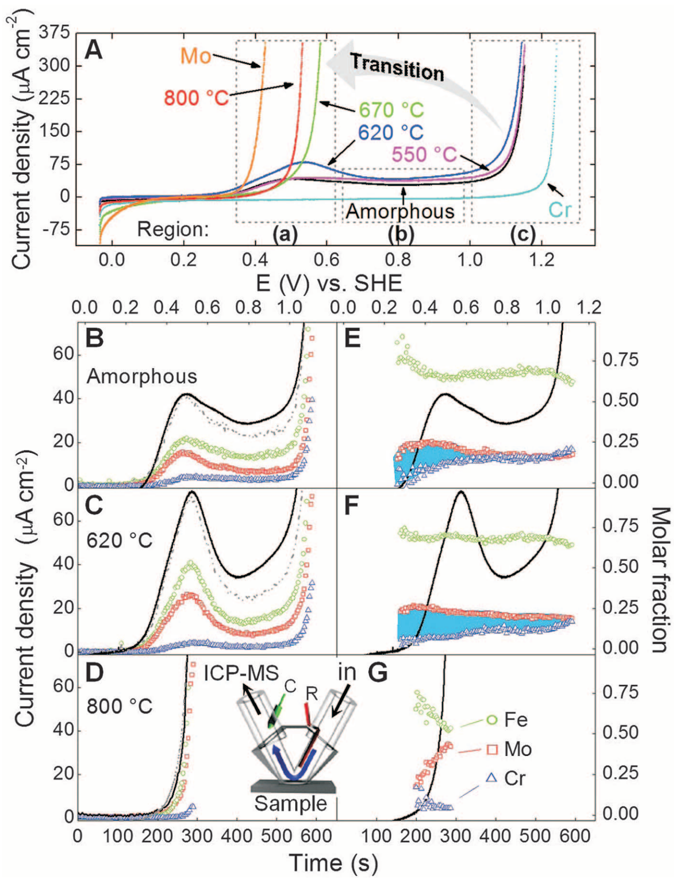

Fig. 2. Electrochemical behavior and element-resolved online analysis. (**A**) Potentiodynamic polarization curves in 0.1 M H_2SO_4 (2 mV/s in the positive direction) of amorphous, partially (620°C) and fully nanocrystalline (800°C) $Fe_{50}Cr_{15}Mo_{14}C_{15}B_6$ together with pure Cr and Mo. (**B** to **D**) Online ICP-MS dissolution profiles converted into dissolution current densities ($i_{Diss,Me}$; Me = Fe, Cr, Mo with green, blue, and red symbols, respectively, and $i_{Diss,total}$ = sum of individual $i_{Diss,Me}$, gray dashed line) for the (B) amorphous, (C) partially nanocrystalline, and (D) fully nanocrystalline alloy. Potential sweep data, i_m, as black line. (**E** to **G**) Dissolution stoichiometry expressed as molar fractions of Fe, Cr, and Mo, for the (E) amorphous, (F) partially nanocrystalline, and (G) fully nanocrystalline alloys. The difference between Mo and Cr dissolution is highlighted in blue. The inset shows a schematic figure of the SFC-ICP-MS.

reveals significant changes at different times and potentials (Fig. 2, E to G). The main species dissolved in the lower range of potentials up to 700 mV for the amorphous sample is Fe, with substoichiometric dissolution of Cr. The time-resolved enrichment of Cr on the surface can thus directly be followed. At higher potentials in the passive range, both Mo and Cr dissolve in equivalent ratios reflecting the substrate composition. A higher contribution of Fe and Mo is observed in the sample annealed at 620°C. Cr dissolves then stoichiometrically only at the breakdown. The formation of Cr-rich crystals, and consequently Cr-depleted regions, leads to the increase in the current density. Formation of passive layers is accompanied by a large etching effect that is enhanced by the codissolution of Cr, because the necessary accumulation of Cr is delayed. The inhomogeneous substrates revealed two time scales, one initial strong dissolution peak and a slower process to reach the final steady state. A relatively thick layer of the amorphous and the partially crystalline surface is removed (about 20 and 30 nm in average, respectively), as can be deduced from the elemental dissolution data. A thicker and significantly Cr-enriched passive film is thus formed after immersion in the electrolyte. Independent x-ray photoelectron spectroscopy (XPS) measurements (fig. S6) confirm the increase in film thickness to about 4 nm and reveal the thickness and composition of the respective passive oxide films to closely resemble the reported films on binary Fe-Cr model alloys or stainless steels. In contrast, the fully nanocrystalline alloy (800°C) shows an increasingly strong contribution of Mo, with Cr being distinctly minor. The dissolution stoichiometry is thus quickly dominated by the Mo-rich phase, and the chemical stability of the system is compromised with the formation of the percolating Cr-depleted structure. The individual amounts of metals dissolved in the specific potential regions are given in Table 1. The ratio of Fe and Mo measured by APT in the Mo-rich phase agrees very well with the dissolution of the nanocrystalline material during the potential sweeps. This supports that the electrochemical behavior in the crystallized alloys is indeed dominated by the Mo-rich and severely Cr-depleted phase, which begins to corrode at low potentials. In parallel to the growth of the adapted passive film, the associated selective etching results in a severe surface roughening on the nanometer length-scale of the formed chemical inhomogeneities. Figure 3A shows an atomic force microscopy (AFM) image of the surface morphology after initial corrosion of the partially crystalline state (annealed at 620°C). The final transpassive breakdown of the layer is here not compromised by the developing defects in the surface morphology and the partial crystallization. The completely amorphous sample shows no difference in roughness before and after formation of the passive layer, confirming its homogeneous nature. Only at high temperatures does a more pronounced chemical partitioning with a fully developed phase percolation cause the mechanism and the breakdown potential to change.

Continuous selective dissolution can be sustained as shown in Fig. 3, B and C, for the alloy crystallized at 800°C. TEM confirms the homogeneity of the sample on larger length scales than APT and the dissolution of a percolating Mo-rich phase. Chemical partitioning is independently confirmed in the high-angle annular dark field (HAADF) scanning TEM (STEM) image as variations in contrast (Fig. 3B), in addition to local energy dispersive x-ray (EDX) analysis (Fig. 3C). The resulting mesoporous Cr-rich carbide is chemically very stable and may be useful for different applications.

The complexity of most applied materials often precludes a thorough understanding of the macroscopic behavior, including corrosion. Here, we followed the role and fate of the individual elements during the corrosion of a complex multi-element material. First, the three-dimensional near-atomistic chemical distribution revealed by APT discloses the increasing Cr partitioning of the alloy at different temperatures, which is essential for understanding the breakdown of effectiveness of passivation. The Cr depletion first occurs homogeneously throughout the remaining matrix—that is, no sensitization is observed. The Cr-depleted η-Fe_3Mo_3C phase does not form surrounding, nor always attached to, the Cr-enriched crystallites. Approaching the fully crystallized state at 700° to 800°C, the η-phase percolates throughout the alloy and the passivation mechanism completely fails.

The sensitive and directly linked online ICP-MS dissolution analysis is a second major point. Alloying elements can considerably influence the behavior of materials; they can block dissolution sites or catalyze reactions, either beneficial or detrimental. Cr is codissolved at all stages in different ratios. Enrichment of Cr on the surface drives passivation and is, according to our time- and element-resolved data, much slower for the partially crystalline sample compared with the completely amorphous one. At the same time, major surface etching (10 to 30 nm) takes place, which results in a higher surface roughness but may also help to overgrow a structurally inhomogeneous substrate. Nevertheless, the finally established passive state exhibits a slightly higher passive current compared with the amorphous state. The transpassive breakdown process occurs at lower potentials for the analyzed alloys compared with pure Cr, thus indicating a further codissolution effect of the alloying elements and marking a change in mechanism during the potential ramp. After a steady state has been reached for a passive film, the samples dissolve with bulk stoichiometry, whereas the early breakdown of the fully nanocrystalline state is associated with a very high Mo dissolution.

As a general remark, the structure of passive films on stainless steels has been recognized as an amorphous-crystalline composite (*30*). Granted, the rigorous nanometer-scale lateral chemical composition of any ultrathin passive film has not been resolved so far. Amorphous steels show a low threshold to develop a protective film of 4 to 5% Cr (*31*) compared with 12 to 13% Cr in crystalline stainless steel alloys (*32*). The origin of this lower threshold remains disputed and was attributed either to the amorphous substrate facilitating an entirely amorphous passive film structure or to a more homogeneous Cr distribution. Although element-resolved solution analysis marks an enormous step for our understanding, more detailed insight into the passive film itself will be necessary to resolve the issue completely.

Finally, beyond the particular amorphous and nanocrystalline alloy presented here, interesting parallels to commercial polycrystalline stainless steels can be drawn. The passive films of both are of the same nature—that is, they have the same thickness and average composition. High-performance austenitic stainless steel grades such as American Iron and Steel Institute (AISI) types 316L, 904L, or 654 SMO contain a relatively high amount of Mo (2 to 7 weight percent) and are employed where corrosion behavior is critical. Passive films are not static but adapt to changes in the environment and are partially able to heal defective regions such as local variations in Cr, weld precipitations, tiny impurity phases, or sensitized grain boundaries. We showed how a passivation scheme for amorphous and nanocrystalline steels reacts to local chemical

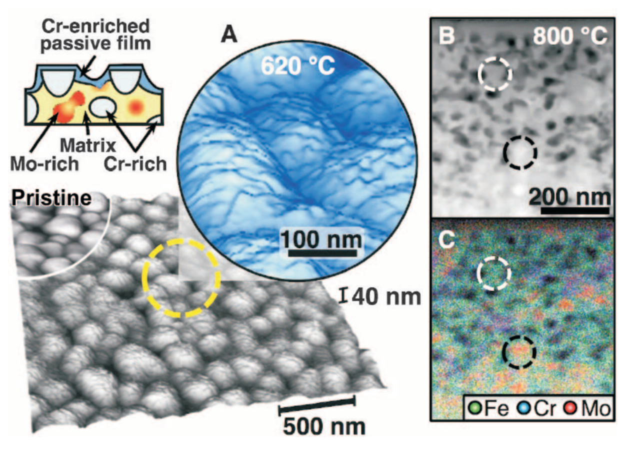

Fig. 3. Surface analysis and cross section after galvanostatic corrosion. (**A**) AFM images and sketch of a rough surface after corrosion of a sample annealed at 620°C for 20 min. (**B**) HAADF-STEM micrograph of the fully crystallized alloy after polarization for 4000 s and (**C**) corresponding EDX map showing the Mo, Fe, and Cr distributions in the porous layer and the bulk. Mo-rich and Cr-rich areas are bordered by black and white dashed circles, respectively.

variations down to the nanometer scale. Herein lies the benefit in studying these types of steels to understand specific aspects of real-world steels.

References and Notes

1. D. E. Williams, R. C. Newman, Q. Song, R. G. Kelly, *Nature* **350**, 216–219 (1991).
2. S. Haupt, H.-H. Strehblow, *Corros. Sci.* **37**, 43–54 (1995).
3. I. Betova *et al*., *Corros. Sci.* **44**, 2675–2697 (2002).
4. J. E. Castle, J. H. Qiu, *J. Electrochem. Soc.* **137**, 2031 (1990).
5. R. C. Newman, *Corros. Sci.* **25**, 331–339 (1985).
6. K. Hashimoto, *Corrosion* **58**, 715–722 (2002).
7. K. Hashimoto, *Appl. Surf. Sci.* **257**, 8141–8150 (2011).
8. C. S. Kiminami *et al*., *J. Non-Cryst. Solids* **356**, 2651–2657 (2010).
9. M. D. Archer, C. C. Corke, B. H. Harji, *Electrochim. Acta* **32**, 13–26 (1987).
10. J. Schroers, *Adv. Mater.* **22**, 1566–1597 (2010).
11. A. Inoue, *Acta Mater.* **48**, 279–306 (2000).
12. A. L. Greer, *Science* **267**, 1947–1953 (1995).
13. C. J. Byrne, M. Eldrup, *Science* **321**, 502–503 (2008).
14. K. E. Heusler, *Corros. Sci.* **39**, 1177–1191 (1997).
15. J. R. Scully, A. Gebert, J. H. Payer, *J. Mater. Res.* **22**, 302–313 (2007).
16. K. Hono, D. H. Ping, *Mater. Charact.* **44**, 203–217 (2000).
17. G. Okamoto, *Corros. Sci.* **13**, 471–489 (1973).
18. P. Marcus, V. Maurice, H.-H. Strehblow, *Corros. Sci.* **50**, 2698–2704 (2008).
19. M. P. Ryan, D. E. Williams, R. J. Chater, B. M. Hutton, D. S. McPhail, *Nature* **415**, 770–774 (2002).
20. Q. Meng, G. S. Frankel, H. O. Colijn, S. H. Goss, *Nature* **424**, 389–390 (2003).
21. C. Punckt *et al*., *Science* **305**, 1133–1136 (2004).
22. V. Ponnambalam, S. J. Poon, G. J. Shiflet, *J. Mater. Res.* **19**, 1320–1323 (2004).
23. T. F. Kelly, M. K. Miller, *Rev. Sci. Instrum.* **78**, 031101 (2007).
24. S. O. Klemm, J. C. Schauer, B. Schuhmacher, A. W. Hassel, *Electrochim. Acta* **56**, 4315–4321 (2011).
25. H. M. Ha, J. R. Miller, J. H. Payer, *J. Electrochem. Soc.* **156**, C246 (2009).
26. S. Pang, T. Zhang, K. Asami, A. Inoue, *Mater. Trans.* **43**, 2137–2142 (2002).
27. S. O. Klemm, A. A. Topalov, C. A. Laska, K. J. J. Mayrhofer, *Electrochem. Commun.* **13**, 1533–1535 (2011).
28. K. Ogle, M. Mokaddem, P. Volovitch, *Electrochim. Acta* **55**, 913–921 (2010).
29. N. Homazava, A. Ulrich, U. Krähenbühl, *Spectrochim. Acta, B At. Spectrosc.* **63**, 777–783 (2008).
30. V. Maurice, W. P. Yang, P. Marcus, *J. Electrochem. Soc.* **145**, 909 (1998).
31. A. Pardo *et al*., *Acta Mater.* **55**, 2239–2251 (2007).
32. S. Fujimoto *et al*., *Corros. Sci.* **35**, 51–55 (1993).

Acknowledgments: We acknowledge A. Kostka for providing TEM, STEM, and EDX measurements and helpful discussions. For assistance in SAEM, we thank P. Keil. A. Mingers is acknowledged for ICP-MS measurements. M.J.D., J.S., and D.C. acknowledge financial support from Micinn MAT2010-14907, Generalitat de Catalunya 2009SGR01225 and 2009SGR01251. M.J.D. and A.H.R. acknowledge support from Conacyt, Mexico, through projects PPROALMEX-DAAD-Conacyt and 152153. A.H.R. was supported by the Marie-Curie Intra-European Fellowship. F.U.R. acknowledges support by DAAD PPP 0811941.

Supplementary Materials

www.sciencemag.org/cgi/content/full/341/6144/372/DC1
Materials and Methods
Supplementary Text
Figures S1 to S6
Reference (*33*)

12 September 2012; accepted 13 June 2013
10.1126/science.1230081

Geometric Frustration of Icosahedron in Metallic Glasses

A. Hirata,[1] L. J. Kang,[1] T. Fujita,[1] B. Klumov,[2] K. Matsue,[3] M. Kotani,[1,3] A. R. Yavari,[4,1] M. W. Chen[1,5]*

Icosahedral order has been suggested as the prevalent atomic motif of supercooled liquids and metallic glasses for more than half a century, because the icosahedron is highly close-packed but is difficult to grow, owing to structure frustration and the lack of translational periodicity. By means of angstrom-beam electron diffraction of single icosahedra, we report experimental observation of local icosahedral order in metallic glasses. All the detected icosahedra were found to be distorted with partially face-centered cubic symmetry, presenting compelling evidence on geometric frustration of local icosahedral order in metallic glasses.

Determining atomic structure of amorphous materials has been a long-standing problem, because the lack of long-range translational and rotational symmetry renders it experimentally inaccessible by conventional diffraction methodologies. More than half a century ago, Frank proposed that the icosahedron is the most favorable local order in monatomic metallic liquids (*1*), successfully explaining the feasibility of achieving undercooling to below the melting points. Metallic glasses can often be formed from liquid alloys near eutectic compositions and, in accordance with Frank's proposal, binary liquid eutectic compositions can be generated by introducing icosahedral clusters (*2*). Icosahedral order is thus the most generally accepted description of atomic structures of metallic liquids and glasses (*3–14*). From a geometrical viewpoint, icosahedra cannot fill the entire three-dimensional (3D) space, even in disordered systems, without distortion where icosahedral rotational symmetry is partially broken (*15–17*). Therefore, the locally preferred icosahedra may not be perfectly consistent with the globally stabilized structure, leading to the theoretical predictions of geometrical frustration of icosahedron (*16–19*). Although a number of neutron and x-ray scattering experiments have been performed to elucidate icosahedral order in metallic liquids and glasses (*18*, *20–22*), only average structural information can be acquired from 1D diffraction profiles generated by the statistical distribution of coexisting polyhedra with various geometrical distortions in real materials. The direct observation of local icosahedral order is still missing. Consequently, the structure features of local icosahedral order and their correlation with the long-range disorder in glasses and liquids are largely unknown. To overcome the experimental difficulty in detecting local atomic configurations in amorphous materials, we recently developed an angstrom-beam electron diffraction (ABED) method to probe local atomic structure using a ~0.4-nm electron beam (*23*). We use the ABED technique to characterize local icosahedral order in a representative $Zr_{80}Pt_{20}$ metallic glass in which the presence of a large fraction of icosahedra has been predicted by computational simulations (*24*, *25*) and this study (fig. S1).

The amorphous structure of the $Zr_{80}Pt_{20}$ metallic glass was confirmed by spherical aberration–corrected high-resolution transmission electron microscopy (TEM), together with selected-area electron diffraction (fig. S2). To obtain local structural information, we employed the ABED technique with a beam diameter of 0.36 nm (full width at half maximum) to characterize a thin foil of the glass (Fig. 1A). To guide the ABED study, we simulated the characteristic ABED patterns of an ideal icosahedron along five-, three-, and twofold directions (Fig. 1B). A large number of ABED patterns were acquired from the thin edge of the TEM foil. When the specimen thickness is thin enough (~3 to 5 nm), individual polyhedra with an appropriate on-axis orientation can be frequently detected by ABED. However, from these measurements we cannot find any ABED pattern that is completely consistent with the simulated icosahedron patterns shown in Fig. 1B. Instead, the acquired ABED patterns only partially match those of the five-, three-, and twofold orientations (Fig. 1C). This is probably due to distorted icosahedra in which icosahedral order is only partially preserved. We thus simulated five-, three-, and twofold ABED patterns of a typical <0 0 12 0> icosahedron taken from the molecular dynamics (MD) model of the metallic glass (fig. S1B). All icosahedra in the MD model are actually distorted from the ideal icosahedron, in agreement with theoretical and computational predictions (*17–19*, *24*, *25*). Figure 1C shows the simulated five-, three-, and twofold ABED patterns of the distorted icosahedron.

[1]WPI Advanced Institute for Materials Research, Tohoku University, Sendai 980-8577, Japan. [2]Joint Institute for High Temperatures, Russian Academy of Sciences, Moscow 125412, Russia. [3]Mathematical Institute, Tohoku University, Sendai 980-8578, Japan. [4]Euronano, SIMAP-CNRS, Institut National Polytechnique de Grenoble, BP 75, 38402 St. Martin d'Heres Campus, Grenoble, France. [5]State Key Laboratory of Metal Matrix Composites, School of Materials Science and Engineering, Shanghai Jiao Tong University, Shanghai 200030, PR China.

*Corresponding author. E-mail: mwchen@wpi-aimr.tohoku.ac.jp

Because the icosahedral symmetry can be only partially retained, the diffraction spot intensities differ considerably from those of the ideal icosahedron. The features of the experimental patterns corresponding to five-, three-, and twofold axes are fairly consistent with the simulated ones in the lengths and angles of diffraction vectors, as indicated by the arrowheads, verifying the existence of distorted icosahedra in the metallic glass (fig. S3).

Although the distorted icosahedra can be detected by ABED, the most common ABED patterns during random diffraction scanning are often very simple and different from the five-, three-, and twofold patterns of icosahedral order. The patterns are basically composed of six nearly symmetrical diffraction spots, as shown in Fig. 2A. To understand the structural origins of the simple ABED patterns, we searched all possible on-axis diffraction patterns of highly frequent polyhedra in the metallic glass predicted by the MD simulation. The simple diffraction patterns were found to originate from the distorted icosahedra, in addition to the well-known five-, three-, and twofold patterns. Figure 2B is a simulated ABED pattern calculated from a distorted <0 0 12 0> icosahedron in which the positions of the 12 coordinated atoms are displaced from those in an ideal icosahedron (Fig. 2C). The incident direction is close to a distorted fivefold orientation (see Fig. 2E). The simulated pattern reproduces well the experimental one in the diffraction vectors (lengths and angles) (Fig. 2, A′ and B′). Note that ABED patterns with the equivalent diffraction vectors cannot be obtained from nonicosahedral clusters (fig. S4). We noticed that this kind of diffraction is also partially similar to that of a face-centered cubic (fcc) structure that is also densely packed with 12 coordinated atoms. Figure 2D shows a [110] diffraction pattern of the fcc structure with six strong spots, which is partially consistent with that of the distorted icosahedron but without the golden-ratio relationship between diffraction vectors. This implies that the distorted part of the icosahedron possesses local fcc-like symmetry.

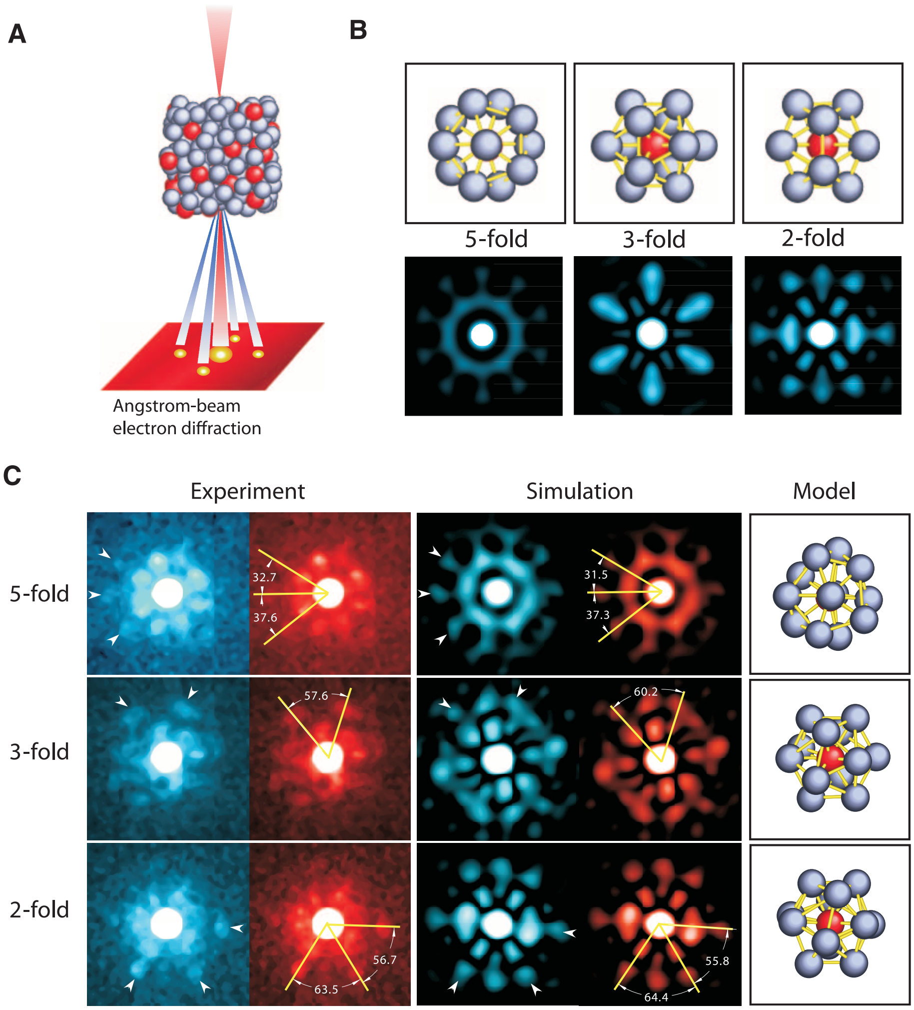

Fig. 1. ABED characterization of icosahedral order in metallic glasses. **(A)** Experimental procedure of ABED of a icosahedral cluster. The coherent electron beam has a diameter of 0.36 nm. **(B)** Simulated ABED patterns of an ideal icosahedron. **(C)** Comparison between experimental and simulated ABED patterns of icosahedral clusters in a $Zr_{80}Pt_{20}$ metallic glass. For comparison, angular information between each diffraction vector is shown in the right side of each panel. Arrowheads indicate characteristic diffraction spots of the icosahedral order.

We investigated the structural similarity between the distorted icosahedron and the fcc cluster. Figure 3A depicts three types of atomic clusters with a coordination number of 12: ideal icosahedron, distorted icosahedron, and fcc cluster. The exact atomic sites where the distorted icosahedron (Fig. 3A, middle) differs structurally from the ideal icosahedron and fcc can be seen. Atoms in the distorted part of the icosahedron can be identified by shifting to fcc coordinates. The distorted icosahedron actually includes icosahedral order and a portion of fcc order (fig. S5), accompanying with the variation of Zr-Pt atomic bond length from 0.277 to 0.347 nm. Separate ab initio calculations (Fig. 3B) verify that the distorted icosahedron has a total energy higher than both the perfect icosahedron and the fcc cluster. This indicates that the distorted icosahedra are in an intermediate state between two densely packed configurations: the ideal icosahedron and the fcc cluster. To confirm that the distorted icosahedron with partial fcc symmetry is representative of the local structure of the Zr-Pt metallic glass, we conducted a bond orientational order analysis based on our MD model containing 12,000 atoms (*6*, *26*). Figure 3C shows a probability distribution function for an invariant $\hat{W}_6$, the most sensitive indicator for icosahedral symmetry, calculated using the averages of spherical harmonics associated with the bond directions (*26*). The values for the ideal icosahedron and the fcc cluster are –0.169754 and +0.013161 (*26*), respectively. The invariant $\hat{W}_6$ of the dominant atomic clusters in the metallic glass is seen to have values in between those of the icosahedron and fcc configurations, suggesting that most local atomic arrangements have an intermediate structure between icosahedron and fcc, which is in agreement with the distorted icosahedron characterized by ABED.

Traditionally, the distortion of icosahedra has been suggested from atomic size disparity of constituent elements and/or kinetic fluctuation during glass formation, giving rise to atomic bonding length variation, as well as atomic scale stress and strain in metallic glasses (*27*, *28*). Nevertheless, different from the indiscriminate geometry variation caused by the chemical and kinetic effects, the distorted icosahedra reported here always possess partial fcc symmetry, indicating that the distortion of icosahedra in the metallic glasses is associated with geometric frustration that derives from the competition between two low-energy states (fcc and icosahedron) with dense atomic packing. The chemical variation and kinetic fluctuation may just provide structural perturbations during the development of the intermediate atomic configuration by preventing the formation of ideal icosahedron and fcc clusters. If each icosahedral cluster is isolated, it would naturally tend to minimize the local energy density by forming the densest and most symmetrical

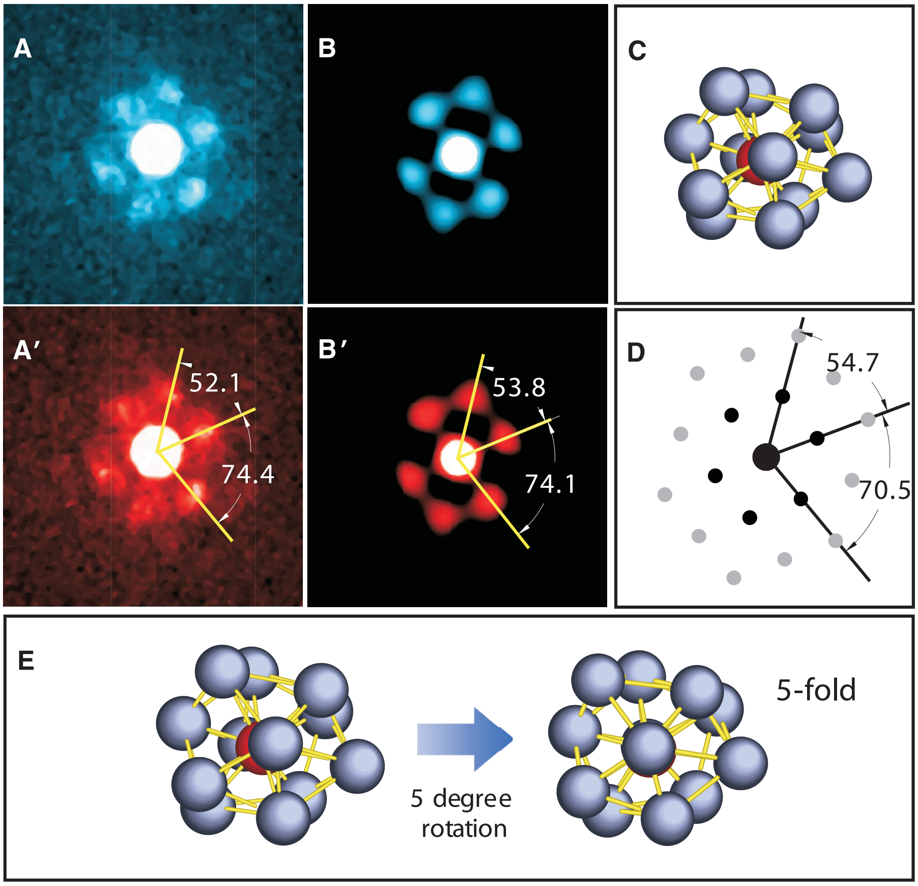

Fig. 2. ABED patterns of a distorted icosahedron taken from the fcc-like orientation. (**A**) Experimental ABED pattern with six distinguishable diffraction spots obtained from $Zr_{80}Pt_{20}$. (**A′**) Characteristic diffraction angles in the experimental ABED pattern shown in (A). (**B**) Simulated ABED pattern calculated from the distorted <0 0 12 0> icosahedron taken from the MD model. (**B′**) Characteristic diffraction angles in the simulated ABED pattern shown in (B). (**C**) Illustration of the distorted icosahedron giving the ABED pattern of (B). (**D**) Calculated [110] diffraction pattern of a fcc cluster. (**E**) Correlation between a local fcc symmetry and a distorted pentagon of icosahedral order.

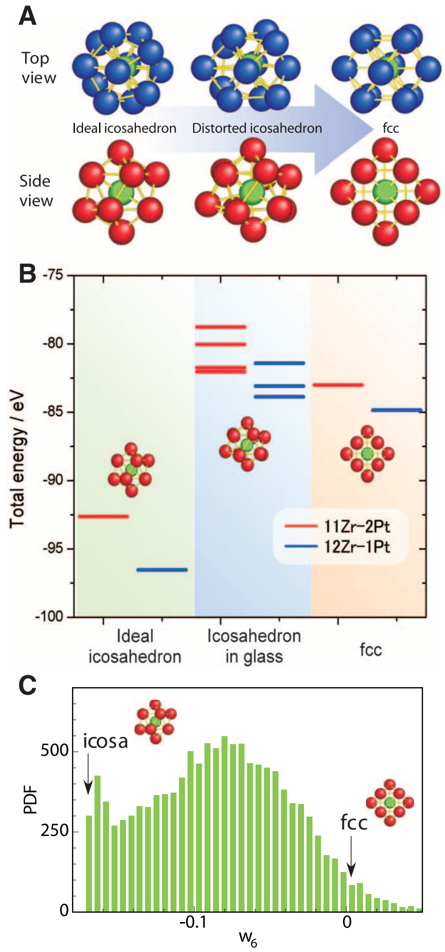

Fig. 3. Energy calculation and bond orientational order analysis. (**A**) Structural relationship among the ideal icosahedron, distorted icosahedron, and fcc cluster. (**B**) Total energy calculations of the three atomic clusters. (**C**) Bond orientational order analysis from a 12,000-atom MD model created at a cooling of 10^{10} K/s. A histogram of the probability distribution function (PDF) of the $\hat{W}_6$ invariant is shown, together with the characteristic values for an ideal icosahedron and fcc cluster.

icosahedron. However, in real metallic glasses, the constituent atoms shared by neighboring clusters may not always sit at the minima of all pairwise interactions with all of their nearest neighbors, owing to chemical variation and kinetic fluctuation. The fcc symmetry is the energetically and geometrically favorable arrangement of the distorted parts of the icosahedron, because an fcc structure has dense atomic packing with 12 coordinated atoms (same as an icosahedron) and a low energy. Importantly, the local translational symmetry of the fcc configuration makes the distorted icosahedra easy to geometrically match with neighboring clusters for long-range dense packing. Thus, the geometric frustration, evidenced by ABED, reflects the intrinsic structural feature of metallic glasses and correlates with their forming ability and mechanical properties.

It is worth noting that other prevailing clusters in the metallic glass—such as <0 3 6 1>, <0 2 8 0>, <0 2 8 1>, <0 1 10 2>—were also detected by ABED (fig. S6). These clusters also contain both icosahedral- and fcc-like structural features associated with the geometric frustration, similar to the distorted <0 0 12 0> icosahedron. The geometric frustration of the atomic clusters can be quantified by topological analysis. Although each distorted icosahedron or icosahedron-like cluster has distinct geometric distortions depending on the surrounding atomic environment, the preliminary computational homology calculations (*29*), for the first time being applied to the analysis of metallic glasses, show that the geometric distortions of the atomic clusters can be depicted in a simple manner in terms of the topological connectivity. The topological analysis of individual atomic clusters can also be scaled up to long-range disorder (figs. S7 and S8), which may be a promising approach to describe the intricate structure of disordered metallic glasses.

To retain dense atomic packing and a low-energy state, the icosahedral order revealed by ABED is geometrically distorted and inclined to form a mixed configuration, composed of a partial icosahedral symmetry and a partial fcc symmetry. This atomic packing scheme of low structure symmetry but dense atomic arrangement has not been found in any crystal or quasicrystal and represents a distinct atomic structural feature of metallic glasses. Although dominant clusters in metallic glasses are diverse and not limited to icosahedra, dense packing with geometrical frustration appears to be the universal structural characteristic of metallic glass formers.

Metallic glasses are essentially a frozen supercooled liquid. In principle, the local structure revealed by ABED corresponds to the inherent structure of the supercooled liquid immediately before its transition to a glassy state. In addition to shedding light on the structural origins of metallic glass formation, this study also provides evidence that dynamic heterogeneity and arrest in supercooled liquids at the glass transition, as determined from computational simulations and theoretical modeling (*30*–*33*), are essentially associated with local atomic ordering and consequent geometric frustration. Therefore, the ABED experiment may have important implications in

solving the puzzles of glass transition (*34*) and may provide a method to explore the atomic structure and atomic-scale properties of disordered materials.

References and Notes

1. F. C. Frank, *Proc. R. Soc. London Ser. A* **215**, 43–46 (1952).
2. W. Hume-Rothery, E. Anderson, *Philos. Mag.* **5**, 383–405 (1960).
3. J. D. Bernal, *Nature* **185**, 68–70 (1960).
4. G. D. Scott, *Nature* **194**, 956–957 (1962).
5. J. L. Finney, *Nature* **266**, 309–314 (1977).
6. P. J. Steinhardt, D. R. Nelson, M. Ronchetti, *Phys. Rev. Lett.* **47**, 1297–1300 (1981).
7. T. Tomida, T. Egami, *Phys. Rev. B* **52**, 3290–3308 (1995).
8. M. W. Chen, T. Zhang, A. Inoue, A. Sakai, T. Sakurai, *Appl. Phys. Lett.* **75**, 1697 (1999).
9. D. B. Miracle, *Nat. Mater.* **3**, 697–702 (2004).
10. H. W. Sheng, W. K. Luo, F. M. Alamgir, J. M. Bai, E. Ma, *Nature* **439**, 419–425 (2006).
11. P. F. Guan, T. Fujita, A. Hirata, Y. H. Liu, M. W. Chen, *Phys. Rev. Lett.* **108**, 175501 (2012).
12. D. Ma, A. D. Stoica, X.-L. Wang, *Nat. Mater.* **8**, 30–34 (2009).
13. T. Takagi *et al*., *Appl. Phys. Lett.* **79**, 485 (2001).
14. A. R. Yavari, *Nat. Mater.* **4**, 2–3 (2005).
15. J. F. Sadoc, R. Mosseri, *Geometrical Frustration* (Cambridge Univ. Press, Cambridge, 1999).
16. D. R. Nelson, *Defects and Geometry in Condensed Matter* (Cambridge Univ. Press, Cambridge, 2002).
17. D. R. Nelson, *Phys. Rev. Lett.* **50**, 982–985 (1983).
18. A. Di Cicco, A. Trapananti, S. Faggioni, A. Filipponi, *Phys. Rev. Lett.* **91**, 135505 (2003).
19. D. R. Nelson, *Phys. Rev. B* **28**, 5515–5535 (1983).
20. T. Schenk, D. Holland-Moritz, V. Simonet, R. Bellissent, D. M. Herlach, *Phys. Rev. Lett.* **89**, 075507 (2002).
21. K. Saksl *et al*., *Appl. Phys. Lett.* **83**, 3924 (2003).
22. K. F. Kelton *et al*., *Phys. Rev. Lett.* **90**, 195504 (2003).
23. A. Hirata *et al*., *Nat. Mater.* **10**, 28–33 (2011).
24. N. A. Mauro *et al*., *Phys. Rev. B* **83**, 184109 (2011).
25. J. Saida *et al*., *J. Phys. Condens. Matter* **21**, 375104 (2009).
26. P. J. Steinhardt, D. R. Nelson, M. Ronchetti, *Phys. Rev. B* **28**, 784–805 (1983).
27. T. Egami, S. Aur, *J. Non-Cryst. Solids* **89**, 60–74 (1987).
28. Y. Q. Cheng, E. Ma, *Prog. Mater. Sci.* **56**, 379–473 (2011).
29. T. Kaczynski, K. Mischaikow, M. Mrozek, *Computational Homology* (Springer, New York, 2003).
30. M. D. Ediger, P. J. Harrowell, *J. Chem. Phys.* **137**, 080901 (2012).
31. L. Berthier, G. Biroli, *Rev. Mod. Phys.* **83**, 587–645 (2011).
32. H. Shintani, H. Tanaka, *Nat. Phys.* **2**, 200–206 (2006).
33. G. Tarjus, S. Kivelson, Z. Nussinov, P. Viot, *J. Phys. Condens. Matter* **17**, R1143–R1182 (2005).
34. J. S. Langer, *Phys. Today* **60**, 8–9 (2007).

Acknowledgments: We thank Y. Hirotsu and T. Egami for constructive discussion and H. Sheng for providing Zr-Pt embedded atom model potentials and J. Saida for $Zr_{80}Pt_{20}$ ribbons. This work was sponsored by "WPI Research Center Initiative for Atoms, Molecules and Materials," Ministry of Education, Culture, Sports, Science and Technology of Japan; Grants-in-Aid for Scientific Research (24360260 and 24656400), Japan Society for the Promotion of Science; "A mathematical challenge to a new phase of materials science," Japan Science and Technology Agency–Core Research for Evolutional Science and Technology; and the National Natural Science Foundation of China (grant 51271113).

Supplementary Materials
www.sciencemag.org/cgi/content/full/science.1232450/DC1
Materials and Methods
Supplementary Text
Figs. S1 to S12
References (*35*–*40*)

6 November 2012; accepted 29 April 2013
Published online 11 July 2013;
10.1126/science.1232450

A General Strategy for the Chemoenzymatic Synthesis of Asymmetrically Branched *N*-Glycans

Zhen Wang,[1]* Zoeisha S. Chinoy,[1,2]* Shailesh G. Ambre,[1,2] Wenjie Peng,[3] Ryan McBride,[3] Robert P. de Vries,[3] John Glushka,[1] James C. Paulson,[3] Geert-Jan Boons[1,2]†

A systematic, efficient means of producing diverse libraries of asymmetrically branched *N*-glycans is needed to investigate the specificities and biology of glycan-binding proteins. To that end, we describe a core pentasaccharide that at potential branching positions is modified by orthogonal protecting groups to allow selective attachment of specific saccharide moieties by chemical glycosylation. The appendages were selected so that the antenna of the resulting deprotected compounds could be selectively extended by glycosyltransferases to give libraries of asymmetrical multi-antennary glycans. The power of the methodology was demonstrated by the preparation of a series of complex oligosaccharides that were printed as microarrays and screened for binding to lectins and influenza-virus hemagglutinins, which showed that recognition is modulated by presentation of minimal epitopes in the context of complex *N*-glycans.

Most cell surface and secreted proteins are modified by covalently linked glycans, which are essential mediators of biological processes such as protein folding, cell signaling, fertilization, embryogenesis, and the proliferation of cells and their organization into specific tissues (*1*). Overwhelming data support the relevance of glycosylation in pathogen recognition, inflammation, innate immune responses, and the development of autoimmune diseases and cancer (*2*, *3*). Although the functional importance of glycoprotein glycosylation is well established, molecular mechanisms by which these compounds exert their functions have been difficult to define. The latter is due to a lack of comprehensive libraries of well-defined complex oligosaccharides that are needed as standards to determine exact structures of glycans in complex mixtures (*4*, *5*) and to examine specificities and biology of glycan-binding proteins that occur in nature (*6*–*8*).

Naturally occurring glycans are typically isolated in small quantities as mixtures of closely related structures that are difficult to separate, and therefore do not provide a reliable source of well-defined oligosaccharides. Thus, it is widely accepted that chemical- or enzymatic approaches must be used for the preparation of diverse glycan libraries needed for biological and structural studies (*7*–*11*). Despite ongoing progress, the chemical synthesis of complex oligosaccharides remains very time consuming, especially when highly complex structures are targeted (*7*). The need for more efficient approaches has stimulated the development of chemo-enzymatic methods in which a synthetic oligosaccharide precursor is modified by a range of glycosyltransferases to give more complex derivatives (*10*, *11*). Such an approach can, however, only provide symmetrically branched oligosaccharides.

Naturally occurring branched oligosaccharides often bear distinctive appendages at each branching point (*12*). In this respect, the biosynthesis of N-linked oligosaccharides is initiated in the endoplasmic reticulum where a dolichol-linked $Glc_3Man_9GlcNAc_2$ oligosaccharide precursor is transferred en bloc to an Asn-X-Ser/Thr sequon, where X is any amino acid, on newly synthesized polypeptides. Subsequent trimming and processing of the transferred oligosaccharide results in a $GlcNAcMan_3GlcNAc_2$ core structure, which is transported to the Golgi where additional *N*-acetylglucosamine moieties (*O*-GlcNAc) can be added. Subsequent conversion of the *O*-GlcNAc stubs into *N*-acetyllactosamine [βGal(1,4) GlcNAc, LacNAc], provide precursors that can be elaborated by various glycosyltransferases to give rise to enormous structural diversity.

The biosynthesis of complex branched oligosaccharides generally leads to positional isomers, which are structurally difficult to assign by mass spectrometry (*4*, *5*). Furthermore, glycan microarray technology has shown that terminal oligosaccharide motifs of complex glycans mediate biological recognition (*13*). However, recent studies indicate a more complex picture in which the core structure can influence terminal glycan recognition (*14*). A synthetic technology that can give libraries of asymmetrically substituted glycans will make it possible to fabricate the next generation of glycan microarray to examine in detail glycan-protein recognition, to develop algorithms for the assignment of mass spectra, and to design probes for elucidating pathways of glycoconjugate biosyn-

[1]Complex Carbohydrate Research Center, University of Georgia, 315 Riverbend Road, Athens, GA 30602, USA. [2]Chemistry Department, University of Georgia, Athens, GA 30602, USA. [3]Departments of Cell and Molecular Biology, and Chemical Physiology, The Scripps Research Institute, 10550 North Torrey Pines Road, La Jolla, CA 92037, USA.

*These authors contributed equally to this work.
†Corresponding author. E-mail: gjboons@ccrc.uga.edu

thesis. Despite the urgent need for libraries of asymmetrically branched *N*-glycans (*15*, *16*), none of the currently available methods can produce collections of such compounds, and previous synthetic efforts have almost exclusively focused on the preparation of symmetrically branched compounds (*17*–*23*).

We envisaged that oligosaccharide **1** would be an attractive starting material for the preparation of libraries of asymmetrically branched *N*-glycans (Fig. 1). This pentasaccharide resembles the core structure common to all eukaryotic N-linked glycans (*12*) and is modified at positions where branching points can occur with the protecting groups levulinoyl (Lev), fluorenylmethyloxycarbonate (Fmoc), allyloxycarbonate (Alloc), and 2-naphthylmethyl (Nap). We show here that these protecting groups are orthogonal, and therefore it was possible to generate libraries of complex branched bi-, tri-, and tetra-antennary structures by sequential removal of the protecting groups followed by chemical glycosylations using a diverse set of glycosyl donors. Furthermore, we anticipated that the use of LacNAc and GlcNAc donors **2** to **5**, followed by removal of all protecting groups except the acetyl esters, would give precursor glycans that at each antenna could be selectively extended by a panel of glycosyltransferases to rapidly give large numbers of highly complex asymmetrically substituted *N*-glycans. Selective extension was expected to be feasible because many relevant glycosyltransferases recognize LacNAc but not GlcNAc as a substrate (*18*). The latter moiety can, however, be converted into LacNAc by enzymatic galactosylation, and the resulting derivative can then be elaborated by other glycosyltransferases. Furthermore, acetylation should render LacNAc and GlcNAc moieties inactive for enzymatic modification; however, the removal of these esters would give an appropriate substrate for extension by glycosyltransferases.

Some applications, such as the use of synthetic glycans as standards for mass spectrometry, require compounds having an unmodified reducing end. Other uses, such as the development of glycan microarrays, need compounds modified with a reactive anomeric linker. To ensure that the glycans prepared by the chemo-enzymatic approach can be employed for multiple pur-

Fig. 1. Orthogonally protected core pentasaccharide 1 and glycosyl donors 2 to 5. Coupling of **1** with these reagents in a parallel combinatorial manner gives oligosaccharide precursors to enzyme substrates.

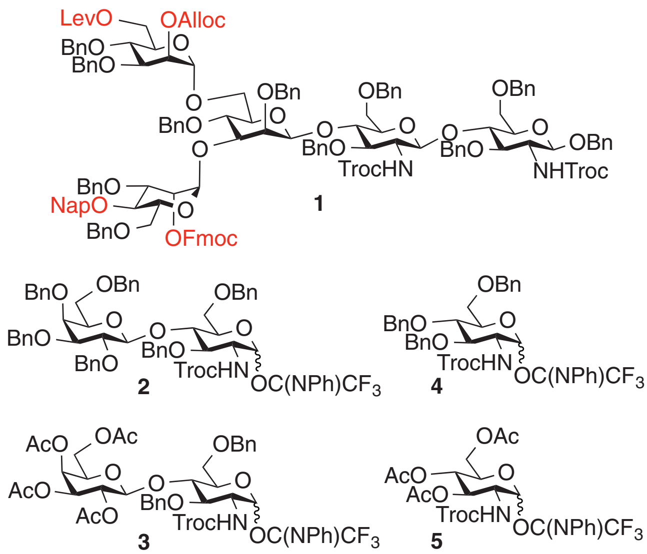

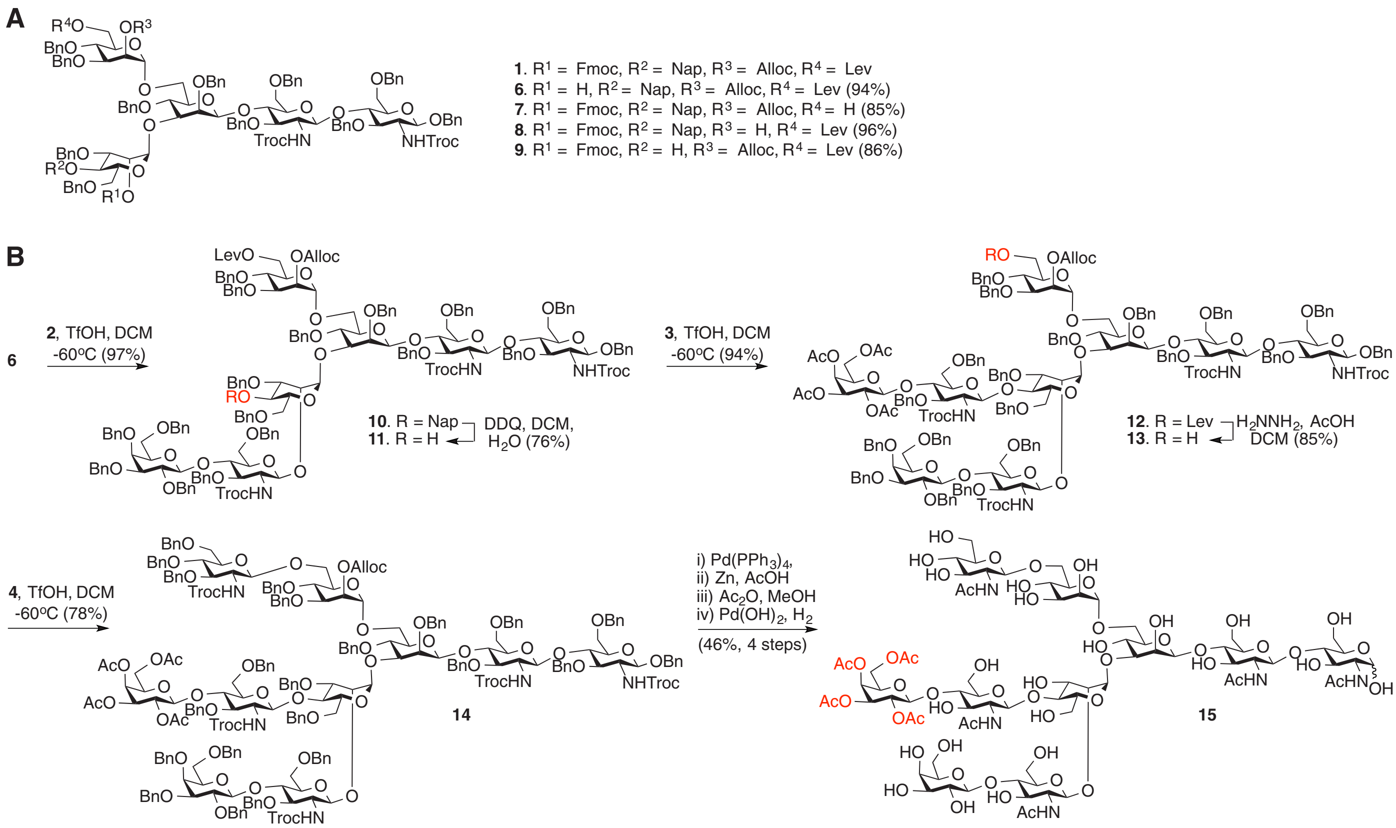

Fig. 2. Chemical synthesis of decasaccharide 15 for branch-specific enzymatic extensions. (**A**) Selective removal of temporary protecting groups. (**B**) Preparation of glycan precursor for enzymatic extension.

poses, the anomeric center of compound **1** was protected as a benzyl glycoside. This protecting group will be removed during the deprotection stage to give glycans having an unmodified reducing end. The latter type of compound can, however, easily be derivatized by a reactive anomeric linker by reaction with an appropriate reagent such as 2-[(methylamino)oxy]ethanamine (*24*).

Pentasaccharide **1** was readily assembled from appropriately protected monosaccharide building blocks (fig. S2). The Fmoc group of **1** could be selectively removed by the non-nucleophilic base triethylamine to give **6,** whereas treatment with the nucleophilic base hydrazine acetate led to cleavage of the Lev ester to provide **7** without affecting the other base-sensitive protecting groups (Fig. 2A). Treatment of **1** with $Pd(PPh_3)_4$ affected only the Alloc protecting group providing the corresponding hydroxyl **8,** and oxidation with 2,3-dichloro-5,6-dicyano-1,4-benzoquinone (DDQ) resulted in the removal of the Nap ether to give **9** in high yield.

Having demonstrated the orthogonality of the temporary protecting groups, we focused on the preparation of tri-antennary oligosaccharide **15**, which was expected to be an appropriate precursor for branch-specific enzymatic modification (Fig. 2). Glycosyl acceptor **6** was coupled with **2** by using trifluoromethanesulfonic acid (TfOH) (*25*, *26*) as the promoter to give heptasaccharide **10**. The Nap ether of **10** was removed by oxidation with DDQ, and the resulting acceptor **11** was glycosylated with **3** to provide nonasaccharide **12**. Next, the Lev ester of **12** was cleaved with hydrazine acetate to give **13**, which was coupled with **4** to give fully protected decasaccharide **14**. Partial deprotection of **14** to give target compound **15** was accomplished by cleavage of the Alloc carbonate with $Pd(PPh_3)_4$ followed by removal of the 2,2,2-trichloroethyoxycarbamate (Troc) groups with Zn in acetic acid, acetylation of the resulting free amines with acetic anhydride, and catalytic hydrogenolysis of the benzyl ethers. Detailed nuclear magnetic resonance (NMR) analysis of **15** showed that the acetyl esters were still intact, and thus a compound was obtained that has characteristic saccharide appendages at each antenna, allowing selective modification by a panel of glycosyltransferases.

In addition to compound **15**, pentasaccharide **1** is an appropriate starting material for the chemical synthesis of other bi-, tri-, and tetra-

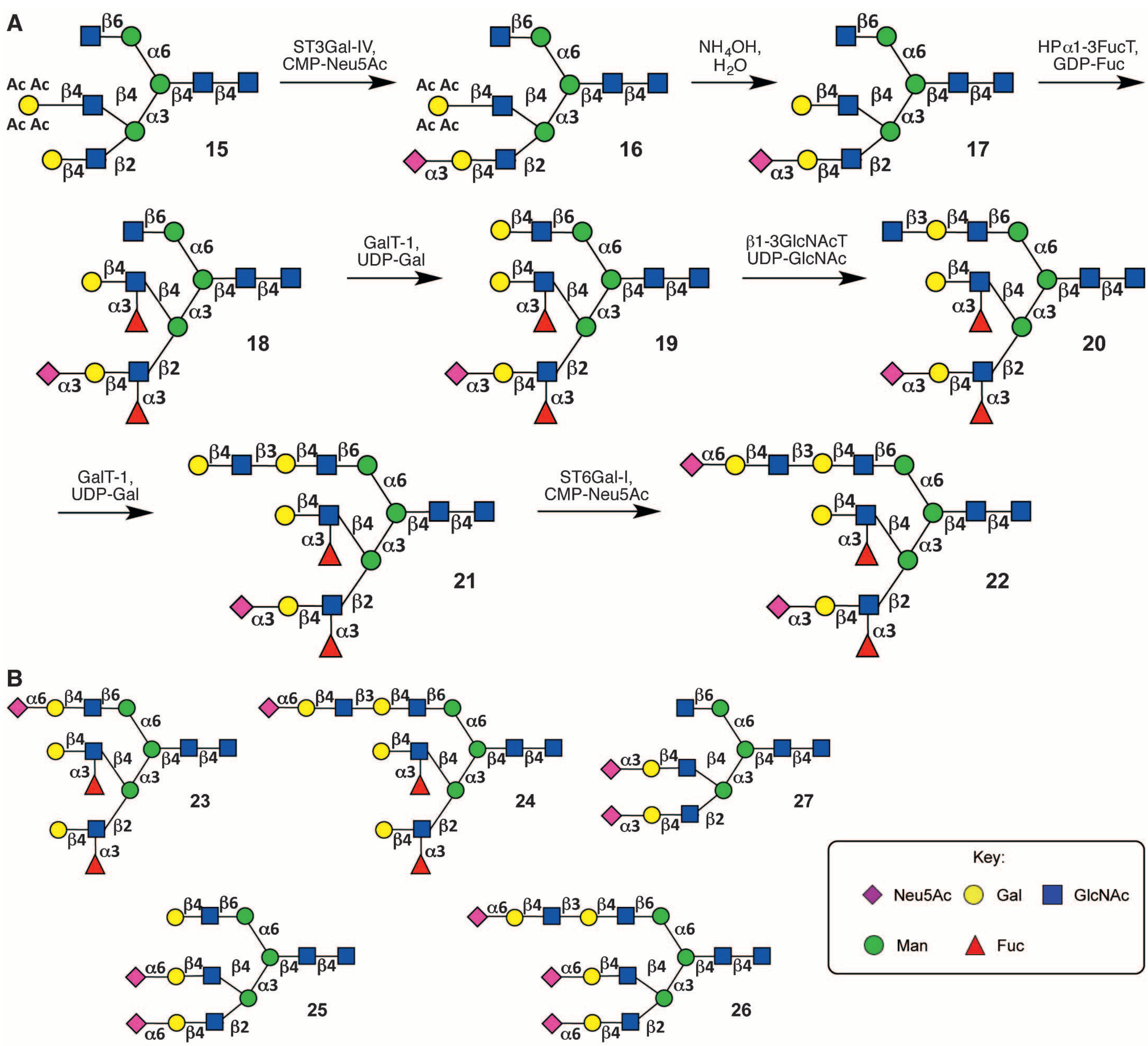

Fig. 3. Chemoenzymatic synthesis of complex oligosaccharides from 15. (**A**) Synthetic route to asymmetrically substituted multi-antennary glycan **22**. (**B**) Structures of compounds **23** to **26** prepared by an analogous approach (see figs. S14 and S15 for synthetic intermediates). *N*-Acetyl neuraminic acid (Neu5Ac, diamonds); D-galactose (Gal, circles); *N*-acetyl-D-glucosamine (GlcNAc, squares); D-mannose (Man, circles); L-fucose (Fuc, triangles).

antennary precursor oligosaccharides by changing the number and sites of attachment of the appendages (**2** to **5**). For example, a positional isomer of **15** was readily prepared by the sequential removal of the Fmoc, Alloc, and Lev groups of **1** and glycosylations with glycosyl donors **2**, **3**, and **4**, respectively (fig. S3).

The precursor oligosaccharide **15** was further extended by glycosyltransferases to demonstrate the possibility of selective modification of each antenna to form highly complex asymmetrically branched *N*-glycans (Fig. 3). Many human *N*-glycans contain terminal sialic acids either exclusively α(2,3)- or α(2,6)-linked to *N*-acetyllactosamine or a combination of these two linkages (*27*). Furthermore, Lewis antigens such as Lewis^y (Le^y), Le^x, and sialyl Lewis^x (SLe^x) are found on many biologically important glycans. Therefore, we focused on the preparation of heptadecasaccharide **22,** which has SLe^x and Le^x appendages at the C-2 and C-4 arm, respectively, and a di-LacNAc moiety extended by α(2,6)-linked sialoside at the C-6 arm. A key aspect of this strategy is that relatively few glycosyltransferases are needed to elaborate these terminal glycan sequences, and enzyme expression systems that produce these and many other mammalian and bacterial glycosyltransferases useful in chemoenzymatic synthesis have already been described (*28*, *29*).

The LacNAc moiety of decasaccharide **15** was sialylated by α2,3-sialyltransferase (ST3Gal-IV), cytidine-5′-monophospho-*N*-acetylneuraminic acid (CMP-Neu5Ac), and calf intestine alkaline phosphatase (CIAP), and as expected, only one of the three antennae was modified to give exclusively compound **16**. Next, the acetyl esters of **16** were removed by treatment with aqueous ammonia to give compound **17**, which then had an unmasked LacNAc moiety at the C-4 of the Man-α3 arm that was expected to be available for enzymatic transformations. Indeed, fucosylation of **17** with α1,3-fucosyltransferase (α3FucT) (*30*) resulted in the modification of the LacNAc and sialyl-LacNAc moieties to give bis-fucosylated derivative **18**. The GlcNAc moiety at the C-6 antenna of **18** was converted into a LacNAc moiety by using β1,4-galactosyltransferase (GalT-1), uridine 5′-diphosphogalactose (UDP-Gal), and CIAP to give **19**. Treatment of **19** with β1,3-*N*-acetylglucosaminyltransferase (β1,3GlcNAcT) (*31*), UDP-GlcNAc, and CIAP resulted in a selective addition of a β(1,3)-linked GlcNAc moiety to the LacNAc moiety of the β1-6 branch to give **20**. The Le^x moiety of **19** was unaffected, highlighting the feasibility of exploiting inherent substrate specificities of glycosyltransferases for the selective modification of multi-antennary glycans. The β1,6-branch was further extended by GalT-1 and α2,6-sialyltransferase (ST6Gal-1) to provide target compound **22**, which has distinctive oligosaccharide appendages at each of the three antennae.

After each step, the product was purified by size exclusion chromatography and the resulting compound fully characterized by NMR and mass spectrometry of the permethylated derivative. If any starting material was observed, the compound was resubjected to the enzyme until a homogeneous product was obtained. In addition to target compound **22**, each intermediate of the enzymatic extension (**17** to **21**) can in principle be used for biological or biophysical studies. The precursor oligosaccharide **15** is an attractive starting material for the preparation of many other highly complex glycans. To illustrate this feature, we prepared compounds **23** to **27** (figs. S14 and S15), which are asymmetrical and have varying numbers of 2,3- or 2,6-linked sialic acids at the various antennae (*27*). Thus, subsequent deacetylation and bis-fucosylation of **15** to give Le^x moieties at the β2 and β4 arm were followed by galactosylation to form a LacNAc moiety at the β6 arm that was capped with 2,6-Neu5Ac to form **23** or further extended with 2,6-Neu5Ac-LacNAc to provide **24**. Similarly, compounds **25** to **27** were synthesized by either bis-α(2-3) (to give **27**) or bis-α(2-6)-sialylation, followed by extension of the β6 arm to provide **25** and **26** (fig. S15).

It was anticipated that compounds **22** to **27** would be useful for examining the activity of the various biologically relevant glycan epitopes in the context of their presence on multiantennary asymmetric structures. Thus, a glycan microarray was constructed composed of the asymmetrical tri-antennary glycans (**22** to **27**) and previously prepared linear and bi-antennary glycans having a terminal β(1-4)Gal (**A** to **D**), α(1-3)-Fuc (**E** and **F**), α(2-6)-Neu5Ac (**G** to **L**), or α(2-3)-Neu5Ac (**M** to **Q**) moiety (table S14). Compounds **22** to **27** were modified with an amino-containing linker by treatment with 2-[(methylamino)oxy]ethanamine (*24*), and the resulting derivatives were printed on *N*-hydroxysuccinimide (NHS)–activated glass slides with the reference compounds (*32*).

Probing the array with the *Erythrina crystagalli* agglutinin (ECA) specific for terminal LacNAc sequences detected the corresponding reference

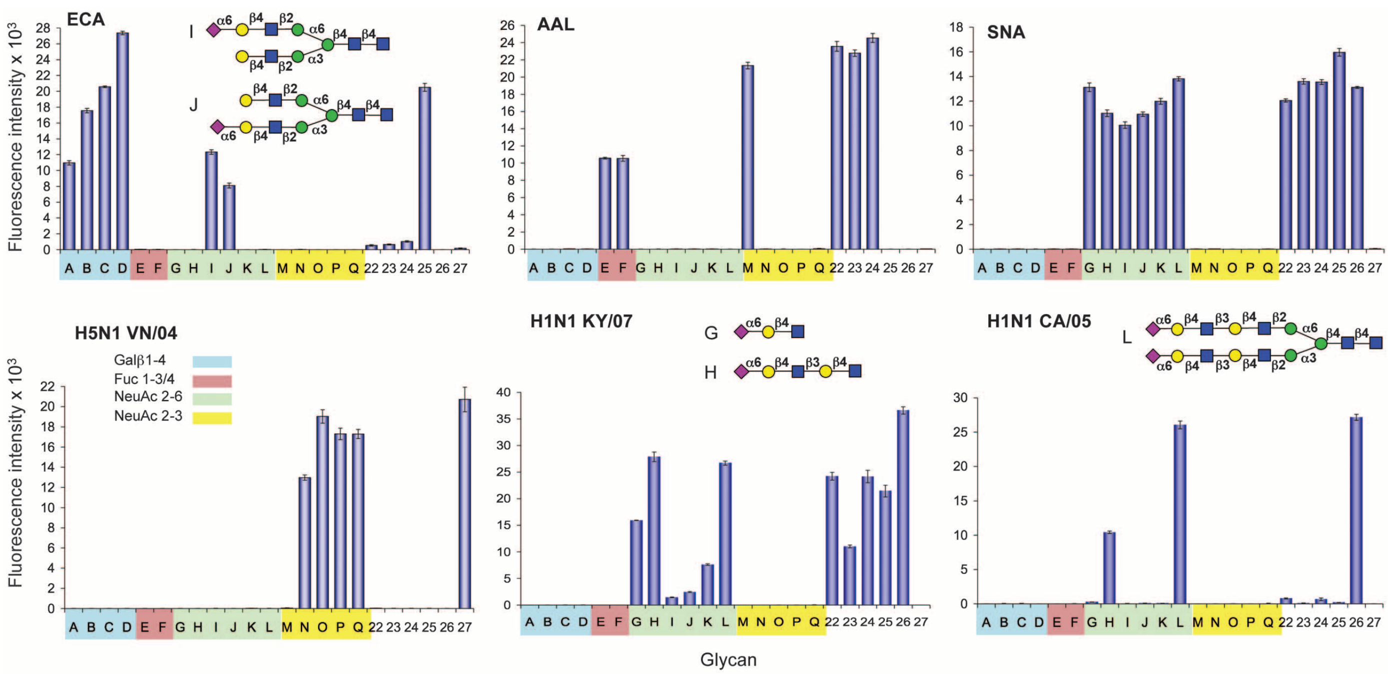

Fig. 4. Glycan microarray binding analyses. Fluorescently labeled lectins (ECA, AAL, and SNA), and recombinant avian (VN/04) and human influenza A (KY/07 and CA/05) HA were assessed for binding to the array. Shown is the mean signal and standard error calculated for six independent replicates on the array. Structures of each of the lettered glycans are found in table S14.

compounds **A** to **D** and compounds **I** and **J**; two biantennary compounds that have one branch modified with a LacNAc structure (Fig. 4). Of the synthetic triantennary compounds, ECA lectin bound strongly to **25** and weakly to **22** to **24**. The latter compounds contain LacNAc substituted with a fucoside, which is known to reduce the affinity of ECA (*33*). By contrast, the fucose-specific *Aleuria aurantia* lectin (AAL) robustly recognized the fucoside containing glycans **22** to **24** as well as the three reference compounds containing a Le^x epitope (**E**, **F**, and **M**). *Sambuccus nigra* agglutinin (SNA) specific for terminal α(2-6)Neu5Ac recognized all structures containing this epitope (**G** to **L** and **22** to **26**).

Influenza viruses recognize sialic acids as receptors, and it is well documented human and avian viruses exhibit differential specificity for glycans with Neu5Acα(2-6)Gal and Neu5Acα(2-3)Gal linkages, respectively. This difference in specificity represents a major barrier for transmission of avian viruses to humans (*34*, *35*), and increasing attention is placed on glycan microarray analysis to understand the receptor requirements of avian and human virus hemagglutinins (HAs) required for species tropism (*36*–*38*). To assess the potential for influenza HA to distinguish between symmetric and asymmetric glycans, we evaluated the specificity of an HA from an exemplary H5N1 avian virus (VN/04), a human seasonal H1N1 virus (KY/07), and an H1N1 virus from the 2009 influenza pandemic (CA/05).

The H5 HA from VN/04 recognized compounds **N** to **Q** and **27**, which contain the Neu5Acα(2-3)Gal, consistent with the consensus receptor specificity of avian viruses (*34*, *39*). Notably, this cloned HA did not recognize the Neu5Acα(2-3)Gal in the fucosylated sequence SLe^x in compound **22** or the reference compound **M**. By contrast, the HA from the two human influenza viruses exhibited binding only to glycans containing the Neu5Acα(2-6)Gal epitope (Fig. 4), but otherwise exhibited different fine specificities. The HA from the H1N1 seasonal strain A/Kentucky/07 (KY/07) recognized all the reference compounds (**G** to **L**) and all the triantennary compounds (**22** to **26**) that contained this linkage. However, relative to the linear reference compounds (**G** and **H**), the compounds that have a Neu5Acα(2–6)Gal moiety on only one branch of a biantennary glycan were bound weakly (**I** and **J**), whereas those that had the Neu5Acα (2–6)Gal sequence on only one branch of the triantennary glycans (**23**, **24**) were recognized equally well. Thus, this HA distinguishes structures with a single sialic acid in the context of linear or biantennary and triantennary chain N-linked glycan chains. More pronounced differences are seen when comparing the seasonal H1 and the pandemic HA H1 from A/California/05/09 (CA/05). The CA/05 HA recognized only reference compounds **H** and **L** and a single triantennary glycan, namely **26**. These compounds have in common the Neu5Acα(2–6) epitope linked to an extended dimeric-LacNAc moiety. However, this motif is also present in triantennary glycans **22** and **24**, which are not recognized by this HA. Compounds **L** and **26** also have in common at least two Neu5Acα(2–6) epitopes on different antennae, but so do compounds **K** and **25**, which have a single LacNAc extension and are not recognized. These results reflect differences in the specificity of these HAs, and not simple differences in avidity, because similar array results were obtained when the concentration of the HA applied to the array was titrated down in twofold dilutions from 100 to 6 μg/ml (fig. S24).

These results demonstrate that glycan epitopes presented on asymmetrically branched N-linked glycans can be distinguished from the same epitopes on linear or symmetrically branched glycans. Such context-dependent recognition can be due to extended binding sites, unfavorable interactions by neighboring antennae, and multivalency by proper spacing of minimal epitopes at two or more antennae. As illustrated by the selected influenza HAs, these differences are relevant to the recognition of receptors by human pathogens. A complete understanding of influenza receptor specificity and its relevance to adaptation of animal viruses to human hosts will require an extensive panel of asymmetric and symmetric glycan structures representative of those found on human and animal airway epithelia (*38*). Such libraries of glycans, which can be produced by the methodology presented here, will begin to define the human glycome and provide tools to understand the biology mediated by both microbial and mammalian glycan-binding proteins that mediate host pathogen interactions and innate and adaptive immune responses (*13*, *40*).

References and Notes

1. G. W. Hart, R. J. Copeland, *Cell* **143**, 672–676 (2010).
2. H. H. Freeze, *Nat. Rev. Genet.* **7**, 537–551 (2006).
3. K. Ohtsubo, J. D. Marth, *Cell* **126**, 855–867 (2006).
4. S. J. North, P. G. Hitchen, S. M. Haslam, A. Dell, *Curr. Opin. Struct. Biol.* **19**, 498–506 (2009).
5. K. Mariño, J. Bones, J. J. Kattla, P. M. Rudd, *Nat. Chem. Biol.* **6**, 713–723 (2010).
6. N. Laurent, J. Voglmeir, S. L. Flitsch, *Chem. Commun. (Camb.)* (37): 4400–4412 (2008).
7. T. J. Boltje, T. Buskas, G. J. Boons, *Nat. Chem.* **1**, 611–622 (2009).
8. B. Lepenies, J. Yin, P. H. Seeberger, *Curr. Opin. Chem. Biol.* **14**, 404–411 (2010).
9. X. M. Zhu, R. R. Schmidt, *Angew. Chem. Int. Ed. Engl.* **48**, 1900–1934 (2009).
10. M. M. Palcic, *Curr. Opin. Chem. Biol.* **15**, 226–233 (2011).
11. R. M. Schmaltz, S. R. Hanson, C. H. Wong, *Chem. Rev.* **111**, 4259–4307 (2011).
12. K. W. Moremen, M. Tiemeyer, A. V. Nairn, *Nat. Rev. Mol. Cell Biol.* **13**, 448–462 (2012).
13. C. D. Rillahan, J. C. Paulson, *Annu. Rev. Biochem.* **80**, 797–823 (2011).
14. H. J. Gabius, S. André, J. Jiménez-Barbero, A. Romero, D. Solís, *Trends Biochem. Sci.* **36**, 298–313 (2011).
15. R. Ranzinger, M. Frank, C. W. von der Lieth, S. Herget, *Glycobiology* **19**, 1563–1567 (2009).
16. Analysis of the glycome-DB database shows that 85% of known glycan structures are asymmetrical. Almost all of the known N-linked glycans have fewer than 25 monosaccharides, and such compounds should be accessible by the strategy presented here.
17. C. Unverzagt, *Angew. Chem. Int. Ed. Engl.* **35**, 2350–2353 (1996).
18. S. Hanashima, S. Manabe, Y. Ito, *Angew. Chem. Int. Ed. Engl.* **44**, 4218–4224 (2005).
19. S. Jonke, K. G. Liu, R. R. Schmidt, *Chemistry* **12**, 1274–1290 (2006).
20. B. Sun, B. Srinivasan, X. F. Huang, *Chemistry* **14**, 7072–7081 (2008).
21. C. Unverzagt *et al.*, *Chemistry* **15**, 12292–12302 (2009).
22. S. Serna, J. Etxebarria, N. Ruiz, M. Martin-Lomas, N. C. Reichardt, *Chemistry* **16**, 13163–13175 (2010).
23. M. A. Walczak, S. J. Danishefsky, *J. Am. Chem. Soc.* **134**, 16430–16433 (2012).
24. O. Bohorov, H. Andersson-Sand, J. Hoffmann, O. Blixt, *Glycobiology* **16**, 21C–27C (2006).
25. R. R. Schmidt, W. Kinzy, *Adv. Carbohydr. Chem. Biochem.* **50**, 21–123 (1994).
26. B. Yu, H. C. Tao, *Tetrahedron Lett.* **42**, 2405–2407 (2001).
27. G. Spik, V. Debruyne, J. Montreuil, H. van Halbeek, J. F. Vliegenthart, *FEBS Lett.* **183**, 65–69 (1985).
28. More then 800 expression constructs of human glycosylation enzymes in multiple expression vectors and protocols to produce the enzymes for biochemical, enzymatic synthesis, and structural studies are available at http://glycoenzymes.ccrc.uga.edu.
29. O. Blixt, N. Razi, *Methods Enzymol.* **415**, 137–153 (2006).
30. W. Wang *et al.*, *Proc. Natl. Acad. Sci. U.S.A.* **106**, 16096–16101 (2009).
31. B. Sauerzapfe *et al.*, *Glycoconj. J.* **26**, 141–159 (2009).
32. O. Blixt *et al.*, *Proc. Natl. Acad. Sci. U.S.A.* **101**, 17033–17038 (2004).
33. Y. Itakura *et al.*, *J. Biochem.* **142**, 459–469 (2007).
34. A. Chandrasekaran *et al.*, *Nat. Biotechnol.* **26**, 107–113 (2008).
35. M. Imai, Y. Kawaoka, *Curr. Opin. Virol.* **2**, 160–167 (2012).
36. L. M. Chen *et al.*, *Virology* **422**, 105–113 (2012).
37. M. B. Pearce *et al.*, *Proc. Natl. Acad. Sci. U.S.A.* **109**, 3944–3949 (2012).
38. T. Walther *et al.*, *PLoS Pathog.* **9**, e1003223 (2013).
39. J. Stevens *et al.*, *Science* **312**, 404–410 (2006).
40. Y. van Kooyk, G. A. Rabinovich, *Nat. Immunol.* **9**, 593–601 (2008).

Acknowledgments: This research was supported by NIH grant P41RR005351 from the National Center for Research Resources (G.J.-B. and J.G.), National Institute of General Medical Sciences grants P41GM103390 (G.J.B. and J.G.) and R01GM090269 (G.J.-B.), Institute of Allergy and Infectious Disease grant AI058113 (J.C.P.), and a contract from the Centers for Disease Control (J.C.P.). R.P.d.V. is a recipient of a Rubicon grant from the Netherlands Organization for Scientific Research (NWO). We thank A. Crie and M. Wolfert for assistance in preparation of the manuscript, K. Moremen (University of Georgia) for providing ST6Gal-1 and ST3Gal-IV, and P. Wu (Albert Einstein College of Medicine) and W. Wakarchuk (Ryerson University) for providing the plasmids for α1,3FucT and β1,3GlcNAcT, respectively. G.J.-B. conceived the idea, Z.W. performed the chemical synthesis, S.G.A. assisted with chemical synthesis, Z.S.C. performed the enzymatic transformations, and W.P. and Z.W. assisted with the enzymatic transformation. Z.S.C. and J.G. performed the analysis of the complex glycans. W.P. performed the attachment of the reactive linker to the glycans, R.M. performed the microarray screening, R.P.d.V. prepared the influenza HA, and J.C.P. supervised and analyzed the microarray studies. G.J.-B. and J.C.P. wrote the paper. The data for this report are archived as supplementary materials on *Science* Online. A patent application related to the described chemoenzymatic approach has been filed by the University of Georgia Research Foundation and lists G.J.-B and Z.W. as inventors. The authors declare no competing financial interests.

Supplementary Materials

www.sciencemag.org/cgi/content/full/341/6144/379/DC1
Materials and Methods
Figs. S1 to S24
Tables S1 to S14
References (*41*–*48*)
Copies of NMR Spectra

7 February 2013; accepted 14 June 2013
10.1126/science.1236231

Identification of a Colonial Chordate Histocompatibility Gene

Ayelet Voskoboynik,[1,2]*‡ Aaron M. Newman,[1]*‡ Daniel M. Corey,[1] Debashis Sahoo,[1] Dmitry Pushkarev,[3]† Norma F. Neff,[3] Benedetto Passarelli,[3] Winston Koh,[3] Katherine J. Ishizuka,[1,2] Karla J. Palmeri,[1,2] Ivan K. Dimov,[1] Chen Keasar,[4] H. Christina Fan,[3] Gary L. Mantalas,[3] Rahul Sinha,[1] Lolita Penland,[3] Stephen R. Quake,[3]‡ Irving L. Weissman[1,2,5]‡

Histocompatibility is the basis by which multicellular organisms of the same species distinguish self from nonself. Relatively little is known about the mechanisms underlying histocompatibility reactions in lower organisms. *Botryllus schlosseri* is a colonial urochordate, a sister group of vertebrates, that exhibits a genetically determined natural transplantation reaction, whereby self-recognition between colonies leads to formation of parabionts with a common vasculature, whereas rejection occurs between incompatible colonies. Using genetically defined lines, whole-transcriptome sequencing, and genomics, we identified a single gene that encodes self–nonself and determines "graft" outcomes in this organism. This gene is significantly up-regulated in colonies poised to undergo fusion and/or rejection, is highly expressed in the vasculature, and is functionally linked to histocompatibility outcomes. These findings establish a platform for advancing the science of allorecognition.

Allorecognition, the capacity to distinguish "self" from allogeneic "nonself," is critical for multicellular life. This process also has important implications for humans, as it underlies maternal tolerance of the fetus (*1*, *2*) and the outcomes of blood or tissue transplants (*3*, *4*). To gain insights into the evolution and molecular characteristics of allorecognition, we are studying *Botryllus schlosseri*, a member of the urochordates, the closest living sister group of vertebrates (*5*). *B. schlosseri* engages in a natural transplantation reaction, whereby colonies undergo self–nonself recognition, which leads to either formation of parabionts with a fused vasculature (i.e., fusion) or an inflammatory rejection response (i.e., rejection) (fig. S1). A polymorphic gene locus governs fusion or rejection outcomes (*6*–*9*). This locus, called Fu/HC for fusion-histocompatibility, encodes multiple codominant alleles, and progeny from crosses between histocompatible *B. schlosseri* colonies are known to segregate as a monogenic trait (*8*, *9*). The rules governing fusibility reactions are as follows: AB = AB leads to fusion, AB = CD to rejection, and AB = BC to fusion. Previously, we identified a highly polymorphic candidate allorecognition gene (*cFuHC*) within the Fu/HC locus (*10*–*12*). As the major histocompatibility regions in vertebrates are haplotypes (that is, sets of linked genes), we analyzed the recently completed *B. schlosseri* genome (*13*) to determine whether a haplotype or single protein–encoding gene encodes self-nonself recognition.

Using diverse sequencing data, we first attempted to validate the genomic structure of the *cFuHC*, which previously appeared to correlate with fusion or rejection outcomes (*12*). The original *cFuHC* model consists of two dominant isoforms, a secreted form and a membrane-bound form encompassing the entire predicted gene (*12*). We found that instead of two isoforms, the *cFuHC* consists of two genes separated by 250 base pairs (bp) (Fig. 1 and tables S1 and S3). We found no evidence for an mRNA isoform bridging these two genes (table S4). One gene, which we term *sFuHC*, is identical to the original secreted isoform; the other, termed *mFuHC*, includes the remaining portion of *cFuHC*, but has a novel N-terminal exon encoding a signal peptide (*14*) (table S5). BLAST analysis revealed a homolog of *mFuHC*, but not *sFuHC*, in *Ciona intestinalis* (gi|198429243) [Expectation value (E-value) = $4E^{-37}$], which further supported our finding. Both genes are highly polymorphic (fig. S2), as previously reported for *cFuHC* (*12*).

Next, we tested whether any genes from the draft assembly encode alleles consistent with a *Botryllus* histocompatibility factor. We used two complementary strategies, one to assess allelic

[1]Institute for Stem Cell Biology and Regenerative Medicine, Stanford University School of Medicine, Stanford, CA 94305, USA. [2]Department of Developmental Biology, Stanford University, Hopkins Marine Station, Pacific Grove, CA 93950, USA. [3]Departments of Applied Physics and Bioengineering, Stanford University, and Howard Hughes Medical Institute, Stanford, CA 94305, USA. [4]Department of Computer Science, Ben-Gurion University of the Negev, Beer-Sheva 84105, Israel. [5]Ludwig Center for Cancer Stem Cell Research and Medicine, Stanford University School of Medicine, Stanford, CA 94305, USA.

*These authors contributed equally to this work.
†Present address: Illumina Inc., Hayward, CA 94545, USA.
‡Corresponding author. E-mail: ayeletv@stanford.edu (A.V.), amnewman@stanford.edu (A.M.N.), quake@stanford.edu (S.R.Q.), irv@stanford.edu (I.L.W.)

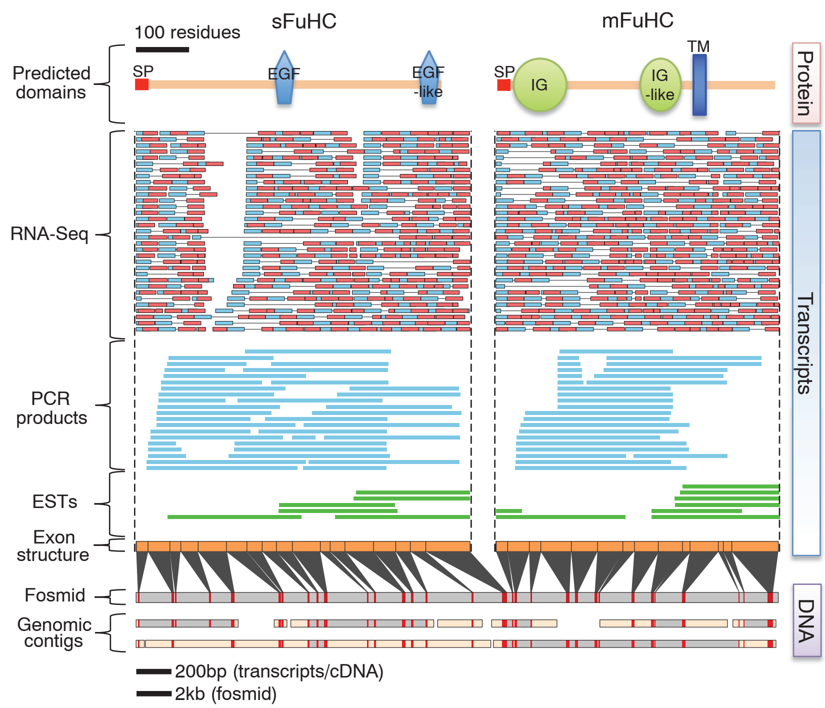

Fig. 1. Genomic characterization of the *cFuHC* locus in *B. schlosseri* reveals two tightly linked genes. The *cFuHC* locus encodes two gene products, sFuHC (a secreted form) and mFuHC (a membrane-bound form). Sequences aligned, from bottom to top: (i) Genomic contigs from *B. schlosseri* draft assembly; (ii) fosmid clone used to characterize *cFuHC* (*12*) (table S5); (iii) predicted exon structures, with genomic coordinates indicated below in red (contigs with identical interexon distances to the fosmid are colored gray); (iv) *B. schlosseri* expressed sequence tags (ESTs) obtained from NCBI; (v) Sanger-sequenced PCR products resulting from selected *cFuHC* amplicons (table S1); (vi) representative RNA-Seq reads (100 bp × 2) from 17 colonies (table S4); (vii) translated primary sequences with predicted functional domains (*14*). All alignments were performed with megablast (mismatch penalty = –2, ≥90% identity, no query filtering, and otherwise default parameters). EGF, epidermal growth factor; IG, immunoglobulin domain; SP, signal peptide; TM, transmembrane domain.

concordance with known fusibility outcomes and the other to evaluate allelic agreement with Fu/HC genotypes defined by breeding experiments. For the former, we developed a computational pipeline that includes methods to accurately and efficiently phase paired-end RNA sequencing (RNA-Seq) reads into haplotypes, compare phased alleles between colonies, and score each gene based on its ability to stratify known fusibility outcomes (figs. S3 to S7) (*15*). For the latter, we established lines of distinct Fu/HC genotypes (AA, BB, AB, and AX) and used a classical genetics approach (fig. S8). By performing RNA-Seq on colonies with defined Fu/HC genotypes (fig. S8), we could precisely screen for allorecognition factor candidates, because any genes inconsistent with defined genotypes must be incorrect.

In all, 17 colonies encompassing 29 pairs of known fusion-rejection outcomes were analyzed. To increase sensitivity, we included pairs of related rejecting colonies bred in our laboratory and unrelated fusing colonies obtained from the wild (fig. S8). Transcriptome sequencing (table S4), followed by haplotype phasing and interallele comparison (fig. S4), revealed that *sFuHC* and, to some extent, *mFuHC*, significantly stratify colony pairs by known fusion-rejection outcomes ($P = 5.6 \times 10^{-5}$ and $P = 0.05$, respectively, as determined by 1 million random permutations of known fusion-rejection labels across the genome) (Fig. 2A and tables S5 and S6). Although significant, segregation was not perfect for either gene (Fig. 2A and fig. S9), and neither *sFuHC* nor *mFuHC* are concordant in primary sequence among all AA colonies (fig. S9), and so, they fail the classical genetics test. These results indicate that the allorecognition factor in *B. schlosseri* is encoded by another gene, consistent with a recent report (*16*).

Our unbiased genome-wide scan revealed three candidate genes with perfect classification performance (Fig. 2A). Among them, only one gene is also fully consistent with genetically defined lines (Fig. 2B and table S6). This gene is free of any amino acid differences between histocompatible pairs (Fig. 2B); is highly polymorphic (Fig. 2C); and, on the basis of RNA-Seq, is expressed more highly than either *sFuHC* or *mFuHC* (fig. S10). It is striking that analysis of the fosmid sequence used to identify *cFuHC* revealed that this gene is located ~62 kb away from *sFuHC* and *mFuHC* (Fig. 2C and table S5). Analysis of the draft genome confirmed physical linkage for these three genes (*13*).

We termed this candidate Fu/HC gene, "*Botryllus* histocompatibility factor" (*BHF*), and further analyzed its sequence, relation to fusibility outcomes, and expression patterns. *BHF* is composed of three exons, encoding a highly charged and partially unstructured 252–amino acid protein (Fig. 2C, fig. S11, and tables S5 and S7), with no detectable domains or signal peptide (*14*). *BHF* has three remote homologs in the National Center for Biotechnology Information (NCBI) database, all of which encode uncharacterized proteins from solitary tunicates (fig. S12). Because colonial, but not solitary, tunicates participate in fusibility reactions, we attempted to amplify *BHF* from two other colonial tunicate species (*Botrylloides* sp. and *Diplosoma* sp.). We succeeded in recovering highly similar sequences from both species (fig. S12), which indicated that BHF may represent a general colonial tunicate allorecognition factor. To validate *BHF*, we sequenced four additional *B. schlosseri* colonies by RNA-Seq (Fig. 3A and table S4) and performed *BHF* Sanger-sequencing on two additional AA colonies (fig. S13). We found that *BHF* absolutely aligns with fusibility outcomes in the validation cohort (Fig. 3A) and is homozygous and identical in sequence among all AA colonies (fig. S14A). Moreover, polymorphisms within the first 100 amino acids could predict the outcomes of all histocompatibility reactions (fig. S14B), and at the nucleotide level, *BHF* remains absolutely predictive (fig. S15).

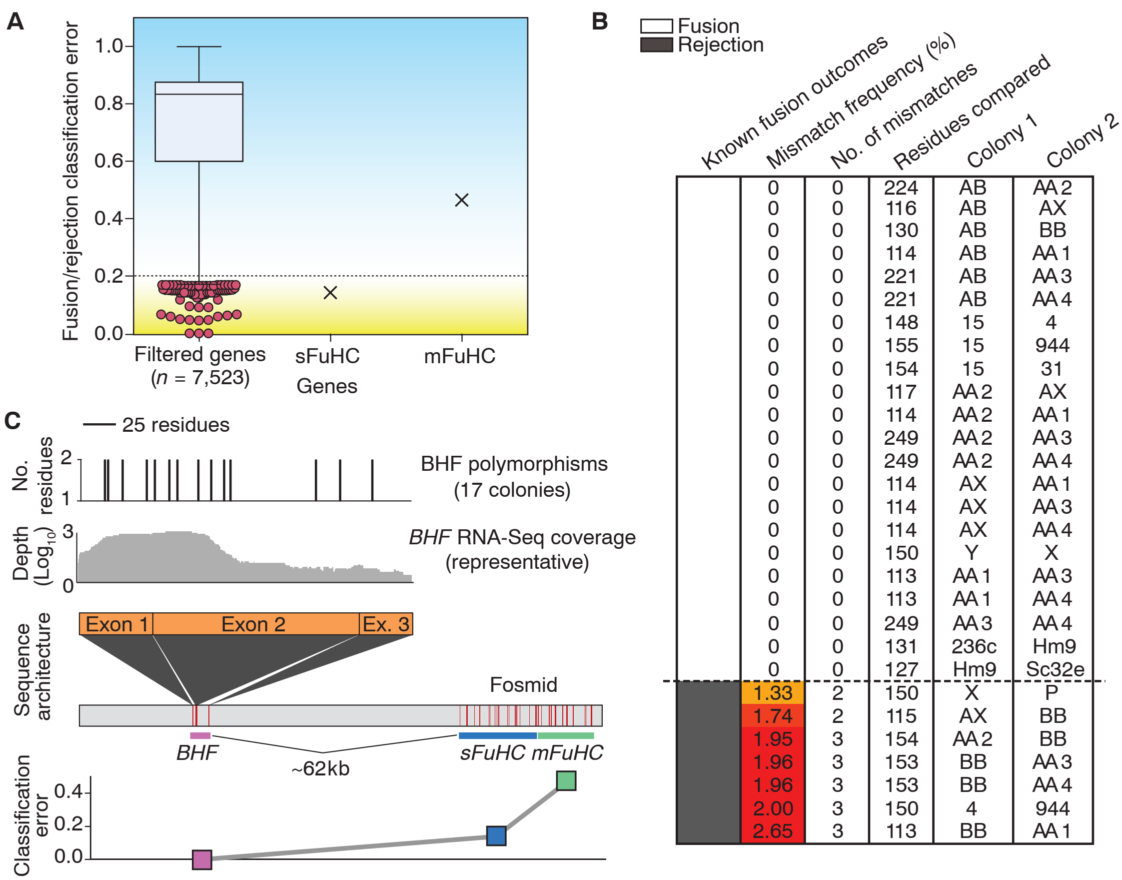

Known fusion outcomes	Mismatch frequency (%)	No. of mismatches	Residues compared	Colony 1	Colony 2
	0	0	224	AB	AA 2
	0	0	116	AB	AX
	0	0	130	AB	BB
	0	0	114	AB	AA 1
	0	0	221	AB	AA 3
	0	0	221	AB	AA 4
	0	0	148	15	4
	0	0	155	15	944
	0	0	154	15	31
	0	0	117	AA 2	AX
	0	0	114	AA 2	AA 1
	0	0	249	AA 2	AA 3
	0	0	249	AA 2	AA 4
	0	0	114	AX	AA 1
	0	0	114	AX	AA 3
	0	0	114	AX	AA 4
	0	0	150	Y	X
	0	0	113	AA 1	AA 3
	0	0	113	AA 1	AA 4
	0	0	249	AA 3	AA 4
	0	0	131	236c	Hm9
	0	0	127	Hm9	Sc32e
	1.33	2	150	X	P
	1.74	2	115	AX	BB
	1.95	3	154	AA 2	BB
	1.96	3	153	BB	AA 3
	1.96	3	153	BB	AA 4
	2.00	3	150	4	944
	2.65	3	113	BB	AA 1

Fig. 2. Genome-wide analysis for candidate *Fu/HC*s reveals a single gene that exhibits perfect alignment with fusibility outcomes and defined *Fu/HC* genotypes. The ability to stratify known fusion or rejection outcomes was tested for all predicted genes from the draft assembly having transcriptome data covering ≥6 fusion and ≥6 rejection pairs, ≥20 common sites sequenced per pair, and at least 1 amino acid polymorphism (after filtering, $n = 7523$ genes) (table S5). (**A**) Classification errors across the genome are depicted as a boxplot showing the median (horizontal line), 25th to 75th percentiles (within the box), and 1st to 99th percentiles (whiskers). Although *sFuHC* is in the top 1% of best-performing genes, novel Fu/HC candidates with equal or better performance were also identified and are indicated in pink beneath the boxplot. Classification errors <0.2 (dotted line) have a *P* value of <0.001, as determined by 1 million random permutations of known fusibility outcomes for each gene analyzed in the assembly (table S6). (**B**) A *B. schlosseri* gene that exhibits perfect sequence concordance with fusion or rejection outcomes and defined genotypes, termed *BHF*. (**C**) *BHF* genomic and message sequence architecture (table S7), representative RNA-Seq coverage, and amino acid polymorphisms across all 17 colonies from the exploratory cohort (table S4).

Among the 23 colonies examined, we determined 10 unique *BHF* alleles that not only agree with all known fusibility outcomes (Fig. 3A and fig. S14) and known pedigree relations (fig. S13) but also allow for the confirmation of precise predictions of *B. schlosseri* self-nonself recognition events. As an example, we predicted that colony 31 (genotype AD) would fuse with colony 944 (genotype AD) and reject colony 4 (genotype BI) and that colony Sc109e would fuse with colony 31. Indeed, we confirmed our predictions for these pairs, along with all other pairs tested (n = 6 of 6) (Fig. 3A and, e.g., fig. S16).

We next asked whether *BHF* is up-regulated under the conditions preceding fusion or rejection, a potential outcome of a bona fide fusibility factor. In tissues that participate in allorecognition (vasculature/tunic), levels of *BHF*, *sFuHC*, and *mFuHC* were assessed by real-time polymerase chain reaction (PCR) in both apposing colonies ("challenged") and physically unpaired colonies ("naïve"). We found a significant up-regulation of *BHF* but not *sFuHC* or *mFuHC* in challenged colonies (two-tailed t test, $P = 0.009$) (Fig. 3B). Moreover, among these three genes, only *BHF* was found among transcripts associated with the *B. schlosseri* rejection response (*17*) (table S6).

We next investigated *BHF* localization and expression. Using whole-mount in situ hybridization, we found high expression levels of *BHF* in blood vessels, including cells in the ampullae (Fig. 3C, top). Increased *BHF* expression was also observed on cells lining the periphery of blood vessels, consistent with epithelium (Fig. 3C, bottom). By RNA-Seq, we found enriched expression of *BHF* in the vasculature compared with endostyle (fig. S17), and by semiquantitative PCR and Sanger-sequencing, we found broad expression of *BHF* in blood, ampullae, bud, endostyle region, tadpole, and sperm (fig. S18). These data are consistent with a histocompatibility-related function for BHF.

Finally, to assess BHF function, we performed morpholino-mediated knockdown experiments (*15*).

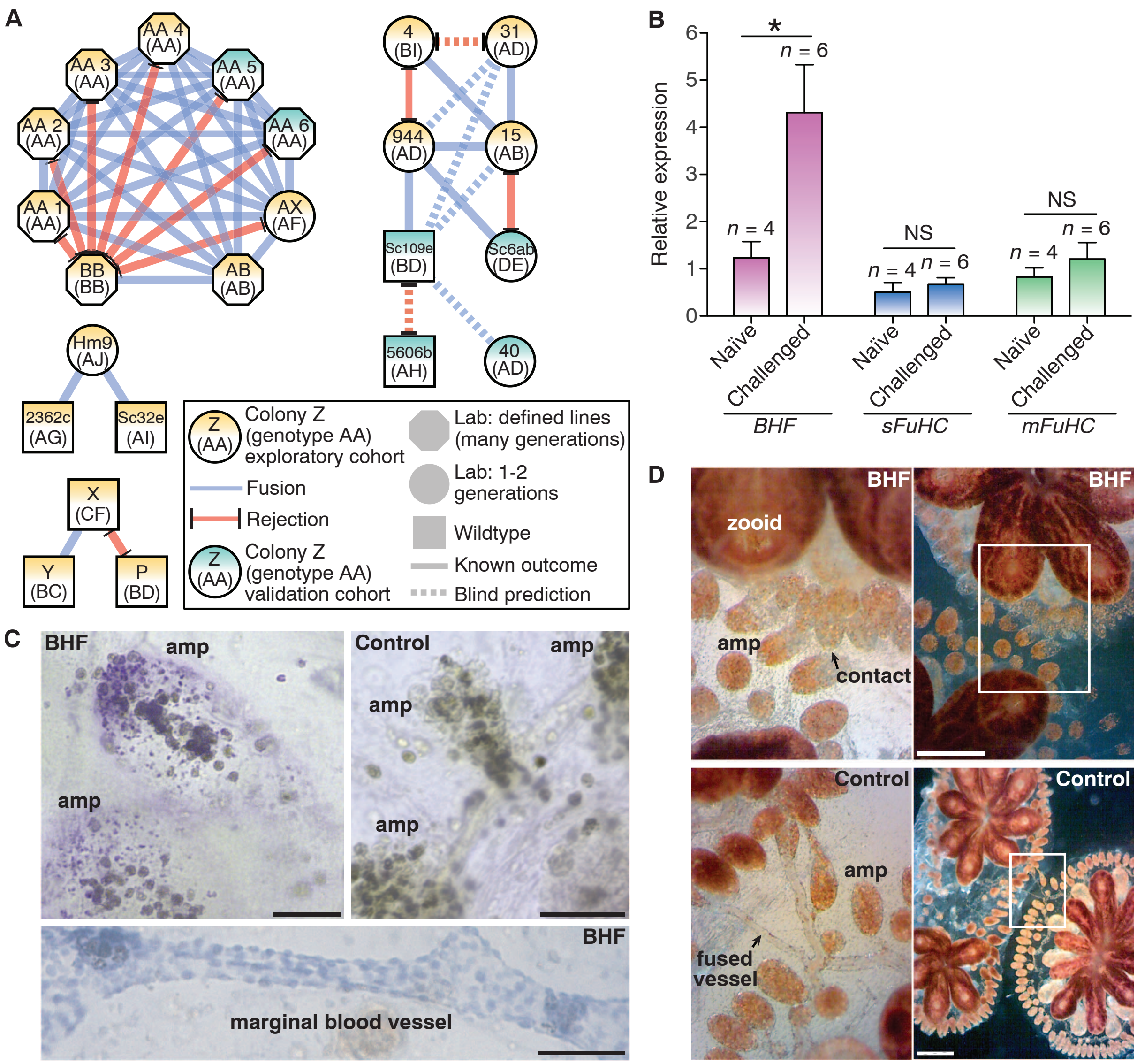

Fig. 3. BHF accurately predicts new fusibility outcomes and has expression patterns and function consistent with a *Botryllus* allorecognition determinant. (**A**) Known and predicted fusion or rejection outcomes among all 23 *B. schlosseri* colonies analyzed (table S4), including exploratory ($n = 17$) and validation cohorts ($n = 6$). All "blind" predictions were confirmed (6 of 6). (**B**) Expression analysis of *BHF*, *sFuHC*, and *mFuHC* under the conditions preceding fusion or rejection ("challenged"; $n = 6$) compared with unchallenged control colonies ("naïve"; $n = 4$) (*$P = 0.009$, two-tailed unequal variance t test; NS, not significant). Values are presented as means ± SEM. (**C**) *BHF* expression patterns assessed by whole-mount in situ hybridization, compared with control (sense probe). amp, ampullae. Scale bars, 50 μm. (**D**) Analysis of morpholino-induced knockdown of BHF. (Top) Unreactive ampullae from apposing colonies under BHF-knockdown conditions (left) and at lower magnification (right). (Bottom) Fused blood vessels between colonies injected with morpholino control (left) and at lower magnification (right). amp, ampullae. Scale bars, 1 mm.

In colony allorecognition assays, three of four isogenic pairs receiving control morpholinos fused within 24 hours of ampullae contact. By contrast, no reactions were observed in isogenic pairs receiving BHF translation-blocking morpholinos ($n = 6$), despite constant physical contact over observational periods ranging from 2 to 7 days (Fig. 3D, fig. S19, and table S8). To exclude nonspecific effects, we also tested *BHF* splice-inhibiting morpholinos, using the progeny of wild-type colonies (*15*). Within 2 days of ampullae contact, all control pairs had fused ($n = 2$) or rejected ($n = 1$), whereas colony pairs receiving splice-inhibiting morpholinos did not react ($n = 5$) (figs. S20 and S21, table S9, and movies S1 and S2). These data support our genomic analysis and indicate that BHF participates in fusion and rejection initiation.

In the jawed vertebrates, the MHC is a haplotype, each sublocus of which specifies a different recognition process, usually by unique subsets of cells (*18–20*). By contrast, the *B. schlosseri* Fu/HC locus is a single gene (*BHF*) embedded in a haplotype of several genes with high polymorphism. Unlike the secreted (*sFuHC*) and membrane-bound (*mFuHC*) genes, *BHF* has none of the domains expected for a cell surface–recognition protein or, in fact, domains that are conserved throughout protein evolution. Because *BHF* does not follow biological precedence by either sequence or domains, future investigations of this gene will likely reveal new mechanisms of recognition.

The ability to reliably predict histocompatibility outcomes on the basis of a single gene has broad implications for the study of allorecognition. For example, after vasculature fusion, stem cells from each *B. schlosseri* colony compete to overtake germline and/or somatic lineages (*21–24*). Stem cell competition may lead to elimination of the other colony's genome or may produce a chimeric colony with mixed genotypes. To date, induction of chimerism using hematopoietic stem-cell transplantation is the only way to achieve long-term donor-specific tolerance to human organ allografts (*25*). Chimerism can be short-lived, and if lost, the threat of allograft rejection emerges. *B. schlosseri* is a unique species for studying stem cell–mediated chimerism, and such research will be facilitated by BHF.

References and Notes

1. A. Nakashima, T. Shima, K. Inada, M. Ito, S. Saito, *Am. J. Reprod. Immunol.* **67**, 304 (2012).
2. G. Girardi, Z. Prohászka, R. Bulla, F. Tedesco, S. Scherjon, *Mol. Immunol.* **48**, 1621 (2011).
3. M. Colonna, S. Jonjic, C. Watzl, *Nat. Immunol.* **12**, 107 (2011).
4. D. F. LaRosa, A. H. Rahman, L. A. Turka, *J. Immunol.* **178**, 7503 (2007).
5. F. Delsuc, H. Brinkmann, D. Chourrout, H. Philippe, *Nature* **439**, 965 (2006).
6. H. Oka, H. Watanabe, *Proc. Jpn. Acad.* **33**, 657 (1957).
7. H. Oka, H. Watanabe, *Bull. Mar. Biol. Stat. Asamushi.* **10**, 153 (1960).
8. A. Sabbadin, *Rend. Accad. Naz. Lincei. Ser.* **32**, 1031 (1962).
9. V. L. Scofield, J. M. Schlumpberger, L. A. West, I. L. Weissman, *Nature* **295**, 499 (1982).
10. A. W. De Tomaso, Y. Saito, K. J. Ishizuka, K. J. Palmeri, I. L. Weissman, *Genetics* **149**, 277 (1998).
11. A. W. De Tomaso, I. L. Weissman, *Immunogenetics* **55**, 480 (2003).
12. A. W. De Tomaso *et al.*, *Nature* **438**, 454 (2005).
13. A. Voskoboynik *et al.*, *eLife* **2**, e00569 (2013).
14. I. Letunic, T. Doerks, P. Bork, SMART 7: recent updates to the protein domain annotation resource. *Nucleic Acids Res.* **40**, D302 and (2012).
15. Materials and methods are available as supplementary materials on *Science* Online.
16. B. Rinkevich, J. Douek, C. Rabinowitz, G. Paz, *Dev. Comp. Immunol.* **36**, 718 (2012).
17. M. Oren, J. Douek, Z. Fishelson, B. Rinkevich, *Dev. Comp. Immunol.* **31**, 889 (2007).
18. The MHC sequencing consortium, *Nature* **401**, 921 (1999).
19. M. Hirano, S. Das, P. Guo, M. D. Cooper, *Adv. Immunol.* **109**, 125 (2011).
20. L. J. Dishaw, G. W. Litman, *Curr. Biol.* **19**, R286 (2009).
21. D. S. Stoner, I. L. Weissman, *Proc. Natl. Acad. Sci. U.S.A.* **93**, 15254 (1996).
22. D. S. Stoner, B. Rinkevich, I. L. Weissman, *Proc. Natl. Acad. Sci. U.S.A.* **96**, 9148 (1999).
23. D. J. Laird, A. W. De Tomaso, I. L. Weissman, *Cell* **123**, 1351 (2005).
24. A. Voskoboynik *et al.*, *Cell Stem Cell* **3**, 456 (2008).
25. D. H. Sachs, M. Sykes, T. Kawai, A. B. Cosimi, *Semin. Immunol.* **23**, 165 (2011).

Acknowledgments: We thank B. Rinkevich for pointing out the difficulty with the original cFuHC assignments and T. Snyder, J. Okamoto, L. Me, L. Ooi, A. Dominguez, C. Lowe, K. Uhlinger, L. Crowder, S. Karten, C. Patton, L. Jerabek, and T. Storm for invaluable technical advice and help. A. De Tomaso provided the fosmid sequence used to characterize *cFuHC* (*12*) (table S5). D.P., A.V., and S.R.Q. have filed U.S. and international patent applications (61/532,882 and 13/608,778, respectively) entitled "Methods for obtaining a sequence." This invention allows for the sequencing of long continuous (kilobase scale) nucleic acid fragments using conventional short read–sequencing technologies, useful for consensus sequencing and haplotype determination. This study was supported by NIH grants 1R56AI089968, R01GM100315, and 1R01AG037968 awarded to I.L.W., A.V., and S.R.Q., respectively, and the Virginia and D. K. Ludwig Fund for Cancer Research awarded to I.L.W. D.S. was supported by NIH grant K99CA151673-01A1 and Department of Defense Grant W81XWH-10-1-0500, and A.M.N., D.M.C., D.S., and I.K.D. were supported by a grant from the Siebel Stem Cell Institute and the Thomas and Stacey Siebel Foundation. The data in this paper are tabulated in the main manuscript and in the supplementary materials. BHF, sFuHC, and mFuHC sequences are available in GenBank under accession numbers KF017887-KF017889, and the RNA-Seq data are available on the Sequence Read Archive (SRA) database: BioProject SRP022042.

Supplementary Materials

www.sciencemag.org/cgi/content/full/341/6144/384/DC1
Materials and Methods
Figs. S1 to S21
Tables S1 to S9
References (*26–42*)
Movies S1 and S2

19 March 2013; accepted 30 May 2013
10.1126/science.1238036

Creating a False Memory in the Hippocampus

Steve Ramirez,[1]* Xu Liu,[1,2]* Pei-Ann Lin,[1] Junghyup Suh,[1] Michele Pignatelli,[1] Roger L. Redondo,[1,2] Tomás J. Ryan,[1,2] Susumu Tonegawa[1,2]†

Memories can be unreliable. We created a false memory in mice by optogenetically manipulating memory engram–bearing cells in the hippocampus. Dentate gyrus (DG) or CA1 neurons activated by exposure to a particular context were labeled with channelrhodopsin-2. These neurons were later optically reactivated during fear conditioning in a different context. The DG experimental group showed increased freezing in the original context, in which a foot shock was never delivered. The recall of this false memory was context-specific, activated similar downstream regions engaged during natural fear memory recall, and was also capable of driving an active fear response. Our data demonstrate that it is possible to generate an internally represented and behaviorally expressed fear memory via artificial means.

Neuroscience aims to explain how brain activity drives cognition. Doing so requires identification of the brain regions that are specifically involved in producing internal mental representations and perturbing their activity to see how various cognitive processes are affected. More specifically, humans have a rich repertoire of mental representations generated internally by processes such as conscious or unconscious recall, dreaming, and imagination (*1*, *2*). However, whether these internal representations can be combined with external stimuli to generate new memories has not been vigorously studied.

Damage to the hippocampus impairs episodic memory (*3–8*). Recently, using fear conditioning in mice as a model of episodic memory, we identified a small subpopulation of granule cells in the dentate gyrus (DG) of the hippocampus as contextual memory-engram cells. Optogenetic stimulation of these cells is sufficient to activate behavioral recall of a context-dependent fear memory formed by a delivery of foot shocks. This finding provided an opportunity to investigate how the internal representation of a specific context can be associated with external stimuli of high valence. In particular, a hypothesis of great interest is

[1]RIKEN–Massachusetts Institute of Technology (MIT) Center for Neural Circuit Genetics at the Picower Institute for Learning and Memory, Department of Biology and Department of Brain and Cognitive Sciences, MIT, Cambridge, MA 02139, USA. [2]Howard Hughes Medical Institute, MIT, Cambridge, MA 02139, USA.

*These authors contributed equally to this work.
†Corresponding author. E-mail: tonegawa@mit.edu

whether artificially activating a previously formed contextual memory engram while simultaneously delivering foot shocks can result in the creation of a false fear memory for the context in which foot shocks were never delivered. To address this, we investigated whether a light-activated contextual memory in the DG or CA1 can serve as a functional conditioned stimulus (CS) in fear conditioning.

Our system uses c-fos-tTA transgenic mice, in which the promoter of the *c-fos* gene drives the expression of the tetracycline transactivator (tTA) to induce expression of a gene of interest downstream of the tetracycline-responsive element (TRE) (*8–12*). We injected an adeno-associated virus (AAV) encoding TRE-ChR2-mCherry into the DG or CA1 of c-fos-tTA animals (Fig. 1A). Channelrhodopsin-2 (ChR2)–mCherry expression was completely absent in the DG of animals that had been raised with doxycycline (Dox) in the diet (on Dox) (Fig. 1B). Exploration of a novel context under the condition of Dox withdrawal (off Dox) elicited an increase in ChR2-mCherry expression (Fig. 1C). We confirmed the functionality of the expressed ChR2-mCherry by recording light-induced spikes in cells expressing ChR2-mCherry from both acute hippocampal slices and in anaesthetized animals (Fig. 1, D to F). Furthermore, optical stimulation of ChR2-mCherry–expressing DG cells induced cFos expression throughout the anterior-posterior axis of the DG (fig. S1, A to I).

We first took virus-infected and fiber-implanted animals off Dox to open a time window for labeling cells activated by the exploration of a novel context (context A) with ChR2-mCherry. The animals were then put back on Dox to prevent any further labeling. The next day, we fear-conditioned this group in a distinct context (context B) while optically reactivating the cells labeled in context A. On the following 2 days, we tested the animals' fear memory in either the original context A or a novel context C (Fig. 1G). If the light-reactivated cells labeled in context A can produce a functional CS during fear conditioning in context B, then the animals should express a false fear memory by freezing in context A, but not in context C.

First, we examined the degree of overlap of the cell populations activated in contexts A and C (*8*, *11*). We injected a group of c-fos-tTA mice with an AAV virus encoding TRE-ChR2-mCherry and exposed them to context A while off Dox so as to label activated DG cells with ChR2-mCherry. These animals were then immediately placed back on Dox to prevent further labeling. The next day, half of the animals were exposed to context C, and the other half were reexposed to context A as a control. Both groups were euthanized 1.5 hours later. DG cells activated by the first exposure to context A were identified by ChR2-mCherry expression, and cells activated by the exposure to context C or the reexposure to context A were identified by the expression of endogenous c-Fos. The c-Fos generated by the first exposure to context A had been degraded by the time the animals underwent their second context exposure (*11*). Contexts A and C recruited statistically independent populations of DG cells. In contrast, two exposures to context A recruited substantially overlapping cell populations in the dorsal DG (Fig. 2, A to E).

When DG cells activated by the exposure to context A were reactivated with light during fear conditioning in a distinct context B, the animals subsequently froze in context A at levels significantly higher than the background levels, whereas freezing in context C did not differ from background levels (Fig. 2F). This increased freezing in context A was not due to generalization, because a control group expressing only mCherry that underwent the exact same training protocol did not show the same effect (Fig. 2F). A separate group of animals expressing ChR2–enhanced yellow fluorescent protein

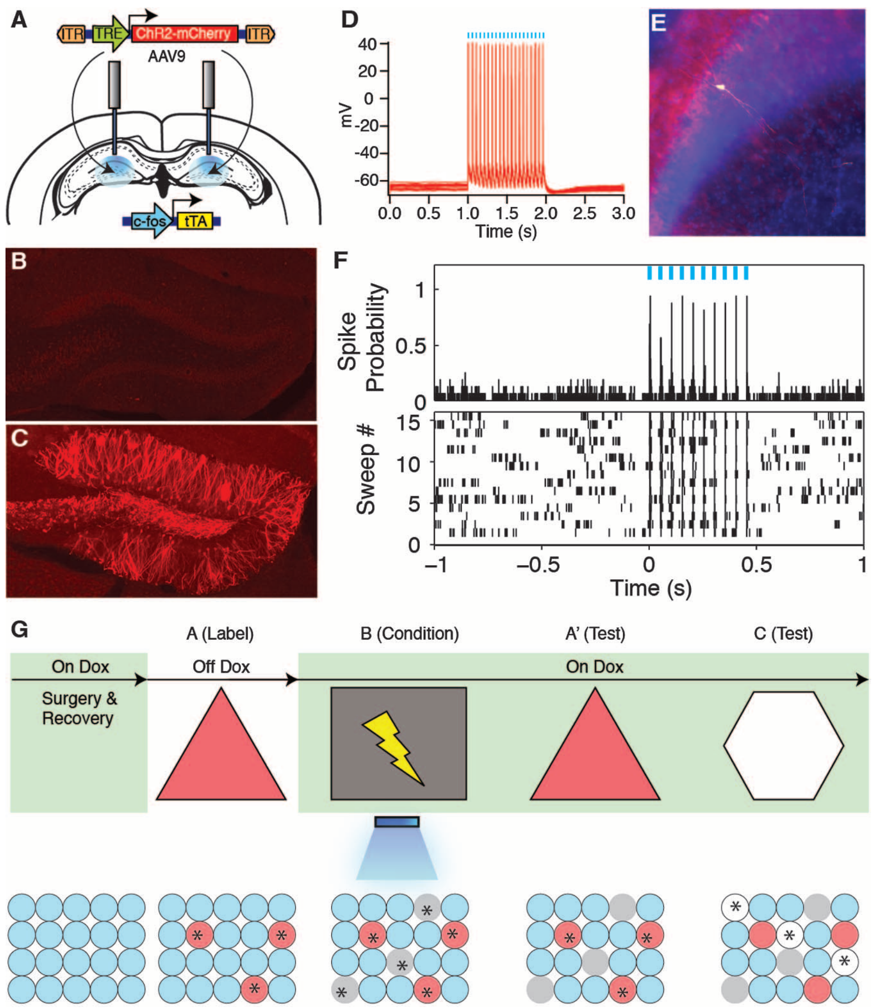

Fig. 1. Activity-dependent labeling and light-activation of hippocampal neurons, and the basic experimental scheme. (**A**) The c-fos-tTA mice were bilaterally injected with AAV_9-TRE-ChR2-mCherry and implanted with optical fibers targeting DG. (**B**) While on Dox, exploration of a novel context did not induce expression of ChR2-mCherry. (**C**) While off Dox, exploration of a novel context induced expression of ChR2-mCherry in DG. (**D**) Light pulses induced spikes in a CA1 neuron expressing ChR2-mCherry. The recorded neuron is shown labeled with biocytin in (**E**). (**F**) Light pulses induced spikes in DG neurons recorded from a head-fixed anesthetized c-fos-tTA animal expressing ChR2-mCherry. (**G**) Basic experimental scheme. Post-surgery mice were taken off Dox and allowed to explore context A in order to let DG or CA1 cells become labeled with ChR2-mCherry. Mice were put back on Dox and fear conditioned in context B with simultaneous delivery of light pulses. Freezing levels were then measured in both the original context A and a novel context C. The light green shading indicates the presence of Dox in the diet during corresponding stages of the scheme. Prime indicates the second exposure to a given context. The yellow lightning symbol and blue shower symbol indicate foot shocks and blue light delivery, respectively. Red circles represent neurons encoding context A that are thus labeled with ChR2-mCherry. Gray and white circles represent neurons encoding context B and C, respectively. Asterisks indicate neurons activated either by exposure to context or light stimulation.

(EYFP) instead of ChR2-mCherry in the DG that underwent the same behavioral schedule also showed increased freezing in context A (fig. S2A).

New experimental and control groups of mice were taken off Dox in context A in order to label activated cells and then placed in context C on the following day while back on Dox. In this experiment, although conditioning took place after the formation of both context A and context C memories, only those cells encoding context A were reactivated by light during fear conditioning. Subsequently, all groups of mice displayed background levels of freezing in context C. In contrast, in the context A test the next day, the experimental group showed increased freezing levels as compared with those of the mCherry-only group, confirming that the recall of the false memory is specific to context A (Fig. 2G). This freezing was not observed in another ChR2-mCherry group that underwent the same behavioral protocol but without light stimulation during fear conditioning in context B, or in a group in which an immediate shock protocol was administered in context B with light stimulation of context A cells (Fig. 2G and fig. S3). In a separate group of animals, we labeled cells active in context C rather than context A and repeated similar experiments as above. These animals showed freezing in context C but not context A (fig. S2B).

The hippocampus processes mnemonic information by altering the combined activity of subsets of cells within defined subregions in response to discrete episodes (*11*–*13*). Therefore, we investigated whether applying the same parameters and manipulations to CA1 as we did to the DG could form a false memory. We first confirmed that light could activate cells expressing ChR2-mCherry along the anterior-posterior axis of the CA1 similar to the DG (fig. S1, J to R). Also similar to the DG (Fig. 2, A to E), the overlap of active CA1 cells was significantly lower across contexts (A and C) as compared with that of a reexposure to the same context (A and A). However, the degree of overlap for the two contexts was much greater in CA1 (30%) than in the DG (~1%). When we labeled CA1 cells activated in context A and reactivated these cells with light during fear conditioning in context B, no increase in freezing was observed in the experimental group expressing ChR2-mCherry as compared with the mCherry-only control group in either context A or context C, regardless of whether the animals were exposed to context C or not before fear conditioning in context B (Fig. 2, M and N).

The simultaneous availability of two CSs can sometimes result in competitive conditioning; the memory for each individual CS is acquired less strongly as compared with when it is presented alone, and the presentation of two simultaneous CSs to animals trained with a single CS can also lead to decrement in recall (*14*). In our experiments, it is possible that the light-activated DG cells encoding context A interfered with the acquisition or expression of the genuine fear memory for context B. Indeed, upon reexposure to context B, the experimental group froze significantly less than the group that did not receive light during fear conditioning or the group expressing mCherry alone (Fig. 3A and fig. S4). During light-on epochs in the context B test, freezing increased in the experimental group and decreased in the group that did not receive light during fear conditioning (Fig. 3A and fig. S2C). We conducted similar experiments with mice in which the manipulation was targeted to the CA1 region and found no differences in the experimental or control groups during either light-off or light-on epochs of the context B test (fig. S5A).

Memory recall can be induced for a genuine fear memory by light reactivation of the corresponding engram in the DG (*8*). To investigate

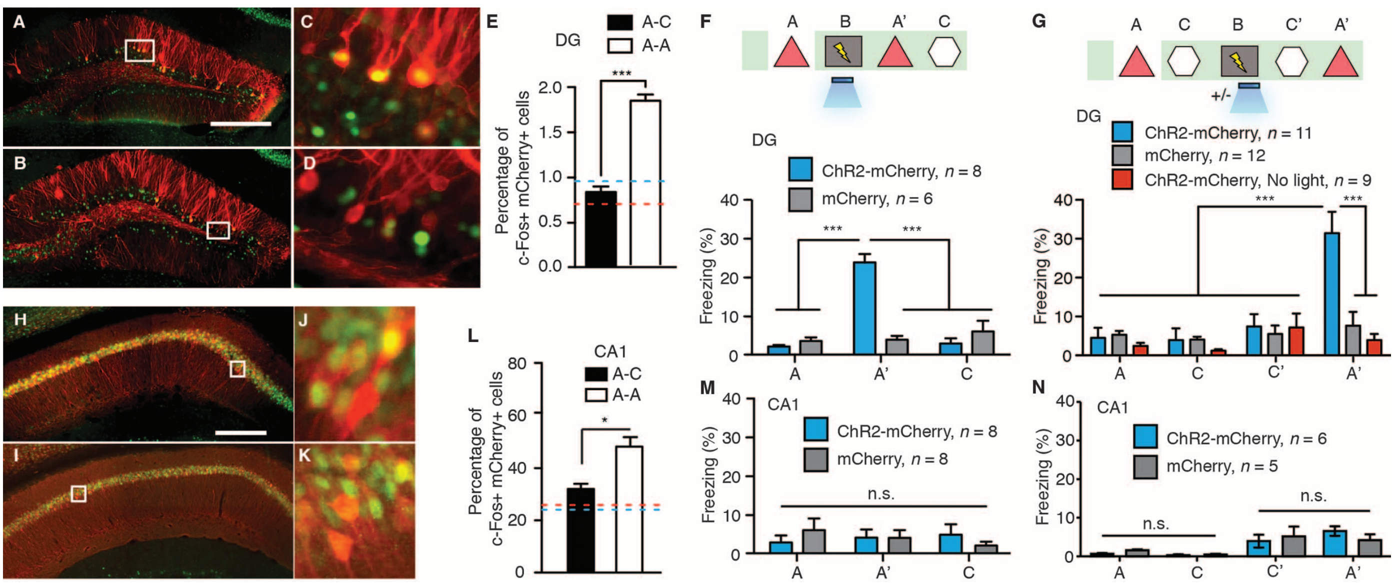

Fig. 2. Creation of a false contextual fear memory. (**A** to **E**) c-fos-tTA mice injected with AAV$_9$-TRE-ChR2-mCherry in the DG were taken off Dox and exposed to context A in order to label the activated cells with mCherry (red), then put back on Dox and exposed to the same context A [(A) and (C)] or a novel context C [(B) and (D)] 24 hours later so as to let activated cells express c-Fos (green). Images of the DG from these animals are shown in (A) to (D), and the quantifications are shown in (E) (n = 4 subjects each; ***P < 0.001, unpaired Student's t test). Blue and red dashed lines indicate the chance level of overlap for A-A and A-C groups, respectively. (**F**) (Top) Training and testing scheme of animals injected with AAV$_9$-TRE-ChR2-mCherry or AAV$_9$-TRE-mCherry. Various symbols are as explained in Fig. 1. (Bottom) Animals' freezing levels in context A before fear conditioning and in context A and C after fear conditioning [n = 8 subjects for ChR2-mCherry group, and n = 6 subjects for mCherry group; ***P < 0.001, two-way analysis of variance (ANOVA) with repeated measures followed by Bonferroni post-hoc test]. (**G**) (Top) Training and testing scheme of animals injected with AAV$_9$-TRE-ChR2-mCherry or AAV$_9$-TRE-mCherry. One control group injected with AAV$_9$-TRE-ChR2-mCherry did not receive light stimulation during fear conditioning (ChR2-mCherry, no light). (Bottom) Animals' freezing levels in context A and C before and after fear conditioning (n = 11 subjects for ChR2-mCherry group, n = 12 subjects for mCherry, and n = 9 subjects for ChR2-mCherry, no-light groups; ***P < 0.001, two-way ANOVA with repeated measures followed by Bonferroni post-hoc test). (**H** to **L**) Animals underwent the same protocol as in (A) to (E), except the virus injection was targeted to CA1. Representative images of CA1 from these animals are shown in (H) to (K), and the quantifications are shown in (L) (n = 4 subjects each; *P = 0.009, unpaired Student's t test). (**M**) Same as (F), except the viral injection and implants were targeted to CA1 (n = 8 subjects for ChR2-mCherry and mCherry groups; n.s., not significant; two-way ANOVA with repeated measures followed by Bonferroni post-hoc test). (**N**) Same as (G), except the viral injection and implants were targeted to CA1 (n = 6 subjects for ChR2-mCherry group and n = 5 subjects for mCherry group). Scale bar in (A) and (H), 250 μm.

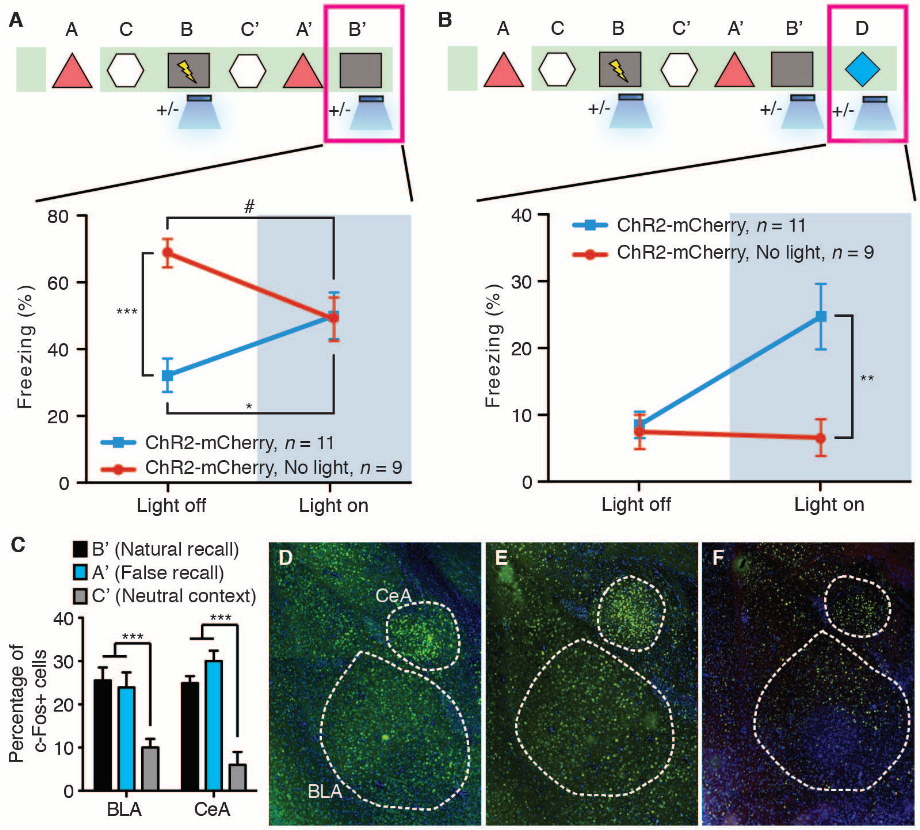

Fig. 3. The false and genuine fear memories interact with each other, and both recruit the amygdala. (**A**) Animals that underwent the behavioral protocol shown in Fig. 2G were reexposed to context B, and the freezing levels were examined both in the absence and presence of light stimulation (n = 11 subjects for ChR2-mCherry group and n = 9 subjects for ChR2-mCherry, no-light group; $*P$ = 0.027; $***P < 0.001$; $\#P$ = 0.034, two-way ANOVA with repeated measures followed by Bonferroni post-hoc test). (**B**) Animals that underwent the behavioral protocol shown in (A) were placed in a novel context D, and the freezing levels were examined both in the absence and presence of light stimulation (n = 11 subjects for ChR2-mCherry group and n = 9 subjects for ChR2-mCherry, no-light group; $**P$ = 0.007, two-way ANOVA with repeated measures followed by Bonferroni post-hoc test). (**C**) Three groups of mice underwent the training shown in (A) and were euthanized after testing in either context B (natural recall), A (false recall), or C (neutral context). The percentage of c-Fos–positive cells was calculated for each group in basolateral amygdala (BLA) and central amygdala (CeA) (n = 6 subjects each; $***P < 0.001$). (**D** to **F**) Images for natural recall, false recall, or neutral context.

whether this applies to a false fear memory, we examined fear-memory recall of experimental and control groups of mice in a distinct context (context D) with light-off and light-on epochs (Fig. 3B). All groups exhibited background levels of freezing during light-off epochs. The experimental group, however, froze at significantly higher levels (~25%) during light-on epochs. This light-induced freezing in context D was not observed in control animals that underwent the same behavioral schedule but did not receive light during fear conditioning in context B, in animals expressing mCherry alone, in animals receiving immediate shock, or in animals in which CA1 was manipulated instead (Fig. 3B and figs. S2D, S3C, S4C, and S5B).

Moreover, we quantified the levels of c-Fos expression in the basolateral amygdala (BLA) and the central amygdala (CeA) during the recall of a false and genuine fear memory (*15*–*20*). Both sessions elicited a significant increase in c-Fos–positive cells in the BLA and CeA compared with a control group exploring a neutral context (Fig. 3, C to F).

Last, a new cohort of mice was trained in a conditioned place avoidance (CPA) paradigm (*21*). Naïve animals did not show an innate preference for either chamber across multiple days (fig. S6A). An experimental group injected with the ChR2-mCherry virus and a control group injected with the mCherry-only virus were taken off Dox and exposed to one chamber of the CPA apparatus in order to label the DG cells activated in this chamber. These animals were then placed back on Dox and on the following day were exposed to the opposite chamber. Next, the mice were fear conditioned in a different context with light stimulation. The following day, they were placed back into the CPA apparatus, and their preference between the chambers was measured (Fig. 4A). After conditioning, the experimental group showed a strong preference for the unlabeled chamber over the labeled chamber, whereas the mCherry-only group spent an equal amount of time exploring both chambers (Fig. 4, B to D, and fig. S6B). Exposure to the two chambers activated a statistically independent population of DG cells (Fig. 4, E to K). We conducted similar behavioral tests targeting the CA1 subregion of the hippocampus, and the experimental group did not show any chamber preference (Fig. 4, L and M).

Our results show that cells activated previously in the hippocampal DG region can subsequently serve as a functional CS in a fear-conditioning paradigm when artificially reactivated during the delivery of a unconditioned stimulus (US). The consequence is the formation of a false associative fear memory to the CS that was not naturally available at the time of the US delivery. This is consistent with previous findings that high-frequency stimulation of the perforant path, an input to DG, can serve as a CS in a conditioned suppression paradigm (*22*).

Memory is constructive in nature; the act of recalling a memory renders it labile and highly susceptible to modification (*23*, *24*). In humans, memory distortions and illusions occur frequently. These phenomena often result from the incorporation of misinformation into memory from external sources (*25*–*27*). Cognitive studies in humans have reported robust activity in the hippocampus during the recall of both false and genuine memories (*28*). However, human studies performed using behavioral and functional magnetic resonance imaging techniques have not been able to delineate the hippocampal subregions and circuits that are responsible for the generated false memories. Our experiments provide an animal model in which false and genuine memories can be investigated at the memory-engram level (*29*). We propose that optical reactivation of cells that were naturally activated during the formation of a contextual memory induced the retrieval of that memory, and the retrieved memory became associated with an event of high valence (a foot shock) to form a new but false memory. Thus, the experimental group of animals showed increased freezing in a context in which they were never shocked (context A). Although our design for the formation and expression of a false memory was for a laboratory setting, and the retrieval of the contextual memory during conditioning occurred by artificial means (light), we speculate that the formation of at least some false memories in humans may occur in natural settings through the internally driven retrieval of a previously formed memory and its association with concurrent external stimuli of high valence.

Our experiments also allowed us to examine the dynamic interaction between the false and genuine memories at different stages of the memory process. During the acquisition phase, the artificial contextual information (context A by light activation) either competed with the genuine contextual cues (context B by natural exposure) for the valence of the US (foot shock), or may have interfered with the perception of the genuine

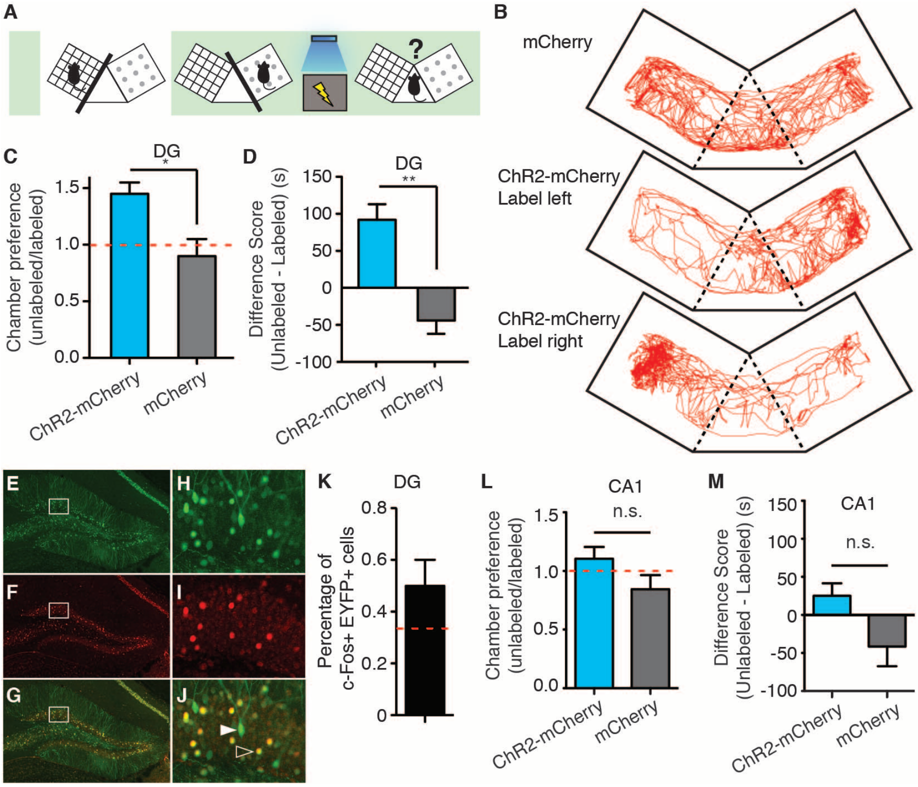

Fig. 4. The false memory supports active fear behavior. (**A**) The scheme for conditioned place-avoidance paradigm. Various symbols are as explained in Fig. 1. (**B**) Locomotion traces during testing from animals injected with AAV$_9$-TRE-mCherry (top), or animals injected with AAV$_9$-TRE-ChR2-mCherry and DG cells subsequently labeled, corresponding to either the left (middle) or right (bottom) chamber. (**C** and **D**) ChR2-mCherry and mCherry group preferences for the labeled versus unlabeled chambers as shown by the ratio (C) or the difference in duration of the time spent in each chamber (D). ($n = 8$ subjects; $^*P = 0.013$; $^{**}P = 0.008$, unpaired Student's t test). The red dashed line indicates no preference. (**E** to **K**), c-fos-tTA mice injected with AAV$_9$-TRE-EYFP in the DG were taken off Dox and exposed to one chamber in order to label the activated cells with EYFP (green) then put back on Dox and exposed to the opposite chamber 24 hours later to let activated cells express c-Fos (red). Expression of EYFP [(E) and (H)], expression of c-Fos [(F) and (I)], and a merged view [(G) and (J)] are shown. Solid arrows indicate cells expressing EYFP. Open arrows indicate cells expressing c-Fos. These cells appear yellow because they express both endogenous c-Fos (red) and the nuclear-localized c-fos-shEGFP (green) from the mouse line (*10*). Quantifications from the dorsal blades of the DG are shown in (K) ($n = 4$ subjects). Red dashed lines indicate the chance level of overlap. (**L** and **M**) Same as (C) and (D), except the viral injection and implants were targeted to CA1 ($n = 6$ subjects each group).

contextual cues. This resulted in reduced expression of both false and genuine fear memories compared with the strength of recall attainable after normal fear conditioning (Fig. 3A, the two groups during the light-off epoch). This could also be related to the overshadowing effects for multiple CSs (*30*). During the recall phase in context B, the false memory and the genuine memory were either additive (Fig. 3A, the with-light group during light-off and light-on epochs) or competitive (Fig. 3A, the no light group during light-off and light-on epochs). All of these observations are consistent with the predictions of an updated Rescorla-Wagner componential model for two independent CSs and suggest that the light-activated artificial CS is qualitatively similar to the genuine CS (*14*).

A previous study applied a similar experimental protocol with pharmacosynthetic methods and failed to see increased freezing upon reexposure to either context A or context B. Instead, they observed a synthetic memory that could only be retrieved by the combination of both contexts A and B (*9*). A key difference in their system is that the c-Fos–expressing cells in the entire forebrain were labeled and reactivated over an extended period by a synthetic ligand. We propose that activating neurons in much wider spatial and temporal domains may favor the formation of a synthetic memory, which may not be easily retrievable by the cues associated with each individual memory. In contrast, activating neurons in a more spatially (only small populations of DG cells) and temporally restricted manner (only a few minutes during light stimulation) may favor the formation of two distinct (false and genuine) memories as observed in our case. In line with this hypothesis, when we manipulated CA1 cells by the same procedures as the ones used for DG cells, we could not create a false memory (freezing in context A). In CA1, the overlap of the cell populations activated by consecutive exposures to a pair of contexts is much greater than in the DG. Although additional work is needed to reveal the nature of CA1 engrams, we hypothesize that our negative CA1 behavioral data could be a result of contextual engrams relying less on a population code and increasingly on a temporal code as they travel through the trisynaptic circuit (*4*, *11*–*13*).

References and Notes

1. D. L. Schacter, D. R. Addis, R. L. Buckner, *Nat. Rev. Neurosci.* **8**, 657–661 (2007).
2. E. Pastalkova, V. Itskov, A. Amarasingham, G. Buzsáki, *Science* **321**, 1322–1327 (2008).
3. H. Gelbard-Sagiv, R. Mukamel, M. Harel, R. Malach, I. Fried, *Science* **322**, 96–101 (2008).
4. C. J. MacDonald, K. Q. Lepage, U. T. Eden, H. Eichenbaum, *Neuron* **71**, 737–749 (2011).
5. G. Buzsáki, E. I. Moser, *Nat. Neurosci.* **16**, 130–138 (2013).
6. T. J. McHugh *et al.*, *Science* **317**, 94–99 (2007).
7. D. Tse *et al.*, *Science* **316**, 76–82 (2007).
8. X. Liu *et al.*, *Nature* **484**, 381–385 (2012).
9. A. R. Garner *et al.*, *Science* **335**, 1513–1516 (2012).
10. L. G. Reijmers, B. L. Perkins, N. Matsuo, M. Mayford, *Science* **317**, 1230–1233 (2007).
11. S. Kubik, T. Miyashita, J. F. Guzowski, *Learn. Mem.* **14**, 758–770 (2007).
12. J. F. Guzowski, B. L. McNaughton, C. A. Barnes, P. F. Worley, *Nat. Neurosci.* **2**, 1120–1124 (1999).
13. J. K. Leutgeb, S. Leutgeb, M. B. Moser, E. I. Moser, *Science* **315**, 961–966 (2007).
14. S. E. Brandon, E. H. Vogel, A. R. Wagner, *Behav. Brain Res.* **110**, 67–72 (2000).
15. J. H. Han *et al.*, *Science* **323**, 1492–1496 (2009).
16. M. T. Rogan, U. V. Stäubli, J. E. LeDoux, *Nature* **390**, 604–607 (1997).
17. J. P. Johansen *et al.*, *Proc. Natl. Acad. Sci. U.S.A.* **107**, 12692–12697 (2010).
18. S. Maren, G. J. Quirk, *Nat. Rev. Neurosci.* **5**, 844–852 (2004).
19. H. Li *et al.*, *Nat. Neurosci.* **16**, 332–339 (2013).
20. S. Ciocchi *et al.*, *Nature* **468**, 277–282 (2010).
21. S. Lammel *et al.*, *Nature* **491**, 212–217 (2012).
22. V. Doyère, S. Laroche, *Hippocampus* **2**, 39–48 (1992).
23. K. Nader, G. E. Schafe, J. E. Le Doux, *Nature* **406**, 722–726 (2000).
24. F. C. Bartlett, *Remembering: A Study in Experimental and Social Psychology* (Cambridge Univ. Press, Cambridge, 1932).
25. E. F. Loftus, *Nat. Rev. Neurosci.* **4**, 231–234 (2003).
26. D. L. Schacter, E. F. Loftus, *Nat. Neurosci.* **16**, 119–123 (2013).
27. H. L. Roediger, K. B. McDermott, *J. Exp. Psychol. Learn. Mem. Cogn.* **24**, 803–814 (1995).
28. R. Cabeza, S. M. Rao, A. D. Wagner, A. R. Mayer, D. L. Schacter, *Proc. Natl. Acad. Sci. U.S.A.* **98**, 4805–4810 (2001).
29. S. M. McTighe, R. A. Cowell, B. D. Winters, T. J. Bussey, L. M. Saksida, *Science* **330**, 1408–1410 (2010).
30. I. P. Pavlov, *Conditioned Reflexes* (Oxford University Press, Oxford, 1927).

Acknowledgments: We thank S. Huang, M. Serock, A. Mockett, J. Zhou, and D. S. Roy for help with the experiments; J. Z. Young and K. L. Mulroy for comments and discussions on the manuscript; and all the members of the Tonegawa lab for their support. This work was supported by the RIKEN Brain Science Institute.

Supplementary Materials

www.sciencemag.org/cgi/content/full/341/6144/387/DC1
Materials and Methods
Figs. S1 to S6
References

12 April 2013; accepted 2 July 2013
10.1126/science.1239073

FtsZ Protofilaments Use a Hinge-Opening Mechanism for Constrictive Force Generation

Ying Li,[1] Jen Hsin,[2]* Lingyun Zhao,[3]* Yiwen Cheng,[1]* Weina Shang,[1] Kerwyn Casey Huang,[2] Hong-Wei Wang,[3] Sheng Ye[1,4]†

The essential bacterial protein FtsZ is a guanosine triphosphatase that self-assembles into a structure at the division site termed the "Z ring". During cytokinesis, the Z ring exerts a constrictive force on the membrane by using the chemical energy of guanosine triphosphate hydrolysis. However, the structural basis of this constriction remains unresolved. Here, we present the crystal structure of a guanosine diphosphate–bound *Mycobacterium tuberculosis* FtsZ protofilament, which exhibits a curved conformational state. The structure reveals a longitudinal interface that is important for function. The protofilament curvature highlights a hydrolysis-dependent conformational switch at the T3 loop that leads to longitudinal bending between subunits, which could generate sufficient force to drive cytokinesis.

In most bacteria, cytokinesis is initiated by the localization of the essential protein FtsZ, a guanosine triphosphatase (GTPase) and tubulin homolog that can form ringlike structures and generate constrictive forces (*1*). Hydrolysis of guanosine triphosphate (GTP) bound to FtsZ protofilaments is thought to drive a straight-to-curved conformational change and generates the constrictive force required for cell division (*2*, *3*). Although multiple crystal structures of FtsZ in different nucleotide states and as monomers and protofilaments are available (*4*–*9*), little is known about the structural mechanism underlying a hydrolysis-mediated conformational change.

We determined the crystal structure of *Mycobacterium tuberculosis* FtsZ (MtbFtsZ)–guanosine diphosphate (GDP) to an R-free factor of 26.7% with data to 2.9 Å resolution (table S1 and figs. S1 and S2; also see the supplementary materials and methods). The MtbFtsZ-GDP subunits were arranged longitudinally in a head-to-tail manner and assembled into two continuous polymers that intertwine to form a left-handed, antiparallel, double-stranded structure in the crystal lattice (Fig. 1A and fig. S3). The polymer curvature is qualitatively similar to previous electron microscopy (EM) images of *Escherichia coli* FtsZ (EcFtsZ) (*2*), *Methanococcus jannaschii* FtsZ (MjFtsZ) (*10*), and *Pseudomonas aeruginosa* FtsZ (PaFtsZ) (*11*). The structure reveals an intersubunit interface formed by highly conserved residues (Fig. 1B and figs. S2 and S4A) and is different from the previously observed longitudinal interface in a MjFtsZ-GTP dimer structure (fig. S4B) (*7*). One amino acid at the center of the hydrophobic intersubunit interactions is Leu[269] (Fig. 1B and fig. S4A), which was previously identified as a key residue in *E. coli* (Leu[272]) (*12*). However, the longitudinal contacts of the MjFtsZ dimer structure do not involve this residue (Leu[297]) (fig. S4B) (*7*).

To confirm the importance of the observed intersubunit contacts, we created 11-point mutants in EcFtsZ based on our crystallographic observations and used a complementation system in *E. coli* to characterized their division phenotypes (table S2) (*13*). As expected, mutant Leu[272]→Glu[272] (L272E) (*14*) failed to complement and was dominant-negative (fig. S5) (*12*). All other point mutants designed to disrupt the MtbFtsZ intersubunit interface by changing hydrophobic residues to acidic residues failed to complement, and three of them were also dominant-negative (fig. S5). Further mutagenesis experiments revealed that Leu[272], Ala[181], and Phe[137] are highly sensitive, with only L272I, L272M, and A181L able to complement (figs. S6 and S7). Double mutants combining two complementing mutations (L272I/A181L and L272M/A181L) did not complement (fig. S8), whereas none of those combining two noncomplementing mutations complemented (fig. S9), indicating that the above point mutants affect FtsZ function by disrupting the intersubunit interface. Thus, the observed intersubunit interface is biologically relevant, and the hydrophobic interactions play a pivotal role.

We observed that MtbFtsZ and EcFtsZ GTPase activities in vitro were dramatically affected by the interfacial mutations (Fig. 1, C and D). As FtsZ GTPase activity depends on proper longitudinal assembly (*15*), we measured the GTP-dependent polymerizations of wild-type (WT) and mutated FtsZ. Although WT MtbFtsZ and EcFtsZ both polymerized, mutants in MtbFtsZ and EcFtsZ (L269E and L272E, respectively) failed to polymerize (Fig. 1E), as did all of the point mutants modifying the interfacial hydrophobic residues (fig. S10, A and B). Assembly of FtsZ in the presence of guanylyl 5′-(β,γ-methylenediphosphonate) showed similar results (fig. S10C). Thus, the observed intersubunit contacts belong to the longitudinal interface.

The MjFtsZ dimer structure (fig. S4B) was initially proposed to reflect a longitudinal interface (*7*). However, a recently determined *Staphylococcus aureus* FtsZ (SaFtsZ) structure (*4*, *5*) revealed a different intersubunit interface from the MjFtsZ dimer (fig. S4, C and D). To distinguish which interface is biologically relevant, we designed two MjFtsZ point mutants, P313E and L297E (fig. S2). Pro[313] is involved in the intersubunit contacts in the MjFtsZ dimer structure, but Leu[297] is not (*7*). WT and P313E MjFtsZ were fully functional and polymerized with the addition of GTP, whereas L297E MjFtsZ had reduced GTPase activity and did not polymerize (figs. S11A and S12A). A series of point mutants disrupting the SaFtsZ longitudinal interface were all inactive (fig. S11B) and failed to polymerize (fig. S12B). The SaFtsZ intersubunit interface is similar to the tubulin longitudinal interface (*16*) and involves highly conserved residues shown to be functionally important in mutagenesis studies (*12*, *13*), indicating that the SaFtsZ-GDP structure represents a genuine FtsZ protofilament.

A structural comparison of the MtbFtsZ-GDP dimer with the straight SaFtsZ-GDP dimer (*4*) revealed two noteworthy features (Fig. 2A). First, the MtbFtsZ-GDP longitudinal interface is similar to that in the SaFtsZ-GDP dimer, with only a slight degree of twist (fig. S13). Second, the major difference stems from a straight-to-curved conformational change with 49.6° of bending between adjacent subunits. This conformational change suggests a "hinge-opening" motion pivoted around the intersubunit interface of our MtbFtsZ-GDP dimer. Such motion has been demonstrated to be feasible (*17*) and is in agreement with functional studies (*18*). MtbFtsZ formed shorter and more highly curved protofilaments in the presence of GDP compared with GTP (fig. S14A). Disruptive mutants that did not polymerize with GDP also failed to polymerize with GTP (fig. S14, A and B). Thus, the observed intersubunit interface is present in both straight and curved protofilaments and serves as a pivot point in the straight-to-curved conformational change. As a further test of the hinge-opening mechanism, disruptive mutants at the T7 loop only polymerized in the presence of GDP (fig. S14, A and B).

How does GTP hydrolysis trigger such intersubunit bending? Despite the overall similarity between the GTPγS-bound MtbFtsZ monomer (*8*) and our GDP-bound MtbFtsZ filament structures, each GDP-bound MtbFtsZ subunit displays a notable nucleotide-dependent structural difference at the T3 loop (Fig. 2B). The GTP γ-phosphate stabilizes the T3 loop conformation in a compact state (tension or T state) (fig. S15A) (*8*). The same T-state conformation is maintained in all GTP-bound and some GDP-bound FtsZ structures (*7*, *19*, *20*) and is necessary for the longitudinal assembly of a straight FtsZ protofilament (*5*), in which the T3 loop interacts extensively with the T7 loop of the top subunit. In contrast, in our

[1]Life Sciences Institute, Zhejiang University, Hangzhou, 310058 Zhejiang, P.R. China. [2]Department of Bioengineering, Stanford University, Stanford, CA 94305, USA. [3]Ministry of Education Key Laboratory of Protein Science, Tsinghua-Peking Center for Life Sciences, Center for Structural Biology, School of Life Sciences, Tsinghua University, Beijing, 100084 Beijing, P.R. China. [4]Institute of Biochemistry, College of Life Sciences, Zhejiang University, Hangzhou, 310058 Zhejiang, P.R. China.

*These authors contributed equally to this work.
†Corresponding author. E-mail: sye@zju.edu.cn

GDP-bound MtbFtsZ structure, the T3 loop adopts a relaxed conformation (R state) in the absence of the γ-phosphate (fig. S15B), indicating that it is flexible and can be in either state. This T3 loop conformational switch was previously predicted based on studies of MjFtsZ (*21*). The SaFtsZ-GDP structure (*4*, *5*) also reveals that the GDP molecule bound between two SaFtsZ subunits is completely occluded. Because both γ- and β-phosphates are negatively charged, the release of γ-phosphate by hydrolysis may trigger the T3 loop transition from a T to an R state. This would weaken the FtsZ longitudinal interactions between the T3 and T7 loops and further drive the hinge-opening event around the pivot point (Fig. 2C and movie S1).

This hydrolysis-mediated structural transition has two functional consequences: (i) generation of mechanical work and (ii) facilitation of

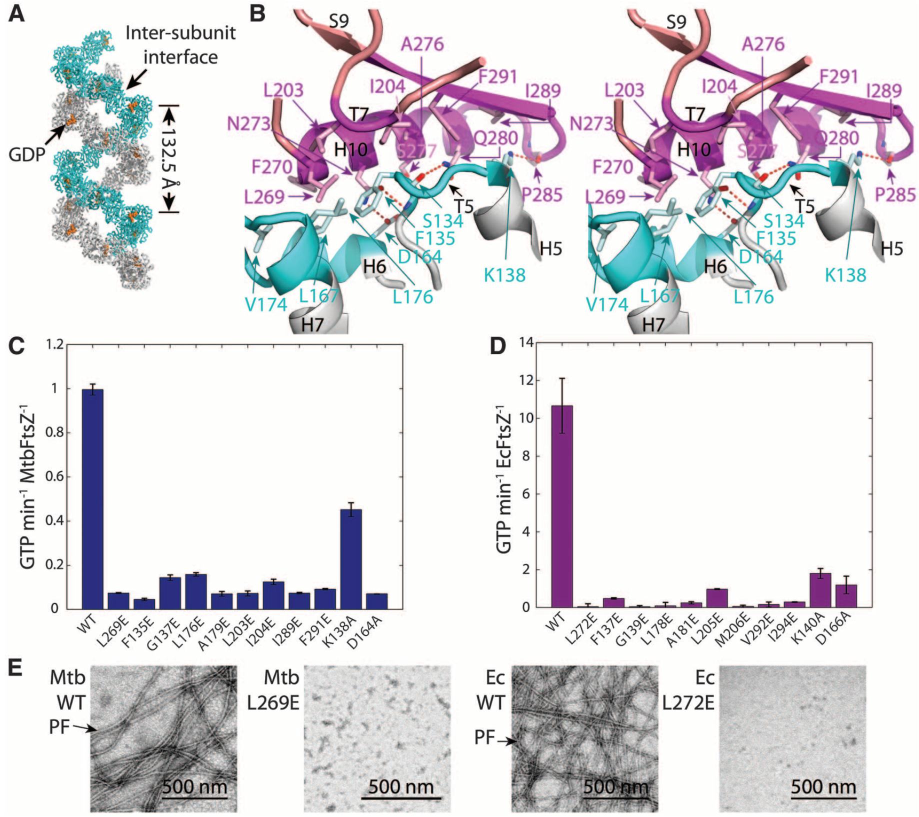

Fig. 1. Structure of a double-stranded MtbFtsZ-GDP polymer reveals key intersubunit contacts. (**A**) Ribbon representation of a double-stranded MtbFtsZ-GDP polymer containing 24 subunits. The FtsZ subunits are shown in gray and blue to distinguish the two protofilaments, and GDP molecules are in orange. (**B**) Detailed stereoview of the intersubunit contacts. The interactions, especially the hydrophobic contacts, are formed by highly conserved residues (fig. S2). Among these residues, Leu[269] of the top subunit is at the center of the hydrophobic interactions, forming van der Waals contacts with several hydrophobic residues of the bottom subunit. (**C** and **D**) GTPase activities of WT and mutant MtbFtsZ (C) or EcFtsZ (D). Means ± SD are shown (n = 3 measurements). (**E**) EM analysis of GTP-dependent polymerization of MtbFtsZ (wild type and L269E) and EcFtsZ (wild type and L272E). Representative protofilaments (PF) are marked with arrows.

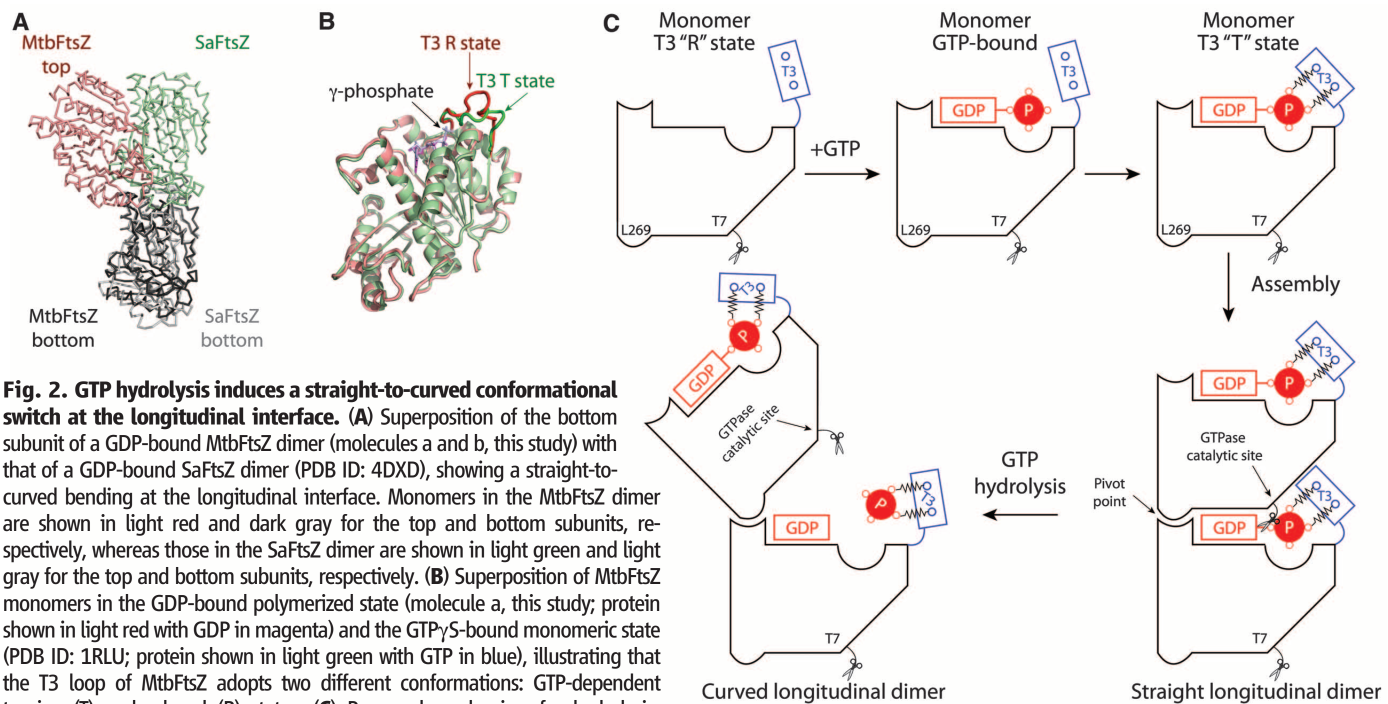

Fig. 2. GTP hydrolysis induces a straight-to-curved conformational switch at the longitudinal interface. (**A**) Superposition of the bottom subunit of a GDP-bound MtbFtsZ dimer (molecules a and b, this study) with that of a GDP-bound SaFtsZ dimer (PDB ID: 4DXD), showing a straight-to-curved bending at the longitudinal interface. Monomers in the MtbFtsZ dimer are shown in light red and dark gray for the top and bottom subunits, respectively, whereas those in the SaFtsZ dimer are shown in light green and light gray for the top and bottom subunits, respectively. (**B**) Superposition of MtbFtsZ monomers in the GDP-bound polymerized state (molecule a, this study; protein shown in light red with GDP in magenta) and the GTPγS-bound monomeric state (PDB ID: 1RLU; protein shown in light green with GTP in blue), illustrating that the T3 loop of MtbFtsZ adopts two different conformations: GTP-dependent tension (T) and relaxed (R) states. (**C**) Proposed mechanism for hydrolysis-mediated conformational switch of the longitudinal interface.

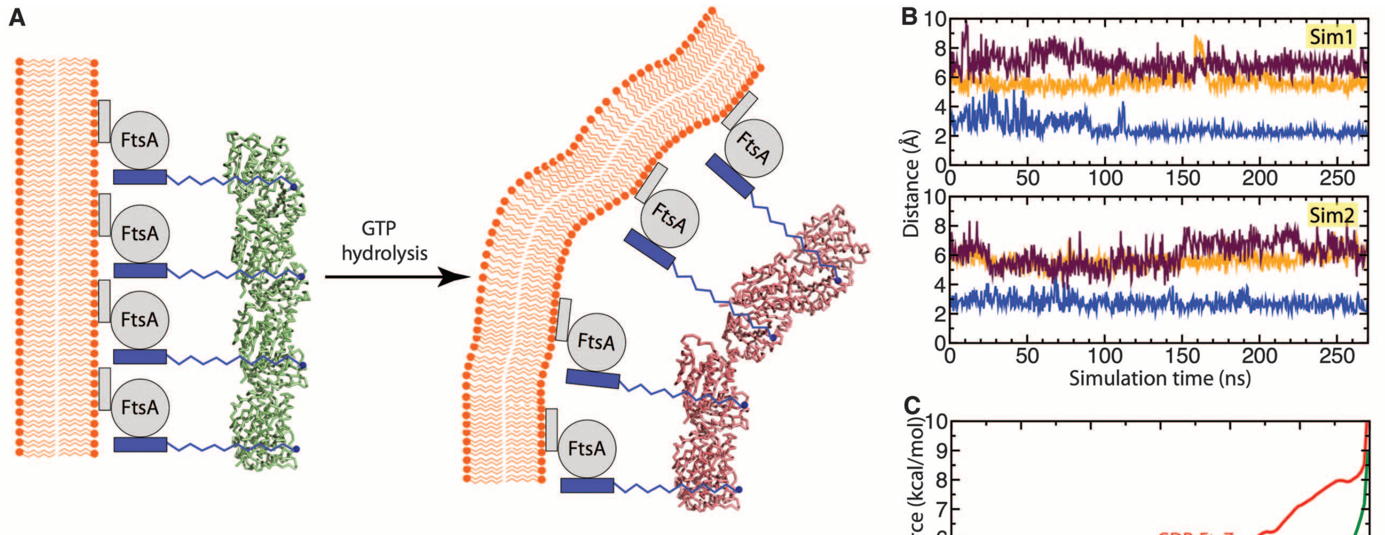

Fig. 3. Bending of FtsZ protofilaments produces an inward force on the membrane. (**A**) Schematic of membrane deformation due to the force produced by hydrolysis-induced FtsZ protofilament bending. (**B**) Intermonomer contacts were maintained in two independent molecular dynamics simulations of the MtbFtsZ-GDP dimer, suggesting stability of the bent conformation. Each time course measures the closest distance between a pair of amino acids: Leu^{272} (top) and Phe^{135} (bottom), blue; Leu^{272} (top) and Leu^{167} (bottom), orange; and Leu^{272} (top) and Leu^{176} (bottom), purple. (**C**) Potential of mean force measurements for MtbFtsZ-GDP (red) and MtbFtsZ-GTP (green) along the hinge-opening pathway demonstrates a preference of MtbFtsZ-GDP protofilaments for a bent conformation and suggests several energetically feasible intermediate conformations.

turnover. FtsZ contains a flexible C terminus that binds FtsA, which is attached to the membrane through its C-terminal amphipathic helix (*22*). The straight SaFtsZ (*5*) and our curved MtbFtsZ protofilament structures give rise to a model of FtsZ structural dynamics in which the bending between two longitudinal subunits causes a 17.5 Å displacement of the C-terminal Phe^{312} (fig. S16). In the context of FtsZ division function, the straight-to-curved transition can exert constrictive forces on the envelope (Fig. 3A). To estimate the magnitude of force generated by GTP hydrolysis–induced bending of an FtsZ protofilament, we used all-atom molecular dynamics simulations to investigate MtbFtsZ-GDP dimer structures. First, we conducted two repeat equilibrium simulations and demonstrated that the intersubunit contacts in the MtbFtsZ-GDP dimer were well maintained (Fig. 3B). To probe the energetics and forces associated with the hinge-opening motion, we performed free-energy calculations of MtbFtsZ dimers in both GDP- and GTP-bound states (Fig. 3C). Both energy profiles along the hinge-opening pathway suggested the existence of intermediate conformations (Fig. 3C), but overall FtsZ-GDP preferred a more bent conformation than FtsZ-GTP (*17*), and this difference in conformational energy can generate constrictive force. For example, when a GDP-FtsZ dimer transitions from a straight (~170°) to a bent (~135°) conformation, 7 kcal/mol is released. With the estimations provided in (*18*) and assuming this energy is fully used for constrictive force, ~20 pN of force can be derived from such a hydrolysis-induced structural transition.

The straight-to-curved structural transition also greatly reduces the buried surface area from 2360 Å^2 for the SaFtsZ longitudinal interface (*5*) to 1040 Å^2 for the MtbFtsZ longitudinal interface, indicating weaker assembly for the curved protofilament than the straight state. These values are comparable with calculations of the transition between GTP- and GDP-bound states in an MjFtsZ dimer (*17*), demonstrating that a hinge-opening motion and reduced buried surface area due to hydrolysis are probably common components of the FtsZ force-generation mechanism, regardless of differences in longitudinal interface. Therefore, a curved FtsZ protofilament is more prone to filament disassembly, in agreement with earlier studies showing that assembly of FtsZ-GDP is weaker than FtsZ-GTP and that hydrolysis destabilizes FtsZ filaments (*10*, *23*–*25*).

Taken together, our studies demonstrate a hinge-opening conformational change between a straight and curved FtsZ protofilament that supports the "hydrolyze-and-bend" model (*3*) and provides a structural basis for constrictive force generation in bacteria.

References and Notes

1. M. Osawa, D. E. Anderson, H. P. Erickson, *Science* **320**, 792–794 (2008).
2. C. Lu, M. Reedy, H. P. Erickson, *J. Bacteriol.* **182**, 164–170 (2000).
3. H. P. Erickson, D. W. Taylor, K. A. Taylor, D. Bramhill, *Proc. Natl. Acad. Sci. U.S.A.* **93**, 519–523 (1996).
4. C. M. Tan *et al.*, *Sci. Transl. Med.* **4**, 126ra35 (2012).
5. T. Matsui *et al.*, *Acta Crystallogr. D Biol. Crystallogr.* **68**, 1175–1188 (2012).
6. M. A. Oliva, D. Trambaiolo, J. Löwe, *J. Mol. Biol.* **373**, 1229–1242 (2007).
7. M. A. Oliva, S. C. Cordell, J. Löwe, *Nat. Struct. Mol. Biol.* **11**, 1243–1250 (2004).
8. A. K. Leung *et al.*, *J. Mol. Biol.* **342**, 953–970 (2004).
9. J. Löwe, L. A. Amos, *Nature* **391**, 203–206 (1998).
10. S. Huecas, J. M. Andreu, *FEBS Lett.* **569**, 43–48 (2004).
11. Y. Chen, S. L. Milam, H. P. Erickson, *Biochemistry* **51**, 3100–3109 (2012).
12. S. D. Redick, J. Stricker, G. Briscoe, H. P. Erickson, *J. Bacteriol.* **187**, 2727–2736 (2005).
13. J. Stricker, H. P. Erickson, *J. Bacteriol.* **185**, 4796–4805 (2003).
14. Single-letter abbreviations for the amino acid residues are as follows: A, Ala; C, Cys; D, Asp; E, Glu; F, Phe; G, Gly; H, His; I, Ile; K, Lys; L, Leu; M, Met; N, Asn; P, Pro; Q, Gln; R, Arg; S, Ser; T, Thr; V, Val; W, Trp; and Y, Tyr.
15. T. M. Sossong Jr., M. R. Brigham-Burke, P. Hensley, K. H. Pearce Jr., *Biochemistry* **38**, 14843–14850 (1999).
16. J. Löwe, H. Li, K. H. Downing, E. Nogales, *J. Mol. Biol.* **313**, 1045–1057 (2001).
17. J. Hsin, A. Gopinathan, K. C. Huang, *Proc. Natl. Acad. Sci. U.S.A.* **109**, 9432–9437 (2012).
18. Y. Chen, K. Bjornson, S. D. Redick, H. P. Erickson, *Biophys. J.* **88**, 505–514 (2005).
19. T. Läppchen *et al.*, *Chem. Biol.* **15**, 189–199 (2008).
20. A. Raymond *et al.*, *BMC Biotechnol.* **9**, 37 (2009).
21. J. F. Díaz *et al.*, *J. Biol. Chem.* **276**, 17307–17315 (2001).
22. S. Pichoff, J. Lutkenhaus, *Mol. Microbiol.* **55**, 1722–1734 (2005).
23. S. Huecas *et al.*, *J. Biol. Chem.* **282**, 37515–37528 (2007).
24. L. Romberg, M. Simon, H. P. Erickson, *J. Biol. Chem.* **276**, 11743–11753 (2001).
25. D. Scheffers, A. J. Driessen, *FEBS Lett.* **506**, 6–10 (2001).

Acknowledgments: We thank H. Erickson for insightful suggestions and the pJSB100 vector; J. Lutkenhaus for the JKD7-1/pKD3 strain; M. Rajagopalan for *M. tuberculosis* genomic DNA; Y. Huang, Y. Jiang, H. Song, X. Feng, and J. T. Shaw for discussions and critical reviews of the manuscript; S. Huang and J. He at the Shanghai Synchrotron Radiation Facility for on-site assistance; and Y. Xu at the National Center for Protein Sciences Beijing for EM facility assistance. This work was supported in part by funds from

the National Natural Science Foundation of China (grant 31070661), the Ministry of Science and Technology (grants 2011CB910500 and 2010CB912401), the Natural Science Foundation of Zhejiang Province (grant R2100439), and the Specialized Research Fund for the Doctoral Program of Higher Education (grant 20110101110122), as well as the Fundamental Research Funds for the Central Universities (to S.Y.); Research Funds of the Tsinghua-Peking Center for Life Sciences (to H.-W.W.); a NIH Director's New Innovator Award DP2OD006466 (to K.C.H.); and a Stanford University School of Medicine Dean's Postdoctoral Fellowship and an NIH Ruth L. Kirschstein National Research Service Award 1F32GM100677-01A1 (to J.H.). Y.C. is supported by the National Science Foundation of China (grant 31090360) and the Ministry of Science and Technology (grant 2012CB966600). All simulations were performed with computer time provided by the Extreme Science and Engineering Discovery Environment, which is supported by NSF grant OCI-1053575, with allocation number TG-MCB110056 (to J.H. and K.C.H.). The structure coordinates and reflection files are deposited in the Protein Data Bank (PDB) under identification (ID) number 4KWE. We declare no competing financial interests.

Supplementary Materials
www.sciencemag.org/cgi/content/full/341/6144/392/DC1
Materials and Methods
Figs. S1 to S17
Table S1 and S2
References (*26*–*40*)
Movie S1

17 April 2013; accepted 28 June 2013
10.1126/science.1239248

Nuclear PTEN Controls DNA Repair and Sensitivity to Genotoxic Stress

C. Bassi,[1] J. Ho,[2] T. Srikumar,[1] R. J. O. Dowling,[2] C. Gorrini,[2,3] S. J. Miller,[4] T. W. Mak,[1,2,3] B. G. Neel,[1,2,4] B. Raught,[1,2] V. Stambolic[1,2]*

Loss of function of the *phosphatase and tensin homolog deleted on chromosome 10 (PTEN)* tumor suppressor gene is associated with many human cancers. In the cytoplasm, PTEN antagonizes the phosphatidylinositol 3-kinase (PI3K) signaling pathway. PTEN also accumulates in the nucleus, where its function remains poorly understood. We demonstrate that SUMOylation (SUMO, small ubiquitin-like modifier) of PTEN controls its nuclear localization. In cells exposed to genotoxic stress, SUMO-PTEN was rapidly excluded from the nucleus dependent on the protein kinase ataxia telangiectasia mutated (ATM). Cells lacking nuclear PTEN were hypersensitive to DNA damage, whereas PTEN-deficient cells were susceptible to killing by a combination of genotoxic stress and a small-molecule PI3K inhibitor both in vitro and in vivo. Our findings may have implications for individualized therapy for patients with PTEN-deficient tumors.

PTEN (phosphatase and tensin homolog on chromosome 10) is encoded by one of the most commonly deleted tumor suppressor genes in human cancer. *PTEN* acts as a 3′-specific phosphatidylinositol phosphatase and counters the activity of the phosphatidylinositol 3-kinase (PI3K) signaling pathway in the cytoplasm (*1*). The PTEN signaling network is implicated in the control of cell metabolism, growth, proliferation, survival, and migration; processes invariably aberrant in cancer (*2*–*6*). PTEN may have roles in maintaining genomic stability, mediated at least in part by PI3K-independent mechanisms (*7*–*10*). PTEN is also found in the nuclei of many normal and cancerous cells and tissues, and various molecular mechanisms of PTEN nuclear localization have been described (*11*).

We noticed that, in addition to the expected PTEN protein of molecular mass ~55 kD, an ~75-kD PTEN protein species could be detected

[1]Department of Medical Biophysics, University of Toronto, Toronto, Ontario M5G 2M9, Canada. [2]Campbell Family Cancer Research Institute, Ontario Cancer Institute, Princess Margaret Cancer Center, University Health Network, Toronto, Ontario M5G 2M9, Canada. [3]Campbell Family Institute for Breast Cancer Research, Princess Margaret Cancer Center, University Health Network, Toronto, Ontario M5G 2C1, Canada. [4]Division of Hematology/Oncology and Cancer Biology Program, Department of Medicine, Beth Israel Deaconess Medical Center, Harvard Medical School, Boston, MA 02115, USA.

*Corresponding author. E-mail: vuks@uhnres.utoronto.ca

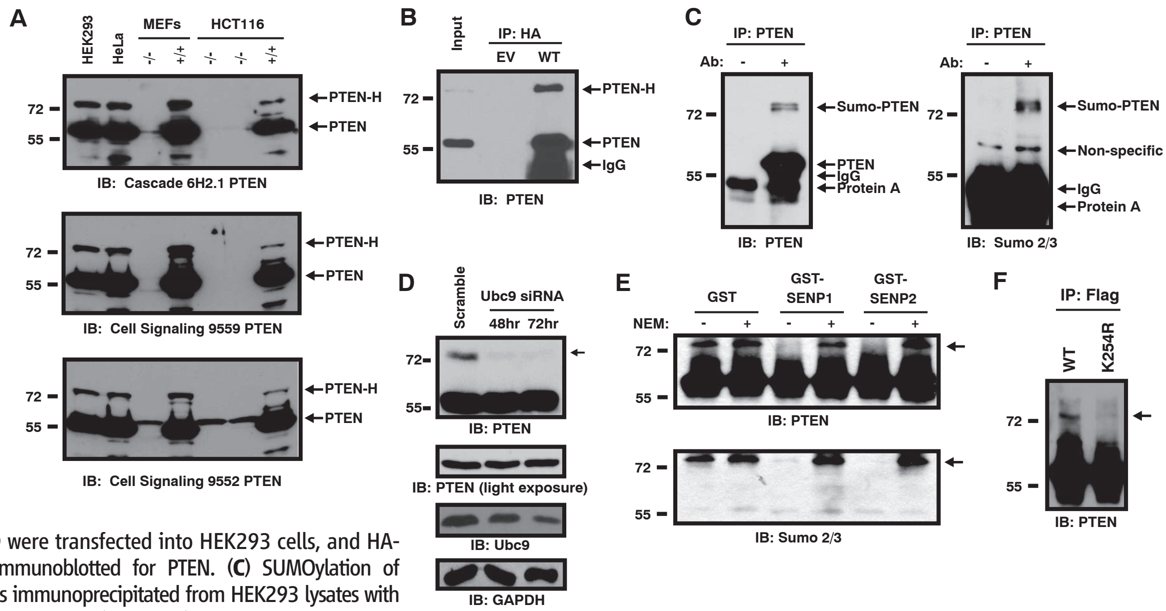

Fig. 1. SUMOylation of PTEN at K254 in vivo. (**A**) Multiple cell lines express a 75-kD form of PTEN. Whole-cell lysates were immunoblotted with three PTEN antibodies: 6H2.1 mouse monoclonal antibody (mAb) (top), rabbit mAb CST number 9559 (middle), or a rabbit polyclonal antibody (pAb) (bottom) CST number 9552. PTEN-H is indicated (arrow). WT, wild type; IB, immunoblot. (**B**) Transfection of minimal PTEN cDNA leads to PTEN-H formation. pcDNA3.1-HA-PTEN (WT) or pcDNA3.1-HA (EV) were transfected into HEK293 cells, and HA-immunoprecipitates (IP) immunoblotted for PTEN. (**C**) SUMOylation of endogenous PTEN. PTEN was immunoprecipitated from HEK293 lysates with protein A beads alone or PTEN antibody (CST 9559) and immunoblotted with the PTEN 6H2.1 antibody (left), then stripped and reprobed with antibodies to Sumo2/3 (right). IgG, immunoglobulin G. (**D**) Formation of SUMO-PTEN requires Ubc9. HEK293 cells were transfected with scrambled or Ubc9 small interfering RNAs and harvested at 48 (middle lane) or 72 (right lane) hours posttransfection. Lysates were immunoblotted for PTEN, Ubc9, and glyceraldehyde-3-phosphate dehydrogenase (GAPDH), as indicated. Arrow indicates SUMO-PTEN. (**E**) Sensitivity of PTEN-H to deSUMOylases. Immunoprecipitated Flag-PTEN was incubated with GST, GST-SENP1, or GST-SENP2, as indicated, in the presence or absence of 20 mM NEM. Reactions were immunoblotted with antibodies against PTEN (6H2.1) (top) or Sumo2 (bottom). (**F**) PTEN is SUMOylated on K254 in vivo. HEK293 cells were transfected with FLAG-PTEN-WT or FLAG-PTEN-K254R, together with His-SUMO2 and myc-His-Ubc9, as indicated. Flag immunoprecipitates were immunoblotted for PTEN.

with three PTEN antibodies in various mammalian cell lines (Fig. 1A). The ~75-kD species, which we termed PTEN-H, represented <10% of the total PTEN in the cell lines tested. PTEN-H was absent from mouse embryo fibroblasts (MEFs) and human colon carcinoma HCT116 cells with a targeted disruption of the *PTEN* gene (Fig. 1A). Transfection of a vector expressing hemagglutinin (HA) epitope–tagged PTEN cDNA gave rise to PTEN and PTEN-H, establishing that PTEN-H arises as a consequence of posttranslational modification rather than alternative initiation or splicing (Fig. 1B). Use of mild detergents largely precluded detection of PTEN-H in cell lysates (fig. S1A). Inclusion of *N*-ethylmaleamide (NEM), an inhibitor of cysteine-based enzymes including deSUMOylases (SUMO, small ubiquitin-like modifier) and deubiquitinases, during cell lysis increased the detection of PTEN-H (fig. S1B). Mono-SUMOylation could explain an apparent ~20-kD increase in molecular mass. Indeed, PTEN-H, but not "regular" PTEN, reacted with the antibodies to SUMO 2 and SUMO 3 in PTEN immunoprecipitates from human embryonic kidney (HEK) 293 cells (Fig. 1C). Depletion of Ubc9, the sole SUMO-conjugating E2 protein (*12*); overexpression of the SENP1 or SENP2 deSUMOylases (Fig. 1D and fig. S2); or treatment of PTEN immunoprecipitates with recombinant SENP1 or SENP2 decreased amounts of PTEN-H levels (Fig. 1E), further indicating that PTEN-H is a SUMOylated form of PTEN (SUMO-PTEN).

In vitro SUMOylation of a series of PTEN deletion mutations (fig. S3A) identified amino acids 238 to 320 as the minimal SUMOylated PTEN polypeptide (fig. S3, B and C). This PTEN portion contains a strong predicted SUMOylation site at position 254, a mutation of which precluded SUMOylation in vitro (fig. S3C). Nanoflow liquid chromatography–tandem mass spectrometry of SUMOylated PTEN polypeptides combined with SUMmOn pattern recognition software (*13*) independently identified K254 (*14*) as a bona fide SUMOylation site (fig. S4, A and B). Consistently, wild-type but not Flag-PTEN K254R (K to R mutation at position 254) was readily SUMOylated in HEK293 cells (Fig. 1F), identifying K254 as the major PTEN SUMOylation site. The PTEN K254R mutant retained the ability to counter PI3K signaling because its expression in PTEN-deficient human U87MG glioblastoma cells (*6*) resulted in comparable decreases in phosphorylation of protein kinase B (PKB) (also called Akt) and of the PKB target glycogen synthase kinase3β, as did expression of wild-type PTEN (fig. S5A), and in vitro displayed equal phosphatase activity toward phosphatidylinositol 3,4,5-trisphosphate [PI(3,4,5)P_3] (fig. S5B).

Unlike wild-type PTEN and an unrelated lysine PTEN K289E mutant, PTEN K254R expressed in HEK293 (Fig. 2A) or U87MG (fig. S6) cells failed to localize to the nucleus, suggesting that SUMOylation might promote nuclear localization of PTEN. In cells treated with leptomycin B, an inhibitor of nuclear export,

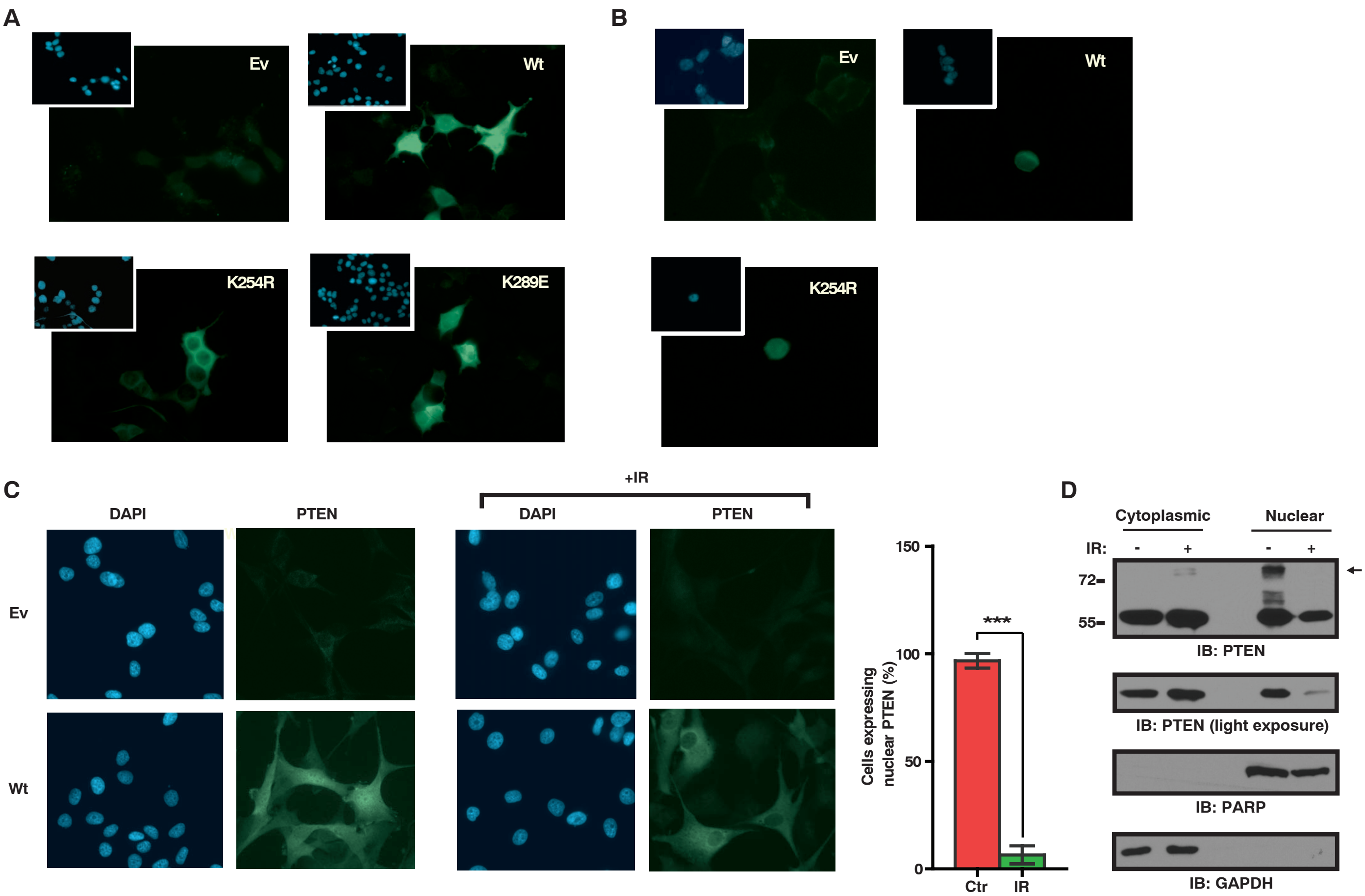

Fig. 2. PTEN SUMOylation regulates nuclear retention, which is sensitive to genotoxic stress. (**A**) Exclusion of the SUMO-deficient mutant PTEN K254R from the nucleus. Flag–fluorescein isothiocyanate (FITC) immunofluorescence images of HEK293 cells transfected as indicated. Insets show DAPI (4′,6-diamidino-2-phenylindole) staining. (**B**) Nuclear retention of SUMOylated PTEN. Immunofluorescence as in (A). Cells were treated with 10 ng/ml of leptomycin B for 4 hours. (**C**) Decreased nuclear PTEN localization after genotoxic stress. Immunofluorescence as in (A) of PTEN-FITC U87MG cells transfected as indicated, 4 hours post-IR. Bar graph represents percentage of cells with nuclear PTEN in control or IR-treated cells ($P < 0.001$, *t* test, $n = 5$, bars represent SEM). (**D**) Decreased nuclear PTEN after genotoxic stress. HeLa cells were treated as indicated, harvested after 4 hours, and separated into cytoplasmic and nuclear fractions followed by immunoblotting for PTEN. Fractionation was monitored by immunoblotting for PARP [poly(ADP-ribose) polymerase, a nuclear protein] and GAPDH (cytoplasmic protein). Arrow indicates SUMO-PTEN.

PTEN-K254R localized in the nucleus, indicating that this mutant can enter the nucleus but is not retained there (Fig. 2B). Treatment of cells with ionizing radiation (IR) led to loss of nuclear PTEN (Fig. 2C). Judging by fractionation of cellular lysates, SUMOylated PTEN was predominantly nuclear and reduced within hours of exposure to DNA damage (Fig. 2D).

We investigated the DNA damage response (DDR) of U87MG cells, HCT116 cells, and their variants with the *PTEN* gene disrupted (HCT116 *PTEN*$^{-/-}$) (*15*)—engineered to express PTEN wild type, K254R, mutants lacking all phosphatase activity (C124S) or only lipid-phosphatase (G129E) activity, or empty vector control (fig. S7A)—by monitoring the formation of p53 binding protein 1 (53BP1) foci (*16*) (Fig. 3A and figs. S7B and S8A). Four hours after IR exposure, 53BP1 foci were visible in all cell lines, indicating the presence of double-strand breaks (DSBs). However, by 24 hours, 53BP1 foci had largely resolved in wild-type PTEN- and G129E-reconstituted cells but not in PTEN-deficient cells, cells lacking nuclear PTEN (K254R), or cells lacking all PTEN phosphatase activity (C124S) (Fig. 3A and figs. S7B and S8A), indicative of deficient DNA repair. Consistently, PTEN-deficient cells or cells expressing PTEN K254R or PTEN C124S were also defective in resolving phosphorylated histone variant H2AX (γH2AX) and *breast cancer gene 1*, early onset (*BRCA1*) foci (Fig. 3, B and C, and figs. S7C and S8B). Indicative of deficiency in homologous recombination (HR)–based repair, PTEN-null cells, as well as their K254R- and C124S-expressing counterparts, failed to recruit RAD51 to the sites of DNA damage (Fig. 3D and figs. S8C and S7D) without affecting *RAD51* mRNA or protein abundance (fig. S9, A to C). Moreover, U87MG cells and cells derived from a mouse mammary tumor cell with a conditional *PTEN* gene disruption (WAP-Cre *PTEN*$^{-/-}$ MMTCs) expressing PTEN-K254R or PTEN-C124S were deficient in repair of a stably integrated, HR-mediated DSB repair reporter (*17*) (Fig. 3E and fig. S10). To distinguish the importance of nuclear localization versus SUMOylation for PTEN function in the response to DSBs, we fused a nuclear localization sequence from SV40 large T antigen (*18*) to the non-SUMOylatable PTEN mutant (NLS-PTEN K254R). Despite constitutive localization to the nucleus (fig. S11A), NLS-PTEN K254R (fig. S11B) did not restore the impaired response of U87MG cells to IR (fig. S11, C and D), indicating that SUMOylation is required

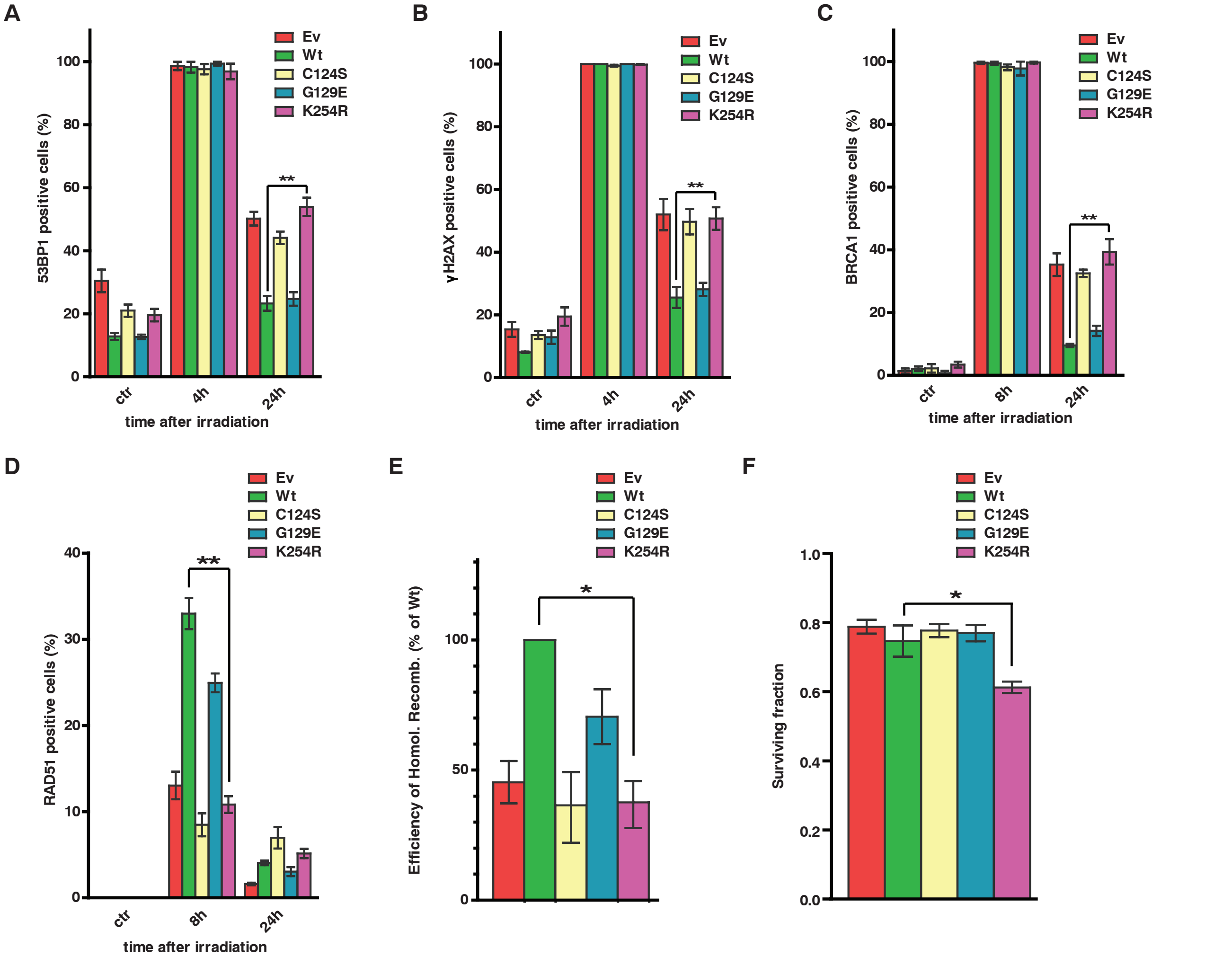

Fig. 3. Requirement of nuclear SUMO-PTEN for homologous recombination repair of DNA DSBs. U87MG cells were reconstituted with the indicated proteins. Cells treated with IR (5 Gy) were immunostained at the indicated times with antibodies to γH2AX, 53BP1, BRCA1, or RAD51. Cells containing more than five foci were scored as positive. Bars represent SEM. ctr, control. PTEN SUMOylation is required for the resolution of 53BP1 foci (P = 0.0014, t test, n = 3) (**A**), γH2AX foci (P = 0.007, t test, n = 3) (**B**), and BRCA1 foci (P = 0.0136, t test, n = 3) (**C**). (**D**) PTEN SUMOylation is required for RAD51 focus formation (P = 0.0016, t test, n = 3). (**E**) Impaired homologous recombination-based DNA repair in PTEN- and SUMO-PTEN–deficient cells. U87MG cells stably expressing a DR–green fluorescent protein reporter were reconstituted with the indicated PTEN proteins, and their HR-mediated repair assessed as previously described (*17*). HR efficiency is expressed relative to that of WT (P = 0.012, t test, n = 2). (**F**) Lack of SUMO-PTEN increases radiosensitivity. Surviving fraction was determined by sulforhodamine B staining 6 days after exposure to 3 Gy of IR (P = 0.02, t test, n = 3).

for PTEN's function in DDR. Reexpression of wild-type PTEN or various PTEN mutants did not yield changes in cell-cycle distribution (fig. S12A) or the engagement of cell-cycle checkpoints after IR (fig. S12B), indicating that DNA repair deficiency was not secondary to the potential effects of PTEN on the cell cycle. We monitored the effects of PTEN on radiosensitivity of cells by scoring the surviving fraction of U87MG cells and *PTEN*$^{-/-}$ MMTCs expressing PTEN mutants 5 days after exposure to IR. Although PTEN K254R-expressing cells exhibited a decreased surviving fraction after IR exposure (Fig. 3F and fig. S13), the survival of PTEN-null cells was indistinguishable from that of wild-type PTEN-expressing cells (Fig. 3F and fig. S13), possibly reflecting the activation of PI3K-mediated cell survival signaling in cells lacking PTEN.

IR led to a gradual reduction in the amounts of SUMO-PTEN beginning 1 hour after IR exposure with the steady-state amounts returning 8 hours later (Fig. 4A). Other forms of genotoxic stress, such as treatment with cisplatin or doxorubicin, also led to depletion of SUMO-PTEN, with the timing consistent with appearance of DNA damage elicited by these agents (fig. S14). Protein kinases ataxia telangiectasia mutated (ATM) and ATM and Rad3–related phosphorylate multiple targets after DNA damage (*16*). Inhibition of ATM impaired SUMO-PTEN turnover in response to

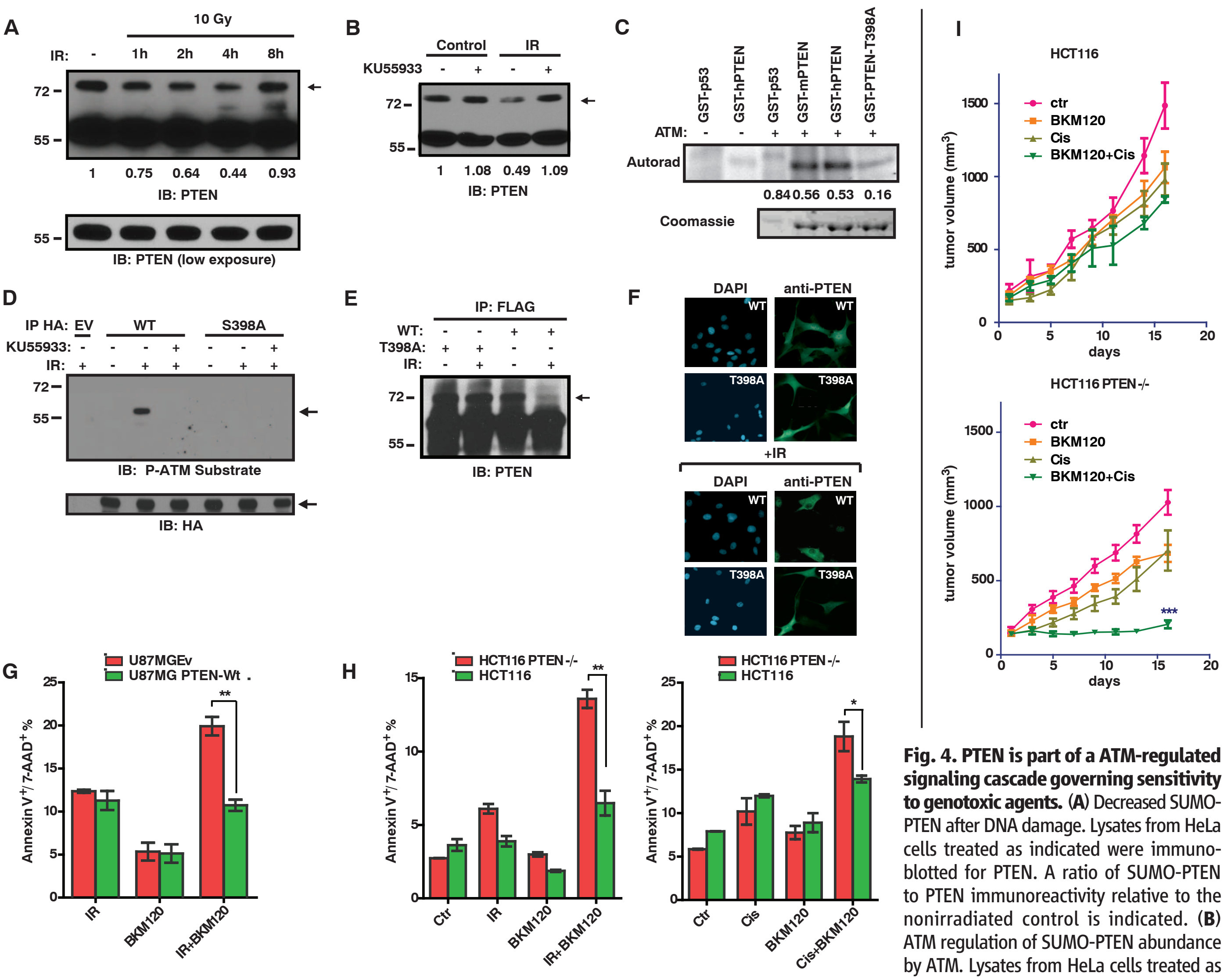

Fig. 4. PTEN is part of a ATM-regulated signaling cascade governing sensitivity to genotoxic agents. (**A**) Decreased SUMO-PTEN after DNA damage. Lysates from HeLa cells treated as indicated were immunoblotted for PTEN. A ratio of SUMO-PTEN to PTEN immunoreactivity relative to the nonirradiated control is indicated. (**B**) ATM regulation of SUMO-PTEN abundance by ATM. Lysates from HeLa cells treated as indicated were immunoblotted for PTEN and quantified as in (A). (**C**) ATM phosphorylates S/T 398 of PTEN in vitro. The indicated GST-fusion proteins were incubated with active ATM in the presence of ^{32}P-ATP. Incorporation of ^{32}P was quantified by PhosphorImager (Molecular Dynamics, Incorporated) and normalized to protein loading. (**D**) Phosphorylation of PTEN S398 in vivo by ATM. HA immunoprecipitates from HEK293 cells transfected and treated as indicated were immunoblotted with antibody against phospho-ATM substrates (CST 9607). (**E**) SUMO-PTEN-T398A is not sensitive to IR. Flag immunoprecipitates from HEK293 cells transfected and treated as indicated were immunoblotted for PTEN. (**F**) PTEN-T398A remains in the nucleus after IR. Cells were treated and imaged as in Fig. 2C. (**G** and **H**) PTEN loss sensitizes cells to combination treatment with IR and a pan-PI3K inhibitor. Bars represent SEM. (G) U87MG cells reconstituted with empty vector or PTEN-WT were treated with either 2 Gy of IR, 500 nM BKM120, or both, and apoptosis was measured by annexin V$^+$/7-AAD$^+$ staining (P = 0.0019, t test, n = 3). (H) HCT116 *PTEN*$^{-/-}$ and parental PTEN-WT cells were treated with either IR (2 Gy) or 1 mM cisplatin alone or in combination with 500 nM BKM120, as indicated. Apoptosis was measured as in (G) (IR+BKM120 P = 0.0025, t test, n = 3) (Cis+BKM120 P = 0.0475, t test, n = 3). (**I**) PTEN-deficient cells are sensitive to the cisplatin and PI3K inhibitor combination in vivo. HCT116 parental or HCT116 *PTEN*$^{-/-}$ cells were injected subcutaneously into nonobese diabeticor severe combined immunodeficient mice (n = 10). Mice were treated with cisplatin, BKM120, or both. Data points represent mean tumor volume ± SEM. Tumor growth difference was measured between day 1 and 16, and one-way analysis of variance was performed (P = 0.0321 for HCT116 parental and P < 0.0001 for HCT116 *PTEN*$^{-/-}$) followed by Dunnet's multiple comparison test (HCT116 *PTEN*$^{-/-}$ BKM120 + cisplatin versus Ctr, P < 0.0001).

IR (Fig. 4B), whereas ATM immunoprecipitated from γ-irradiated cells phosphorylated both human and mouse glutathione *S*-transferase (GST)–PTEN to a similar extent as it did p53, a known ATM substrate (Fig. 4C). PTEN contains a putative ATM phosphorylation site (*19*) at position 398. Mutation of this residue to alanine (T398A in human, S398A in mouse) decreased PTEN phosphorylation by ATM (Fig. 4C). PTEN was also phosphorylated at this site in vivo after IR in an ATM-dependent manner (Fig. 4D) establishing this residue as a likely ATM phosphorylation site within PTEN. Unlike wild-type SUMO-PTEN, SUMO-PTEN S/T398A was resistant to IR-induced turnover (Fig. 4E) and was not excluded from the nucleus in cells exposed to IR (Fig. 4F).

We compared the sensitivity of U87MG cells reconstituted with either empty vector or wild-type PTEN and the parental HCT116 and HCT116 *PTEN*$^{-/-}$ cells to BKM120, a small molecule pan-PI3K inhibitor; IR (2 Gy; 1 Gy = 100 rads); or a combination thereof at doses that produced minimal toxicity when administered alone (Fig. 4, G and H, and fig. S15). PTEN-deficient U87MG cells displayed increased sensitivity to a combination of IR and BKM120, whereas a combination of BKM120 with the genotoxic agent cisplatin had an enhanced effect in HCT116 *PTEN*$^{-/-}$ cells (Fig. 4H). In vivo, immunocompromised mice carrying HCT116 and HCT116 *PTEN*$^{-/-}$ xenografts were treated with a single dose of cisplatin, daily BKM120 for 15 days, or a combination thereof (Fig. 4I). Although either drug alone had limited effect [<30% tumor growth inhibition (TGI) over the course of the treatment], the combination reduced the growth of HCT116 *PTEN*$^{-/-}$ xenografts (>90% TGI) but not their PTEN-proficient counterparts (Fig. 4I). Such synthetic sensitivity of PTEN-deficient cells to the combined action of DNA-damaging agents and PI3K pathway inhibitors might be useful in treating PTEN-deficient tumors (fig S16). By contrast, our results suggest that administering genotoxic agents alone to such tumors could accelerate the acquisition of additional mutations (fig S16). The ongoing clinical development of numerous agents countering activated PI3K signaling in cancer (*20*, *21*) and next-generation genotoxic agents (*22*) should facilitate testing of these concepts in the clinic.

References and Notes

1. T. Maehama, J. E. Dixon, *J. Biol. Chem.* **273**, 13375–13378 (1998).
2. P. Cairns *et al.*, *Cancer Res.* **57**, 4997–5000 (1997).
3. P. Guldberg *et al.*, *Cancer Res.* **57**, 3660–3663 (1997).
4. N. N. Ahmed, H. L. Grimes, A. Bellacosa, T. O. Chan, P. N. Tsichlis, *Proc. Natl. Acad. Sci. U.S.A.* **94**, 3627–3632 (1997).
5. B. K. Rasheed *et al.*, *Cancer Res.* **57**, 4187–4190 (1997).
6. P. A. Steck *et al.*, *Nat. Genet.* **15**, 356–362 (1997).
7. J. Puc *et al.*, *Cancer Cell* **7**, 193–204 (2005).
8. M. Fraser *et al.*, *Clin. Cancer Res.* **18**, 1015–1027 (2012).
9. W. H. Shen *et al.*, *Cell* **128**, 157–170 (2007).
10. L. C. Trotman *et al.*, *Cell* **128**, 141–156 (2007).
11. S. M. Planchon, K. A. Waite, C. Eng, *J. Cell Sci.* **121**, 249–253 (2008).
12. J. Anckar, L. Sistonen, *Biochem. Soc. Trans.* **35**, 1409–1413 (2007).
13. P. G. Pedrioli *et al.*, *Nat. Methods* **3**, 533–539 (2006).
14. Single-letter abbreviations for the amino acid residues are as follows: A, Ala; C, Cys; E, Glu; G, Gly; K, Lys; R, Arg; S, Ser; and T, Thr.
15. Y. Samuels *et al.*, *Cancer Cell* **7**, 561–573 (2005).
16. L. H. Thompson, *Mutat. Res.* **751**, 158–246 (2012).
17. B. Elliott, M. Jasin, *Mol. Cell. Biol.* **21**, 2671–2682 (2001).
18. D. Kalderon, W. D. Richardson, A. F. Markham, A. E. Smith, *Nature* **311**, 33–38 (1984).
19. S. Matsuoka *et al.*, *Science* **316**, 1160–1166 (2007).
20. K. K. Wong, J. A. Engelman, L. C. Cantley, *Curr. Opin. Genet. Dev.* **20**, 87–90 (2010).
21. P. Liu, H. Cheng, T. M. Roberts, J. J. Zhao, *Nat. Rev. Drug Discov.* **8**, 627–644 (2009).
22. C. J. Lord, A. Ashworth, *Nature* **481**, 287–294 (2012).

Acknowledgments: We thank P. Fraser for reagents, D. Durocher for advice on DNA repair assays, R. Hakem for critical reading of the manuscript, A. Wakeham for advice on xenograft experiments, and Novartis for BKM120. Supported by grants from the Canadian Cancer Society to V.S. (2011-700891) and from NIH to B.G.N. (R37 CA49152) and partially supported by a grant from the Ontario Ministry of Health and Long Term Care and the Princess Margaret Hospital Foundation. B.G.N. and T.W.M. hold Canada Research Chairs (Tier I), and B.R. holds Canada Research Chair (Tier II). C.B. was supported by the Excellence in Radiation Research for the 21st century (EIRR21st) fellowship, and R.J.O.D. was supported by a Banting Postdoctoral Fellowship from the Canadian Institutes of Health Research. C.B. and V.S. designed research; C.B., J.H., T.S., R.D., C.G., and S.J.M. performed research; C.B., T.S., B.G.N., B.R., and V.S. analyzed data; T.M., B.G.N., B.R., and V.S. supervised research; and C.B., B.G.N., and V.S. wrote the paper.

Supplementary Materials

www.sciencemag.org/cgi/content/full/341/6144/395/DC1
Materials and Methods
Figs. S1 to S16
References (*23*–*25*)

6 February 2013; accepted 3 July 2013
10.1126/science.1236188

A Secreted PTEN Phosphatase That Enters Cells to Alter Signaling and Survival

Benjamin D. Hopkins,[1,2,3] Barry Fine,[2,3] Nicole Steinbach,[1,2,3] Meaghan Dendy,[1] Zachary Rapp,[3] Jacquelyn Shaw,[2,3,4] Kyrie Pappas,[1,2,3] Jennifer S. Yu,[2,3]* Cindy Hodakoski,[1] Sarah Mense,[1] Joshua Klein,[2,3,4] Sarah Pegno,[2,3] Maria-Luisa Sulis,[2,3,5] Hannah Goldstein,[3,6] Benjamin Amendolara,[3,6] Liang Lei,[3,7] Matthew Maurer,[2,3,4] Jeffrey Bruce,[6] Peter Canoll,[3,7] Hanina Hibshoosh,[3,7] Ramon Parsons[1]†

Phosphatase and tensin homolog on chromosome ten (*PTEN*) is a tumor suppressor and an antagonist of the phosphoinositide-3 kinase (PI3K) pathway. We identified a 576–amino acid translational variant of *PTEN*, termed PTEN-Long, that arises from an alternative translation start site 519 base pairs upstream of the ATG initiation sequence, adding 173 N-terminal amino acids to the normal PTEN open reading frame. PTEN-Long is a membrane-permeable lipid phosphatase that is secreted from cells and can enter other cells. As an exogenous agent, PTEN-Long antagonized PI3K signaling and induced tumor cell death in vitro and in vivo. By providing a means to restore a functional tumor-suppressor protein to tumor cells, PTEN-Long may have therapeutic uses.

PTEN (*phosphatase and tensin homolog on chromosome ten*) is a tumor suppressor that is mutated in multiple types of cancer (*1*, *2*). *PTEN* encodes a dual-specificity phosphatase whose primary substrate is phosphatidylinositol 3,4,5 trisphosphate (PIP3) (*3*–*7*). Through this activity, PTEN antagonizes phosphoinositide 3-kinase (PI3K) signaling and thereby affects a myriad of cellular processes, including growth, proliferation, and survival (*8*–*11*). In mice, loss of *Pten* in tumors or the tumor microenvironment results in neoplastic growth (*12*–*14*), indicating that *PTEN*'s tumor-suppressive functions are not confined to tumor cells alone.

Inspection of the *PTEN* mRNA transcript (Fig. 1A) revealed an alternative translation initiation codon (CUG) at base pair 513 that was 5′ of and in-frame with the canonical translation initiation codon (AUG) at base pair 1032. Alternative trans-

[1]Department of Oncological Sciences, Icahn School of Medicine at Mount Sinai, 1470 Madison Avenue, New York, NY 10029, USA. [2]Institute for Cancer Genetics, Columbia University, 1130 St. Nicholas Avenue, New York, NY 10032, USA. [3]Herbert Irving Comprehensive Cancer Center, Columbia University, 1130 St. Nicholas Avenue, New York, NY 10032, USA. [4]Department of Medicine, Columbia University Medical Center, 630 West 168th Street, New York, NY 10032, USA. [5]Department of Pediatrics, Columbia University Medical Center, 630 West 168th Street, New York, NY 10032, USA. [6]Department of Neurological Surgery, Neurological Institute, New York Presbyterian Hospital Columbia University, 710 West 168th Street, New York, NY 10032, USA. [7]Department of Pathology and Cell Biology, Columbia University Medical Center, 630 West 168th Street, New York, NY 10032, USA.

*Present address: Department of Radiation Oncology and Department of Stem Cell Biology and Regenerative Medicine, Cleveland Clinic, 9500 Euclid Avenue, Cleveland, OH 44195, USA.

†Corresponding author. E-mail: ramon.parsons@mssm.edu

lation beginning at base pair 513 was predicted to encode a 576–amino acid translational variant, which we termed PTEN-Long. PTEN-Long contains a 173–amino acid domain at its N terminus followed by the classical 403 amino acids of PTEN (fig. S1) (*15*). Search of the Catalogue of Somatic Mutations in Cancer (www.sanger.ac.uk/genetics/CGP/cosmic) database found five somatic missense mutations specific for PTEN-Long in tumor samples (fig. S1). Alignment of the predicted 173–amino acid sequence of the PTEN-Long–specific region with predicted protein sequences from other species indicated that it is evolutionarily conserved (fig. S2).

To determine whether PTEN-Long is translated in cells, we transfected human breast (BT549) and glioblastoma (GBM) (U87MG) cells that lack PTEN with a cDNA expression vector containing the PTEN-Long and PTEN open reading frames. Immunoblots of these lysates revealed two forms of PTEN: a ~75-kD form (PTEN-Long) and a ~55-kD species that corresponded to the conventional translated protein. Expression of PTEN-Long was increased by mutating the alternate start site (CTG) to a classical start site (ATG) (*16*), was not diminished when the canonical ATG was mutated to ATA, and was lost if the alternatively translated region was deleted or if a frame shift was introduced between the alternate start site at 513 and the classic start site at 1032 (fig. S3). PTEN-Long showed a different enzymatic profile across the tested range of lipid substrate concentrations [soluble di-C8-phosphatidylinositol-3,4,5-trisphosphate (di-C8-PIP3)] (Fig. 1B and fig. S4) [$P < 0.001$ by means of analysis of variance (ANOVA)] (*17*). A missense mutation in the phosphatase domain of PTEN-Long (G302R)—analogous to PTEN (G129R), a tumor mutation—decreased the phosphatase activity of the protein (fig. S5) (*1*, *18*, *19*). Immunoblots of U87MG cells overexpressing equivalent amounts of transfected PTEN, PTEN-Long, or their mutated analogs confirmed that similar to PTEN, PTEN-Long decreased signaling through the PI3K pathway in a phosphatase-dependent manner (fig. S6). Immunoblots of mouse embryonic stem cells and human cancer cell lines with antibodies either specific for PTEN-Long or an epitope shared by PTEN and PTEN-Long showed that a ~75-kD PTEN-Long band was present in wild-type but not in cells lacking PTEN (Fig. 1C). Immunoprecipitations with antibodies to PTEN or PTEN-Long confirmed that PTEN-Long contains canonical PTEN peptides and is therefore a translational variant of PTEN (Fig. 1D and fig. S7). Amounts of PTEN-Long were reduced in primary human breast tumors as compared with those of matched normal breast samples (Fig. 1E, fig. S8, and table S1). Immunohistochemistry of brain tissue from a mouse GBM caused by the deletion of *Pten* and *p53* and overexpression of *PDGF* revealed that PTEN-Long was more abundant in the tumor microenvironment than in the tumor or normal tissue (fig. S9) (*20*). PTEN-Long was similarly abundant in the tumor microenvironment in 4 of 50 samples from primary breast cancers (fig. S10).

Computer modeling indicated that PTEN-Long contained a secretion signal sequence with a predicted cleavage site at amino acid 22 (fig. S11) (*21*). Thus, we tested whether PTEN-Long might exist outside of cells. We overexpressed V5 epitope-tagged PTEN, PTEN-Long, and a mutant with an altered signal sequence predicted to abolish secretion (PTEN-LongΔA^6) (fig. S12) in human embryonic kidney (HEK) 293 cells. We concentrated the proteins from conditioned medium by means of immunoprecipitation with antibody to PTEN (138G6) or with heparin columns (fig. S13). With antibodies that recognized the V5 tag or the endogenous C terminal region of PTEN and PTEN-Long, we detected PTEN-Long but not PTEN nor PTEN-LongΔA^6 in conditioned medium (Fig. 2A and fig. S14). Brefeldin-A, an inhibitor that interferes with retrograde transport of vesicles in the endoplasmic reticulum, inhibited the secretion of PTEN-Long (Fig. 2B) (*22*). Endogenous PTEN-Long from HEK293 cells bound to concanavalin A-sepharose, a hallmark of a secreted glycoprotein (fig. S15). Furthermore, PTEN-Long but not PTEN was present in both human plasma and serum (fig. S16). A screen for PTEN-interacting proteins identified multiple heparan-sulfate–modified cell-surface proteins in the glypican and syndecan families (fig. S17) (*23*). Thus, PTEN-Long appears to be secreted from cells and to interact with cell-surface proteins.

We noted the presence of a poly-arginine stretch in the specific region of PTEN-Long that was evolutionarily conserved (fig. S2) and bore a resemblance to the poly-basic residues of the cell-penetrating element of the HIV transactivator of transcription (TAT) protein (*24*, *25*). To determine whether this sequence conferred similar properties to PTEN-Long, we constructed a PTEN-LongΔR^6 construct in which these six arginines were deleted (fig. S18). After treating cells with 100 nM purified red fluorescent protein

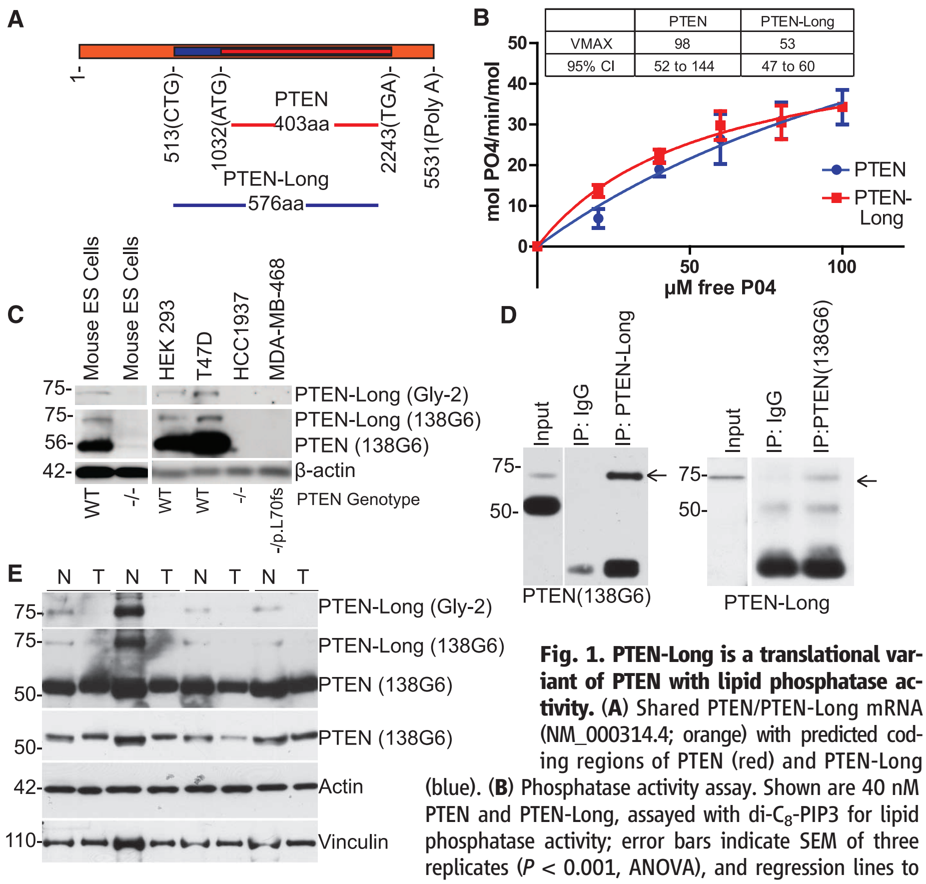

Fig. 1. PTEN-Long is a translational variant of PTEN with lipid phosphatase activity. (**A**) Shared PTEN/PTEN-Long mRNA (NM_000314.4; orange) with predicted coding regions of PTEN (red) and PTEN-Long (blue). (**B**) Phosphatase activity assay. Shown are 40 nM PTEN and PTEN-Long, assayed with di-C_8-PIP3 for lipid phosphatase activity; error bars indicate SEM of three replicates ($P < 0.001$, ANOVA), and regression lines to Michaelis-Menten kinetics with V_{max} and 95% confidence interval (CI) are shown in the inset as moles PO4/min/moles enzyme. This is a representative experiment of three. (**C**) Immunoblot of whole-cell lysates from wild-type and *Pten* null embryonic stem cells and cancer cell lines of known *PTEN* status. PTEN-Long (Gly-2) recognizes an epitope specific to the PTEN-Long–specific region. PTEN (138G6) recognizes an epitope that is common to both PTEN and PTEN-Long. (**D**) Reciprocal immunoprecipitations of proteins from whole-cell lysates of HEK293 cells with PTEN-Long–specific antibody, probed with an antibody that recognizes an epitope that is common to PTEN/PTEN-Long and vice versa. Input lanes are from longer exposure of the same membrane. Arrows indicate PTEN-Long. (**E**) Immunoblots of four randomly selected PTEN wild-type sets of matched breast tumor (T)/normal breast (N) pairs.

(RFP)–V5/His, PTEN-Long–RFP-V5/His, or PTEN-LongΔR[6]–RFP-V5/His, we detected PTEN-Long–RFP but not RFP nor PTEN-LongΔR[6]–RFP in the cells with fluorescence microscopy (Fig. 3A and fig. S19). We confirmed this observation through subcellular fractionation (Fig. 3B and fig. S20). Fusion of the PTEN-Long–specific region (PL) to RFP enabled cellular uptake of the fusion protein (fig. S21). Therefore, the PL domain facilitates cell penetration of tethered peptide sequences. We next tested whether PTEN-Long affected cellular signaling as an exogenous agent. Treatment of cells in culture for 15 min with purified PTEN-Long reduced basal phosphorylation of the protein kinase AKT on Thr^{308} in the majority of cell lines (Fig. 3C and figs. S22 and S23). When starved, U87MG cells were incubated with PTEN-Long for 10 min, and subsequent stimulation of phosphorylation of AKT Thr^{308} by insulin or epidermal growth factor (EGF) was inhibited. Inhibition of PI3K signaling appeared to be dependent on the poly-arginine sequence of PTEN-Long because the PTEN-LongΔR[6] mutant did not block insulin or EGF-induced phosphorylation of AKT (fig. S24). Dose-response experiments in cells deprived of serum and treated for 24 hours showed that PTEN-Long decreased PI3K signaling as indicated by the decreased phosphorylation of AKT, FOXO, and PRAS40 and induced cell death as indicated by cleavage of caspase 3 (Fig. 3, D and E). We confirmed this effect on cell survival by treating U87MG and MDA-MB-468 cells grown in 0.1% serum with various doses of PTEN-Long or PTEN-LongΔR[6] (Fig. 3F).

Upon treatment of mice with PTEN-Long, we observed in blood a transient increase in glucose

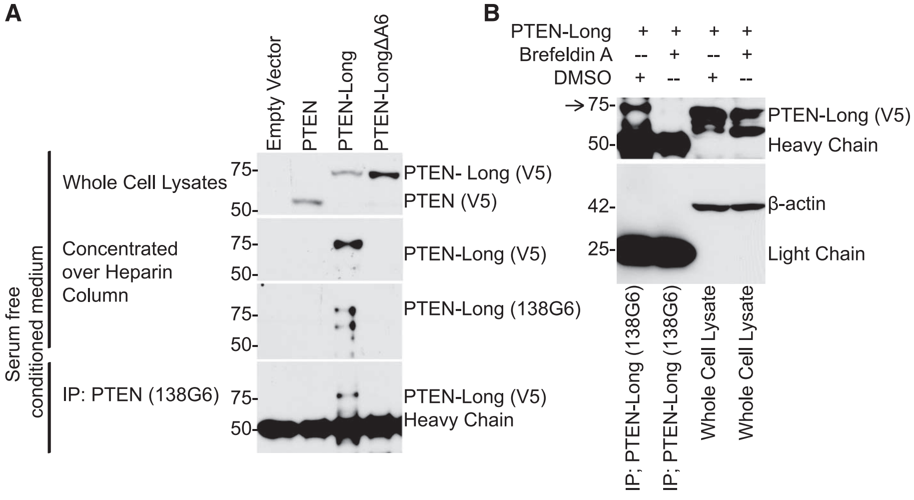

Fig. 2. Secretion of PTEN-Long. (**A**) PTEN, PTEN-Long, and PTEN-LongΔA[6] from serum-free conditioned medium of transfected HEK293 cells eluted from a heparin column or immunoprecipitated with C-terminal PTEN antibody 138G6. (**B**) Cellular (lanes 3 and 4) or secreted PTEN-Long from culture medium (lanes 1 and 2) of transfected HEK293 cells treated with or without brefeldin A at 1 µg/ml. Arrow indicates PTEN-Long.

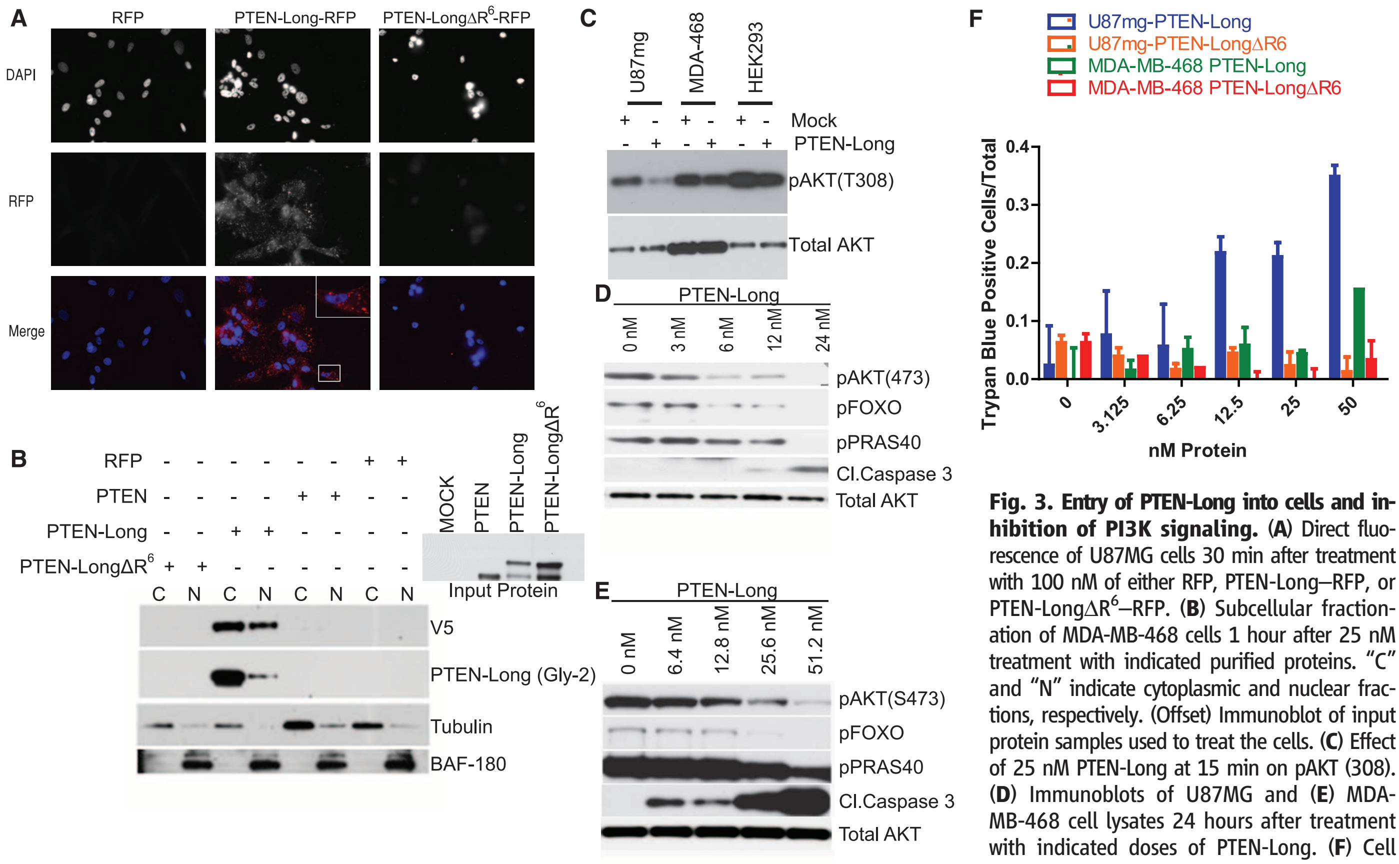

Fig. 3. Entry of PTEN-Long into cells and inhibition of PI3K signaling. (**A**) Direct fluorescence of U87MG cells 30 min after treatment with 100 nM of either RFP, PTEN-Long–RFP, or PTEN-LongΔR[6]–RFP. (**B**) Subcellular fractionation of MDA-MB-468 cells 1 hour after 25 nM treatment with indicated purified proteins. "C" and "N" indicate cytoplasmic and nuclear fractions, respectively. (Offset) Immunoblot of input protein samples used to treat the cells. (**C**) Effect of 25 nM PTEN-Long at 15 min on pAKT (308). (**D**) Immunoblots of U87MG and (**E**) MDA-MB-468 cell lysates 24 hours after treatment with indicated doses of PTEN-Long. (**F**) Cell viability assay. U87MG and MDA-MB-468 cells were treated with the indicated doses of PTEN-Long or PTEN-LongΔR[6] for 24 hours before scoring of the fraction of cells with trypan blue staining. Assayed in quadruplicate, and error bars indicate SEM.

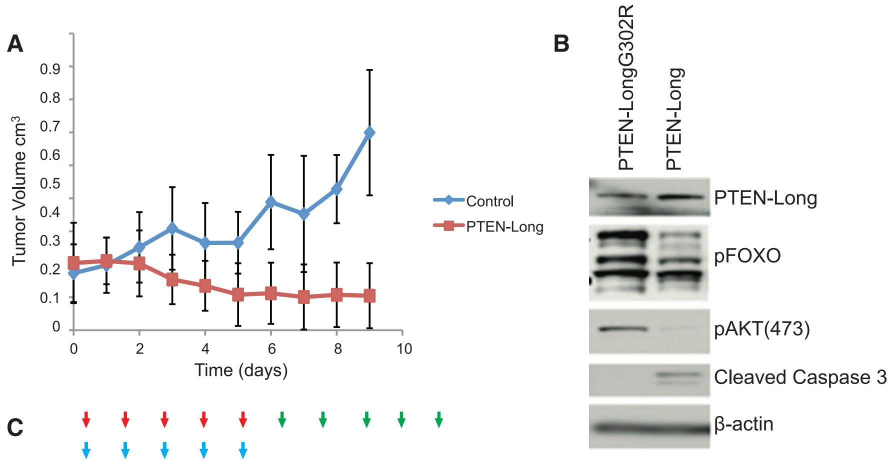

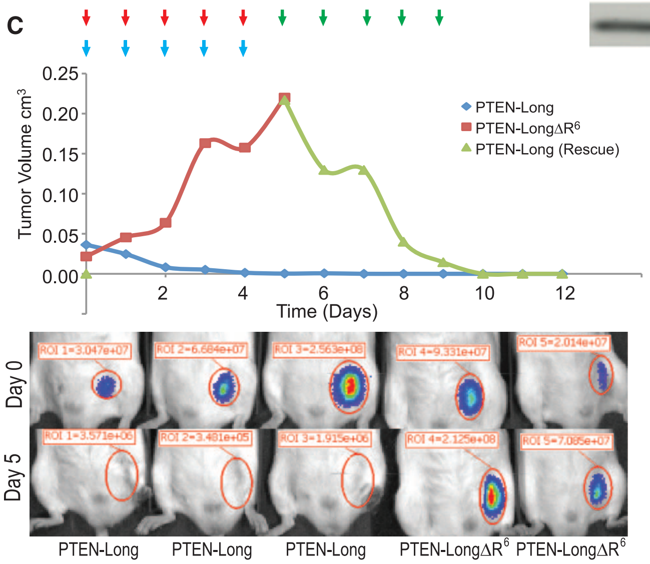

Fig. 4. Effects of PTEN-Long on signaling and tumor development in mice. (A) Graph of U87MG tumor volumes as measured by calipers and treated with either PTEN-Long (4 mg/kg) or an equal volume of mock purified material ($n = 5$ mice/treatment; error bars indicate ±SD). **(B)** Immunoblots of markers of PI3K signaling in U87MG xenografts treated for 5 days with PTEN-Long or phosphatase mutant PTEN-Long (G302R). **(C)** $Pten^{-/-}$-, $p53^{-/-}$-, and PDGF-overexpressing cells derived from the genetically engineered mouse model of GBM were allografted into the flank of syngeneic hosts and treated with 4 mg/kg of PTEN-Long or PTEN-LongΔR^6 for 5 days. Tumor volume was assessed daily with caliper measurements and on days 0 and 5 with a xenogen imaging system, as shown. After 5 days of treatment, the mice in the PTEN-LongΔR^6 (red arrows) cohort were then treated with PTEN-Long (green arrows), followed with caliper measurements. Blue arrows indicate initial PTEN-Long treatment (days 0 to 4).

concentration (fig. S25) and PTEN-Long (fig. S26). Similar to what we observed in culture, PTEN-Long was detected in mouse tissues, including a xenografted breast tumor (MDA-MB-468), and could alter cell signaling (figs. S27 to S29). PTEN-Long derivatives lacking phosphatase or cell-penetrating activity were unable to cause these signaling changes. TAT-PTEN only recapitulated some of the effects of PTEN-Long, indicating that the PTEN-Long–specific region may have other functions beyond the cell permeability conferred by TAT (fig. S30).

We further explored the effect of PTEN-Long in mouse tumor models. We engrafted U87MG cells subcutaneously into athymic nude mice and allowed them to grow until their tumor volume reached ~0.2 cm^3. Animals were then injected intraperitoneally with PTEN-Long (4 mg/kg) or a control preparation. PTEN-Long caused tumor regression after 4 days of treatment (Fig. 4A and fig. S31). Similar regressions were also observed in multiple other xenograft models, with the exception of the human colon cancer tumor cell line HCT116 (figs. S32 and S33). Although both PTEN-Long and PTEN-Long G302R were detected within tumor tissues after 5 days of treatment, only the wild-type protein affected PI3K signaling or induced apoptosis (Fig. 4B). Immunohistochemistry of serial sections of tumor xenografts confirmed exogenous PTEN-Long within tumor cells and a concomitant reduction of pAKT staining. We also treated syngeneic allografts from a mouse model of GBM. After treatment with PTEN-Long (4 mg/kg), tumors derived from $Pten^{-/-}$-, $p53^{-/-}$-, and PDGF-overexpressing GBM cells underwent complete tumor regression within 5 days, whereas treatment with PTEN-LongΔR^6 did not prevent tumor growth (Fig. 4C) (*20*). Mutant PTEN-Long proteins derived from three cancers (fig. S1) in which PTEN-Long underwent somatic mutation all showed reduced ability to affect signaling in vitro and in vivo, suggesting that there may be selective pressure to mutate PTEN-Long during tumor development (fig. S34). Thus, PTEN-Long protein appears to alter PI3K signaling in vivo to inhibit tumor growth, and this effect is dependent on its entrance into cells.

PTEN-Long is a translational variant of *PTEN* that, like classical PTEN, acts as an antagonist of the PI3K pathway. As a secreted product of a tumor suppressor gene capable of entering cells, endogenous PTEN-Long may contribute to an organism's maintenance of signaling, tissue homeostasis, and suppression of cancer. Recombinant PTEN-Long and derivative fusion proteins may be useful for delivering proteins in a variety of experimental and clinical settings.

References and Notes

1. J. Li *et al.*, *Science* **275**, 1943 (1997).
2. P. A. Steck *et al.*, *Nat. Genet.* **15**, 356 (1997).
3. T. Maehama, J. E. Dixon, *J. Biol. Chem.* **273**, 13375 (1998).
4. M. Cully, H. You, A. J. Levine, T. W. Mak, *Nat. Rev. Cancer* **6**, 184 (2006).
5. S. J. Baker, *Cell* **128**, 25 (2007).
6. N. R. Leslie, C. P. Downes, *Biochem. J.* **382**, 1 (2004).
7. L. C. Cantley, *Science* **296**, 1655 (2002).
8. V. Stambolic *et al.*, *Cell* **95**, 29 (1998).
9. H. Sun *et al.*, *Proc. Natl. Acad. Sci. U.S.A.* **96**, 6199 (1999).
10. F. B. Furnari, H. Lin, H. S. Huang, W. K. Cavenee, *Proc. Natl. Acad. Sci. U.S.A.* **94**, 12479 (1997).
11. J. Li *et al.*, *Cancer Res.* **58**, 5667 (1998).
12. A. Di Cristofano, B. Pesce, C. Cordon-Cardo, P. P. Pandolfi, *Nat. Genet.* **19**, 348 (1998).
13. K. Podsypanina *et al.*, *Proc. Natl. Acad. Sci. U.S.A.* **96**, 1563 (1999).
14. A. J. Trimboli *et al.*, *Nature* **461**, 1084 (2009).
15. Materials and methods are available as supplementary materials on *Science* Online.
16. M. Kozak, *Mol. Cell. Biol.* **9**, 5073 (1989).
17. G. McConnachie, I. Pass, S. M. Walker, C. P. Downes, *Biochem. J.* **371**, 947 (2003).
18. M. P. Myers *et al.*, *Proc. Natl. Acad. Sci. U.S.A.* **95**, 13513 (1998).
19. Single-letter abbreviations for the amino acid residues are as follows: A, Ala; C, Cys; D, Asp; E, Glu; F, Phe; G, Gly; H, His; I, Ile; K, lys; L, Leu; M, Met; N, Asn; P, Pro; Q, Gln; R, Arg; S, Ser; T, Thr, V, Val; W, Trp; and Y, Tyr.
20. L. Lei *et al.*, *PLoS ONE* **6**, e20041 (2011).
21. H. Nielsen, A. Krogh, *Proc. Int. Conf. Intell. Syst. Mol. Biol.* **6**, 122 (1998).
22. R. D. Klausner, J. G. Donaldson, J. Lippincott-Schwartz, *J. Cell Biol.* **116**, 1071 (1992).
23. B. Fine *et al.*, *Science* **325**, 1261 (2009).
24. T. Subramanian, R. Govindarajan, G. Chinnadurai, *EMBO J.* **10**, 2311 (1991).
25. S. R. Schwarze, A. Ho, A. Vocero-Akbani, S. F. Dowdy, *Science* **285**, 1569 (1999).

Acknowledgments: We thank L. Greene, T. Ludwig, D. Yamashiro, K. Olive, and members of the Parsons laboratory for their assistance. This work was supported by NIH grant CA082783, NCI grant CA097403, NIH grant R01NS066955, the Avon Foundation, and the OctoberWoman Foundation. B.D.H. is supported by NIH grant 2T32 CA09503. Columbia University has applied for patents on PTEN-Long. NM_000314.4 is curated by GenBank. Additional data are present in the supplementary materials.

Supplementary Materials

www.sciencemag.org/cgi/content/full/science.1234907/DC1
Materials and Methods
Figs. S1 to S34
Table S1
References (*26–29*)

8 January 2013; accepted 24 May 2013
Published online 6 June 2013;
10.1126/science.1234907

Xk-Related Protein 8 and CED-8 Promote Phosphatidylserine Exposure in Apoptotic Cells

Jun Suzuki,[1] Daniel P. Denning,[2] Eiichi Imanishi,[1] H. Robert Horvitz,[2] Shigekazu Nagata[1,3]*

A classic feature of apoptotic cells is the cell-surface exposure of phosphatidylserine (PtdSer) as an "eat me" signal for engulfment. We show that the Xk-family protein Xkr8 mediates PtdSer exposure in response to apoptotic stimuli. Mouse *Xkr8*$^{-/-}$ cells or human cancer cells in which Xkr8 expression was repressed by hypermethylation failed to expose PtdSer during apoptosis and were inefficiently engulfed by phagocytes. Xkr8 was activated directly by caspases and required a caspase-3 cleavage site for its function. CED-8, the only *Caenorhabditis elegans* Xk-family homolog, also promoted apoptotic PtdSer exposure and cell-corpse engulfment. Thus, Xk-family proteins have evolutionarily conserved roles in promoting the phagocytosis of dying cells by altering the phospholipid distribution in the plasma membrane.

Phospholipids are distributed asymmetrically between the outer and inner leaflets of plasma membranes (*1*): Phosphatidylserine (PtdSer) and phosphatidylethanolamine (PtdEtn) localize exclusively to the inner leaflet, whereas 60 to 70% of phosphatidylcholine (PtdCho) and sphingomyelin (SM) are found on the outer leaflet. This asymmetric distribution is disrupted during apoptosis, and exposed PtdSer on dying cells serves as an "eat me" signal to facilitate phagocytosis (*2*, *3*). PtdSer exposure and the more general transfer of phospholipids between the inner and outer leaflets are probably mediated by phospholipid scramblases (*1*), the identities of which are disputed (*4*).

We previously generated a mouse Ba/F3 pro-B cell line (Ba/F3-PS19) with a high level of PtdSer exposure, constructed a cDNA library (of clones >2.5 kb), and discovered TMEM16F, a transmembrane protein required for Ca^{2+}-dependent phospholipid scrambling but not apoptosis-dependent PtdSer exposure (*5*, *6*). To identify molecules that mediate apoptotic PtdSer exposure, we introduced a Ba/F3-PS19 cDNA library (of clones 1.0 to 2.5 kb) into Ba/F3 cells, serially enriched for cells with high PtdSer exposure, and established a cell line (LD-PS5-2-2) with a high level of PtdSer exposure (Fig. 1A) (see supplementary materials and methods). LD-PS5-2-2 cells carried a cDNA encoding Xkr8, a member of the evolutionarily conserved XK protein family (*7*) (figs. S1 and S2). With the use of the programs Transmembrane Prediction (www.ch.embnet.org) and Transmembrane Hidden Markov Model (www.cbs.dtu.dk), analyses of the amino acid sequences of vertebrate Xkr8 orthologs suggested that Xkr8 contains six transmembrane regions flanked by cytosolic N and C termini (fig. S3).

We transformed mouse T cell lymphoma WR19L cells with Fas (*8*) (WR-Fas). Fas ligand (FasL) efficiently induced apoptosis of the WR-Fas cells, accompanied by caspase-3 activation and PtdSer exposure (Fig. 1B and fig. S4). The introduction of mouse Xkr8-GFP [mXkr8 fused to green fluorescent protein (GFP)], but not mTMEM16F-GFP, increased the fraction of PtdSer-exposing cells generated by FasL (Fig. 1B). The expression of m*Xkr8* short hairpin RNAs (shRNAs) in WR-Fas cells decreased the amount of the endogenous m*Xkr8* mRNA by 76 to 82% (fig. S5) and the fraction of cells with FasL-induced PdtSer-exposure (Fig. 1C), but not levels of caspase-3 activation (fig. S5). The transformation of m*Xkr8* shRNA-expressing cells with human (h)*Xkr8* cDNA, which is not recognized by the m*Xkr8* shRNAs, restored FasL-induced PdtSer exposure. hXkr8-GFP expressed in human 293T cells localized primarily to the plasma membrane (Fig. 1D), suggesting that Xkr8 functions at the cell surface to promote apoptotic PtdSer exposure.

Human PLB-985 leukemia and Raji lymphoma cells do not expose PtdSer during apoptosis (*9*, *10*). Studies using real-time reverse transcription polymerase chain reaction (RT-PCR) indicated that the amount of *Xkr8* mRNA in PLB-985 and Raji cells was 8 and 9%, respectively, of those in Namalwa cells (Fig. 2A). PLB-985 or Raji cell transformants expressing hXkr8 responded to apoptotic stimuli by exposing PtdSer (Fig. 2B). PtdSer exposure is necessary for the recognition of apoptotic cells by phagocytes

[1]Department of Medical Chemistry, Graduate School of Medicine, Kyoto University, Yoshida-Konoe, Sakyo-ku, Kyoto, Kyoto 606-8501, Japan. [2]Howard Hughes Medical Institute and Department of Biology, Massachusetts Institute of Technology, Cambridge, MA 02139, USA. [3]Core Research for Evolutional Science and Technology, Japan Science and Technology Corporation, Yoshida-Konoe, Sakyo, Kyoto 606-8501, Japan.

*Corresponding author. E-mail: snagata@mfour.med.kyoto-u.ac.jp

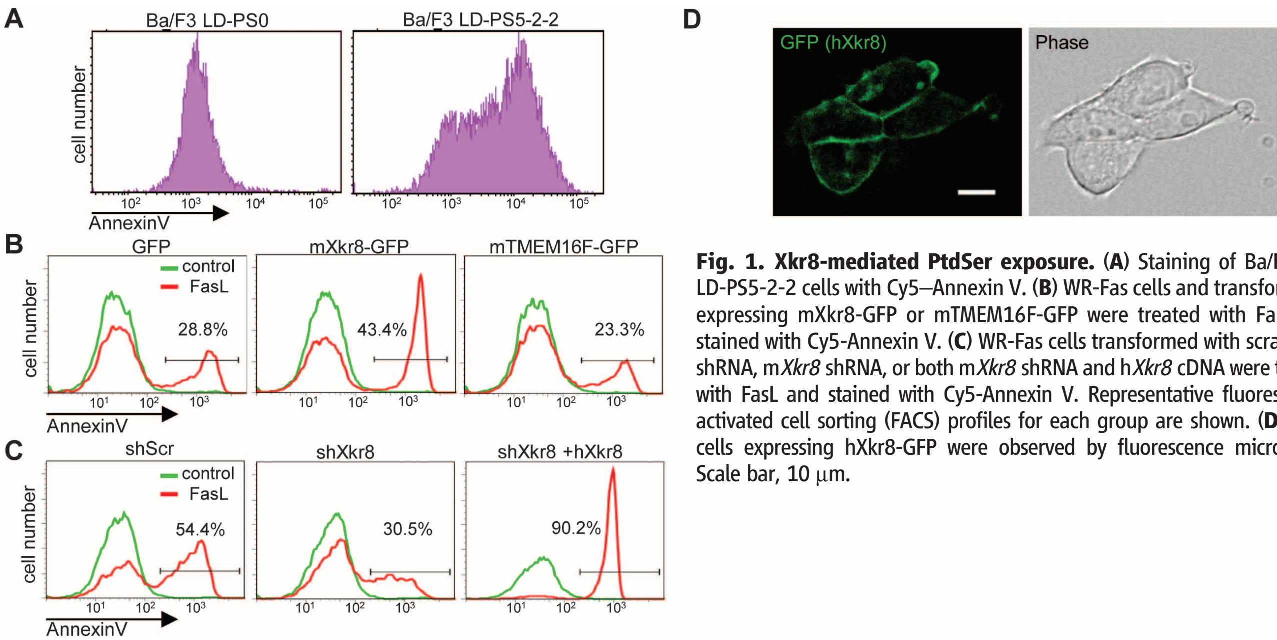

Fig. 1. Xkr8-mediated PtdSer exposure. (**A**) Staining of Ba/F3 and LD-PS5-2-2 cells with Cy5–Annexin V. (**B**) WR-Fas cells and transformants expressing mXkr8-GFP or mTMEM16F-GFP were treated with FasL and stained with Cy5-Annexin V. (**C**) WR-Fas cells transformed with scrambled shRNA, m*Xkr8* shRNA, or both m*Xkr8* shRNA and h*Xkr8* cDNA were treated with FasL and stained with Cy5-Annexin V. Representative fluorescence-activated cell sorting (FACS) profiles for each group are shown. (**D**) 293T cells expressing hXkr8-GFP were observed by fluorescence microscopy. Scale bar, 10 μm.

(*3*, *10*, *11*). Accordingly, whereas apoptotic PLB-985 cells were rarely engulfed by macrophages, their Xkr8 transformants were frequently internalized (Fig. 2C). Caspase-3 activation, DNA fragmentation, cell death, and cell shrinkage occurred similarly in PLB-985 cells with or without Xkr8 expression, indicating that Xkr8 and PtdSer exposure had no obvious effects on other aspects of the apoptotic process (fig. S6). The program CpG Island Searcher (http://cpgislands.usc.edu) identified two CpG islands near the transcription start site of the h*Xkr8* gene (fig. S7). Bisulfite DNA sequencing (*12*) indicated that none of the 23 CpGs between –232 and +4 of the h*Xkr8* gene was methylated in peripheral blood leukocyte, Jurkat, or Namalwa cells (fig. S7). By contrast, these CpGs were methylated with more than 90% probability in PLB-985 and Raji cells. Treatment of PLB-985 cells with 5-aza-2′-deoxycytidine (DAC) increased *Xkr8* mRNA levels (Fig. 2D). After 7 days of DAC treatment, all CpGs were demethylated (fig. S7), and *Xkr8* mRNA levels were 91% of that in Namalwa cells. Accordingly, DAC-treated PLB-985 cells exposed PtdSer upon ultraviolet (UV) irradiation (Fig. 2E). We suggest that the methylation of CpG islands in the *Xkr8* promoter in PLB-985 and Raji cells blocks *Xkr8* gene expression and prevents apoptotic PtdSer exposure.

We used RO09-0198 to assay staurosporine-treated, Xkr8-expressing PLB-985 cells for PtdEtn exposure, and we used 1-oleoyl-2-{6-[(7-nitro-2-1,3-benzoxadiazol-4-yl)amino]hexanoyl}-sn-glycero-3-phosphocholine (NBD-PC) and NBD-sphingosine-1-phosphocholine (NBD-SM) to assay for PtdCho and SM internalization, respectively. Inhibitor of caspase-activated DNase (ICAD) was cleaved equally well in PLB-985 and its hXkr8 transformants after staurosporine treatment (fig. S8). By contrast, apoptotic hXkr8-expressing cells (but not parental cells) stained with RO09-0198 and internalized NBD-PC and NBD-SM (fig. S8), indicating that Xkr8, like TMEM16F (*5*), promotes the scrambling of multiple lipid species. Unlike TMEM16F, Xkr8 had no effect on the Ca^{2+}-induced exposure of PtdSer (fig. S9), suggesting that distinct pathways control Ca^{2+}-induced phospholipid scrambling and apoptosis-induced scrambling. These findings are consistent with reports that B cell lines from Scott syndrome patients, who carry a null mutation in *TMEM16F*, respond to apoptotic stimuli by exposing PtdSer (*13*), and that mouse $Bak^{-/-}Bax^{-/-}$ platelets, which do not undergo apoptosis, expose PtdSer upon Ca^{2+} ionophore treatment (*14*).

We used the program CASVM (www.casbase.org) to analyze Xkr8 sequences from six vertebrates and, thus, identify a conserved caspase-3–recognition site near the Xkr8 C terminus (fig. S1). We generated a mutant version of hXkr8 (2DA) in which the putative caspase-recognition sequence at position 355 was changed from PDQVDG to PAQVAG (P, Pro; D, Asp; Q, Gln; V, Val; G, Gly; A, Ala) (fig. S3). PLB-985 cells expressing wild-type (WT) hXkr8-GFP exposed PtdSer in response to staurosporine (Fig. 3A), accompanied by the loss of a 52-kD hXkr8-GFP band on polyacrylamide gels and the appearance of a 29-kD band detected with antibodies to GFP (anti-GFP) (Fig. 3B). After staurosporine treatment, hXkr8(2DA)-GFP failed to promote PtdSer exposure and was not proteolytically processed; ICAD was cleaved in cells expressing either the WT or 2DA mutant of hXkr8, indicating similar caspase-3 activity in both cell lines. Processing of mXkr8-GFP at the caspase-recognition site during apoptosis was also observed in WR-Fas cells after treatment with FasL (Fig. 3C). The solubilized membrane fraction from cells expressing hXkr8-GFP was then incubated with human caspases. Western blot analysis with anti-GFP showed that caspases-3 and -7 cleaved the WT but not 2DA mutant hXkr8 (Fig. 3D). Thus, mammalian Xkr8 is activated to expose PtdSer via caspase-mediated cleavage of its cytosolic C terminus.

Mouse *Xkr8* mRNA was detectable in most mouse tissues (fig. S10), with notably high expression in the testes. We established m*Xkr8*-conditional knockout mice (fig. S11), from which we prepared mouse embryonic fibroblasts (MEFs). After treatment with staurosporine, $Xkr8^{+/-}$ but not $Xkr8^{-/-}$ MEFs exposed PtdSer (Fig. 4A). Similarly, $Xkr8^{flox/flox}$ and $TMEM16F^{-/-}$ but not $Xkr8^{-/-}$ fetal thymocyte (IFET) cell lines exposed PtdSer in response to FasL (Fig. 4B), although caspase-3 was activated similarly in these cell lines (fig. S12). The transformation of $Xkr8^{-/-}$ IFETs with mXkr8 restored PtdSer exposure in response to FasL.

The protein CED-8 is the only *Caenorhabditis elegans* homolog of Xk proteins and was previously shown to control the timing of programmed cell deaths (*15*) (fig. S2). To determine if CED-8 (like Xkr8) promotes phagocytosis, we examined *ced-8* eggs for "floater" cells, which are generated in embryos defective in engulfment; floaters are a subset of apoptotic cells that, if not engulfed (e.g., in *ced-1*, *-2*, *-5*, *-6*, *-7*, *-10*, or *-12* mutants), detach from the embryo (Fig. 4C and fig. S13) (*16*, *17*). *ced-8* eggs contained floaters, and *ced-8* mutations synergistically enhanced the number of floaters in mutants partially defective in engulfment.

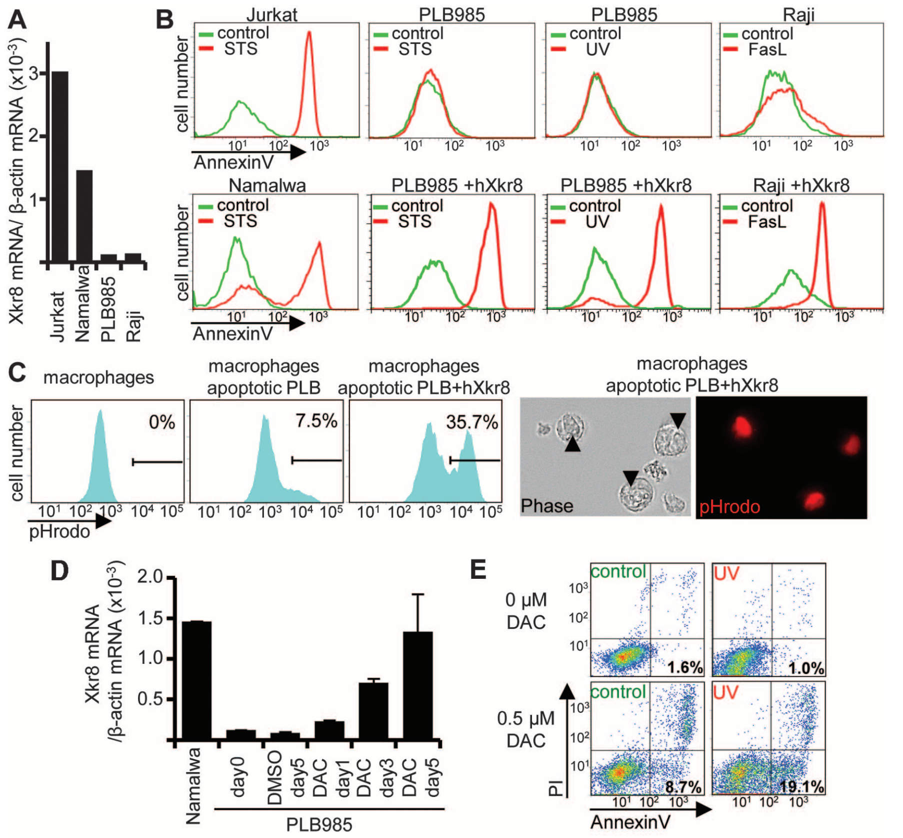

Fig. 2. Epigenetic repression of Xkr8 in human cancer cell lines. (**A**) Abundance of h*Xkr8* mRNA relative to β-*actin* mRNA was determined by real-time RT-PCR. (**B**) The indicated cell lines and hXkr8 transformants were treated with apoptotic stimuli and stained with Cy5–Annexin V. STS, staurosporine. (**C**) PLB-985 cells and hXkr8 transformants were treated with UV, labeled with pHrodo, and incubated with $CD11b^+$ peritoneal macrophages. (Left) FACS profiles for pHrodo-positive $CD11b^+$ cells are shown, as is the average percentage of $pHrodo^+$ cells from three experiments. (Right) Macrophages (arrowheads) engulfing apoptotic cell were observed by fluorescence microscopy. (**D**) PLB-985 cells were treated with DAC, and *Xkr8* mRNA was quantified relative to *GADPH* mRNA by real-time RT-PCR. DMSO, dimethyl sulfoxide. (**E**) PLB-985 cells were treated with DAC for 5 days, exposed to UV, and stained with Cy5–Annexin V and propidium iodide.

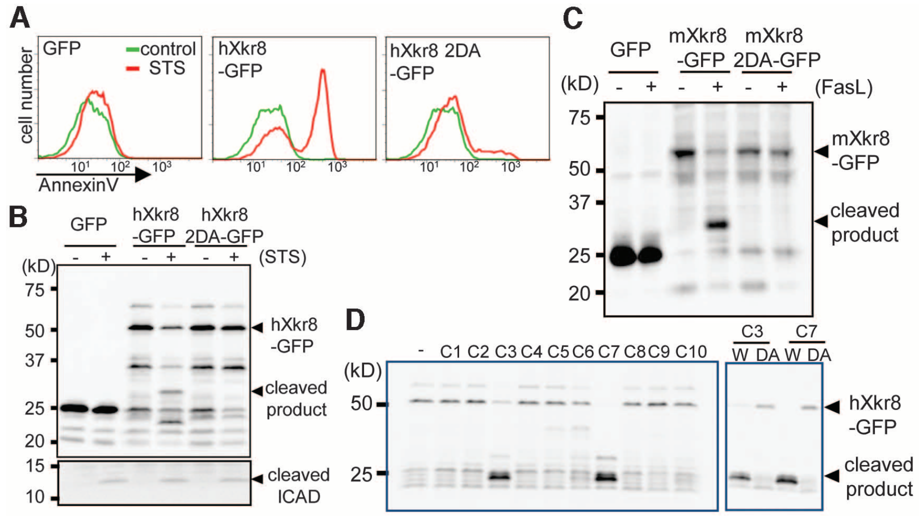

Fig. 3. Activation of Xkr8 by caspase cleavage. (**A** and **B**) PLB-985 and transformants expressing hXkr8-GFP or hXkr8 2DA-GFP were treated with STS and stained with Cy5–Annexin V (A). In (B), the cell lysates were analyzed by Western blotting with anti-GFP and anti-ICAD antibodies. (**C**) WR-Fas and transformants expressing GFP, mXkr8-GFP, or mXkr8 2DA-GFP were treated with FasL. Cell lysates were analyzed by Western blotting with anti-GFP. (**D**) The membrane fraction of PLB-985 cells expressing hXkr8-GFP (W) or the 2DA mutant (DA) was incubated with human caspases (C1 to C10, caspase-1 to caspase-10) and analyzed by Western blotting with anti-GFP antibody.

This enhancement was dependent on the caspase gene *ced-3* (fig. S14), which is required for apoptosis. The PtdSer-binding protein MFG-e8::Venus (*18*) associated with 94% of apoptotic cell corpses in the ventral cords of WT animals, but only with 21% of those in *ced-8* mutants (Fig. 4D). Similarly, PtdSer was exposed on newly detached floaters from *ced-1* but not *ced-8* or *ced-1*; *ced-8* embryos (fig. S15). Because 21% of *ced-8* ventral cord cell corpses had normal PtdSer exposure, additional factors probably contribute to this process.

In short, the Xk-related proteins Xkr8 and CED-8 promote caspase-dependent PtdSer exposure during apoptosis. Based on the following observations, Xkr8 and CED-8 probably act at a late step in PtdSer exposure, possibly in phospholipid scrambling: (i) *Xkr8*-deficient cells expose PtdSer in response to Ca^{2+}, indicating that Xkr8 is dispensable for steps before PtdSer exposure, including PtdSer biogenesis and localization; (ii) Xkr8 is directly activated by caspase cleavage, suggesting Xkr8 does not function before the onset of apoptosis; and (iii) Xkr8 and CED-8 are transmembrane proteins at the plasma membrane and, therefore, are positioned to effect, or interact with partners that effect, the externalization of PtdSer during apoptosis.

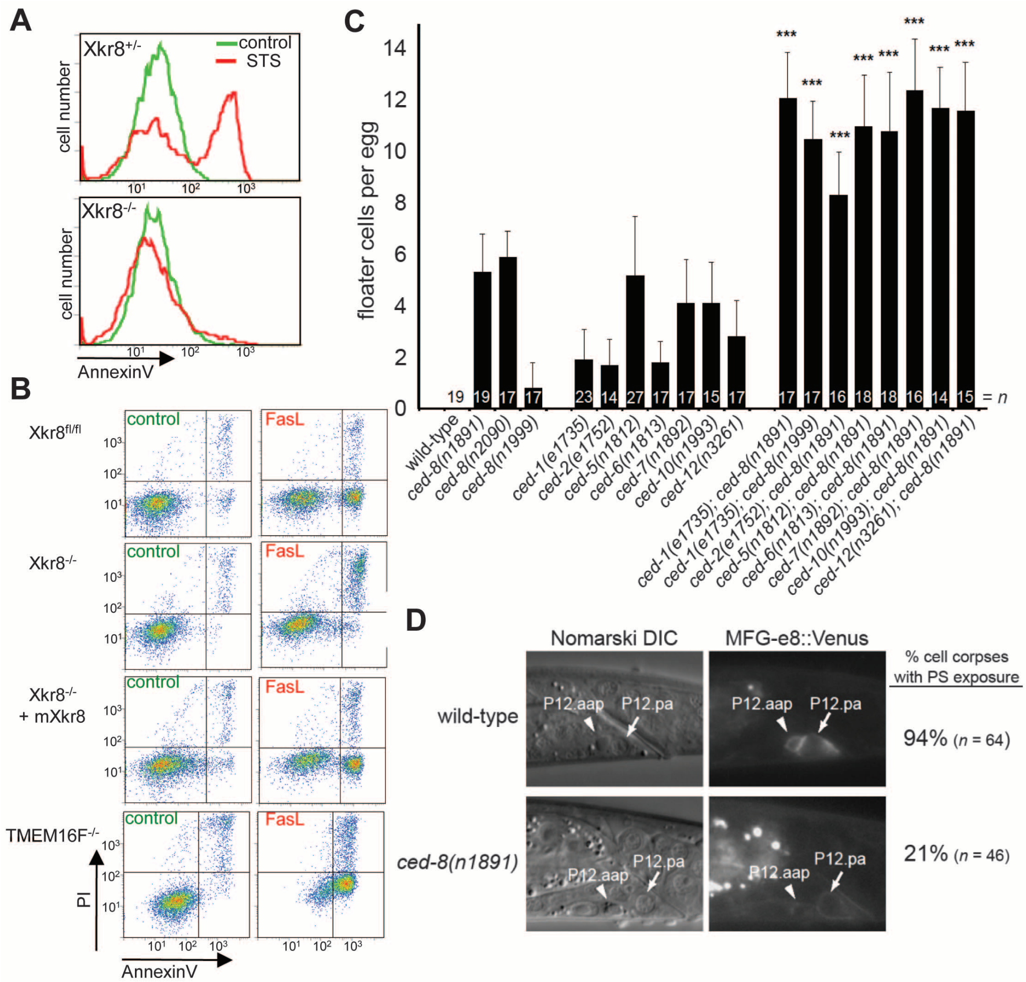

Fig. 4. Promotion of PtdSer exposure and cell-corpse engulfment by mouse Xkr8 and *C. elegans* CED-8. (**A**) MEFs from $Xkr8^{+/-}$ and $Xkr8^{-/-}$ embryos were treated with STS or control buffer for 8 hours and stained with Cy5–Annexin V. (**B**) IFETs of the indicated genotypes were treated with FasL and stained with Cy5–Annexin V and PI. (**C**) The number of floater cells per egg (n) was counted for each genotype. Error bars indicate SD. $^{***}P < 0.0001$ in a Student's *t* test for each pairwise comparison between *ced-x* and *ced-8*; *ced-x* double mutants. (**D**) PtdSer was detected using MFG-e8::Venus. Shown is the cell corpse of P12.aap (arrowhead), which undergoes apoptosis and is engulfed by P12.pa (arrow). The death of P12.aap is accompanied by PtdSer exposure in WT but not in *ced-8* (*n1891*) animals. In addition, P12.pa, like other *C. elegans* engulfing cells (*23*, *24*), exposes PtdSer on its outer plasma membrane during engulfment. DIC, differential interference contrast microscopy.

Although intracellular concentrations of Ca^{2+} increase during apoptosis (*19*, *20*), the involvement of Ca^{2+} in apoptotic PtdSer exposure is unclear (*4*), and our observations do not support a generalization. We found that FasL-induced PtdSer exposure was Ca^{2+}-dependent in WR19L cells, but not Ba/F3 cells, and that when WR19L cells were transformed with Xkr8, they lost the Ca^{2+} requirement for the apoptotic exposure of PtdSer. These results, together with the constitutive activity of overexpressed Xkr8 in Ba/F3 but not other cells, suggest that Xkr8 might cooperate with Ca^{2+}-regulated proteins in some cell-specific contexts.

The swift clearance of dead cells is essential for maintaining homeostasis, and the masking of PtdSer on apoptotic cells or the failure of the engulfment system can cause autoimmune disorders like systemic lupus erythematosus (*3*, *21*). Our finding that Xkr8 is epigenetically repressed in cancer cells suggests a mechanistic link among inflammation, autoimmunity, and cancer (*22*).

References and Notes

1. P. A. Leventis, S. Grinstein, *Annu. Rev. Biophys.* **39**, 407–427 (2010).
2. K. S. Ravichandran, U. Lorenz, *Nat. Rev. Immunol.* **7**, 964–974 (2007).
3. S. Nagata, R. Hanayama, K. Kawane, *Cell* **140**, 619–630 (2010).
4. E. M. Bevers, P. L. Williamson, *FEBS Lett.* **584**, 2724–2730 (2010).
5. J. Suzuki, M. Umeda, P. J. Sims, S. Nagata, *Nature* **468**, 834–838 (2010).
6. J. Suzuki *et al.*, *J. Biol. Chem.* **288**, 13305–13316 (2013).
7. G. Calenda *et al.*, *Gene* **370**, 6–16 (2006).
8. S. Nagata, *Cell* **88**, 355–365 (1997).
9. B. Fadeel *et al.*, *Biochem. Biophys. Res. Commun.* **266**, 504–511 (1999).
10. V. A. Fadok, A. de Cathelineau, D. L. Daleke, P. M. Henson, D. L. Bratton, *J. Biol. Chem.* **276**, 1071–1077 (2001).
11. R. Hanayama *et al.*, *Nature* **417**, 182–187 (2002).
12. J. G. Herman, J. R. Graff, S. Myöhänen, B. D. Nelkin S. B. Baylin, *Proc. Natl. Acad. Sci. U.S.A.* **93**, 9821–9826 (1996).
13. P. Williamson *et al.*, *Biochemistry* **40**, 8065–8072 (2001).
14. S. M. Schoenwaelder *et al.*, *Blood* **114**, 663–666 (2009).
15. G. M. Stanfield, H. R. Horvitz, *Mol. Cell* **5**, 423–433 (2000).
16. Y.-C. Wu, G. M. Stanfield, H. R. Horvitz, *Genes Dev.* **14**, 536–548 (2000).
17. D. P. Denning, V. Hatch, H. R. Horvitz, *Nature* **488**, 226–230 (2012).
18. V. Venegas, Z. Zhou, *Mol. Biol. Cell* **18**, 3180–3192 (2007).
19. D. L. Bratton *et al.*, *J. Biol. Chem.* **272**, 26159–26165 (1997).
20. M. B. Hampton, D. M. Vanags, M. I. Pörn-Ares, S. Orrenius, *FEBS Lett.* **399**, 277–282 (1996).
21. L. E. Muñoz, K. Lauber, M. Schiller, A. A. Manfredi, M. Herrmann, *Nat. Rev. Rheumatol.* **6**, 280–289 (2010).
22. A. L. Franks, J. E. Slansky, *Anticancer Res.* **32**, 1119–1136 (2012).
23. J. Mapes *et al.*, *Curr. Biol.* **22**, 1267–1275 (2012).
24. Y. Zhang, H. Wang, E. Kage-Nakadai, S. Mitani, X. Wang, *Curr. Biol.* **22**, 1276–1284 (2012).

Acknowledgments: We thank W. Hiraoka, M. Umeda, and M. Fujii for the PLB-985 cell line, the RO09-0198 peptide, and secretarial assistance, respectively. This work was supported in part by Grants-in-Aid for Specially Promoted Research from the Japan Society for the Promotion of Science (JSPS) to S.N., a Grant-in-Aid for Young Scientists (B) from JSPS to J.S., and postdoctoral fellowships from the Damon Runyon Cancer Research Foundation and the Charles A. King Trust to D.P.D. H.R.H. is the David H. Koch Professor of Biology at the Massachusetts Institute of Technology and is a Howard Hughes Medical Institute Investigator.

Supplementary Materials
www.sciencemag.org/cgi/content/full/science.1236758/DC1
Materials and Methods
Figs. S1 to S15
References (*25*–*44*)

19 February 2013; accepted 26 June 2013
Published online 11 July 2013;
10.1126/science.1236758

Reprogramming of Intestinal Glucose Metabolism and Glycemic Control in Rats After Gastric Bypass

Nima Saeidi,[1,2,3]* Luca Meoli,[1]* Eirini Nestoridi,[1]* Nitin K. Gupta,[1] Stephanie Kvas,[1] John Kucharczyk,[1] Ali A. Bonab,[2] Alan J. Fischman,[2] Martin L. Yarmush,[2,3] Nicholas Stylopoulos[1]†

The resolution of type 2 diabetes after Roux-en-Y gastric bypass (RYGB) attests to the important role of the gastrointestinal tract in glucose homeostasis. Previous studies in RYGB-treated rats have shown that the Roux limb displays hyperplasia and hypertrophy. Here, we report that the Roux limb of RYGB-treated rats exhibits reprogramming of intestinal glucose metabolism to meet its increased bioenergetic demands; glucose transporter-1 is up-regulated, basolateral glucose uptake is enhanced, aerobic glycolysis is augmented, and glucose is directed toward metabolic pathways that support tissue growth. We show that reprogramming of intestinal glucose metabolism is triggered by the exposure of the Roux limb to undigested nutrients. We demonstrate by positron emission tomography–computed tomography scanning and biodistribution analysis using 2-deoxy-2-[18F]fluoro-D-glucose that reprogramming of intestinal glucose metabolism renders the intestine a major tissue for glucose disposal, contributing to the improvement in glycemic control after RYGB.

Roux-en-Y gastric bypass (RYGB) induces substantial and sustained weight loss and is a highly effective treatment for severe obesity (*1*–*3*). The results of three recent prospective studies suggest that RYGB is the best treatment option for obesity-related diabetes (*4*–*6*). Interestingly, the improvement in glucose homeostasis occurs early after the RYGB procedure, before any appreciable weight loss, and patients are often able to discontinue their antidiabetic medications before hospital discharge (*4*, *5*, *7*, *8*). The precise mechanisms underlying the resolution of diabetes after RYGB have not been determined (*3*, *8*–*10*).

Several studies in rodents and one study in humans have previously described that the Roux limb displays morphological changes, characterized by hypertrophy and hyperplasia after RYGB (*11*–*16*). However, the importance of the morphological adaptation of the Roux limb, in itself, in the metabolic effects of RYGB remains largely unknown. Because the construction of the Roux limb is one of the fundamental components of the RYGB procedure (Fig. 1A) (*17*, *18*), we hypothesized that the beneficial effect of RYGB on glucose homeostasis may stem from changes in the metabolism within this reconfigured jejunal segment to meet the increased bioenergetic demands of tissue growth and maintenance, possibly in response to its exposure to undigested nutrients. To study the Roux limb, we performed RYGB in rats (*19*). RYGB led to substantial and sustained weight loss and improvement in glucose metabolism in diet-induced obese (DIO) rats, recapitulating the effects observed in humans (fig. S1, A to E). RYGB also improved glycemic control in two nonobese, diabetic rodent models with impaired insulin secretion: streptozotocin (STZ)–induced diabetic and Goto-Kakizaki (GK) rats (Fig. 1, B to D, and fig. S1, F to I). We also observed intestinal remodeling, characterized by increased intestinal mass due to hyperplasia and hypertrophy, in the Roux limb of RYGB-treated rats (figs. S2 to S4 and supplementary text 1).

To test our hypothesis, we initially sought to identify possible metabolic changes in the Roux limb of RYGB-treated rats. We compared its metabolic profile with the profile of corresponding segments of the jejunum of sham-operated rats, using a quantitative polar metabolomic profiling platform. The metabolomic profiling showed increased concentrations of glucose-6-phosphate, d-gluconate, 6-phospho-d-gluconate and nicotinamide adenine dinucleotide phosphate ($NADP^+$) in the Roux limb, suggesting that the oxidative phase of the pentose phosphate pathway (PPP) is stimulated (fig. S5, A and B, and table S1). The changes in the metabolites of the nonoxidative phase of the PPP did not reach statistical significance,

[1]Center for Basic and Translational Obesity Research, Division of Endocrinology, Boston Children's Hospital, Harvard Medical School, Boston, MA 02115, USA. [2]Shriners Hospital for Children, Boston, MA 02114, USA. [3]Center for Engineering in Medicine, Massachusetts General Hospital, Harvard Medical School, Boston, MA 02114, USA.

*These authors contributed equally to this work.
†Corresponding author. E-mail: Nicholas.Stylopoulos@childrens.harvard.edu

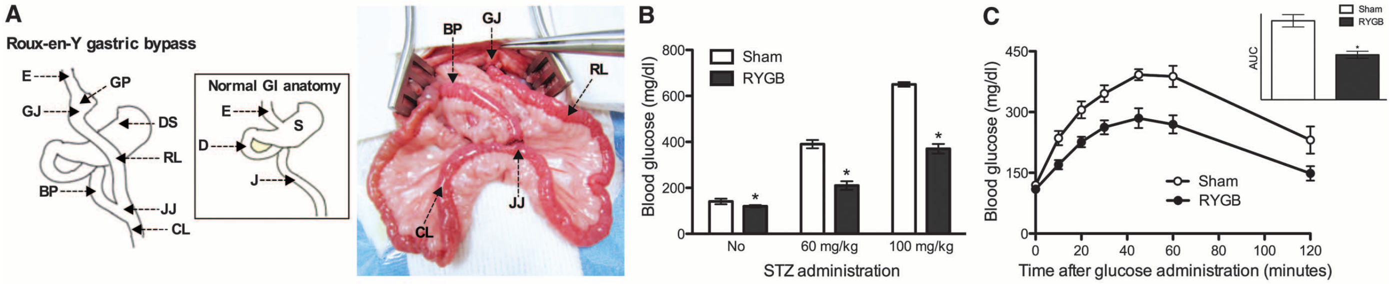

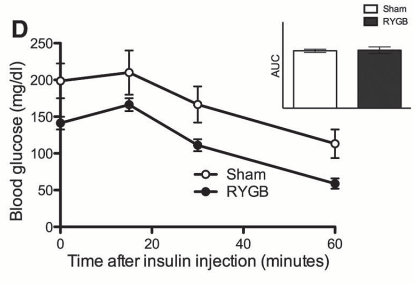

Fig. 1. RYGB improves glycemic control. (**A**) Schematic drawing of RYGB (left). Intraoperative picture of RYGB in rats (right). RYGB in rats closely resembles the procedure performed in humans. The stomach (S) is divided, and a small gastric pouch is created (GP). The jejunum (J) is transected, and the distal part is brought up and connected through a gastro-jejunostomy (GJ) to the GP [this jejunal loop is called the Roux limb (RL)]. The continuation of the gastrointestinal (GI) tract is reestablished by reconnecting at the jejuno-jejunostomy (JJ), the proximal part of the jejunum further down to the RL [this is called the biliopancreatic limb (BP) because it drains the gastric, hepatic, and pancreatic secretions]. The part of the small intestine distal to the JJ is called the common limb (CL). RYGB reconfigures the GI tract and alters the flow of nutrients; nutrients flow from the esophagus (E) to the GP and then to the RL directly, bypassing the distal stomach (DS), the duodenum (D), and part of the proximal jejunum. Thus, the RL is exposed to undigested nutrients; the BP is exposed to the gastric, hepatic, and pancreatic secretions but no nutrients; and the CL is exposed to a mixture of nutrients with the gastric, hepatic, and pancreatic secretions. (**B**) Blood glucose levels were lower in RYGB-treated rats in comparison with sham-operated rats, 7 days after diabetes was induced by the administration of STZ. (**C**) RYGB-treated GK rats exhibited better glucose excursion curves after oral glucose administration. The inset shows the area under the curve (AUC) of the oral glucose tolerance test. (**D**) There was no difference in the insulin tolerance test between RYGB-treated and sham-operated GK rats. The inset shows the AUC of the insulin tolerance test. [(B) to (D)] N = 5 to 7 rats, 2 months postoperatively; mean ± SEM; *P < 0.05; unpaired t test.

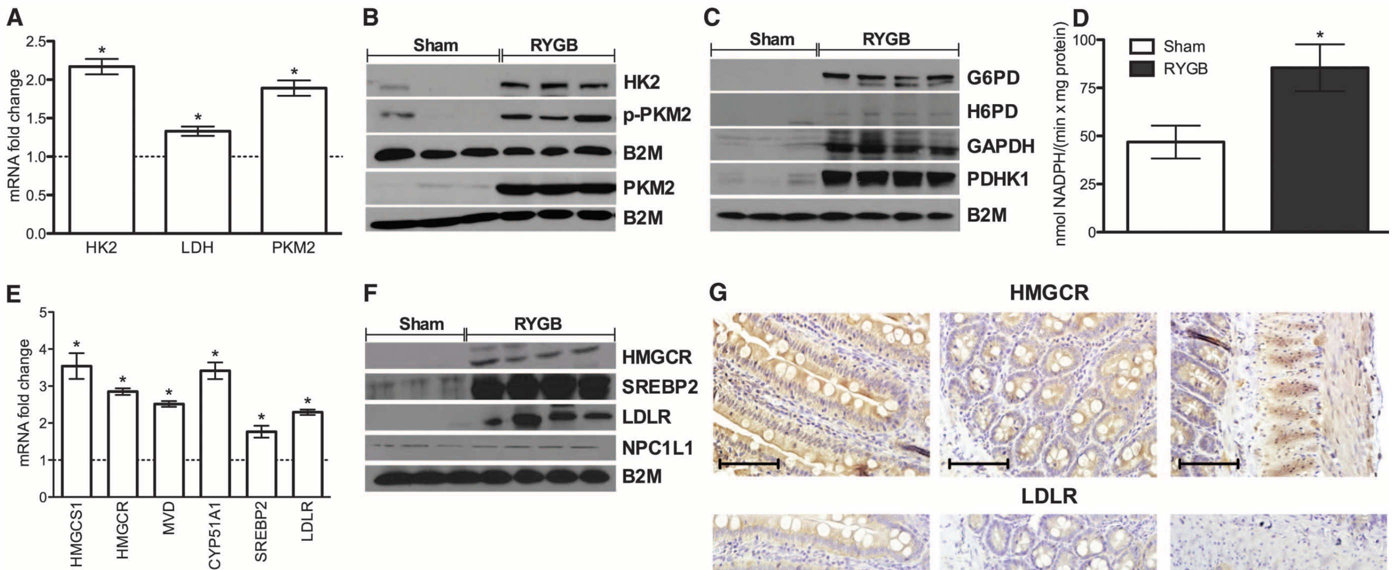

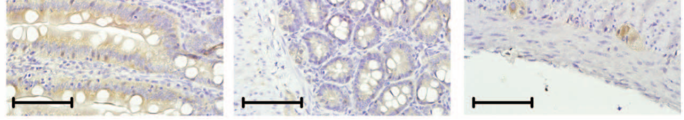

Fig. 2. RYGB increases the gene and protein expression levels of key factors and enzymes involved in glucose and cholesterol metabolism in the Roux limb. (**A** to **C**) RNA and protein levels of glycolytic enzymes and G6PD were increased in the Roux limb of RYGB-treated rats. B2M, β2 microglobulin. (**D**) The enzymatic activity of G6PD was increased in the Roux limb of RYGB-treated rats. (**E** and **F**) RNA and protein levels of factors and enzymes involved in cholesterol biosynthesis and uptake were increased in the Roux limb of RYGB-treated rats. HMGCS1, 3-hydroxy-3-methylglutaryl-CoA synthase 1; HMGCR, 3-hydroxy-3-methylglutaryl-CoA reductase; MVD, mevalonate (diphospho) decarboxylase; CYP51A1, cytochrome P450, family 51, subfamily A, polypeptide 1 (lanosterol 14-α demethylase); SREBP2, sterol regulatory element binding protein 2; LDLR, low-density lipoprotein receptor. There was no difference in the protein levels of Niemann-Pick C1-like 1 (NPC1L1). (**G**) Representative images of Roux limb sections of RYGB-treated rats stained with antibodies against HMGCR and LDLR (scale bar, 100 μm). Left to right: villi, crypts, and muscular layer. HMGCR expression was increased in the villi, the crypt cells, and the muscular layer while LDLR expression was increased in the villi and in the ganglia of the muscular layer. [(A) to (G)] N = 7 to 9 rats; [(A) to (F)] 2 months postoperatively; the results were reproduced at 1 and 6 months postoperatively; (G) 2 months postoperatively; mean ± SEM; *P < 0.05; [(A) and (E)] one sample t test; (D) unpaired t test.

but there was an increase in the intermediates of the pyrimidine and purine biosynthetic pathways. Lactate was increased, whereas there was a decrease or no change in the intermediates of the tricarboxylic acid (TCA) cycle. The serine and the hexosamine biosynthetic pathways, two metabolic pathways that branch off from glycolysis, were also augmented. The glutamine/glutamate pathway was enriched, and the metabolism of several other amino acids appeared to be enhanced. This metabolic profile of the Roux limb indicates that glycolysis may be up-regulated in favor of accumulation of glycolytic intermediates that are shunted to metabolic pathways that support cellular growth and proliferation (fig. S5, A and B, and table S1).

We next examined gene and protein expression patterns of enzymes involved in glucose metabolism. In comparison with corresponding segments of the jejunum of sham-operated rats, the Roux limb of RYGB-treated rats showed increased RNA and protein levels of hexokinase 2 (HK2), glyceraldehyde 3-phosphate dehydrogenase (GAPDH), and lactate dehydrogenase (LDH), which are key glycolytic enzymes (Fig. 2, A to C, and fig. S5C). M2 isoform expression of pyruvate kinase (PKM2) and phosphorylated PKM2 were also up-regulated in the Roux limb, further suggesting an increase in aerobic glycolysis to generate upstream glycolytic intermediates that are diverted into anabolic pathways (Fig. 2, A and B) (*20*, *21*). The decreased glucose flux through the TCA cycle is also supported by the higher expression levels of pyruvate dehydrogenase kinase 1 (PDHK1), which phosphorylates and inactivates pyruvate dehydrogenase (PDH) (Fig. 2C). There was also an increase in the protein levels of both G and H forms and the enzymatic activity of glucose-6-phosphate dehydrogenase (G6PD), the rate-limiting enzyme of the PPP (Fig. 2, C and D). RNA levels of key enzymes of gluconeogenesis were suppressed or unchanged in the Roux limb of RYGB-treated rats (fig. S5D).

We also detected augmented RNA and protein levels of factors and enzymes involved in the biosynthesis of cholesterol in the Roux limb of RYGB-treated rats (Fig. 2, E to G, and

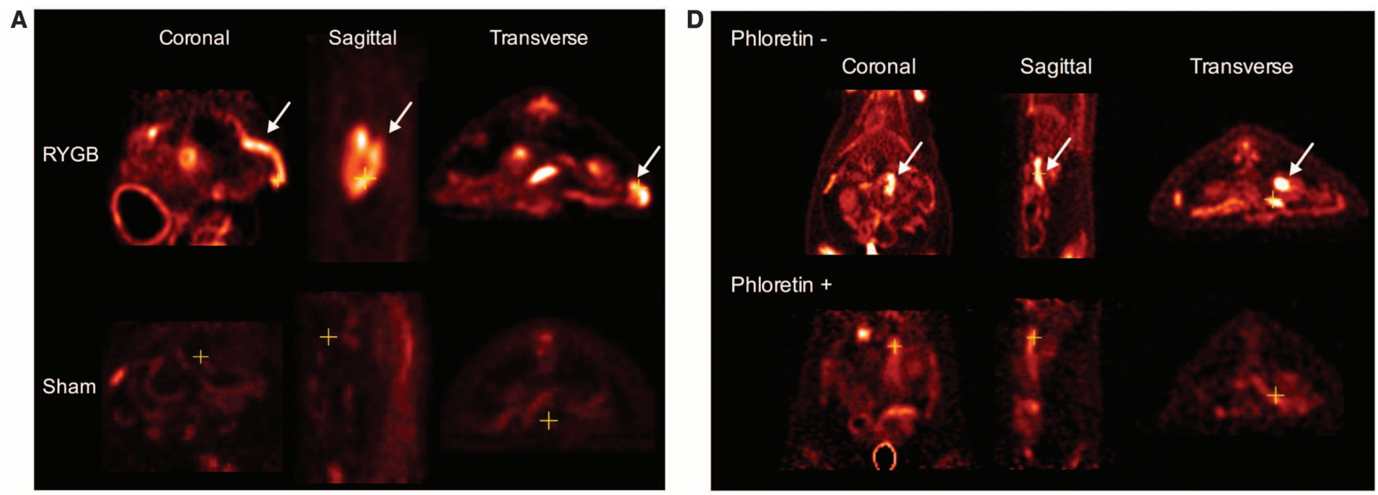

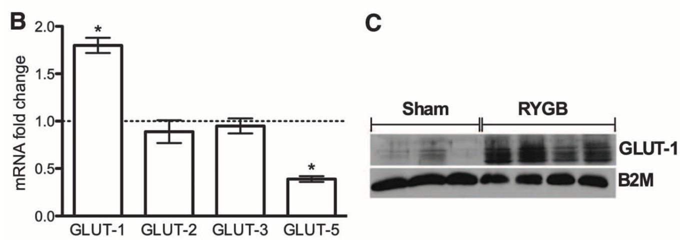

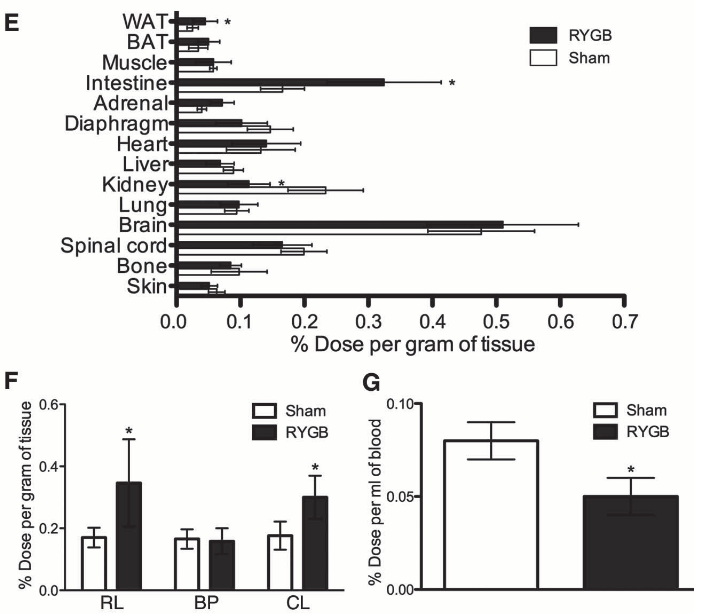

Fig. 3. RYGB enhances intestinal GLUT-1–mediated basolateral glucose uptake and utilization, which contributes to the improved whole-body glucose disposal. (**A**) Representative images of whole-body [18F]FDG PET/CT scanning in RYGB-treated and sham-operated rats. [18F]FDG uptake is color-coded, and areas of increased signal exhibit red-orange color. There was intense [18F]FDG uptake by the Roux limb (marked with an arrow) of RYGB-treated rats in comparison with the corresponding jejunum of sham-operated rats. The cross indicates the exact same point of the intestine in all images. (**B** and **C**) GLUT-1 RNA and protein levels were increased in the Roux limb of RYGB-treated rats. (**D**) Representative images of whole-body [18F]FDG PET/CT scanning in RYGB-treated rats, with or without the administration of phloretin, a GLUT-1 inhibitor. Phloretin substantially blunted [18F]FDG uptake by the Roux limb (marked with an arrow). The cross indicates the exact same point of the intestine in all images. (**E** and **F**) [18F]FDG biodistribution analysis in RYGB-treated and sham-operated rats demonstrated higher [18F]FDG uptake by the intestine of RYGB-treated rats. WAT, white adipose tissue; BAT, brown adipose tissue. The RL of RYGB-treated rats displayed the highest [18F]FDG uptake. The uptake by the CL of RYGB-treated rats was also increased. There was no difference in the [18F]FDG uptake between the BP of RYGB-treated rats and the corresponding intestinal segment of sham-operated rats. The [18F]FDG uptake was constant along the intestine of sham-operated rats. (**G**) Consistent with improved whole-body glucose disposal, RYGB-treated rats exhibited lower [18F]FDG signal in the blood. [(A) to (G)] $N = 7$ to 9 rats; [(A) to (C)] and [(E) to (G)] 2 months postoperatively; the results were reproduced at 1 and 6 months postoperatively; (D) 6 months postoperatively; mean ± SEM; $^*P < 0.05$; (B) one sample t test; [(E) to (G)] unpaired t test.

fig. S6A). Cholesterol is essential for cellular growth and proliferation. The up-regulation of intestinal cholesterol biosynthesis may further explain the enhanced utilization of glucose by the Roux limb through the PPP, because the PPP provides a reduced form of $NADP^+$ (NADPH), which is involved as a donor of reducing equivalents in cholesterol biosynthesis. The expression of low-density lipoprotein receptor (LDLR) was also higher in the Roux limb, suggesting that cholesterol uptake may also be augmented (Fig. 2, E to G, and fig. S6B). The hepatic cholesterol biosynthetic pathway was not changed (fig. S6C). Serum and hepatic lipid profiles were improved after RYGB (fig. S6, D to I).

Taken together, our results support our hypothesis that the Roux limb of RYGB-treated rats exhibits reprogramming of intestinal glucose metabolism to meet the increased anabolic demands of intestinal tissue growth and maintenance. We also found that the PI3K/AKT/mTOR signaling pathway was activated in the Roux limb of RYGB-treated rats, which also indicates that there is augmented anabolic activity and increased glucose utilization (fig. S7) (*21*). To confirm that RYGB induces enhanced intestinal glucose uptake and utilization, we performed positron emission tomography–computed tomography (PET/CT) scanning using 2-deoxy-2-[18F]fluoro-D-glucose ([18F]FDG). These experiments were done with RYGB-treated and sham-operated DIO, STZ-induced diabetic, and GK rats. [18F]FDG is taken up at a rate proportional to the rate of glucose utilization within a given tissue. There was intense [18F]FDG uptake by the Roux limb of all groups of RYGB-treated rats in comparison with the jejunum of sham-operated rats (Fig. 3A and movie S1). To further characterize the reprogramming of intestinal glucose metabolism in the Roux limb, we focused our study on basolateral glucose transporters, since in PET/CT scanning, [18F]FDG is administered intravenously and enters the intestinal cells through their basolateral and not their luminal side. The Roux limb of RYGB-treated rats displayed an increase in RNA and protein levels of glucose transporter-1 (GLUT-1) but no significant change in GLUT-2 and GLUT-3 levels (Fig. 3, B and C, and fig. S8, A to C). GLUT-1 is normally abundantly present in fetal intestine but progressively disappears until it is barely detected in adult intestine (*22*). It is considered to play a role in early intestinal tissue growth in the fetus (*23*). PET/CT scanning with or without the administration of phloretin, a GLUT-1 inhibitor, showed that phloretin substantially blunted [18F]FDG uptake by the Roux limb (Fig. 3D and fig. S8D). These results suggest that increased intestinal glucose uptake is primarily mediated through GLUT-1 after RYGB.

To quantify the relative contribution of the intestine to whole-body glucose disposal, we performed biodistribution analysis using [18F]FDG in RYGB-treated and sham-operated rats. The intestine exhibited the highest rate of glucose uptake and became a major tissue for glucose disposal after RYGB (Fig. 3E). Specifically, glucose disposal per gram of tissue doubled in the intestine of RYGB-treated rats, with the glucose uptake by the Roux limb and common limb being higher in comparison with the glucose uptake by the jejunum of sham-operated rats (Fig. 3, E and F). We observed interanimal variability in the intestinal glucose uptake of RYGB-treated rats, and this variability correlated with the degree of intestinal remodeling (fig. S9A). Importantly, there was a positive correlation between the improvement in glycemic control after RYGB and the intestinal glucose uptake (fig. S9, B and C). Consistent with improved whole-body glucose disposal, the [18F]FDG blood signal was lower in RYGB-treated rats, because they displayed a higher rate of [18F]FDG disposal from the blood into the tissues in comparison with sham-operated rats (Fig. 3G). These data demonstrate that reprogramming of intestinal glucose metabolism, marked by enhanced intestinal GLUT-1–mediated basolateral glucose uptake and utilization, contributes to the improvement in glycemic control after RYGB, independently of weight loss, improved insulin secretion, or improved insulin sensitivity (supplementary text 2).

RYGB alters the flow of nutrients and reroutes undigested nutrients to the Roux limb (Fig. 1A). We wanted to investigate whether intestinal remodeling and reprogramming of intestinal glucose metabolism are triggered by the exposure of the Roux limb to undigested nutrients. To this end, we developed a rat model in which a loop of jejunum is transected and transposed between the esophagus and the stomach without performing any other anatomic alterations of the RYGB procedure [esophago-stomach jejunal loop interposition (ES-JLI) model] (Fig. 4A and movie S2). This transposed jejunal loop resembles the Roux limb of RYGB as it is exposed to undigested nutrients. ES-JLI–treated DIO and GK rats exhibited improved glycemic control, similar to RYGB-treated rats (fig. S10). We observed the same morphological adaptation between the transposed jejunal loop of ES-JLI–treated rats and the Roux limb of RYGB-treated rats. GLUT-1 and HK2 RNA and protein levels were increased in the transposed jejunal loop of ES-JLI–treated rats, and [18F]FDG PET/CT scanning also showed intense [18F]FDG uptake by the transposed jejunal loop (Fig. 4, B and C). These data are consistent with our hypothesis that intestinal remodeling and reprogramming of intestinal glucose metabolism are triggered by the exposure of the Roux limb to undigested nutrients. To further support this hypothesis, we compared gene expression levels of key factors and

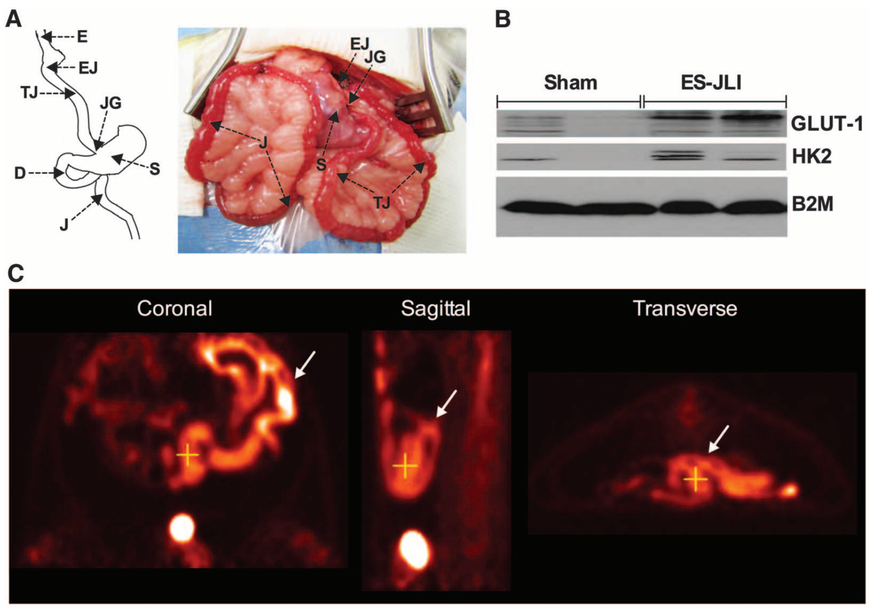

Fig. 4. Reprogramming of intestinal glucose metabolism is triggered by the exposure of the Roux limb to undigested nutrients. (**A**) Schematic drawing (left) and intraoperative picture (right) of the ES-JLI rat model. A loop of jejunum is transected and transposed between the esophagus and the stomach without performing any other anatomic alterations of the RYGB procedure; that is, the stomach is not divided, the duodenum is not excluded, and the continuity of the gastrointestinal tract remains intact. Nutrients flow from the esophagus (E) through the esophago-jejunostomy (EJ) to the transposed jejunal loop (TJ) and then through the jejuno-gastrostomy (JG) to the stomach (S), the duodenum (D), the jejunum (J), and the rest of the gastrointestinal tract. (**B**) GLUT-1 and HK2 protein levels were increased in the transposed jejunal loop of ES-JLI–treated rats. (**C**) Representative images of whole-body [18F]FDG PET/CT scanning in ES-JLI–treated rats. [18F]FDG uptake is color-coded, and areas of increased signal exhibit red-orange color. There was intense [18F]FDG uptake by the transposed jejunal loop (marked with an arrow) of ES-JLI–treated rats. The cross indicates the exact same point of the intestine in all images. [(B) and (C)] *N* = 5 to 7 rats, 1 month postoperatively; the results were reproduced at 6 months postoperatively.

enzymes involved in glucose and cholesterol metabolism between the various intestinal segments of RYGB-treated rats and corresponding segments of the intestine of sham-operated rats. A gradient in the change in RNA levels of key factors and enzymes involved in glucose uptake and utilization and in cholesterol biosynthesis and uptake was observed along the altered nutrient flow path in the intestine of RYGB-treated rats (figs. S11 and S12). The highest increase was detected in the Roux limb, which is exposed to undigested nutrients, but no change was found in the biliopancreatic limb, which is exposed to the gastric, hepatic, and pancreatic secretions but no nutrients, or in the distal common limb, which is exposed to fully digested nutrients.

The effectiveness of RYGB in the resolution of type 2 diabetes attests to the important role of the gastrointestinal tract in glycemic control. Most studies have attributed the improved glucose metabolism to a number of advantageous changes in the levels of gastrointestinal hormones that control glucose homeostasis and occur after RYGB, with enhanced postprandial glucagon-like peptide-1 (GLP-1) secretion being cited as the most important (*3*, *8*, *24*). However, the primary role of GLP-1 as a mediator of the beneficial effect of RYGB on glycemic control is debated (*25*, *26*). It has also been reported that release of glucose, via intestinal gluconeogenesis, into the portal vein of mice that underwent enterogastric anastomosis (EGA), resulted in improved insulin sensitivity of hepatic glucose production; thus, it has been hypothesized that intestinal gluconeogenesis could account for the improvement in glucose homeostasis after RYGB (*27*). It should be noted that EGA is not similar to RYGB, because the Roux-en-Y configuration is not constructed and no intestinal segment is representative of the Roux limb. Also, two recent reports in obese diabetic animals and in humans with type 2 diabetes and our study did not find evidence for induction of intestinal gluconeogenesis after RYGB (*28*, *29*). A decrease in intestinal glucose absorptive capacity due to the exclusion of the duodenum after RYGB has also been proposed as a mechanism underlying the improvement in glycemic control (*11*), but other studies have found that RYGB does not suppress glucose absorption from the intestinal lumen (*10*, *30–32*).

Our study shows that changes in the metabolism of the Roux limb itself may play a direct role in the improvement in glucose homeostasis after RYGB. We report that the Roux limb exhibits reprogramming of intestinal glucose metabolism to meet the increased bioenergetic demands of intestinal remodeling. We show that intestinal remodeling and reprogramming of intestinal glucose metabolism are triggered by the exposure of the Roux limb to undigested nutrients. We demonstrate that reprogramming of intestinal glucose metabolism renders the intestine a major organ for glucose disposal, contributing to the improvement in glycemic control after RYGB. Enhancing intestinal glucose uptake and utilization could offer an opportunity to regulate whole-body glucose disposal and improve glycemic control in type 2 diabetes. Exploitation of the changes that occur in intestinal metabolism after RYGB could represent an approach to bypass the bypass, that is, to replace the gastric bypass by equally effective, but less invasive, treatments for obesity-related diabetes.

References and Notes

1. H. Buchwald *et al.*, *JAMA* **292**, 1724–1737 (2004).
2. L. Sjöström *et al.* Swedish Obese Subjects Study Scientific Group, *N. Engl. J. Med.* **351**, 2683–2693 (2004).
3. M. A. Stefater, H. E. Wilson-Pérez, A. P. Chambers, D. A. Sandoval, R. J. Seeley, *Endocr. Rev.* **33**, 595–622 (2012).
4. G. Mingrone *et al.*, *N. Engl. J. Med.* **366**, 1577–1585 (2012).
5. P. R. Schauer *et al.*, *N. Engl. J. Med.* **366**, 1567–1576 (2012).
6. L. M. Carlsson *et al.*, *N. Engl. J. Med.* **367**, 695–704 (2012).
7. W. J. Pories *et al.*, *Ann. Surg.* **222**, 339–352 (1995).
8. B. Laferrère, *Endocrine* **40**, 162–167 (2011).
9. D. E. Cummings, *Nat. Med.* **18**, 656–658 (2012).
10. D. Bradley *et al.*, *J. Clin. Invest.* **122**, 4667–4674 (2012).
11. A. T. Stearns, A. Balakrishnan, A. Tavakkolizadeh, *Am. J. Physiol. Gastrointest. Liver Physiol.* **297**, G950–G957 (2009).
12. M. B. Mumphrey, L. M. Patterson, H. Zheng, H. R. Berthoud, *Neurogastroenterol. Motil.* **25**, e70–e79 (2013).
13. E. Spak *et al.*, *Histopathology* **57**, 680–688 (2010).
14. E. Taqi *et al.*, *J. Pediatr. Surg.* **45**, 987–995 (2010).
15. C. W. le Roux *et al.*, *Ann. Surg.* **252**, 50–56 (2010).
16. M. Bueter *et al.*, *Gastroenterology* **138**, 1845–1853, 1853.e1 (2010).
17. J. Kucharczyk, E. Nestoridi, S. Kvas, R. Andrews, N. Stylopoulos, *J. Surg. Res.* **179**, e91–e98 (2013).
18. E. Nestoridi, S. Kvas, J. Kucharczyk, N. Stylopoulos, *Endocrinology* **153**, 2234–2244 (2012).
19. Materials and methods are available as supplementary materials on *Science* Online.
20. S. Y. Lunt, M. G. Vander Heiden, *Annu. Rev. Cell Dev. Biol.* **27**, 441–464 (2011).
21. M. G. Vander Heiden, L. C. Cantley, C. B. Thompson, *Science* **324**, 1029–1033 (2009).
22. B. Thorens, *Am. J. Physiol.* **270**, G541–G553 (1996).
23. J. Pácha, *Physiol. Rev.* **80**, 1633–1667 (2000).
24. Y. Falkén, P. M. Hellström, J. J. Holst, E. Näslund, *J. Clin. Endocrinol. Metab.* **96**, 2227–2235 (2011).
25. J. M. Isbell *et al.*, *Diabetes Care* **33**, 1438–1442 (2010).
26. H. E. Wilson-Pérez *et al.*, *Diabetes* **62**, 2380–2385 (2013).
27. S. Troy *et al.*, *Cell Metab.* **8**, 201–211 (2008).
28. B. S. Wolff, K. Meirelles, Q. Meng, M. Pan, R. N. Cooney, *Am. J. Physiol. Gastrointest. Liver Physiol.* **297**, G594–G601 (2009).
29. M. T. Hayes, J. Foo, V. Besic, Y. Tychinskaya, R. S. Stubbs, *Obes. Surg.* **21**, 759–762 (2011).
30. F. Rubino *et al.*, *Ann. Surg.* **244**, 741–749 (2006).
31. F. Rodieux, V. Giusti, D. A. D'Alessio, M. Suter, L. Tappy, *Obesity (Silver Spring)* **16**, 298–305 (2008).
32. G. Wang *et al.*, *Obes. Surg.* **22**, 1263–1267 (2012).

Acknowledgments: We thank N. Li for help with tissue sectioning, G. Gorski for help with electron microscopy, M. Markle and M. Luitje for help with biodistribution analysis, and A. Moses for help with lipid analysis. This research was supported by funds from the Department of Medicine and the Clinical and Translational Executive Committee at Boston Children's Hospital (N. Stylopoulos) and grants T32DK007191 (N.K.G.) and F32DK095558 (N. Saeidi) from the National Institutes of Health (NIH). We used the core services of the Lipidomics Lab at the Nutrition Obesity Research Center of the University of Michigan (Ann Arbor, MI), which is supported by grant DK089503 from NIH.

Supplementary Materials
www.sciencemag.org/cgi/content/full/341/6144/406/DC1
Materials and Methods
Supplementary Text 1 and 2
Figs. S1 to S12
Table S1
Movies S1 and S2
References (*33–37*)

14 January 2013; accepted 13 June 2013
10.1126/science.1235103

H7N9 Influenza Viruses Are Transmissible in Ferrets by Respiratory Droplet

Qianyi Zhang,[1,2]* Jianzhong Shi,[1]* Guohua Deng,[1]* Jing Guo,[1]* Xianying Zeng,[1]* Xijun He,[1] Huihui Kong,[1] Chunyang Gu,[1,2] Xuyong Li,[1] Jinxiong Liu,[1] Guojun Wang,[1,2] Yan Chen,[1] Liling Liu,[1] Libin Liang,[1] Yuanyuan Li,[1] Jun Fan,[1] Jinliang Wang,[1] Wenhui Li,[1] Lizheng Guan,[1] Qimeng Li,[1,2] Huanliang Yang,[1] Pucheng Chen,[1] Li Jiang,[1] Yuntao Guan,[1] Xiaoguang Xin,[1] Yongping Jiang,[1] Guobin Tian,[1] Xiurong Wang,[1] Chuanling Qiao,[1] Chengjun Li,[1] Zhigao Bu,[1] Hualan Chen[1,2]†

A newly emerged H7N9 virus has caused 132 human infections with 37 deaths in China since 18 February 2013. Control measures in H7N9 virus–positive live poultry markets have reduced the number of infections; however, the character of the virus, including its pandemic potential, remains largely unknown. We systematically analyzed H7N9 viruses isolated from birds and humans. The viruses were genetically closely related and bound to human airway receptors; some also maintained the ability to bind to avian airway receptors. The viruses isolated from birds were nonpathogenic in chickens, ducks, and mice; however, the viruses isolated from humans caused up to 30% body weight loss in mice. Most importantly, one virus isolated from humans was highly transmissible in ferrets by respiratory droplet. Our findings indicate nothing to reduce the concern that these viruses can transmit between humans.

The influenza A virus genome comprises eight genes: *basic polymerase 2* (*PB2*), *basic polymerase 1* (*PB1*), *acidic polymerase* (*PA*), *hemagglutinin* (*HA*), *nucleoprotein* (*NP*), *neuraminidase* (*NA*), *matrix* (*M*), and *nonstructural protein* (*NS*). On the basis of differences in the antigenicity of the two surface glycoproteins, HA and NA, influenza A viruses are categorized into

different subtypes. Currently, 17 HA subtypes and 10 NA subtypes have been identified. All subtypes were identified initially from avian species, except for the H17N10 subtype, which was found in bats (*1*).

Animal influenza viruses continue to present a challenge to human health. On 31 March 2013, the National Health and Family Planning Commission of China announced that human infections with a previously undescribed influenza A (H7N9) virus had occurred in Shanghai and Anhui province, China. Additional infections were subsequently reported in seven other provinces. As of 30 May, 132 human infections have been identified, 37 of which were fatal (*2*). Because the H7N9 virus has not previously been detected in humans or other animals, the situation raises many urgent questions and global public health concerns. We performed active surveillance in animals to identify the source of human infection and evaluated the virulence and transmission potential of H7N9 viruses isolated from birds and humans in poultry and mammalian models.

[1]State Key Laboratory of Veterinary Biotechnology, Harbin Veterinary Research Institute, Chinese Academy of Agricultural Sciences, Harbin 150001, People's Republic of China. [2]College of Veterinary Medicine, Gansu Agricultural University, Lanzhou 730030, People's Republic of China.

*These authors contributed equally to this work.
†Corresponding author. E-mail: chenhualan@caas.cn

To investigate the possible origins of the H7N9 viruses that caused these human infections, we collected 10,703 samples from poultry markets, poultry farms, wild bird habitats, and poultry and swine slaughterhouses in Shanghai and in Anhui, Zhejiang, Jiangsu, Shandong, Hubei, Henan, Jiangxi, Guangdong, Fujian, and Hunan provinces from 30 March to 2 May 2013 (*3*). All samples were inoculated individually into 10-day-old embryonated chicken eggs for virus isolation; 136 Newcastle disease viruses and 238 influenza viruses were isolated from these samples, of which 52 viruses were confirmed as the H7N9 subtype (table S1). Except for one virus isolated from a homing pigeon farm and one virus isolated from a wild pigeon, all of the H7N9 viruses were isolated from samples collected from live poultry markets (*4*) (table S1).

To understand the genetic relationship of these viruses, we fully sequenced the genome of 37 representative H7N9 viruses that came from different bird species, markets, and locations in the markets for the environmental samples (table S1) and compared the sequences with those of the five human isolates that have been reported (*5*, *6*). The genome similarities of the 37 avian viruses and four human viruses were compared with the human isolate A/Anhui/1/2013 (AH/1) as shown in table S2. The *HA* genes and *NA* genes of these 41 H7N9 viruses shared 99.29 to 100% homology and 99.36 to 99.93% homology, respectively, with those of the AH/1 virus at the nucleotide level and were closely clustered in the phylogenetic tree (table S2 and fig. S1, A and B). The *PB2*, *PB1*, *PA*, *NP*, *M*, and *NS* genes of the 41 viruses shared 96.67 to 99.96%, 96.79 to 99.96%, 97.95 to 99.95%, 97.66 to 100%, 97.66 to 100%, and 97.61 to 100% homology, respectively, at the nucleotide level, with those of AH/1 virus, indicating that the internal genes of the H7N9 viruses are more diverse than their *HA* and *NA* genes and that the viruses are still subject to frequent reassortment and rapid evolution. Of note, in the phylogenetic trees, the six internal genes of the H7N9 viruses were mixed with those of the H9N2 viruses that were previously found in chickens in Shanghai, Zhejing, Jiangsu, Anhui, and Shandong provinces and in a brambling in Beijing (fig. S1, C to H).

Two amino acids in PB2, lysine at position 627 (627K) (*7*) and 701N, are important for influenza virulence and transmission in mammals (*8*–*11*). A detailed comparison of the amino acid differences among the H7N9 viruses indicated that all of the viruses isolated from birds or the environment had the amino acid combination 627E/701D in their PB2; however, all of the

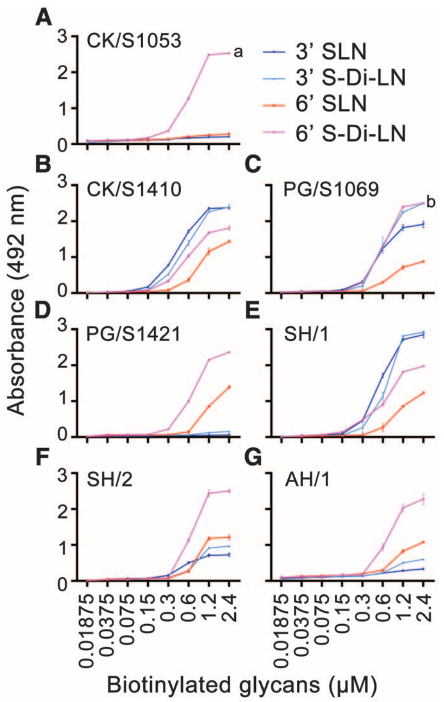

Fig. 1. Characterization of the receptor-binding properties of H7N9 viruses. The binding of the viruses to four different biotinylated glycans (two α-2,3 glycans, blue and Cambridge blue; two α-2,6 glycans, red and pink) was tested. (**A**) CK/S1053; (**B**) CK/S1410; (**C**) PG/S1069; (**D**) PG/S1421; (**E**) SH/1; (**F**) SH/2; (**G**) AH/1. Data shown are the mean of three repeats; the error bars indicate the standard deviations. Significant differences were detected between the affinity of each two of the four glycans with two exceptions: (i) no significant difference was detected between the affinities to 3'SLN and 3'S-Di-LN of the CK/S1053 virus (a), and (ii) no significant difference was detected between the affinities to 3'S-Di-LN and 6'S-Di-LN of PG/S1069 virus (b).

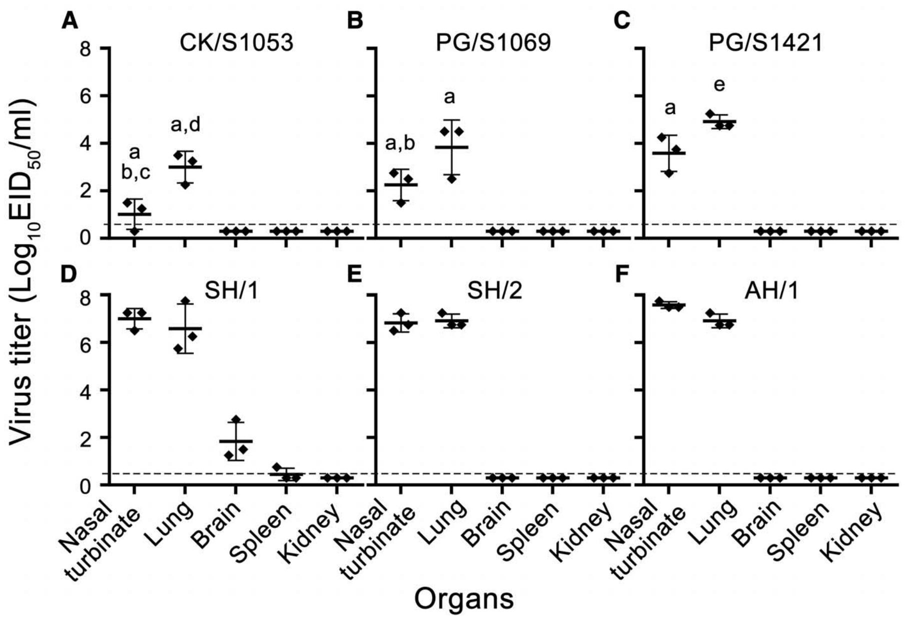

Fig. 2. Replication of H7N9 viruses in mice. Virus titers in organs of mice on day 3 p.i. with 10^6 EID_{50} of the test virus. (**A**) CK/S1053; (**B**) PG/S1069; (**C**) PG/S1421; (**D**) SH/1; (**E**) SH/2; (**F**) AH/1. The data shown are the mean ± standard deviation for each group. a, $P < 0.01$ compared with the corresponding value for the SH/1-, SH/2-, or AH/1-inoculated group; b, $P < 0.01$ compared with the corresponding value for the PG/S1421-inoculated group; c, $P < 0.05$ compared with the corresponding value for the PG/S1069-inoculated group; d, $P < 0.05$ compared with the corresponding value for the PG/S1421-inoculated group; e, $P < 0.05$ compared with the corresponding value for the SH/1-, SH/2-, or AH/1-inoculated group. The dashed lines indicate the lower limit of detection.

human isolates had either 627K or 701N in their PB2 (table S3), suggesting that the PB2 627K or 701N mutations may have occurred during replication of the virus in humans.

The receptor-binding preference of HA has important implications for influenza virus replication and transmission (*12–16*). The HA of human-infective influenza subtypes preferentially recognizes α-2,6-linked sialic acids (SAs) (humanlike receptors), whereas the HA of avian-infective influenza subtypes preferentially recognizes α-2,3-linked SAs (avian-like receptors) (*15*, *17*). Mutations at 158D or 160A (H3 numbering used throughout), which result in the absence of glycosylation at position 158 to 160 in HA, combined with mutations at 224K and 226L or at 226L and 228S are important for H5N1 avian influenza virus binding to α-2,6-linked SAs (*10*, *14*). All 42 of the H7N9 viruses isolated from poultry markets and humans had conserved 160A, 224N, and 228G in their HA; 36 isolates had 226L, one had 226I, and the remaining six had 226Q. The amino acid I at position 243 in HA was detected in six isolates, whereas the other 36 viruses had V at 243 in HA (table S3). We, therefore, tested the receptor specificity of seven H7N9 viruses by using a solid-phase binding assay with four different glycans [two α-2,6 glycans: Neu5Acα2-6Galβ1-4GlcNAcβ-SpNH-LC-LC-Biotin (6′SLN) and Neu5Acα2-6[Galβ1-4GlcNAcβ1-3]$_2$β-SpNH-LC-LC-Biotin (6′S-Di-LN); two α-2,3 glycans: Neu5Acα2-3Galβ1-4GlcNAcβ-SpNH-LC-LC-Biotin (3′SLN) and Neu5Acα2-3[Galβ1-4GlcNAcβ1-3]$_2$β-SpNH-LC-LC-Biotin (3′S-Di-LN)] as described previously (*18*): four isolated from birds, A/chicken/Shanghai/S1053/2013 (CK/S1053), A/pigeon/Shanghai/S1069/2013 (PG/S1069) (containing HA 243I), A/chicken/Shanghai/S1410/2013 (CK/S1410) (containing HA 226Q), and A/pigeon/Shanghai/S1421/2013 (PG/S1421), and three isolated from humans, A/Shanghai/1/2013 (SH/1) (containing HA 226Q), A/Shanghai/2/2013 (SH/2), and AH/1. CK/S1053, PG/S1421, SH/2, and AH/1 (Fig. 1, A, D, F, and G) have the same HA, and all four viruses bound to α-2,6-linked SA, 6′S-Di-LN, with high affinity and to α-2,3-linked SAs with very low affinity. However, their affinity for α-2,6-linked SA, 6′SLN, was variable. The factors that contributed to this variability remain unknown. CK/S1410 and SH/1 bound to both α-2,3-linked and α-2,6-linked SAs, with significantly higher affinity for α-2,3-linked SAs than for α-2,6-linked SAs (Fig. 1, B and E). PG/S1069 bound to both α-2,3-linked and α-2,6-linked SAs, and its affinity for the glycans 6′S-Di-LN and 3′S-Di-LN was similar (Fig. 1C). The I to V change at 243 (I243V) is the only amino acid difference in HA between PG/S1069 and AH/1, SH/2, or CK/S1053, and the Q to L change at 226 (Q226L) is the only amino acid difference in HA between CK/S1410 and AH/1, SH/2, or CK/S1053. We therefore speculated that, similar to the Q226L mutation in HA, the I243V mutation may play an important role in the exclusive binding of CK/S1053, PG/S1421, AH/1, and SH/2 to α-2,6-linked SAs.

All H7N9 viruses have a single basic amino acid in their *HA* genes, a characteristic of low pathogenic influenza virus in chickens (*4*, *6*, *19*). To confirm their virulence, we selected two early isolates, one chicken virus (CK/S1053) and one pigeon virus (PG/S1069), which have different receptor binding properties, and tested their intravenous pathogenicity index (IVPI) in chickens (*20*). Groups of 10 6-week-old specific-pathogen-free (SPF) chickens were inoculated intravenously with 0.1 ml of a 1:10 dilution of bacteria-free allantoic fluid containing CK/S1053 or PG/S1069. None of the chickens showed signs of disease or died during the 10-day observation, yielding an IVPI value of 0 (with 3.0 being the most pathogenic and 0 being the least pathogenic), indicating that these H7N9 viruses are nonpathogenic in chickens (table S4).

Infection experiments (*3*) indicated that chickens are easily infected by H7N9 viruses and efficiently shed virus for up to 7 days, suggesting that these birds may be one of the major carriers and spreaders of H7N9 viruses in the live poultry markets.

H7N9 virus infection of humans has caused a 21% mortality rate among hospitalized cases (*21*); however, the wide clinical spectrum of these infections in humans, from mild infection to death, prompted us to investigate the virulence of these viruses in mammals. Mice have been widely used to evaluate the virulence of influenza viruses, and correlations of virulence in mice and in humans have been observed with H5N1 viruses (*22*, *23*).

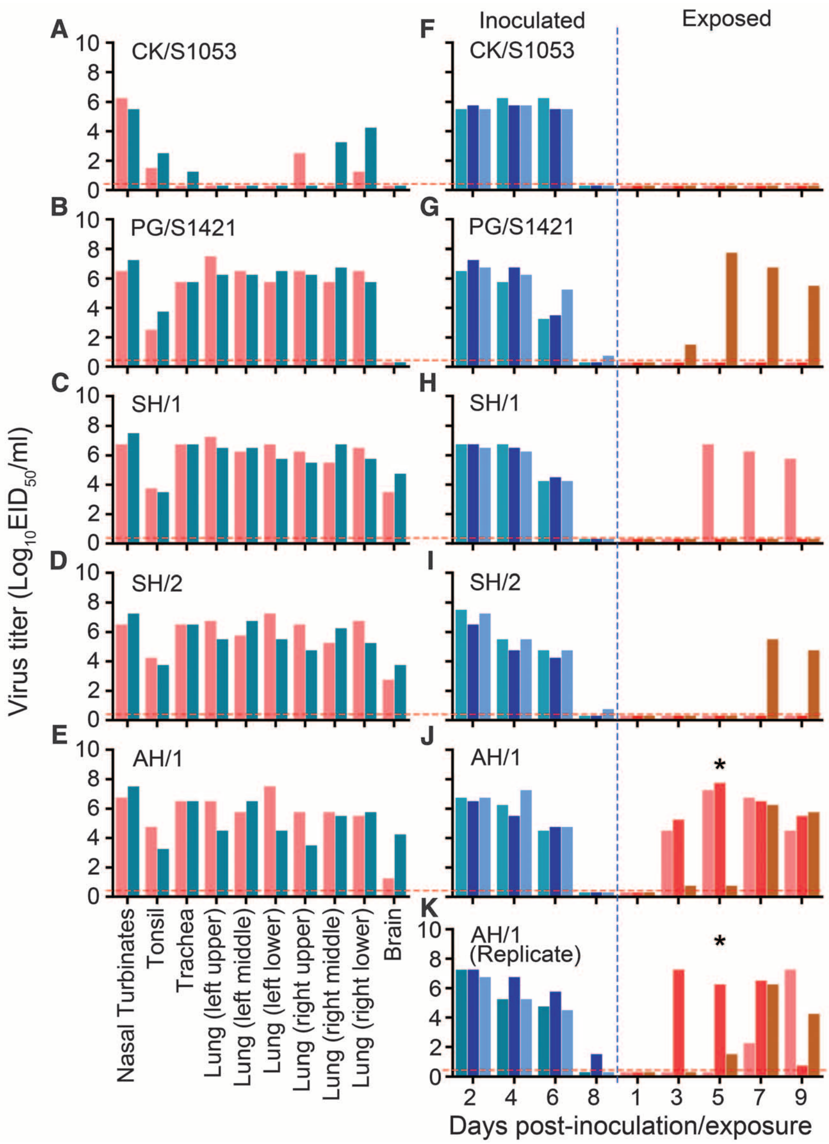

Fig. 3. Replication and respiratory droplet transmission in ferrets of H7N9 viruses. Virus replication: (**A**) CK/S1053; (**B**) PG/S1421; (**C**) SH/1; (**D**) SH/2; (**E**) AH/1. Virus respiratory droplet transmission: (**F**) CK/S1053; (**G**) PG/S1421; (**H**) SH/1; (**I**) SH/2; (**J**) AH/1; (**K**) AH/1 (replicate). Each color bar represents the virus titer from an individual animal. The dashed red lines indicate the lower limit of detection. Asterisks indicate that transmission efficacy was significantly higher than that of the CK/S1053 virus.

We therefore used BALB/c mice to evaluate the replication and virulence of six of the H7N9 viruses: three isolated from poultry, CK/S1053, PG/S1069, and PG/S1421, and three isolated from humans, SH/1, SH/2, and AH/1 (*5*). PG/S1421 and AH/1 are similar in their genome and only differ by a single amino acid at position 627 in their PB2 (table S3).

Mouse lethal dose (MLD_{50}) values were determined by intranasally (i.n.) inoculating groups of five mice with $10^{1.0}$ to $10^{6.0}$ 50% egg infectious dose (EID_{50}) of the virus, and body weight, disease signs, and death were monitored daily for 2 weeks. No disease signs or deaths were observed among mice inoculated with the three viruses isolated from birds, and all mice gained body weight during the observation period (fig. S2, A to C and G to I); in contrast, mice infected with high doses (>10^4 EID_{50}) of the three human isolates experienced weight loss (fig.S2, D to F), and the mice inoculated with 10^6 EID_{50} of SH/1 were killed because they became very sick and lost over 30% of their body weight on day 7 postinfection (p.i.). SH/1 was lethal for mice with an MLD_{50} of 5.4 logEID_{50}, and one mouse in each of the 10^5 and 10^6 EID_{50} of AH/1-inoculated groups and the 10^6 EID_{50} of SH/2-inoculated group died (fig. S2, J to L).

To evaluate the replication of the viruses in mammals, we inoculated groups of three mice i.n. with 10^6 EID_{50} of virus. Mice were killed on day 3 p.i., and their organs, including nasal turbinates, lungs, spleen, kidneys, and brain, were collected for virus titration. Replication of CK/S1053, PG/S1069, PG/S1421, SH/2, and AH/1 was detected in the nasal turbinates and lungs of mice but not in their spleens, kidneys, or brains (Fig. 2, A to C, E, and F); however, SH/1 was detected in the turbinates, lungs, and brains of all three mice and also in the spleen of one mouse (Fig. 2D). Viral titers in the nasal turbinates and lungs of the three human isolate–inoculated mice were significantly

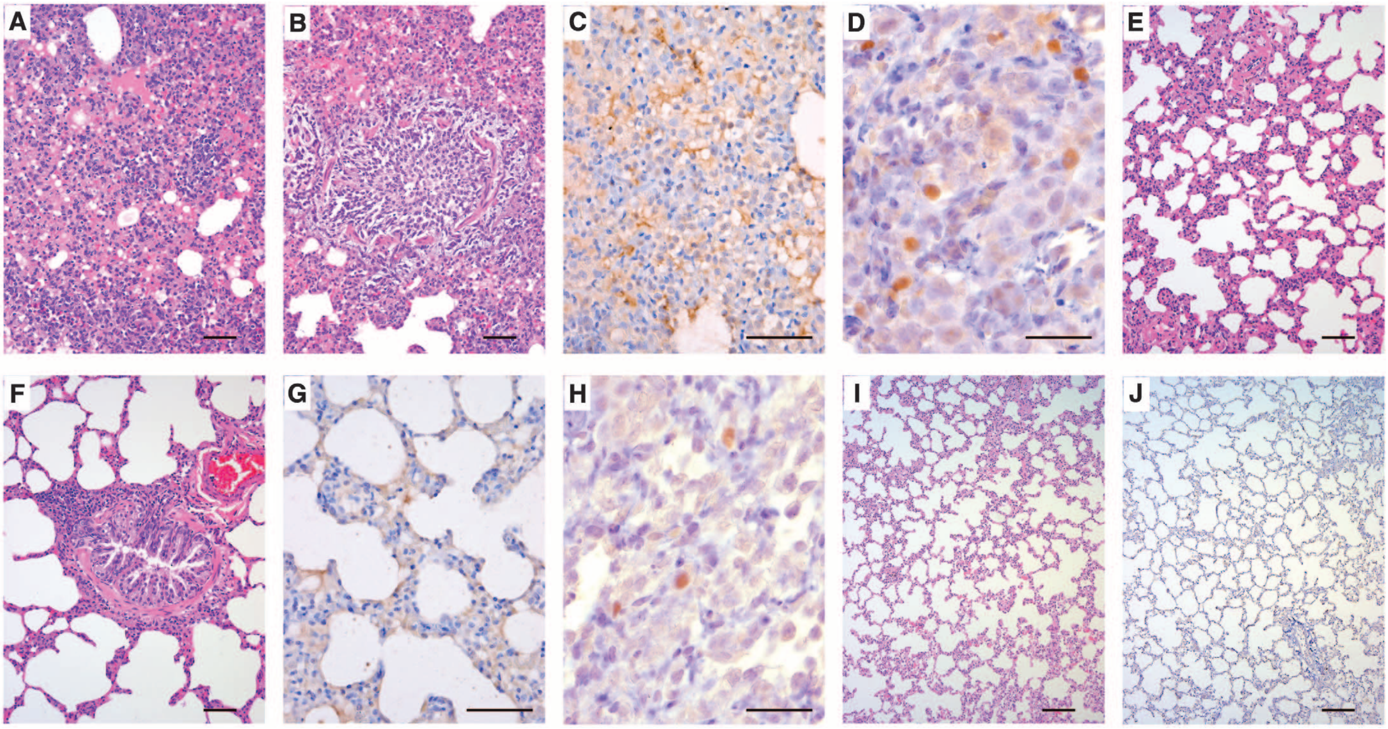

Fig. 4. Histological lesions caused by H7N9 viruses in the lungs of ferrets. Ferrets were killed on day 4 p.i. with 10^6 EID_{50} of the test virus, and the lungs were collected for pathological study. The lungs from the AH/1 virus-infected ferrets developed prominent features of bronchointerstitial pneumonia with massive recruitment of lymphocytes into the lumen and surrounding alveoli and peribronchus, as well as sloughing and necrosis of the respiratory epithelium in the peribronchiolar lumen and submucosal edema of the bronchiolar wall [hematoxylin and eosin (H&E) staining] (**A** and **B**). Viral antigen of AH/1 virus was detected in the epithelial cells of alveoli by means of immunohistochemical (IHC) staining (**C** and **D**). The lungs of a CK/S1053 virus–inoculated animal showed only mild histopathological changes (H&E staining) (**E** and **F**). Limited viral antigen was detected in the lung tissues from CK/S1053 virus–inoculated animals (IHC staining) (**G** and **H**). Normal lung tissues from PBS-inoculated animals [H&E staining (**I**); IHC staining (**J**)]. Scale bars in (A), (C), and (E) to (G), 50 μm; in (D) and (H), 30 μm; in (I) and (J), 100 μm.

Table 1. Virulence and transmission of H7N9 viruses in ferrets. Data shown are from the animal in that group with the maximum body-temperature increase or maximum body-weight loss. Seroconversion was confirmed from the sera of ferrets collected on day 14 (the repeat AH/1 experiment) or on day 21 p.i. The AH/1 transmission experiment was conducted twice; the combined data are presented.

Virus	Maximum body temperature increase (°C)		Maximum body weight loss (%)		Seroconversion (HI antibody titer range)		Respiratory droplet transmission
	Inoculated	Exposed	Inoculated	Exposed	Inoculated	Exposed	
CK/S1053	1.5	0.5	2	1.1	3/3 (160–320)	0/3	None
PG/S1421	2	1.0	7.6	5.8	3/3 (160–320)	1/3 (160)	Lowly efficient
SH/1	1.5	1.3	3.1	2.1	3/3 (160–320)	1/3 (160)	Lowly efficient
SH/2	2.3	1.8	3.5	2.8	3/3 (160–320)	1/3 (80)	Lowly efficient
AH/1	1.7	1.4	3.7	3.1	6/6 (160–640)	6/6 (80–320)	Highly efficient

higher than those in the three bird isolate–inoculated mice (Fig. 2). These results indicate that the H7N9 human isolates replicated much more efficiently and were more lethal in mice than were the viruses isolated from birds and that the PB2 627K mutation likely contributed to the increased virulence of the human isolates to mice, as was observed with H5N1 viruses (*11*).

The H7N9 viruses have caused in excess of 100 human cases in a relatively short period, and the biggest concern around the world is whether these viruses can transmit efficiently from human to human. If these viruses acquire the ability to efficiently transmit among humans, there is a high chance of an influenza pandemic, because humans have no immunity to H7N9 viruses. Therefore, evaluation of the transmissibility of these viruses is important.

Ferrets and guinea pigs have been widely used as animal models for influenza virus transmission studies (*10*, *14*, *15*, *24*, *25*), and human influenza viruses transmit similarly in these two models (*24*, *26*). Transmission studies of influenza mutants with changes in their HA indicate that respiratory droplet transmission appears to be restricted in ferrets if the virus does not exclusively or preferentially bind to α-2,6-linked SA (*24*, *27*); the same may be true for humans, because all widely circulating human influenza viruses preferentially bind to α-2,6-linked SA (*15*, *17*). We therefore tested the replication and respiratory droplet transmission of two avian H7N9 viruses, CK/S1053 and PG/S1421, that preferentially bind to α-2,6-linked SAs and that of the three human H7N9 viruses, SH/1, SH/2, and AH/1, in ferrets.

Two ferrets were inoculated i.n. with 10^6 EID_{50} of each virus, and the nasal turbinates, tonsils, trachea, lungs, spleen, kidneys, brain, and liver from each ferret were collected on day 4 p.i. for virus titration in eggs. The five viruses replicated to similar levels in the nasal turbinates, but the viral titers in the tonsils, trachea, and lungs of ferrets inoculated with CK/S1053 were notably lower than those in ferrets inoculated with PG/S1421 or the three human isolates (Fig. 3, A to E). Virus was also detected in the brains of the ferrets inoculated with the three human isolates but was not detected in the spleen, kidney, or liver of any ferret (Fig. 3, A to E).

Pathological studies were performed on lung samples from the virus-infected ferrets. The lungs of PG/S1421-, SH/1-, SH/2-, and AH/1-infected ferrets showed severe bronchopneumonia with prominent viral antigen expression (Fig. 4, A to D, and fig. S3). By contrast, most of the lung appeared normal after infection with CK/S1053 (Fig. 4, E to H).

To investigate respiratory droplet transmission, we inoculated three ferrets i.n. with 10^6 EID_{50} of test virus and then housed them separately in solid stainless-steel cages within an isolator (fig. S4). Twenty-four hours later, three naïve ferrets were placed in adjacent cages. Each pair of animals was separated by a double-layered net divider (4 cm apart) as described previously (*18*) (fig. S4). Nasal washes were collected every 2 days from all of the animals beginning 2 days p.i. [1 day postexposure (p.e.)] for the detection of virus shedding. Sera were collected from all animals on day 21 p.i. for hemagglutinin inhibition (HI) antibody detection. Respiratory droplet transmission was confirmed when virus was detected in the nasal washes and by seroconversion of the naïve exposed animals at the end of the 3-week observation period.

Virus was detected in all directly infected animals (Fig. 3, F to J). In the exposed groups, virus was not detected in any of the animals exposed to the CK/S1053-inoculated ferrets. However, virus was detected in one ferret exposed to the ferrets that had been inoculated with PG/S1421, SH/1, or SH/2 and in all three ferrets exposed to the ferrets that had been inoculated with AH/1 (Fig. 3J). Because there have been no reports to date of transmission of H7N9 virus among humans, we repeated this respiratory droplet transmission study with AH/1 virus in ferrets and found the results to be reproducible (Fig. 3K). We sequenced the viruses recovered from the inoculated animals on day 6 postinoculation and the viruses recovered from the exposed animals on day 7 p.e. and did not detect any amino acid changes in any of the viruses. Infection of ferrets with the five viruses did not cause marked changes in body temperature (Table 1). The ferrets that were exposed or inoculated with PG/S1421 experienced a 5.8 to 7.6% weight change, and the body-weight loss of ferrets inoculated with the other four viruses was 1.1 to 3.7% (Table 1). Seroconversion occurred in the virus-inoculated animals and in all exposed animals that were virus-positive (Table 1). These results indicate that four of the five H7N9 viruses tested can transmit between ferrets, and one virus, AH/1, transmits highly efficiently between ferrets by respiratory droplet.

Transmission of influenza virus is a polygenic trait. The mutations in HA that confer binding to α-2,6-linked SAs are important for transmission; however, CK/S1053 and AH/1 had similar *HA* genes and bound similarly to the α-2,6-linked SAs, but their transmissibility in ferrets was totally different. PB2 627K is also important for transmission, but SH/1 and SH/2, which both bear PB2 627K, transmitted similarly to PG/S1421, which does not have PB2 627K. Therefore, it is difficult to conclude which amino acid substitution alone makes the virus highly transmissible. However, the amino acid differences between the avian viruses and the AH/1 virus range from 1 to 27 (table S3), suggesting that only a few amino acid changes would be needed to make the avian H7N9 viruses highly transmissible in mammals. Moreover, these changes can occur easily during replication in humans.

In summary, our studies characterized the H7N9 viruses isolated from poultry and humans and demonstrated that these naturally isolated viruses can bind humanlike airway receptors and replicate efficiently in ferrets. Most importantly, one virus isolated from humans is able to transmit efficiently between ferrets by respiratory droplet. The widespread detection of H7N9 viruses from live poultry markets in Shanghai and eight other provinces in a relatively short time period indicates that the viruses transmit efficiently among poultry, especially chickens, and have spread across a wide geographic area in China. Currently, implementation of compulsory control measures in H7N9 virus–positive live poultry markets is preventing further human infections; however, the elimination of the H7N9 virus from nature is a huge and long-term challenge. Its nonpathogenic nature in poultry enables the avian H7N9 virus to replicate silently in avian species and to transmit to humans. Its replication in humans will provide further opportunities for the virus to acquire more mutations and become more virulent and transmissible in the human population.

Reference and Notes

1. S. Tong *et al.*, *Proc. Natl. Acad. Sci. U.S.A.* **109**, 4269–4274 (2012).
2. World Health Organisation, Number of confirmed human cases of avian influenza A(H7N9) reported to WHO, www.who.int/influenza/human_animal_interface/influenza_h7n9/08_ReportWebH7N9Number.pdf (May 2013).
3. See supplementary materials on *Science* Online.
4. J. Shi *et al.*, *Chin. Sci. Bull.* **58**, 1857–1863 (2013).
5. R. Gao *et al.*, *N. Engl. J. Med.* **368**, 1888–1897 (2013).
6. Y. Chen *et al.*, *Lancet* **381**, 1916–1925 (2013).
7. Single-letter abbreviations for the amino acid residues are as follows: A, Ala; C, Cys; D, Asp; E, Glu; F, Phe; G, Gly; H, His; I, Ile; K, Lys; L, Leu; M, Met; N, Asn; P, Pro; Q, Gln; R, Arg; S, Ser; T, Thr; V, Val; W, Trp; and Y, Tyr.
8. E. K. Subbarao, W. London, B. R. Murphy, *J. Virol.* **67**, 1761–1764 (1993).
9. Z. Li *et al.*, *J. Virol.* **79**, 12058–12064 (2005).
10. Y. Gao *et al.*, *PLoS Pathog.* **5**, e1000709 (2009).
11. M. Hatta, P. Gao, P. Halfmann, Y. Kawaoka, *Science* **293**, 1840–1842 (2001).
12. L. Glaser *et al.*, *J. Virol.* **79**, 11533–11536 (2005).
13. M. Matrosovich *et al.*, *J. Virol.* **74**, 8502–8512 (2000).
14. M. Imai *et al.*, *Nature* **486**, 420–428 (2012).
15. S. Herfst *et al.*, *Science* **336**, 1534–1541 (2012).
16. A. Vines *et al.*, *J. Virol.* **72**, 7626–7631 (1998).
17. G. N. Rogers, J. C. Paulson, *Virology* **127**, 361–373 (1983).
18. Y. Zhang *et al.*, *Science* **340**, 1459–1463 (2013).
19. T. Kageyama *et al.*, *Euro Surveill.* **18**, 20453 (2013).
20. *Manual of Diagnostic Tests and Vaccines for Terrestrial Animals* (Office International des Epizooties, Paris, 2011).
21. Q. Li *et al.*, *N. Engl. J. Med.* 130424140638006 (2013).
22. X. Lu *et al.*, *J. Virol.* **73**, 5903–5911 (1999).
23. Y. Li *et al.*, *J. Virol.* **84**, 8389–8397 (2010).
24. Y. Zhang *et al.*, *J. Virol.* **86**, 9666–9674 (2012).
25. A. C. Lowen, S. Mubareka, T. M. Tumpey, A. García-Sastre, P. Palese, *Proc. Natl. Acad. Sci. U.S.A.* **103**, 9988–9992 (2006).
26. C. W. Seibert *et al.*, *J. Virol.* **84**, 11219–11226 (2010).
27. T. M. Tumpey *et al.*, *Science* **315**, 655–659 (2007).

Acknowledgments: We thank S. Watson for editing the manuscript, Y. Shu from the China Centers for Disease Control and Prevention for providing the H7N9 viruses isolated from humans, and the Consortium for Functional Glycomics (Scripps Research Institute, Department of Molecular Biology, La Jolla, CA) for providing the glycans. This work was supported by the Ministry of Agriculture (CARS-42-G08) and by the Ministry of Science and Technology (KJYJ-2013-01-01 and 2012ZX10004214). Virus sequence data from this study were deposited in GenBank with the accession numbers CY146905 to CY147200 and in Global Initiative on Sharing Avian Influenza Data with the accession numbers EPI440678 to 440701 and EIP457614 to 457885.

Supplementary Materials

www.sciencemag.org/cgi/content/full/science.1240532/DC1
Materials and Methods
Supplementary Text
Figs. S1 to S4
Tables S1 to S4
References

15 May 2013; accepted 2 July 2013
Published online 18 July 2013;
10.1126/science.1240532

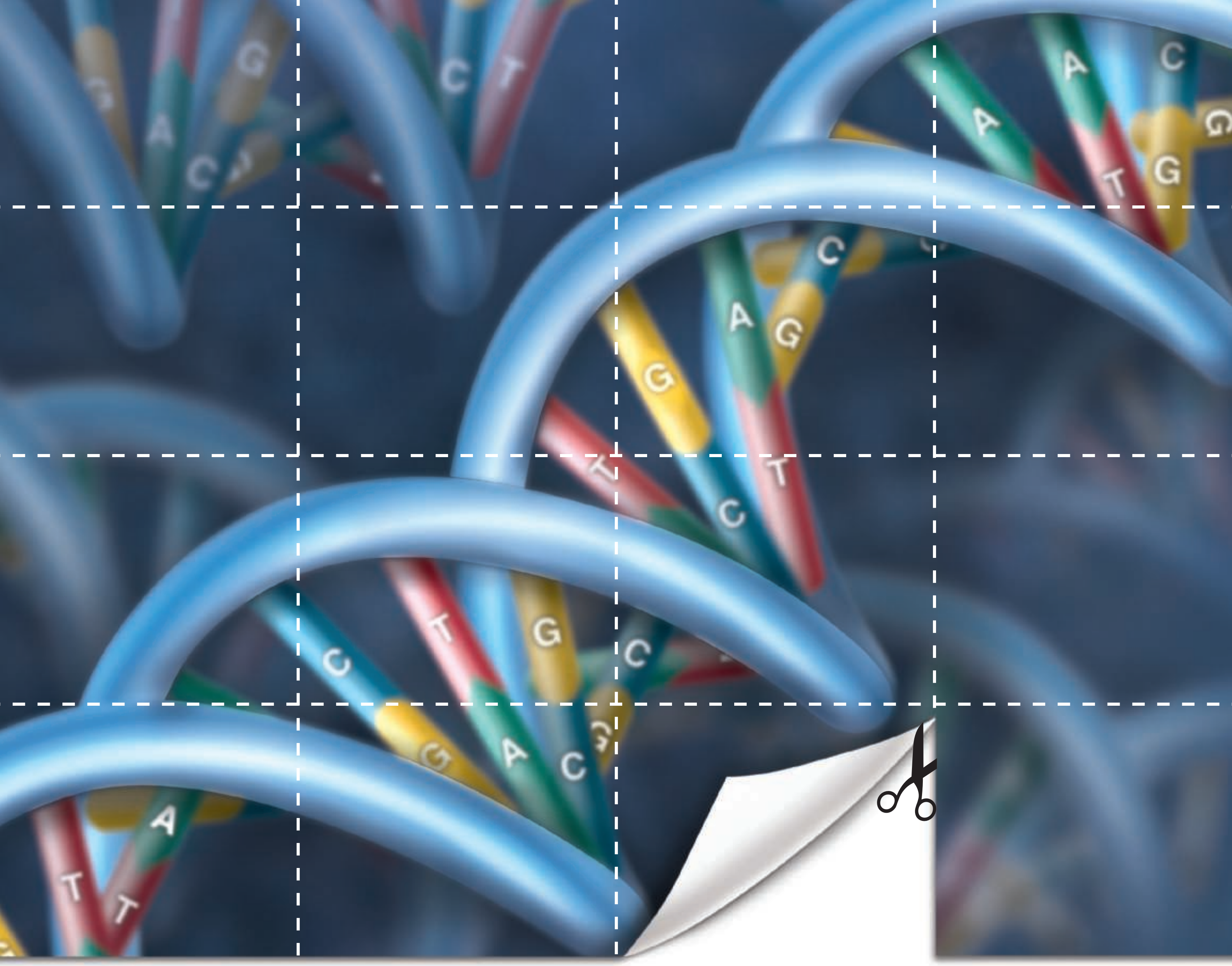

CutSmart
NotI-HF™
Lot: 0021201
Exp: 2/15
Store at -20°C
S R3189S
500 units
20,000 units/ml
NEW ENGLAND BioLabs Inc.

eppendorf

Future included

50 years of experience in highest quality

Eppendorf consumables are the result of 50 years constant improvement and development. With the new Eppendorf Tubes® 5.0 mL a new tube format in the medium volume range will complete the legendary Eppendorf Tubes family.

Laboratory processes will become easier and more convenient.

Purest assay results are no coincidence:

> Unique features to make every day routines faster and easier
> Minimized risk of chemical leaching from consumables
> Purity grades tailored to even the highest requirements

www.eppendorf.com/consumables

FILTRATION CENTRIFUGE

The Hermle Sieva-2 Filtration centrifuge offers a wide range of applications in chemical, pharmaceutical, biotech, food processing, and research laboratories. The two options of either perforated or non-perforated rotor baskets make the Sieva-2 ideal for filtration or solid/liquid sedimentation (decantation). The rotors are designed with cone-shaped centers to guarantee an even spread of filtered material and rinsing agent. The powerful induction drive motor reaches speeds of 10,000 RPM or 7,825x g. Enhanced features include: speed selection from 250–10,000 RPM, transparent lid to visually monitor samples, imbalance detection system for added safety, 500 mL rotor basket with 10 rows of perforations, and intuitive control panel and large digital LED display.

Labnet International

For info: 888-522-6381 | www.labnetinternational.com

HIGH PURITY REAGENTS

The new, highly purified Chondroitinase ABC is supplied protease-free, carrier-free, and with low-endotoxin levels for use in neuroscience and regenerative medicine research. Chondroitin Sulfate Proteoglycans (CSPGs) are involved in the inhibition of axon regeneration after various forms of damage to the central nervous system, including stroke or spinal cord injury. The enzyme Chondroitinase ABC purified from *Proteus vulgaris*, degrades these CSPGs, and has been shown to promote functional recovery and neural regeneration.

AMS Biotechnology

For info: Tel: +44-(0)-1235-828200 | www.amsbio.com

CIRCULATING TUMOR CELL DETECTION

The combined subtraction enrichment and immunostaining-fluorescence in situ hybridization (iFISH) kits specialize in isolating and identifying various circulating tumor cells. Unlike a tumor cell surface molecule dependent antibody capture platform, whose application is restricted to only certain types of solid tumors, this novel technology efficiently enriches circulating tumor cells of various solid tumors via efficiently depleting white blood cells, followed by unique identification performed with integrated tumor marker immunostaining and chromosome enumeration. The kits are available for both human and mouse blood samples.

Cytelligen

For info: 858-509-9209 | www.cytelligen.com

COMBINED MICROPLATE READER/IMAGER

The Cytation3 Cell Imaging Multi-Mode Reader is the first combination Hybrid multimode microplate reader and imaging system. By combining multidetection and automated digital microscopy in one instrument, researchers can now glean data-rich quantitative and qualitative information from their cells like never before. Modular architecture allows users to select only what they need now and upgrade with additional modes as their needs evolve. The automated digital fluorescence microscope features brightfield imaging and color switching through onboard filter cubes. Red (Texas Red), green (GFP), and blue (DAPI) cubes are standard, with a fourth position available. Automated XY stage, autofocus, autoexposure, and software features increase throughput of CCD-based image capture, cell counting, and other tasks that are tedious when performed with manual microscopy systems. Onboard objectives in a magnification range from 2x to 20x allow the user to view an entire microplate well or to examine the minute details of intracellular activities.

BioTek Instruments

For info: 888-451-5171 | www.biotek.com

SIRTUIN ACTIVITY ASSAY

The SIRTainty Class III HDAC assay allows for simple, sensitive detection of sirtuin activity on any desired substrate. The assay utilizes a novel patent-pending technology for the sensitive detection of all known sirtuin family members. Unlike conventional assays that are dependent upon a single pre-labeled fluorescently tagged substrate, the SIRTainty Class III HDAC assay employs untagged acetylated peptide substrates. This approach not only enables unparalleled flexibility in the choice of sirtuin isoform and peptide substrate, but also eliminates the potential for artifacts due to the use of artificial substrates containing bulky fluorophores. Sirtuins are a class of enzyme that removes acetyl groups from a variety of proteins that play key roles in multiple biological processes. These enzymes, also known as class III HDAC (histone deacetylases), have been implicated in a variety of age-related diseases such as cancer, Alzheimer's disease, and type 2 diabetes.

EMD Millipore

For info: 800-645-5476 | www.millipore.com

CALCIUM ASSAY KITS

The FLIPR Calcium 6 Assay Kits address diversified GPCR and ion channel targets. Featuring a proprietary fluorophore, the dye offers the highest quantum yield of any calcium indicator on the market, delivering the greatest signal window available in a calcium assay kit. This substantial increase in signal enables researchers to monitor low-responders, including biorelevant reactions from endogenous, primary, or stem cell targets. FLIPR 6 Calcium Assay Kits provide a comprehensive method for detecting intracellular calcium changes in a simple and reliable homogeneous assay format. Combining the novel fluorophore with proven proprietary quench technology, the new assay affords the highest signal to background ratio. The unique dye is more resistant to anion-exchange proteins, enabling measurement with minimal to no probenecid, an exchange inhibitor, when studying cell lines containing an organic anion transporter.

Molecular Devices

For info: 800-635-5577 | www.moleculardevices.com

Electronically submit your new product description or product literature information! Go to **www.sciencemag.org/products/newproducts.dtl** for more information.

POSITIONS OPEN

GRU GEORGIA REGENTS UNIVERSITY | Medical College of Georgia

FACULTY POSITIONS in Systems Neuroscience

The Brain and Behavior Discovery Institute (BBDI) at the Medical College of Georgia of the Georgia Regents University (GRU) is seeking up to six faculty members who will be appointed as tenure-track **ASSISTANT PROFESSOR,** tenured **ASSOCIATE PROFESSOR,** or **FULL PROFESSOR.** Candidates should have a Ph.D. or M.D. degree with a strong record of research accomplishment working in systems neuroscience. Approaches using molecular genetics, in vivo imaging, neural recordings, optogenetics, circuits mapping, or large-scale neural computation/modeling, are highly encouraged. Faculty members are expected to establish or have creative, cutting-edge research programs and may participate in teaching medical and graduate students. GRU is a state supported academic medical center located in a historic city with outstanding recreational and lifestyle opportunities.

Consideration of candidates is ongoing and will continue until the search has been successfully concluded. Please submit curriculum vitae, a statement of current and future research interests, and arrange three letters of recommendation to:

Joe Z. Tsien, Ph.D.
Neuroscience Faculty Search
The Brain and Behavior Discovery Institute (BBDI)
Medical College of Georgia
Georgia Regents University
1120 15th Street, CL-3033
Augusta, GA 30912-4750
ATTN: Toni Goodly
E-mail: lgoodly@gru.edu

You are also required to complete an online application at **website: http://www.gru.edu/facultyjobs/** (**Req #'s 4781, 4782, 4783, 4785, 4786, 4788).** *Equal Employment Opportunity/Affirmative Action/Equal Access Employer.*

ASSISTANT PROFESSOR in Animal Physiology/Systems Neurobiology

The Smith College Department of Biological Sciences in Northampton, Massachusetts, invites applications for a full-time, tenure-track Assistant Professor in animal physiology/systems neurobiology beginning July 1, 2014. We seek candidates with a strong commitment to undergraduate education and an active research program that focuses on systems neurobiology. A Ph.D. is required; teaching and/or postdoctoral experience is preferred. For more information and to apply, visit **website: https://secure.interfolio.com/apply/21905.** Review will begin September 15, 2013. *Smith College is an Equal Opportunity Employer encouraging excellence through diversity.*

POSTDOCTORAL POSITION to Study HMGA Chromatin Remodeling Proteins In Cancer, Cancer Stem Cells & Normal Stem Cell Biology at the Johns Hopkins University School of Medicine

Departments of Medicine, Oncology & Institute for Cellular Engineering. Experience with cancer or normal stem cells required. Please send cover letter, curriculum vitae, and three references to **Dr. L. Resar, e-mail: lindaresar@yahoo.com.**

POSITIONS OPEN

TENURE-TRACK FACULTY POSITIONS Available at the NIH-funded Center of Biomedical Research Excellence (COBRE) in Inflammation and Dietary Supplements at the University of South Carolina

The University of South Carolina (USC) invites applications for several tenure-track **ASSISTANT PROFESSOR** positions in Inflammation and Dietary Supplements. Outstanding applicants working in the area of inflammation and willing to incorporate dietary supplements research are encouraged to apply. Current areas of research are highlighted at the following **websites: http://cobre.med.sc.edu/** and **http://camcenter.med.sc.edu/.** The successful candidates will be recruited, based on research experience and interest, in a department at any of the participating schools/colleges, namely the School of Medicine, School of Public Health, School of Pharmacy, College of Engineering, School of Nursing and College of Arts and Sciences. The candidates must have Ph.D. or equivalent, and postdoctoral research experience. The recruits will be eligible to apply for funds from the NIH COBRE grant at USC. However, recruits with major independent funding, current or past, such as NIH R01 or K99/R00 are not eligible to apply for COBRE funding. Furthermore, recruits with NIH R03, R21, or smaller grants are eligible to apply for COBRE funding. Successful candidates are expected to develop a strong extramurally funded (such as NIH R01) research program. They must participate in the teaching and service mission of the respective departments. Competitive salary and start-up funds are available. The candidates will also receive excellent mentoring by senior faculty to pursue successful independent careers. Please submit curriculum vitae, statement of research plans and three letters of recommendation to: **Dr. Mitzi Nagarkatti, Chair, Department of Pathology, Microbiology, and Immunology, University of South Carolina School of Medicine, Columbia, SC 29208; e-mail: COBRE@uscmed.sc.edu.** The search will start immediately and continue until the positions are filled. *USC Columbia is an Equal Opportunity/Affirmative Action Employer and encourages applications from women and minorities and is responsive to the needs of dual career couples.*

The Department of Biochemistry at the University of Wisconsin-Madison invites applications for a full-time **ASSOCIATE** or **FULL PROFESSOR** of Biochemistry. We are seeking an individual with an outstanding record of accomplishments in the field of biomolecular NMR. Candidates must have an international reputation for excellence in biomolecular NMR, with a sustained record of professional achievement as indicated by sponsored research, publications, teaching, and leadership activities in the field, over a minimum of at least four years. The successful candidate will be expected to: co-direct the National Magnetic Resonance Facility at Madison (NMRFAM); continue to grow a vigorous independent research program in the area of biomolecular NMR that is both nationally and internationally recognized; participate in the Department's graduate teaching program; and contribute to UW-Madison's strong commitment to faculty governance through department, university, professional, and public service.

To be considered for this position, please send curriculum vitae, the names and addresses of three references, and a three-page summary of research accomplishments and future goals in a single PDF file to **e-mail: jobs@biochem.wisc.edu.** To ensure full consideration, applications must be received by November 1, 2013. Candidates must have a Ph.D. in Biochemistry or a related field.

Please note: Unless confidentiality is requested in writing, information regarding applicants must be released upon request. Finalists cannot be guaranteed confidentiality. UW-Madison is an Equal Opportunity/Affirmative Action Employer.

For more information on the Department of Biochemistry at UW-Madison and NMRFAM, please visit websites: **http://www.biochem.wisc.edu** or **http://www.nmrfam.wisc.edu.**

Associate Professor/Professor
Jinan University, Guangzhou, China

Job description

The Guangdong-Hongkong-Macau Institute of CNS regeneration (GHMICR) at Jinan University, Guangzhou, China (**http://ghmicr.jnu.edu.cn**) is recruiting young leading neuroscientists who use innovative approaches to investigate problems from molecular and cellular level to systems in neuroscience related to neural protection and regeneration. Successful candidates will be expected to develop thriving, well-funded research programs and to contribute to graduate education. Positions will be for a three-year period with extensions to long-term positions pending performance. Jinan University will provide attractive annual salary (150 to 400 thousand RMB), start-up fund, housing allowance and others.

Qualifications

Successful candidates must have a PhD degree or equivalent and display high potential based on publications. The successful candidates are expected to develop projects independently.

Application

Application is open until the candidates are selected. Please send electronic application including a statement of interest, full CV, a brief description of research goals and accomplishments, a summary of current and past grant support, names of 3 references, and representative reprints of 3~4 original reports to:

Prof. Libing Zhou, Associate director
GHM Institute of CNS Regeneration, Jinan University.
Huangpu Avenue W. 601, Guangzhou, P. R. China, 510632
Email: tlibingzh@jnu.edu.cn, Tel: (+86) 20-85228362

CBG
Max Planck Institute of Molecular Cell Biology and Genetics

The **Max Planck Society** is seeking a

DIRECTOR (m/f)

at the **Max Planck Institute of Molecular Cell Biology and Genetics Dresden**.

Areas of interest include Experimental Biophysics and Cell, Developmental and Evolutionary Biology. The successful candidate will be expected to bridge to the strong theoretical and computational biology in Dresden.

The Max Planck Institute of Molecular Cell Biology and Genetics in Dresden (Germany) (http://www.mpi-cbg.de) has a general interest in mechanisms helping to understand "How cells form tissues". The institute addresses this question using a variety of experimental approaches at the molecular, cellular and organismic levels.

Please send a letter of interest or suggestions of candidates to the Managing Director, Elisabeth Knust, Max Planck Institute of Molecular Cell Biology and Genetics, Pfotenhauerstr. 108, 01309 Dresden (Germany) (knust@mpi-cbg.de). All enquiries will be treated confidentially.

The Max Planck Society for the Advancement of Science is an independent, nonprofit research organization that primarily promotes and supports basic research. The Max Planck Society, an equal opportunity employer, is committed to diversity and inclusion in all aspects of recruiting and employment. The Max Planck Society is aiming at increasing the percentage of women among its scientific leadership, particularly at the director level and therefore strongly encourages expressions of interest from and nominations of qualified women.

The Max Planck Society is committed to employ more handicapped individuals and actively seek their applications.

MAX-PLANCK-GESELLSCHAFT

WASHINGTON STATE UNIVERSITY

Assistant/Associate/Full Professor of Neuroscience

The Department of Integrative Physiology and Neuroscience (IPN) at Washington State University in Pullman, WA is seeking an outstanding academic scientist to fill a full-time, tenure-track faculty position in neuroscience at the rank of Assistant/Associate/Full Professor. The position is a permanent 75% state funded 12-month appointment, with state support for summer salary available the first two years of appointment. Required: Applicants must have one of the following earned degrees: PhD in neuroscience or related biomedical discipline, MD, or DVM degree and at least 2 years post-doctoral research experience. The successful candidate's research focus will be on control of food intake/energy homeostasis.

Applicants for associate or full professor positions must have an active established extramurally funded independent research program, and a record of peer-reviewed publication and national/international recognition commensurate with rank. The successful candidate will have a record of substantive scholarly contributions to understanding control of food intake/energy homeostasis, and will be expected to maintain an innovative, extramurally funded research program in this area.

Applicants for an assistant professor position must have demonstrated potential to establish and maintain an externally funded research program focused on understanding control of food intake/energy homeostasis. The successful applicant will have a record of peer-reviewed publication appropriate to rank and will be able to articulate an innovative agenda for their future research program in this area.

Instructional duties will include teaching a portion of a team-taught physiology course for professional DVM students. Additional instructional opportunities in the graduate and/or undergraduate Programs in Neuroscience also are possible. Ability to support and mentor graduate students and postdoctoral trainees is essential. The successful applicant must be able to effectively communicate and work collegially and collaboratively with a diverse population of colleagues and students.

Salary and rank are dependent upon qualifications. Generous start-up packages are available. Laboratory space will be assigned in a newly-completed state-of-the-art research building specifically designed and equipped for neuroscience research. Ongoing departmental research interests include drug addiction, food intake and energy homeostasis, sleep and circadian rhythms, synaptic plasticity, neurodegenerative disease, and affective neuroscience.

Washington State University has a vibrant neuroscience community and is located in a region having a high quality of life with excellent access to outdoor activities, the arts, and the multidisciplinary collegiality of a large research university.

Screening of applications will begin **September 3, 2013**. The application must include the following: a cover letter which states what rank is being applied for, curriculum vitae, description of teaching experience and philosophy, summary of research interests and goals, and names and contact information (including email addresses) for three references. Applicants please follow this link: **www.wsujobs.com/applicants/Central?quickFind=58662**. No paper submissions accepted. Direct questions to **kinslow@vetmed.wsu.edu**, **http://www.vetmed.wsu.edu/neuroscience/**

EEO/AA

USDA

United States Department of Agriculture
National Institute of Food and Agriculture

ASSISTANT DIRECTOR OF THE INSTITUTE OF BIOENERGY, CLIMATE, AND ENVIRONMENT

The National Institute of Food and Agriculture (NIFA) in the Department of Agriculture is seeking to fill the position of **Assistant Director of the Institute of Bioenergy, Climate, and Environment (IBCE)**. This is a Senior Executive Service (SES) position.

As the Assistant Director of IBCE, the incumbent is responsible for providing scientific and managerial leadership and direction in formulating and implementing policies and programs that support research, education, and extension programs that will ensure energy independence through identifying and developing sustainable biobased energy systems; to ensure sustainable supply of agriculture products through identifying and developing adaptive agro-ecosystems in response to climate change; and to identify sustainable ecosystem services from the nation's limited natural resources base. The incumbent serves as a principal scientific and management advisor to the Deputy Director for Agriculture and Natural Resources in administering, evaluating, planning, directing and coordinating activities related to the mission and function of NIFA, in execution of policies and practices of grants management, and in the allocation of resources to carry out these policies and practices. The incumbent is instrumental in elevating the standing of agricultural sciences within the Federal science enterprise and provides scientific, technical, and administrative input to the Director and Deputy Directors of NIFA. More information about NIFA can be found at **http://www.nifa.usda.gov/**.

A copy of the job announcement (**AG-22-2013-0004**) is available at **https://www.usajobs.gov/**. All applications must be received by **August 21, 2013**.

U.S. CITIZENSHIP REQUIRED.
USDA IS AN EQUAL OPPORTUNITY PROVIDER AND EMPLOYER.

Faculty Position Translational Microenvironment/ Viral Oncology Center University of Pittsburgh Cancer Institute

The University of Pittsburgh Cancer Institute (UPCI) (**www.upci.upmc.edu**) at the University of Pittsburgh has developed a new center for Translational Microenvironment and Viral Oncology (TMV) (**www.upci.upmc.edu/tmv/**) and seeks to recruit faculty to develop outstanding research programs that bring approaches complementing our existing strengths. The TMV Center includes three areas of research: Cancer cell-stromal/inflammatory cell interactions, host response and biomarkers of progression in patients with virus-associated malignancy, and inflammatory, viral and stromal-specific therapeutic strategies. It is anticipated that the TMV Center will play a pivotal role in identifying novel microenvironmental targets for therapeutic intervention that will be tested in combination with more conventional treatments in patients with a variety of cancers.

Candidates with a track record of independent funding and publications in high impact journals will be given the highest consideration. Successful candidates will be expected to run a vibrant collaborative program supported by external funding. A competitive salary and research start-up package will be provided.

Positions will be coordinated with Departments in the University of Pittsburgh and are tenure track. To apply, please send your curriculum vitae, a one-page summary of your research plans, and three letters of recommendation to the search coordinator: **Clayton Mathis, UPCI Research Pavilion, Hillman Cancer Center Suite 2.26, 5117 Centre Avenue, Pittsburgh, PA 15213-1863, email: mathisc@upmc.edu**.

Applications will be reviewed and evaluated upon receipt of full applications on an ongoing basis.

The University of Pittsburgh is an Affirmative Action, Equal Opportunity Employer.

RESEARCH SCIENTISTS

Regenerative Medicine

The Texas Heart Institute's Regenerative Medicine Research Program is recruiting established and promising investigators who have records of innovative research in cardiovascular stem cell biology, cardiovascular physiology, or electrophysiology. The positions offer excellent opportunities for translational and collaborative research in a rich academic environment with state-of-the-art facilities, under the direction of an internationally known principal investigator. Texas Heart Institute is located in the world-renowned Texas Medical Center. Post-doctoral fellows are also needed. Please visit **www.texasheart.org/careers** and follow the instructions to apply. EOE

TEXAS HEART® INSTITUTE

www.texasheart.org/careers

Drug Discovery in Chengdu, China

Xizang Haisco Pharmaceutical Group Co. LTD. is a young fast growing fully integrated pharmaceutical company based in Chengdu in Sichuan province of China with annual sales over 100 million US$. Haisco has made major commitment in new drug discovery and has built a fully integrated drug discovery group of 80 scientists in a 10,000 sq.ft. laboratory including animal facility. We are now recruiting highly motivated individuals as supported by strong publication record in top tiered journals to join our efforts:

Senior Position: Formulation

PhD in pharmaceutical sciences with 5 - 10 years experience in oral formulation research in pharmaceutical industry with strong track record.

Senior position: Medicinal Chemistry

PhD in synthetic organic chemistry with extensive experience in the total synthesis of complex organic molecules. In-depth knowledge and understanding in modern synthetic organic chemistry as supported by strong publication record.

Senior position: Biology/Pharmacology

PhD in Biology/pharmacology with working experience in Cardiovascular/Diabetes/Oncology/CNS preclinical / early clinical development.

Chengdu is fast becoming a world class city with strong state supports yet with small city charm. We offer a competitive compensation package and an open, challenging and smoke-free environment. Please forward your resume to **zhangyan1@haisco.com** for immediate consideration.

www.haisco.com

THE HONG KONG UNIVERSITY OF SCIENCE AND TECHNOLOGY

School of Science Joint Faculty Positions

The School of Science of The Hong Kong University of Science and Technology seeks applicants for joint tenure-track positions at the rank of Assistant Professor or Associate Professor. The School is seeking applicants with expertise in interdisciplinary areas, such as super-resolution imaging and biological physics, that bridge life science, physics, and chemistry. Successful applicants should have a doctoral degree plus several years of postdoctoral experience. They will be expected to establish an independent, internationally recognized research program and to contribute to the undergraduate and graduate teaching missions of the School.

The School of Science is located in the vibrant international atmosphere of the University, on a quiet, picturesque sea-side campus, just 40 minutes from downtown Hong Kong. Teaching and research are carried out in an outstanding intellectual environment that is rich in technical resources. The medium of instruction in the University is English.

Starting salary will be commensurate with qualifications and experience. Fringe benefits including medical/dental benefits and annual leave will be provided. Housing benefits will also be provided where applicable. The School of Science is committed to diversity in its ranks and strongly supports equal opportunity employment.

Applications should include a curriculum vitae, a short statement of research interests and the names and addresses of three individuals who can serve as referees for the candidate. These materials should be sent to Prof. Yung Hou Wong, Chair of **the Adhoc Joint Search and Appointment Committee for Interdisciplinary Recruitment, Division of Life Science, The Hong Kong University of Science and Technology, Clear Water Bay, Kowloon, Hong Kong**. Electronic submissions are strongly encouraged (email: indissearch@ust.hk). Review of applications will start immediately and will continue until the positions are filled.

(Information provided by applicants will be used for recruitment and other employment-related purposes.)

Be the difference that drives our excellence.

MACC Fund Endowed Professor in Pediatric Oncology

The Department of Pediatrics and the Cancer Center of the Medical College of Wisconsin (MCW) and The Division of Hematology-Oncology-Bone Marrow Transplant at Children's Hospital of Wisconsin (CHW) invite applicants and nominations for a visionary leader to be the MACC (Midwest Athletes Against Childhood Cancer) Fund Endowed Professor in Pediatric Oncology. This is an opportunity to build and lead a cancer research program with the support of a well-established, nationally recognized Pediatric Hematology-Oncology-Bone Marrow Transplant program.

The candidate will have the resources and the expectations to establish a vigorous extramurally funded research program and participate in collaborative interdisciplinary research projects. The candidate will lead and expand oncology research in the Department of Pediatrics. The MACC Fund Professor will be provided the resources to mentor young investigators in Pediatric Oncology.

Cancer research is a top priority of MCW and CHW. Under new leadership, the Cancer Center has expanded space and resources, enhanced its research programs and has developed an ambitious plan for growth. Pediatric oncology is an essential component of this growth.

Applicants must have an MD or MD PhD degree in a relevant area and a strong record of research accomplishments. Competitive salary, start-up funds and laboratory space are available to successful candidates.

Interested applicants should submit a letter of interest, statement of research goals and Curriculum Vitae to the MACC Fund Professor Search Committee at **facultyaffairs@mcw.edu**. Questions may also be submitted at this email address or to the Office of Faculty Affairs at 414-955-8666.

Medical College of Wisconsin encourages application from women and minority candidates. Equal Opportunity/Affirmative Action Employer M/F/D/V

MEDICAL COLLEGE OF WISCONSIN

THE UNIVERSITY OF HONG KONG
香 港 大 學

School of Biological Sciences

Applications are invited for the following three tenure-track appointments in the School of Biological Sciences, from as soon as possible. The position will initially be made on a three-year term basis, with the possibility of renewal and with consideration for tenure during the second three-year contract. For exceptionally outstanding candidates, appointments can be made with tenure.

Current strategic research areas of the School include: Food Safety and Food for Health, Endocrinology, Ecology, and Plant Evolution and Adaptation. Further information about the School can be obtained at http://www.biosch.hku.hk/.

(1) Associate Professor/Assistant Professor in Ecology (Ref.: 201300539)

(2) Associate Professor/Assistant Professor in Endocrinology (Ref.: 201300540)

(3) Associate Professor/Assistant Professor in Molecular Toxicology/Food Toxicology (Ref.: 201300566)

For post (1), candidates with a strong publication record in any area of ecology are encouraged to apply, although preference will be given to those with expertise in Biodiversity-Ecosystem Function relationships. The appointee must be able to contribute strongly to the strategic research area of ecology in the School. He/She should be able to teach a broad spectrum of courses within the general area of ecology. **For post (2)**, applicants should have a strong publication record in endocrinology, although preference will be given to those with expertise in biopeptide. The appointee must be able to contribute to at least one of the strategic research areas of the School. The appointee is expected to teach courses related to endocrinology/molecular biology/cell biology. **For post (3)**, applicants should have a strong publication record in Molecular Toxicology and/or Food Toxicology, and be able to contribute to at least one of the strategic research areas of the School. The appointee is expected to teach courses related to food toxicology, food safety, environmental toxicology and molecular toxicology. Applicants who have responded to the previous advertisement (Ref.: 201101147 and 201300065) need not re-apply.

A globally competitive remuneration package commensurate with the appointee's qualifications and experience will be offered. At current rates, salaries tax does not exceed 15% of gross income. The appointment will attract a contract-end gratuity and University contribution to a retirement benefits scheme, totalling up to 15% of basic salary, as well as leave, and medical benefits. Housing benefits will be provided as applicable.

For enquiries about the existing research activities and the specific job requirements, please write to Professor S.S. Wu, Director of the School of Biological Sciences (e-mail: rudolfwu@hku.hk). Interested applicants should submit a completed application form, together with a full C.V., a research plan, and a statement on teaching philosophy to scsbs@hku.hk. Please indicate clearly the reference number and *which* level they wish to be considered for in the subject of the email. Application forms (341/1111) can be obtained at http://www.hku.hk/apptunit/form-ext.doc. Further particulars can be obtained at http://jobs.hku.hk/. **Closes August 31, 2013**.

The University thanks applicants for their interest, but advises that only shortlisted applicants will be notified of the application result.

The University is an equal opportunity employer and is committed to a No-Smoking Policy

AWARDS

eni
award
2013

ideas for a brighter future

eni award is the prize granted to the world's most outstanding researchers in the field of energy efficiency.
Only the most brilliant ideas can give rise to a new energy.
The award ceremony was held at Palazzo Quirinale in Rome, in the presence of the President of the Republic.

eni
eni.com

POSITIONS OPEN

JOHNS HOPKINS
SCHOOL *of* MEDICINE

Director of the Center for Cell Dynamics

The Institute for Basic Biomedical Sciences at Johns Hopkins University is seeking an accomplished scientist to lead the Center for Cell Dynamics (**http://www.centerforcelldynamics.org/**). The goal of the Center is to define the sequence of molecular events that control key cellular behaviors, including cytokinesis, chemotaxis, excitability, and synapse formation through analysis of spatially localized, dynamic events. The Center includes 15 faculty from 8 departments in the School of Medicine, who share an interest in understanding how cellular and molecular dynamics lead to normal development and disease.

Applicants should have a Ph.D. or M.D., a record of outstanding research accomplishments, and strong leadership experience. The Center Director will receive a primary appointment in an appropriate department in the School of Medicine, and have access to considerable resources to recruit additional faculty and enhance the Center's research capabilities. Successful applicants will be expected to establish a significant, independent research program, and participate in graduate and medical student instruction. The Johns Hopkins University is committed to enhancing the diversity of its faculty and encourages applications from women and minorities.

Applicants should submit a single PDF file containing curriculum vitae and a brief description of current and future research plans to the Chair of the Search Committee, at **CellDynamicsSearch@jhmi.edu**. Deadline for applications is **September 1st, 2013**.

Johns Hopkins University is an EEO/AA Employer.

CONFERENCE

Partnering Registration Open!

Towards A New Biotechnology Revolution

BioJapan 2013
World Business Forum
October 9th -11th, 2013
Yokohama, JAPAN

BioJapan is the largest Bio business related partnering event in Asia. Make full use of the matching system and arrange meetings that are sure to lead to new business opportunities!

Organizer

BioJapan Organizing Committee
ICS Convention Design, Inc.

www.ics-expo.jp/biojapan